



QUENCH - LOCA - REPORTS Nr. 1

**Results of the commissioning  
bundle test QUENCH-L0 performed  
under LOCA conditions (SR-7571)**

J. Stuckert, M. Große, C. Rössger, M. Steinbrück, M. Walter





**Karlsruher Institut für Technologie**

in der Helmholtz-Gemeinschaft

Wissenschaftliche Berichte

**QUENCH-LOCA-REPORTS Nr. 1**

Results of the commissioning bundle test  
QUENCH-L0 performed under LOCA conditions  
(SR-7571)

J. Stuckert\*, M. Große\*, C. Rössger\*, M. Steinbrück\*, M. Walter\*\*

Institut für Angewandte Materialien:

\* Angewandte Werkstoffphysik (IAM-AWP)

\*\* Werkstoff- und Biomechanik (IAM-WBM)

Programm Nukleare Sicherheitsforschung

Karlsruher Institut für Technologie

2015

## Impressum

Karlsruher Institut für Technologie (KIT)  
Institut für Angewandte Materialien  
Angewandte Werkstoffphysik IAM-AWP-KOR  
Nukleare Sicherheitsforschung  
Hermann-von-Helmholtz-Platz 1  
76344 Eggenstein-Leopoldshafen  
[www.iam.kit.edu/awp/666.php](http://www.iam.kit.edu/awp/666.php)  
DOI: 10.5445/IR/1000083018

# Zusammenfassung

## **Ergebnisse des unter Bedingungen eines LOCA-Störfalls ausgeführten Inbetriebnahmeversuches QUENCH-LOCA-0**

Der QUENCH-L0-Versuch wurde als Inbetriebnahmetest für die QUENCH-LOCA-Testserie konzipiert. Ziel der Bündel-Testserie ist die Prüfung von Brennstabhüllrohrmaterial hinsichtlich Verformung, Bersten und Wasserstoffaufnahme bei der für deutsche Reaktoren repräsentativen LOCA-Auslegungsstörfallszenarien. Des Weiteren sollten mittels detaillierter mechanischer Nachuntersuchungen anhand von Festigkeitseigenschaften Versprödungskriterien für Hüllrohre ermittelt werden. Das QUENCH-L0-Testbündel bestand aus 21 elektrisch beheizten Brennstabsimulatoren mit Hüllrohren aus Zircaloy-4 im Lieferzustand. Jeder Brennstabsimulator wurde separat mittels Krypton druckbeaufschlagt. Enddrücke von 35, 40, 45, 50 und 55 bar wurden eingestellt. Während 185 s wurde die Temperatur in der transienten Phase von 520 auf 1070°C erhöht. Die verringerte Festigkeit und die erhöhte Duktilität des Hüllrohrmaterials führten zu Ballooning und Bersten aller druckbeaufschlagten Brennstabsimulatoren in der transienten Phase. Das Experiment wurde durch Abschrecken des Bündels mit Wasser ohne die übliche Langsam-Abkühl-Phase beendet. Nachuntersuchungen ergaben Werte für die Dehnung zwischen 20% und 35% im Bereich der Hüllrohre mit einem maximalen Oxidationsgrad von 2% ECR. Die Neutronenradiographie der Hüllrohre zeigt eine erhöhte Konzentration von absorbiertem Wasserstoff in den Hüllrohren in der Nähe der geplatzten Beulen. Wasserstoff wurde in bandförmigen Bereichen an der Grenze zur inneren Oxidationszone absorbiert. Zugversuche an den Hüllrohren mit erhöhtem Wasserstoffgehalt zeigten, dass die meisten Hüllrohre am Wasserstoffband reißen.

## **Abstract**

The QUENCH-L0 experiment was defined as commissioning test for the new QUENCH-LOCA test series. The overall objective of this bundle test series is the investigation of ballooning, burst and secondary hydrogen uptake of the cladding under representative design basis accident conditions as well as detailed post-test investigation of cladding mechanical properties to check the embrittlement criteria. The QUENCH-L0 test bundle contained 21 electrically heated fuel rod simulators with as-received Zircaloy-4 claddings. Each rod was separately pressurized with krypton gas with initial pressures of 35, 40, 45, 50, and 55 bar for different rods. The transient phase with heating from 520°C to 1070°C lasted 185 s. The decreased yield strength and increased ductility of the heated cladding resulted in a progressive ballooning and consequent burst of all of the pressurized rods during the transient. The test was terminated by water quenching of the bundle without usual intermediate slow cooling phase. Post-test investigations showed strain values between 20 and 35% at cladding positions with oxidation degree corresponding to 2% ECR. Neutron radiography of cladding tubes has allowed to observe elevated concentration of absorbed hydrogen near to burst positions in band shaped cladding regions formed at the boundary of inner oxidised zone. During the tension test the cladding tubes with increased hydrogen content were ruptured mostly along the hydrogenated bands.

**Contents**

- Introduction ..... 1**
- 1 Description of the Test Facility ..... 3**
- 2 Test Bundle Instrumentation..... 5**
  - 2.1 Hydrogen Measurement System ..... 6
- 3 Data Acquisition and Process Control ..... 7**
- 4 Test Conduct and Pertinent Results..... 7**
- 5 Posttest Examination ..... 9**
  - 5.1 Results of Profilometry with Laser Cladding Scanner ..... 9
    - 5.1.1 The Linear Laser Scanning Table ..... 9
    - 5.1.2 Main Characteristics of the Measuring Device and Procedures ..... 9
    - 5.1.3 Results of the Scans ..... 9
  - 5.2 Nondestructive Eddy Current Measurement ..... 10
  - 5.3 Optical Observation of Outer Cladding Surface ..... 10
  - 5.4 Metallographic Examination ..... 11
  - 5.5 Analysis of Absorbed Hydrogen by Means of Neutron Radiography and Tomography..... 11
    - 5.5.1 Basic Principles ..... 11
    - 5.5.2 Technique..... 12
    - 5.5.3 Results of Radiography ..... 13
    - 5.5.4 Results of Tomography ..... 14
    - 5.5.5 Conclusions of the Neutron Radiography and Tomography Results..... 14
  - 5.6 X-Ray Diffractometry ..... 15
  - 5.7 Measurements of Microhardness ..... 16
    - 5.7.1 Objective and Procedure ..... 16
    - 5.7.2 Results ..... 17
  - 5.8 Mechanical Tests ..... 18
    - 5.8.1 Tensile Tests ..... 18
    - 5.8.2 Ring Compression Tests ..... 19
- 6 Summary and Conclusions ..... 20**
- Acknowledgments..... 21**
- References ..... 21**

## List of Tables

- Table 1: QUENCH Test Matrix 1997 – 2009 (tests on severe accidents)
- Table 2: Design characteristics of the QUENCH-L0 test bundle
- Table 3: Properties of Zircaloy-4 cladding tubes
- Table 4: Main characteristics of the ZrO<sub>2</sub> pellet material, yttria-stabilized (type FZY)
- Table 5: QUENCH-L0; Electrical resistances of rods [mΩ]
- Table 6: Properties of zirconia fiber insulating boards
- Table 7: List of instrumentation for the QUENCH-L0 test
- Table 8: QUENCH-L0; Bundle thermocouples positions
- Table 9: QUENCH-L0; Sequence of events
- Table 10: QUENCH-L0; Burst parameters
- Table 11: QUENCH-L0; Strain parameters
- Table 12: QUENCH-L0; Results of tensile tests
- Table 13: QUENCH-L0; Results of ring compression tests

## List of Figures

- Fig. 1: Flow diagram of the QUENCH test facility.
- Fig. 2: QUENCH Facility - Main components.
- Fig. 3: QUENCH Facility; Containment and test section.
- Fig. 4: QUENCH-L0; Test section with flow lines.
- Fig. 5: QUENCH-L0; Fuel rod simulator bundle (cross section) including rod type indications.
- Fig. 6: QUENCH-L0; Heated fuel rod simulator.
- Fig. 7: QUENCH-L0; Rod pressure control and measurement panel.
- Fig. 8: QUENCH-L0; Rod pressurization.
- Fig. 9: QUENCH-L0; Rod pressurization process.
- Fig. 10: QUENCH-L0; Concept for TC fastening at the test rod.
- Fig. 11: Axial temperature measurement locations in the QUENCH-L0 test section.
- Fig. 12: QUENCH-L0; Test bundle; TC instrumentation and rod designation (top view).
- Fig. 13: QUENCH-L0; Arrangement of the thermocouples inside the corner rods.
- Fig. 14: QUENCH Facility; H<sub>2</sub> measurement with the GAM 300 Mass spectrometer
- Fig. 15: Mass spectrometer sampling position at the off-gas pipe of the QUENCH test facility.
- Fig. 16: QUENCH-L0; QL0 test progression.
- Fig. 17: QUENCH-L0; current limitation of DC generators.
- Fig. 18: QUENCH-L0; Surface thermocouple readings at 17 elevations between -250 and 1350 mm.
- Fig. 19: QUENCH-L0; Temperatures measured by rod cladding (TFS 7/1) thermocouples at -250 mm elevation.
- Fig. 20: QUENCH-L0; Temperatures measured by rod cladding (TFS 7/2) thermocouples at -150 mm elevation.
- Fig. 21: QUENCH-L0; Temperatures measured by rod cladding (TFS 7/3) and shroud (TSH 3/0) thermocouples at -50 mm elevation.
- Fig. 22: QUENCH-L0; Temperatures measured by rod cladding (TFS 7/4) and shroud (TSH 4/90) thermocouples at 50 mm elevation.
- Fig. 23: QUENCH-L0; Temperatures measured by rod cladding (TFS 7/5) and shroud (TSH 5/180) thermocouples at 150 mm elevation.
- Fig. 24: QUENCH-L0; Temperatures measured by rod cladding (TFS) and shroud (TSH 6/270) thermocouples at 250 mm elevation.
- Fig. 25: QUENCH-L0; Temperatures measured by rod cladding (TFS) and shroud (TSH 7/0) thermocouples at 350 mm elevation.
- Fig. 26: QUENCH-L0; Temperatures measured by rod cladding (TFS) and shroud (TSH 8/0) thermocouples at 450 mm elevation.
- Fig. 27: QUENCH-L0; Temperatures measured by rod cladding (TFS) and shroud (TSH 9/180) thermocouples at 550 mm elevation.

- Fig. 28: QUENCH-L0; Temperatures measured by rod cladding (TFS) and shroud (TSH 10/270) thermocouples at 650 mm elevation.
- Fig. 29: QUENCH-L0; Temperatures measured by rod cladding (TFS) and shroud (TSH 11/0), and corner rod internal (TIT D/11) thermocouples at 750 mm elevation.
- Fig. 30: QUENCH-L0; Temperatures measured by rod cladding (TFS) and shroud (TSH 12/90), and corner rod internal (TIT C/12) thermocouples at 850 mm elevation.
- Fig. 31: QUENCH-L0; Temperatures measured by rod cladding (TFS) and shroud (TSH 13/90), and corner rod internal (TIT A/13) thermocouples at 950 mm elevation.
- Fig. 32: QUENCH-L0; Temperatures measured by rod cladding (TFS) and shroud (TSH 14/270) thermocouples at 1050 mm elevation.
- Fig. 33: QUENCH-L0; Temperatures measured by rod cladding (TFS) and shroud (TSH 15/90) thermocouples at 1150 mm elevation.
- Fig. 34: QUENCH-L0; Temperatures measured by rod cladding (TFS) thermocouples at 1250 mm elevation.
- Fig. 35: QUENCH-L0; Temperatures measured by rod cladding (TFS 7/17) thermocouple at 1350 mm elevation.
- Fig. 36: QUENCH-L0; Overview of the TCI (inner cooling jacket).
- Fig. 37: QUENCH-L0; Axial and radial temperature distribution on time of the first burst case.
- Fig. 38: QUENCH-L0; Axial temperature profile TFS internal and external rod group together with TSH, left, and axial temperature profile of all TFS, right, at 112 s (first cladding burst).
- Fig. 39: QUENCH-L0; Axial temperature profile TFS internal and external rod group together with TSH, left, and axial temperature profile of all TFS, right, at 174 s (last cladding burst).
- Fig. 40: QUENCH-L0; System pressure measured at test section inlet P 511, at outlet P 512, and in the off-gas pipe P 601.
- Fig. 41: QUENCH-L0; Argon pressure between shroud and cooling jacket P 406 demonstrates tightness of the shroud.
- Fig. 42: QUENCH-L0; Quench measurement of collapsed water level (L 501), top, water mass flow rate (F 104), center, condensed water (L 701), bottom.
- Fig. 43: QUENCH-L0; Steam rate, top, Hydrogen, center, Krypton, bottom, measured by mass spectrometry (MS).
- Fig. 44: QUENCH-L0; Pressure changing during heating phase; ballooning and burst.
- Fig. 45: QUENCH-L0; Mass spectrometer measurements: Krypton as burst indicator.
- Fig. 46: QUENCH-L0; Consequences of ballooning.
- Fig. 47: QUENCH-L0; Burst positions.
- Fig. 48: QUENCH-L0; Axial burst positions.
- Fig. 49: QUENCH-L0; Tube scanner laser profilometry.
- Fig. 50: QUENCH-L0, rod #1; longitudinal circumferential strain changing (top); azimuthal diameter changing downwards from burst (bottom).
- Fig. 51: QUENCH-L0, rod #2; longitudinal circumferential strain changing (top); azimuthal diameter changing downwards from burst (bottom).



- Fig. 52: QUENCH-L0, rod #3; longitudinal circumferential strain changing (top); azimuthal diameter changing downwards from burst (bottom).
- Fig. 53: QUENCH-L0, rod #4; longitudinal circumferential strain changing (top); azimuthal diameter changing downwards from burst (bottom).
- Fig. 54: QUENCH-L0, rod #5; longitudinal circumferential strain changing (top); azimuthal diameter changing downwards from burst (bottom).
- Fig. 55: QUENCH-L0, rod #6; longitudinal circumferential strain changing (top); azimuthal diameter changing downwards from burst (bottom).
- Fig. 56: QUENCH-L0, rod #7; longitudinal circumferential strain changing (top); azimuthal diameter changing downwards from burst (bottom).
- Fig. 57: QUENCH-L0, rod #8; longitudinal circumferential strain changing (top); azimuthal diameter changing downwards from burst (bottom).
- Fig. 58: QUENCH-L0, rod #9; longitudinal circumferential strain changing (top); azimuthal diameter changing downwards from burst (bottom).
- Fig. 59: QUENCH-L0, rod #10; longitudinal circumferential strain changing (top); azimuthal diameter changing downwards from burst (bottom).
- Fig. 60: QUENCH-L0, rod #11; longitudinal circumferential strain changing (top); azimuthal diameter changing downwards from burst (bottom).
- Fig. 61: QUENCH-L0, rod #12; longitudinal circumferential strain changing (top); azimuthal diameter changing downwards from burst (bottom).
- Fig. 62: QUENCH-L0, rod #13; longitudinal circumferential strain changing (top); azimuthal diameter changing downwards from burst (bottom).
- Fig. 63: QUENCH-L0, rod #14; longitudinal circumferential strain changing (top); azimuthal diameter changing downwards from burst (bottom).
- Fig. 64: QUENCH-L0, rod #16; longitudinal circumferential strain changing (top); azimuthal diameter changing downwards from burst (bottom).
- Fig. 65: QUENCH-L0, rod #17; longitudinal circumferential strain changing (top); azimuthal diameter changing downwards from burst (bottom).
- Fig. 66: QUENCH-L0, rod #18; longitudinal circumferential strain changing (top); azimuthal diameter changing downwards from burst (bottom).
- Fig. 67: QUENCH-L0, rod #19; longitudinal circumferential strain changing (top); azimuthal diameter changing downwards from burst (bottom).
- Fig. 68: QUENCH-L0, rod #20; longitudinal circumferential strain changing (top); azimuthal diameter changing downwards from burst (bottom).
- Fig. 69: QUENCH-L0, rod #21; longitudinal circumferential strain changing (top); azimuthal diameter changing downwards from burst (bottom).
- Fig. 70: QUENCH-L0; Blockage of coolant channel.
- Fig. 71: QUENCH-L0; Eddy current results.
- Fig. 72: QUENCH-L0; Overview of burst structures of rods #1 - #4.
- Fig. 73: QUENCH-L0; Overview of burst structures of rods #5 - #8.
- Fig. 74: QUENCH-L0; Overview of burst structures of rods #9 - #12.
- Fig. 75: QUENCH-L0; Overview of burst structures of rods #13 - #17.
- Fig. 76: QUENCH-L0; Overview of burst structures of rods #18 - #21.
- Fig. 77: QUENCH-L0; Upper and low edges of burst opening of rods #8 and #14.

- Fig. 78: QUENCH-L0; Overview of cladding surface along burst line (azimuth 60°) of rod #1.
- Fig. 79: QUENCH-L0; Overview of cladding surface around burst position of rod #1.
- Fig. 80: QUENCH-L0; Overview of cladding surface near to burst position at different azimuths of rod #1.
- Fig. 81: QUENCH-L0; Overview of cladding surface under burst position of rod #2 at burst azimuth and opposite side.
- Fig. 82: QUENCH-L0; Overview of cladding surface above burst position of rod #2 at burst azimuth of 116°.
- Fig. 83: QUENCH-L0; Overview of cladding surface structure near to burst position for rod #3
- Fig. 84: QUENCH-L0; Overview of cladding surface structure near to burst position for rod # 6.
- Fig. 85: QUENCH-L0; Overview of cladding surface structure near to burst position for rod # 10.
- Fig. 86: QUENCH-L0; Overview of cladding surface Structure near to burst position for rod # 17.
- Fig. 87: QUENCH-L0; Overview of cladding surface of rod #21 at burst azimuth of 41°.
- Fig. 88: QUENCH-L0; “Self-healing” surface cracks developed during ballooning rod #3 (55 bar), angle 140°.
- Fig. 89: QUENCH-L0; Longitudinal sections at outer surface of rod #3 at azimuth shifted with 90° to the burst position.
- Fig. 90: QUENCH-L0; Similar internal and external oxidation degree at burst elevation rod #3 (55 bar).
- Fig. 91: QUENCH-L0; Different internal and external oxidation degree outside burst elevation rod #3 (55 bar).
- Fig. 92: QUENCH-L0; Top view of cross section of rod #8 at elevation 1004 mm. Very thin internal oxide layer at inner surface oppositely to burst opening.
- Fig. 93: QUENCH-L0; Top view of cross section of rod #8 at elevation 1018 mm. Very thin internal oxide layer at inner cladding surface.
- Fig. 94: QUENCH-L0; Neutron radiography method.
- Fig. 95: QUENCH-L0; ICON facility for neutron radiography.
- Fig. 96: QUENCH-L0; Calibration specimens.
- Fig. 97: QUENCH-L0; Calibration procedure.
- Fig. 98: QUENCH-L0; Radiography, rod 15 ( $p_i = 3$  bar).
- Fig. 99: QUENCH-L0; Radiography, rod #3 (initial pressure  $p_i = 55$  bar, time between burst and quench  $\Delta t_q = 104$  s).
- Fig. 100: QUENCH-L0; Neutron radiography for rod #3: intensity distribution.
- Fig. 101: QUENCH-L0; Radiography, rod 6 ( $p_i = 35$  bar,  $\Delta t_q = 93$  s).
- Fig. 102: QUENCH-L0; Radiography, rod 8 ( $p_i = 50$  bar,  $\Delta t_q = 101$  s).
- Fig. 103: QUENCH-L0; Radiography, rod 10 ( $p_i = 50$  bar,  $\Delta t_q = 49$  s).

- Fig. 104: QUENCH-L0; Radiography, rod 17 ( $p_i = 40$  bar,  $\Delta t_q = 71$  s).
- Fig. 105: QUENCH-L0; Tomography, rod 1.
- Fig. 106: QUENCH-L0; Tomography, rod 3.
- Fig. 107: QUENCH-L0; Tomography, rod 5.
- Fig. 108: QUENCH-L0; correspondence between reconstruction of tomography image and plots of mean, minimal, and maximal hydrogen concentrations in rod #1.
- Fig. 109: QUENCH-L0; correspondence between radiography image and plots of mean, minimal, and maximal hydrogen concentrations in rod #3.
- Fig. 110: QUENCH-L0; Results of X-ray diffractometry for the rod #3 at the hydrogen band.
- Fig. 111: QUENCH-L0; Microhardness and elastic indentation modulus of Rod 3 at 225°.
- Fig. 112: QUENCH-L0; Elastic deformation obtained during microhardness testing. Rod 3 at 225°.
- Fig. 113: QUENCH-L0; Microhardness and elastic indentation modulus of Rod 8 at 285°.
- Fig. 114: QUENCH-L0; Elastic deformation obtained during microhardness testing. Rod 8 at 285°.
- Fig. 115: QUENCH-L0; Testing facility for tensile tests.
- Fig. 116: QUENCH-L0; Tensile test at rod #17: dependence of tube segment ductility from oxidation degree.
- Fig. 117: QUENCH-L0; Three types of cladding failure during tensile tests.
- Fig. 118: QUENCH-L0; Rupture positions of rods of inner group after tensile tests; ruler position adjusted to burst middle.
- Fig. 119: QUENCH-L0; Rupture positions of rods of outer group after tensile tests; ruler position adjusted to burst middle.
- Fig. 120: QUENCH-L0; Results of the tensile tests: claddings from the inner group of the bundle.
- Fig. 121: QUENCH-L0; Results of the tensile tests: claddings from the outer group of the bundle.
- Fig. 122: QUENCH-L0; Rupture position outside ballooning rod #17 (40 bar).
- Fig. 123: QUENCH-L0; Testing machine for the ring compression tests.
- Fig. 124: QUENCH-L0; General failure behaviour of the rings.
- Fig. 125: QUENCH-L0; Results of the ring compression tests: rings of the upper part of the claddings.
- Fig. 126: QUENCH-L0; Results of the ring compression tests: rings of the lower part of the claddings.



## Introduction

Under the licensing procedures for pressurized water reactors (PWR) evidence must be given that the impacts of all pipe ruptures hypothetically occurring in the primary loop and implying a loss of coolant can be controlled. The double-ended break of the main coolant line between the main coolant pump and the reactor pressure vessel is considered to constitute the design basis for the emergency core cooling system (ECCS) in a loss-of-coolant accident (LOCA). The break of a main coolant line leads to the loss of coolant in the primary circuit of a PWR and the decrease in system pressure from 15.5 MPa to eventually around 0.32 MPa (boiling point, corresponding to 135°C). Consequently, the remaining coolant in the core as well as the emergency cooling water fed into the reactor core evaporate, the temperature of the fuel elements rises and the fuel rods balloon because the rods contain pressurized filling gas and fission gas products. At a temperature high enough, the metallic wall loses its strength and bursts.

Upon rupture of the reactor coolant line the reactor is shut down. However, as the production of decay heat will be continued, reliable sustainment of the reactor core rod geometry and long-term emergency cooling of the core are required. To retain the core rod geometry it should be established the acceptable limit of cladding embrittlement, which is increased during oxidation in steam. The current LOCA criteria and their safety goals are applied worldwide with minor modifications since the NRC release in 1973 [1, 2]. The criteria are given as limits on peak cladding temperature ( $T_{PCT} \leq 1200^{\circ}\text{C}$ ) and on oxidation level ECR (equivalent cladding reacted) calculated as a percentage of cladding oxidized ( $\text{ECR} \leq 17\%$  using the Baker-Just oxidation correlation). These two rules constitute the criterion of cladding embrittlement due to oxygen uptake and, according to the RSK (Reactor Safety Commission) Guidelines, are included in current German LOCA criteria, too [3].

The results elaborated worldwide in the 1980s on the Zircaloy-4 (Zry-4) cladding tubes behavior (oxidation, deformation and bundle coolability) under LOCA conditions constitute a reliable data base and an important input for the safety assessment of LWRs. With respect to the LOCA conditions for German LWRs, different off-pile [4, 5, 6], the FR2 in-pile [7] single rod as well as the REBEKA bundle tests [8, 9] were performed. It was concluded that the ECC-criteria established by licensing authorities are conservative and that the coolability of an LWR and the public safety can be maintained in a LOCA [10]. In-pile test data (with burn-up up to 35 MWd/kgU) were consistent with the out-of-pile data and did not indicate an influence of the nuclear environment on cladding deformation.

Due to major advantages in fuel-cycle costs, optimised reactor operation, and waste management, the current trend in the nuclear industry is to increase fuel burn-up. At high burn-up, fuel rods fabricated from conventional Zry-4 often exhibit significant oxidation, hydriding, and oxide spallation. Thus, fuel vendors have developed and proposed the use of new cladding alloys, such as Duplex DX-D4, M5<sup>®</sup>, ZIRLO<sup>™</sup> and other. Therefore, it is important to verify the safety margins for high burn-up fuel and fuel claddings with advanced alloys. In recognition of this, LOCA-related behaviour of new types of cladding is being actively investigated in several countries [11, 12]. Due to long cladding hydriding period for the high fuel burn-up, post-quench ductility is strongly influenced by not only oxidation but also hydrogen concentration. The 17% ECR limit is inadequate to ensure post-quench

ductility at hydrogen concentrations higher than  $\approx 500$  wppm [13]. Due to so called secondary hydriding (during oxidation of inner cladding surface after burst), which was firstly observed in JAERI [14], the hydrogen content can reach 4000 wppm in Zircaloy cladding regions around burst [15].

To investigate the influence of these phenomena on the applicability of the embrittlement criteria for the German nuclear reactors it was decided to perform the QUENCH-LOCA bundle test series at KIT in the QUENCH facility, which is supported by the association of the German utilities (VGB). Additionally, the QUENCH-LOCA bundle tests could support experiments performed in-pile and in-cell, respectively, e.g. single-rod tests as those planned in the OECD SCIP-2 project [16]. Compared to single-rod experiments, bundle tests have the advantage of studying the mutual interference of rod ballooning among fuel rod simulators as well as the local coolant channel blockages in a more realistic arrangement.

The first test was performed on 22.07.2010 with Zry-4 cladding tubes not pre-oxidised as commissioning test.

# 1 Description of the Test Facility

The QUENCH facility was constructed 1997 at KIT for investigation of so called hydrogen source term, i.e. to measurement of hydrogen release during the reflood of an overheated reactor core. Since then 15 bundle tests were successfully performed under severe accident conditions ([Table 1](#)). The main components of the QUENCH test facility are presented in [Fig. 1](#). The test section is enclosed by a safety containment with a wall thickness of 5.6 mm and an inner diameter of 801.8 mm. The facility can be operated in two modes: a forced-convection mode depicted in the flow diagram of [Fig. 2](#) and a boil-off mode. In the forced-convection mode (relevant for QUENCH-LOCA-0) superheated steam from the steam generator and superheater together with argon as a carrier gas enter the test bundle at the bottom ([Figs. 3 and 4](#)). The system pressure in the test section for the QUENCH-LOCA test is about 0.3 MPa. The argon, steam and hydrogen produced in the zirconium-steam reaction flow upward inside the bundle and from the outlet at the top through a water-cooled off-gas pipe to the condenser where the remaining steam is separated from the non-condensable gases argon and hydrogen. The water cooling circuits for bundle head and off-gas pipe are temperature-controlled to guarantee that the steam/gas temperature is high enough so that condensation at the test section outlet and inside the off-gas pipe can be avoided. The temperature at the bundle head is kept at 348 K, and the flow rate of the cooling water is ~250 g/s. The off-gas pipe consists of a water-cooled inner pipe with a countercurrent flow and a flow rate of ~370 g/s. The water inlet temperature is controlled at 393 K. Between the off-gas pipe and inner cooling jacket there is stagnant off-gas. The main dimensions of the tubes that make up the off-gas pipe are:

Inner pipe:	outer diameter 139.7 mm, wall thickness 4.5 mm
	total length 3256 mm, material: stainless steel
Inner cooling jacket:	outer diameter 154 mm, wall thickness 2 mm,
	material: stainless steel
Outer cooling jacket:	outer diameter 168.3 mm, wall thickness 5 mm,
	material: stainless steel

The quenching water is injected through a separate line marked “bottom quenching” in [Fig. 4](#). The design characteristics of the test bundle are given in [Table 2](#). The test bundle is made up of 21 fuel rod simulators, each with a length of approximately 2.5 m, and of four corner rods (see cross section in [Fig. 5](#)). The bundle is surrounded by shroud, which has two functions: 1) The shroud acts as steam and gas guide tube; 2) It simulates an adiabatic surrounding of the reactor core. The consideration of heated rod claddings, corner rods and shroud, manufactured from similar zirconium alloys, results in the surface of 37 effective rod simulators.

The fuel rod simulators ([Fig. 6](#)) are held in their positions by five grid spacers, four of Zry-4, and one of Inconel 718 in the lower bundle zone. This bundle design is applied with a pitch of 14.3 mm. All test rods are heated electrically over a length of 1024 mm. The Zry-4 cladding of the fuel rod simulator has an outside diameter of 10.75 mm and a wall thickness of 0.725 mm (see also [Table 2](#)). The cladding properties are listed in [Table 3](#).

Tungsten heating elements of 6 mm diameter are installed in the center of rods and are surrounded by annular yttria-stabilized ZrO<sub>2</sub> pellets. The physical properties of the ZrO<sub>2</sub> pellets are described in [Table 4](#). The tungsten heaters (chemically clean tungsten) are connected to electrodes made of molybdenum (chemically clean molybdenum) and copper (material 2.1293 with Cr 0.8, Zr 0.08 and balance Cu) at each end of the heater. The molybdenum and copper electrodes are joined by high-frequency/high-temperature brazing under vacuum ( $2 \times 10^{-3}$  mbar) using an AuNi 18 powder (particle size <105 μm). The electrical resistance of the internal rod heating system, combined of W heater and Mo-(Cu alloy) electrodes, was measured before (at the end of bundle assembling) and after the test ([Table 5](#)). For electrical insulation the surfaces of both types of electrodes are plasma-coated with 0.2 mm ZrO<sub>2</sub>. To protect the copper electrodes and the O-ring-sealed wall penetrations against excessive heat they are water-cooled (lower and upper cooling chambers filled with demineralized water). The copper electrodes are connected to the DC electric power supply by means of special sliding contacts at the top and bottom. The total heating power is limited by a maximal current of 7200 A and voltage of 9 V. Two DC-generators were used for two groups of rods connected in parallel: 1) 10 internal rods: #1 - #9 and rod #16; 2) 11 external rods: #10-#14 and #16-#21. The measured electric resistance of a single heater (W+Mo+Cu sections) is about 3.3 mΩ at room temperature. This value increases significantly with temperature. The additional resistance of the external electric circuit between the axial end of the single heater and the connection to the generator (sliding contacts, cables, and bolts) is 3.75 mΩ for the inner rod group and 4.05 mΩ for the outer rod group. These values can be taken as constant because the external electric circuit remains at ambient temperature throughout the experiment.

The lower boundary for the lower cooling chamber is a sealing plate made of stainless steel with plastic inlays for electrical insulation, sealed toward the system by O-shaped rings. The upper boundary of the lower cooling chamber is a sealing plate of stainless steel. An insulation plate made of plastic (PEEK) forms the top of the upper cooling chamber, and a sealing plate of Al<sub>2</sub>O<sub>3</sub>, functioning as a heat-protection shield, is the lower boundary of the upper cooling chamber (see [Fig. 6](#)).

In the region below the upper Al<sub>2</sub>O<sub>3</sub> plate the copper electrode is connected firmly to the cladding. This is done by rotary swaging the cladding onto the electrode. In the swaging region a sleeve of boron nitride is put between electrode and cladding for electrical insulation. The axial position of the fuel rod simulator in the test bundle is fixed by a groove and a locking ring in the top Cu electrodes. Referred to the test bundle the fixing point of the fuel rod simulators is located directly above the upper edge of the upper insulation plate. So, during operation the fuel rod simulators are allowed to expand downwards. Clearance for expansion of the test rods is provided in the region of the lower sealing plate. Also in this region, relative movement between cladding and internal heater/electrode can take place.



The test bundle is surrounded by a 3.17 mm thick shroud (79,66 mm ID) made of Zr 702 with a 37 mm thick ZrO<sub>2</sub> fiber insulation (physical properties are given in [Table 6](#)) and an annular cooling jacket made of Inconel 600 (inner tube) and stainless steel (outer tube; see Fig. 5). The annulus between shroud and cooling jacket was filled (after several cycles of degasing) with stagnant argon of 0.22 MPa and was connected to a flow-controlled argon feeding system in order to prevent steam access to the annulus after possible shroud failure. The 6.7 mm annulus of the cooling jacket is cooled by an argon flow. Above the heated zone, i.e. above the 1024 mm elevation there is no ZrO<sub>2</sub> fiber insulation to allow for higher radial heat losses. This region of the cooling jacket is cooled by a water flow (Figs. 3 and 4). Both the lack of ZrO<sub>2</sub> insulation above the heated region and the water cooling force the axial temperature maximum downward.

Insertion of four corner rods avoids an atypically large flow cross section at the outer positions and hence helps to obtain a rather uniform radial temperature profile.

According to LOCA scenarios the fuel rod simulators were loaded by inner pressures. The gas supply system ([Fig. 7](#)) for individual pressurization of rods consists of pressure controller, 21 valves, 21 pressure transducers, and 21 justified compensation volumes for setting of original volume value of 31.5 cm<sup>3</sup> (the compensation is needed because of the absence of empty plenums inside the rod simulators). The gas supply is connected with capillary tubes (with inner diameter 1 mm, length ca. 1.2 m) to each rod at its lower end with drilled copper electrode ([Fig. 8](#)). The gas gap under the cladding is: 0.15 mm in the region of Cu/Mo electrodes and 0.075 mm in the region of W-heater/ZrO<sub>2</sub>-pellets. Before gas filling the rods and gas supply system were evacuated.

At the beginning of experiment, the fuel rod simulators were backfilled with Kr gas to 20 bar. Then, before the transient, they were separately pressurized to the target pressures of 35, 40, 45, 50, and 55 bar as shown in [Fig. 9](#). Different pressure levels were used to investigate the influence of the pressure on the involved processes.

## 2 Test Bundle Instrumentation

The test bundle was instrumented with sheathed thermocouples (TC) attached to the rod claddings ([Fig. 10](#)) at 17 different elevations between -250 mm and 1350 mm and at different orientations according to [Figs. 11 and 12](#). The NiCr/Ni thermocouples (1 mm diameter, stainless steel sheath 1.4541 (X6CrNiTi18-10), MgO insulation) are used for temperature measurement of rod cladding and shroud outer surfaces. The TC tip is held in place by a Zr ferrule welded to the surface. The compensation leads of the thermocouples from the -250 mm to the 850 mm level leave the test section at the bottom of the test section whereas those of the TCs above 850 mm are routed out of the top of the test section to prevent TC cables to pass the hot zone. The thermocouples attached to the outer surface of the rod cladding are designated "TFS" for all heated rods. The shroud thermocouples (designation "TSH") are mounted at the outer surface between -250 mm and 1250 mm. The thermocouples that are installed inside the Zry-4 instrumentation rods at the three corner positions of the bundle (positions A, C and D) are designated "TIT" (see [Fig. 13](#)). The thermocouples of the cooling jacket are installed inside the wall of the inner cooling tube (from -250 mm to 1150 mm, designation "TCI") and at the outer surface of the outer cooling tube (from -250 mm to 950 mm, designation "TCO").

A list of all instruments for experiment QUENCH-L0 installed in the test section and at the test loop is given in [Table 7](#). The distribution of the thermocouples along the bundle is shown in [Table 8](#). No failed thermocouples were detected during the test.

The flow rates of noble gases (Ar, Kr) are regulated with the BRONKHORST flow controllers. Steam and water flows are controlled with the SIEMENS flow controllers. Numerous pressure transmitters from WIKA measure absolute and differential pressures along the gas supply system, at inlet and outlet of the test section.

## 2.1 Hydrogen Measurement System

The released hydrogen is analyzed by a Balzers mass spectrometer (MS) “GAM 300” ([Fig. 14](#)). Due to its location at the off-gas pipe in the facility the mass spectrometer responds almost immediately (less than 10 s). The “BALZERS GAM 300” is a completely computer-controlled quadrupole MS with an 8 mm rod system which allows reliable quantitative measurement of gas concentrations down to about 10 ppm. For the MS measurement a sampling tube is inserted in the off-gas pipe located approx. 2.7 m downstream from the test section outlet (see [Fig. 2](#) and [4](#)). It has several holes at different elevations to guarantee that the sampling of the gas to be analyzed is representative (see [Fig. 15](#)). To avoid steam condensation in the gas pipes between the sampling position and the MS the temperature of the gas at the MS inlet is controlled by heating tapes to be between 110 and 150 °C (the upper operating temperature of the MS inlet valves). This allows the MS to analyze the steam production rate. Besides, the concentrations of the following species were continuously measured by the mass spectrometer during all test phases: argon, hydrogen, steam, nitrogen, oxygen, and krypton. The fuel rod simulators are filled with krypton which can be used as an indicator for a cladding failure. Additionally, the MS is used to control the atmosphere in the facility, e.g., to monitor the gas composition at the beginning of the test.

The temperature and pressure of the analyzed gas are measured near the inlet valve of the MS. The MS is calibrated for hydrogen, oxygen and nitrogen with well-defined argon/gas mixtures and for steam with mixtures of argon and steam supplied by a Bronkhorst controlled evaporator mixing (CEM) device. The MS off-gas is released into the atmosphere because the amount of hydrogen taken out of the system is negligible. A heated measuring gas pump was used to ensure a continuous flow of the steam-gas mixture from the off-gas pipe to the mass spectrometer.

For the MS the hydrogen mass flow rate is calculated by referring the measured H<sub>2</sub> concentration to the known argon mass flow rate according to equation (1):

$$\dot{m}_{H_2} = \frac{M_{H_2}}{M_{Ar}} \cdot \frac{C_{H_2}}{C_{Ar}} \cdot \dot{m}_{Ar} \quad (1)$$

with M representing the molecular masses, C the concentrations in vol% and  $\dot{m}$  the mass flow rates of the corresponding gases.

### 3 Data Acquisition and Process Control

A LabView-based control and data acquisition system is used in the QUENCH facility. Data acquisition, data storage, online visualization as well as process control, control engineering and system protection are accomplished by three computer systems that are linked in a network.

The data acquisition system allows recording of about 200 measurement channels at a maximum frequency of 25 Hz per channel. The experimental data and the date and time of the data acquisition are stored as raw data in binary format. After the experiment the raw data are converted into SI units and stored as ASCII data.

For process control, a system flow chart with the most important actual measurement values is displayed on the computer screen. Furthermore, the operating mode of the active components (pumps, steam generator, superheater, DC power system, valves) is indicated. Blocking systems and limit switches ensure safe plant operation. Operating test phases, e.g. heating or quenching phases, are pre-programmed and can be started on demand during the experiment. The parameter settings of the control circuits and devices can be modified online.

Online visualization allows to observe and to document the current values of selected measurement positions in the form of tables or plots. Eight diagrams with six curves each can be displayed as graphs. This means that altogether 48 measurement channels can be selected and displayed online during the course of the experiment.

The data of the main data acquisition system and of the mass spectrometers were stored on different computers. Both computers were synchronized. The data of the main acquisition system were stored at a frequency of 10 Hz. The mass spectrometer data were recorded at a frequency of approx. 1 Hz during the entire test.

### 4 Test Conduct and Pertinent Results

The test procedure was based on pre-test calculations performed by the Paul Scherrer Institute (PSI, Villigen) using the SCDAP/RELAP5 and IBRAE (Moscow) using the SOCRAT code systems. According to the planned LOCA scenario, the transient phase should be performed with 8 K/s followed by slow cool-down phase and quenching.

The sequence of the test events is represented in [Table 9](#). The experiment started ([Fig. 16](#)) by stabilizing the bundle conditions with an application of electrical bundle power of 4.6 kW (corresponded the linear heat rate of  $\sim 1$  W/cm) in argon - superheated steam mixture (with rates of 6 g/s argon and 2 g/s steam, or specific rates 0.2 g/s/(effective rod) and 0.07 g/s/(effective rod) correspondingly) resulting in maximum bundle temperatures of 800 K. Due to limitation of the maximal electrical current of the DC generators the heating rate of 2.5 K/s was realised only ([Fig. 17](#)).

The transient was initiated by rapidly increasing the electrical power to 27 kW (linear heat rate  $\sim 6$  W/cm) followed by steady increase to 44 kW (linear heat rate  $\sim 10$  W/cm) within 185 s. During this period the temperatures increased from their initial values to a maximum in

excess of 1300 K, as planned. [Fig. 18](#) shows the development of maximum temperature at each elevation (marking TFS x/y means a surface thermocouple for rod x at elevation y). The readings of thermocouples at each bundle elevation are shown in [Figs. 19-35](#). The temperatures of cooling jacket were practically not changed during the whole test ([Fig. 36](#)).

The axial temperature profile in the bundle has a pronounced maximum between 850 and 1050 mm ([Figs. 37-39](#)). There is also a radial temperature gradient due to two reasons: 1) radial heat flux to the shroud, 2) electrical power supplied to internal rod group was higher than the power for external group because both DC generators reached current limit (~3600 A) but electrical resistance of 11 external parallel connected rods is lower than for 10 internal rods.

The experiment continued with power decrease to 3.4 kW to simulate decay heat and subsequent (after delay of 30 s) injection of steam at a nominal of 50 g/s at 215 s, resulting in immediate and rapid cooling of claddings to about 400 K which was caused by entrainment of water condensed in steam pipe line. Intensive evaporation of this water was indicated by sharp system pressure increase at time point of about 220 s ([Fig. 40](#)). The rate of the heat transfer through the shroud and corner rod wall can be estimate on the basis of the delayed reaction of TSH and TIT thermocouples ([Figs. 29-31](#)). The cooling phase was followed by a second, minor reheating to about 660 K and terminated by 90 g/s water injection at 360 s ([Fig. 42](#)). No damage of shroud was observed during the whole test ([Fig. 41](#)). Notable oxidation of bundle was indicated by hydrogen production between 100 and 220 s ([Fig. 43](#)), leading to an integral value of 1 g hydrogen.

The decreased yield strength and increased ductility of claddings during the transient phase resulted in a progressive ballooning and consequent burst of all of the pressurized rods ([Table 10](#)). The first burst occurred 111 s after initiation of the transient phase at about 1069 K at rod 1 which was pre-pressurized to 50 bar. All 20 pressurized rods failed within 63 s ([Fig. 44](#)). The individual rod failures were indicated by internal pressure readings and precisely correlated with krypton peaks measured in the off-gas pipe by mass spectrometer. Two peaks of Kr release indicate failure of inner and outer rod groups ([Fig. 45](#)). The first failed rod was the central rod #1, the last one was the peripheral rod #10. The temperature range for bursts is estimated from thermocouple readings to be between 1049 and 1141 K. The burst time is mainly controlled by the rod temperature, which has a much stronger influence on the burst time than the internal pressure. All pressurized rods revealed axial contraction by ~10 mm due to Zircaloy anisotropy ([Fig. 46](#), right). No significant rod bending was observed.

The radial burst positions of all rods, except the central one, correspond to the hottest rod region and are directed to the bundle centre ([Fig. 47](#)). All bursts are axially located between 930 and 1010 mm ([Fig. 48](#)). The measured burst lengths are between 8 (rod #6) and 19 mm (rod #14) and there is only very weak dependence on internal pressure (slight length increase with increased pressure). No global blockage was formed due to the variation of the ballooning positions.

## 5 Posttest Examination

### 5.1 Results of Profilometry with Laser Cladding Scanner

#### 5.1.1 The Linear Laser Scanning Table

The most recent measuring device added to the evaluation equipment of the QUENCH Workgroup is a Linear Laser Scanner, also known as Profilometer ([Fig. 49](#)). It was custom built by ANT Antriebstechnik GmbH for quantifying the deformations produced on the rods as a result of the QUENCH LOCA experiments. The ballooned parts of the bundle rods submitted to LOCA scenarios acquire a variety of shapes and sizes due to different pressure and temperature conditions. Therefore a precise method to detect the local variations in diameter along the rod was required.

#### 5.1.2 Main Characteristics of the Measuring Device and Procedures

The measuring mechanism is based upon photocells which compare the amount of laser light blocked by the rod in relation to the portion of light that reaches the sensors. The equipment is mounted vertically and supported on a wall of the experimental hall in order to minimize the effects of shocks and vibrations propagated by the floor. The rod to be measured is placed vertically and linked to a stepper motor which is responsible for the precise turning of the rod according to a given number of measurements that should be made each 360°. A resolution of 0.25° is provided. The laser scanner itself moves a predetermined length up or down the driving rails in order to cover a specific section of the examined rod. The smallest vertical step is 100 µm and the maximum length which the scanner can handle is 2000 mm.

Automatic settings allow the scanner to work for many hours without the need of supervision. On the other hand, for safety reasons and because of mechanical limitations, the data gathering is quite slow. A total of approximately 5700 points are measured each hour. This means that a scanning of a 1500 mm rod section takes roughly 4 days considering a measurement every 1 mm and 1°.

All data generated can be processed in various ways in order to determine different information. For instance, it allows the exact location and orientation of each burst, determination of radial strain, calculation of cross-section area reduction and thus blockage. Also, a digital 3D rendered image is generated as a record and for further analysis, since every rod is sooner or later damaged by mechanical testing or cut for metallographic examination.

#### 5.1.3 Results of the Scans

The evaluation of the scans can be divided into azimuthal and longitudinal analysis.

The azimuthal plots ([Figs. 50-69, bottom](#)) clearly show the orientation of the bursts and also give an idea of the shape. It was revealed that the bursts were oriented to the center of the bundle, mainly because of the radial thermal gradient which was established in the test section.

The shape of the bursts vary widely, neither size nor symmetry have any apparent correlation to pressure.

Also based on these scans, the circumferential strains can be calculated ([Table 11](#)), which are depicted on Figs. 50-69, [top](#). There is a clear correlation of the burst mean location and the temperature distribution on the longitudinal axis. Maximum strain of 49% was observed on the inner rod #8, minimum strain of 25.3% was observed on the inner rod #10.

For all rods the deformation starts at elevations about 250 mm and end at 1250 mm. The portions of the rods which suffered more than 5% strain are usually smaller than 185 mm. These high strain sections are not symmetrically distributed around the burst and are located with 75% on the lower levels of the burst.

The blockage is obtained by the sum of the cross-section of the rods along their lengths and subtracted from the void between bundle and shroud. Since the burst locations are scattered between elevations 930 and 1010 mm, the blockage wasn't too significant. As shown in [Fig. 70](#), the maximum blockage occurs at 994 mm and reaches 21% of area reduction. If, hypothetically, all burst were located at the same level, the blockage would be 46%.

## 5.2 Nondestructive Eddy Current Measurement

Before cutting of cladding tubes for further investigations, the oxidation degree of each cladding was measured with the eddy current measurement device ISOSCOPE FMP30 from Helmut Fischer GmbH. The device was calibrated with two plastic foils of 24.3 and 99.3  $\mu\text{m}$  thicknesses, which were disposed to the surface of as-received Zry-4 tube. At least 20 circumferential measurements at each axial position were used to achieve the averaged result. The axial step was 20 mm. The measurement results for nine cladding tubes and one solid corner rod (the calibration for this rod was specially performed) are depicted in [Fig. 71](#). The device shows distance between the gauge and internal metallic layer; i.e. the measured value corresponds to the sum of the thicknesses of  $\text{ZrO}_2$  and  $\alpha\text{-Zr(O)}$  layers. Indeed, the comparison of eddy current results with metallography results (circles in [Fig. 71](#)) confirms this fact.

Two groups of curves are clearly separated in the diagram: a more oxidized inner rod group of the bundle and a less oxidized outer group together with the corner rod. Irregular thickness changings were observed inside of the axial zone with the pronounced ballooning of gas loaded tubes due to deviation of cladding thickness from this parameter for the original calibration sample. Only the unloaded cladding #15 and the solid corner rod show regular axial distribution of the oxidation degree. The most oxidized region is between 850 and 1050 mm, what corresponded to the axial temperature profile ([Fig. 37](#)).

## 5.3 Optical Observation of Outer Cladding Surface

Observations of cladding surface were performed with a Keyence digital microscope equipped with a macroscopic objective. The form of burst openings and the structure of oxidized cladding surface near to openings are shown in [Figs. 72-77](#). It can be seen that the cladding surface is covered with a network of crossed longitudinal cracks developed during the ballooning process. [Figs. 78-87](#) show regions of this "tree bark" structures in details.

Large scale cells of crack network are located near to the burst opening, whereas small scale cells are typical for the cladding side opposite to burst (e.g. Fig. 84 for rod #6, two upper pictures right). It is illustrated in Figs. 79 and 80 for rod #1. The rod #2 has more linear (not cell) structure of cracks (black linear structures in Figs. 81 and 82); the distance between these black lines decreased with the relative azimuth increase. But mostly the crack structure in oxide is the celled structure as for rods #3, #6, #10, #17, and #21 (Figs. 83 – 87 correspondingly). The cell size changed not only circumferentially, but also longitudinally: cell size decreased with increase of the distance to the burst location. The cracks are disappeared practically at distances between 50 and 60 mm from the burst position – accordingly to the sharp strain decrease in upper diagrams of Figs. 50-69. The cell size strongly depends on strain: The higher the strain the larger are the cells.

## 5.4 Metallographic Examination

Large magnification ( $\times 1000$ ) micrographs made by the Keyence microscope at the cladding cross sections evidence wavy structure of  $ZrO_2$  and  $\alpha$ -Zr(O)-layers (Fig. 88): the cracks, growing during the ballooning process, are self-healed due to continuous oxidation in steam. The average azimuthal distance between pits varied between 20 and 50  $\mu m$ , whereas a typical longitudinal distances are 100 – 150  $\mu m$  (Fig. 89).

The metallographic investigation of the cross section of rod #3 at the elevation of the burst middle (962 mm) evidences oxide layer growth at the outer cladding surface as well as oxidation of the inner surface (Fig. 90). The averaged maximal outer oxide thickness of 12  $\mu m$  and corresponding  $\alpha$ -Zr(O) thickness of 16  $\mu m$  was reached at elevation of 947 mm (oxide thickness at some azimuth positions reached 15  $\mu m$ ). The thickness of the inner oxide layer decreases axially, and at the elevation of 982 mm (i.e. 13 mm above the burst opening edge) no inner oxide layer was observed at the azimuth of the burst line (Fig. 91).

Only very thin inner oxide layer was observed opposite to the burst line for rod #8 at the elevation 1004 mm, corresponding to the middle of the burst opening (Fig. 92). The axial extension of internal oxidation is about 11 mm from the burst opening edges, what can be seen with metallographic investigation of corresponding cross sections (Fig. 93 shows layer structures at the elevation of 1018 mm).

The internal cladding oxidation is caused by steam penetration through the burst opening. It can be assumed that the hydrogen, released during the oxidation of the inner cladding surface, propagated in the gap between cladding and pellet up to boundary of the inner oxidised region. Outside of this region there is no more barrier for the absorption of hydrogen by the metal, and this internally oxidised region should be surrounded by hydrided zones. This assumption was confirmed by neutron radiography. Even inside the hydride zones no zirconium hydrides were detected by optical microscopy.

## 5.5 Analysis of Absorbed Hydrogen by Means of Neutron Radiography and Tomography

### 5.5.1 Basic Principles

Neutron radiography is a powerful tool for the determination of hydrogen concentration and distribution in zirconium alloys [17-21]. Hydrogen can be quantitatively and non-destructively

determined with a spatial resolution of about 25  $\mu\text{m}$ . The method was applied for the posttest hydrogen analysis of selected QUENCH-L0 cladding tubes.

Firstly, a short introduction into neutron radiography will be given. [Fig. 94](#) shows a scheme of the experiments. The sample is positioned into a parallel neutron beam. The intensity distribution behind the sample is measured for each pixel. From the intensity the transmission  $T$  can be calculated:

$$T(x, y) = \frac{I(x, y) - I_B(x, y)}{I_0(x, y) - I_B(x, y)} \quad (1)$$

$x$  and  $y$  are the coordinates of the pixel position.  $I$ ,  $I_0$  and  $I_B$  are the intensities behind and before the sample and the background intensity, respectively. From the neutron transmission the total macroscopic neutron cross section  $\Sigma_{\text{total}}$  can be calculated:

$$\Sigma_{\text{total}}(x, y) = \frac{-\ln(T(x, y))}{s(x, y)} \quad (2)$$

$s$  is the neutron path length through the material. The total macroscopic neutron cross section is the sum of the total microscopic cross section  $\sigma$  of the isotopes  $i$  multiplied their number density  $N$ :

$$\Sigma_{\text{total}}(x, y) = \sum_i \sigma_i \cdot N_i = \underbrace{N_{\text{Zry}}(x, y) \overline{\sigma_{\text{Zry}}}}_{\Sigma_{\text{samples reserved}}} + N_{\text{O}}(x, y) \sigma_{\text{O}} + N_{\text{H}}(x, y) \sigma_{\text{H}} \quad (3)$$

In the case of steam oxidation of cladding materials it can be assumed that only the amount of oxygen and hydrogen is changed whereas the amount of zirconium and the alloying elements is not influenced significantly.

In order to reconstruct the specimen three-dimensionally, radiography projections have to be taken from different orientations. According to the sampling theorem, the number  $n$  of projections is connected with the resolution  $d$  and the radius  $R$  of the object circle that fully encompasses the object formed by the rotating of the sample:

$$n = \sqrt{2\pi} \frac{R}{d} \quad (4)$$

### 5.5.2 Technique

The neutron radiography and tomography measurements were performed in two beam times at the ICON facility at the Swiss neutron source SINQ at Paul Scherrer Institute Villigen. [Fig. 95](#) shows QUENCH-L0 rods mounted in front of the detector system of the ICON facility. The investigations were performed applying the so called micro-tomography setup providing the highest resolution (pixel distance 13  $\mu\text{m}$ ). The field of view is 28 mm x 28 mm. The samples were scanned through the field of view with a step width of 20 mm.

For the radiography investigations exposure times of 300 s were applied. The specimens were measured horizontally. For the tomography 625 projections per sample position were



measured with an exposure time of 85 s per frame. According to Eq. (4) this results in a lateral resolution of about 50  $\mu\text{m}$ . In order to fit the detector resolution to the sampling theorem and save measurement time, the number of image pixels was reduced. 2 x 2 pixels were transformed into one. The specimens were investigated vertical oriented.

### 5.5.3 Results of Radiography

The radiography measurements were performed from 13<sup>th</sup> to 16<sup>th</sup> August 2010. The investigations comprise measurements of the rods #3, #6, #8, #10, #15 and #17. Firstly, the calibration of the correlation between hydrogen concentration and total macroscopic neutron cross section was performed for the experimental setup applied. Calibration specimens were produced by annealing of Zry-4 cladding tube segments in argon/hydrogen atmosphere with different hydrogen partial pressures at various temperatures. [Fig. 96](#) depicts a dependence of neutron cross section from neutron wave length for three different hydrogen contents. The hydrogen uptake of calibration samples was determined by measurement of the weight gain. [Fig. 97](#) shows the results of the calibration. From the slope of the curve the calibration was determined:

$$\frac{H}{Zr} = \frac{\Sigma_{total} - 0.21 \text{ cm}^{-1}}{1.9541 \text{ cm}^{-1}} \quad (5)$$

[Fig. 98, top](#) shows the radiographs taken from rod 15. This rod was not overpressured during the QUENCH test. [Fig. 98, bottom](#) shows the radiograph taken at the axial position  $z = 950 \text{ mm}$ . At this axial position the highest temperatures occurred during the test. From the intensity distribution a total macroscopic neutron cross section of  $0.215 \text{ cm}^{-1}$  was determined, which is inside the error bar range for the as-received state. This shows that the effect of the oxide layer has not to be taken into account.

[Fig. 99](#) shows the radiographs of the ballooning region of rod #3 in two orientations. On both sides of the burst opening sloping and bended hydrogen containing bands can clearly be seen. [Fig. 100](#) gives the intensity distribution perpendicular to the rod axis in the range marked at radiograph of [Fig. 99](#). An asymmetric intensity distribution is found. Because of the uncertainties concerning the wall thickness and the contribution of backwards and forewards wall to the attenuation of the neutron beam, it is not possible to determine the hydrogen concentration from this intensity distribution seriously. In the direct burst region and far away from the burst opening no hydrogen is detectable.

The non-symmetric hydrogen distribution has consequences for the interpretation of the hydrogen determination in former investigations of LOCA specimens [14, 15]. Here the hydrogen was determined by hot extraction of rod segments. This method determines only the mean hydrogen concentration of the segment. In the case of a sloped hydrogenated band, the width of this band is lower but the hydrogen concentrations in this band is higher than determined by hot extraction of segments.

[Figs. 101 – 104](#) show radiographs of the rods #6, #8, #10 and #17. Different sizes of burst openings are obvious. Hydrogen containing bands are found in the rods #6, #8 and #17 but not in the rod #10. No clear dependence of the hydrogen uptake on the inner pressure is observed. The main parameter determining the hydrogen uptake is the time between

bursting and quenching  $\Delta t_q$ . In this time the gas filled in the rod flows out of the burst opening, the steam penetrates into the rod and oxidation of the inner cladding surface takes place in significant manner. It seems to be that a threshold time exists in which the fill gas flows out. This threshold is between 49 s (rod #10, no hydrogen containing band) and 71 s (rod #17, hydrogen containing band exists).

#### 5.5.4 Results of Tomography

As discussed before, a serious determination of the hydrogen concentration in the sloped and bended bands is not possible. But, neutron tomography provides values of the total macroscopic neutron cross section averaged for each voxel ( $50 \times 50 \times 50 \mu\text{m}^3$ ). The calibration of the tomography data was performed on the basis of a linear dependence of  $\Sigma_{total}$  on the H/Zr atomic ratio according to equation (5). The gray value outside the hydrogenated band was set a cross section of  $0.21 \text{ cm}^{-1}$ . The connection between cross section and the other gray values was extrapolated. However, this analysis has to be proved by tomography measurements of calibration specimens in future beam times. Therefore, the quantitative results given below are preliminary.

The tomography investigations were performed from 10<sup>th</sup> to 16<sup>th</sup> September 2010. Three specimens were measured, rod #1 and #3 completely and rod #5 at one side of the burst opening.

Fig. 105, right shows cross sections of rod #1 in the region of a hydrogenated band. The darker the gray level, the higher is the total macroscopic neutron cross section. In the picture of the cross section two dark segments are visible. The hydrogen concentration seems to be homogeneous over the tube wall thickness.

The investigation of the interesting range of rod #1 needed the tomography of three sample regions moved by 20 mm. The three data sets were combined to one. Fig. 105 left gives a colored 3D projection of the results. The dark blue hydrogen containing bands are clearly visible. Similar 3D reconstructions were performed for rods #3 and #5 (Fig. 106 and Fig. 107 correspondingly). The hydrogen distribution is very complicated (Fig. 108, Fig. 109). The analysis is not yet finished. Maximal hydrogen concentrations of 2560, 2140, 1940 and 1050 wppm were determined for the rods #1, #3, #7 and #14, respectively.

#### 5.5.5 Conclusions of the Neutron Radiography and Tomography Results

Neutron radiography and tomography give new information about the secondary hydrogen uptake during LOCA scenarios, not yet obtained by other methods. Spatial resolutions of about 25 and 50  $\mu\text{m}$  were achieved in the radiography and the tomography investigations, respectively.

Hydrogen is distributed in sloped and bended bands in regions close to the burst position. Positions of hydrogen containing bands for rods #1 and #8 correspond to boundaries of inner oxide regions observed by the metallographic investigations. The extension of the hydrogenated zone seems to depend on the time between bursting and quenching. No influence of inner pressure or burst opening length is obvious. For a quantitative analysis

neutron tomography is needed. Maximal hydrogen concentrations of about 2500 wppm were found.

## 5.6 X-Ray Diffractometry

X-ray diffractometry (XRD) analysis was applied to investigate the phases existing in the tested rods including possibly precipitated hydrides. A Seifert C3000 equipped with a Meteor 1D linear detector and a MZ4 goniometer was used. As commonly applied in this technique, a monochromatic radiation corresponding to the copper  $\text{CuK}\alpha$  emission line was used ( $E = 8047 \text{ eV}$ ,  $\lambda = 0.154 \text{ nm}$ ). The objective of crystallographic diffraction was to identify crystalline components in a sample by a search/match method [22]. Since the X-ray diffraction pattern of a pure substance is very characteristic, the powder diffraction method can be used for identification and quantification of polycrystalline phases. Additionally, the areas under the peak are related to the amount of each phase present in the sample. However, the method can fail if for instance one of the crystalline phases is strongly texturized, the grain size of a phase is less than a few microns or if the lattice is strongly disturbed. The CIF files (Crystallographic Information File) for inorganic compounds ("Inorganic Crystal Structure Database") can be consulted at the "Fachinformationszentrum Karlsruhe" (FIZ) and also at the JCPDS files.

Each of the two samples were arranged of 4 small longitudinal strips of ca.  $0.725 \text{ mm} \times 1 \text{ mm} \times 15 \text{ mm}$  that were axially cut out from rod #3 (at the hydrogen enriched zones) and from as-received Zry-4 cladding rod, respectively. The X-rays reach a maximum depth of about  $15 \mu\text{m}$ , so that the most important factor is a sufficient probe area which should also be flat [23].

In both of the obtained diffraction pattern only metallic zirconium was detected (Fig. 110). The agreement with the JCPDS card 5-665, corresponding to pure metallic zirconium, revealed to fit almost perfectly, despite the presence of 1.5 wt% tin and the intrinsic crystallographic texture of the samples extracted from the rods. The line shift of  $\approx 0.1^\circ$  between the pattern obtained from the as-received specimen and the specimen from the hydrogen enriched zone was observed. This indicates that hydrogen is at least partially dissolved in the  $\alpha$ -Zr lattice.

The green and red bars shown in Fig. 108 represent the diffraction peaks of  $\delta$ - and  $\epsilon$ -Zr hydrides, respectively, accordingly to JCPDS card numbers 5-665 and 36-1340. The detection limit of the applied laboratory diffractometer is about 2 vol%. A raw estimation shows that this detection limit corresponds to a hydrogen concentration less than 370 wppm for hydrogen bonded in zirconium hydrides. This is a factor of about 4 lower than the results obtained by neutron radiography. The discrepancy can be explained by 1) partial solution of hydrogen in the lattice, and/or 2) a low grain size and/or a strong lattice distortion of the hydrides.

Whereas the integral intensity of a Bragg lines depends on the chemical position, the crystalline structure, the volume fraction and the texture of the phase, the width of the reflection is determined by the crystallite size and lattice distortion. According to Scherrer's formula, the line broadening due to low grain size  $\Delta B \sim \lambda/L$  becomes noticeable for grain sizes less than  $L \sim 100 \text{ nm}$ . From the metallography investigations it is known that no hydrides are visible by optical microscope (visibility limit  $\sim 1 \mu\text{m}$ ). Therefore, the results of both methods, XRD and metallography are consistent and give hints that the size of the hydrides - if existent

- is very small. However, both methods are not appropriate in this case to deliver information on the existence, size and structure of zirconium hydrides. Therefore it is intended to apply other methods like neutron small-angle scattering of specimens loaded with deuterium and transmission electron microscopy to get more information on the status of hydrogen in zirconium additionally to solid solution indicated with XRD.

## 5.7 Measurements of Microhardness

### 5.7.1 Objective and Procedure

The evaluation by microhardness measurements may indicate the changes of mechanical properties due to variation of microstructure or chemical composition of a material throughout a determined region. Since the neutron tomography examinations revealed the existence of hydrogen containing bands around the bursts of some rods, it was to investigate to which extent the local properties of Zry-4 were altered at these positions. Beside measurement of the Vickers hardness values, the reduced elastic modulus and the amount of elastic deformation were estimated. Microhardness was analyzed using stepwise indentation with the simultaneous measurement of load and depth. However, the result obtained by this procedure is strongly dependent on the load applied, as well as on the sample preparation. Thus, the results are to be analyzed in a more comparative way rather than on its absolute values. The dependence of hardness by the load is known as "indentation size effect"- ISE. Up to now, various factors such as strain-hardening and friction effects have been linked to the phenomenon of ISE [24, 25].

The Young's modulus is obtained by the derivative of the unloading curve. Usually, the values at the lower end of the unloading curve are excluded from the calculations because of the intrinsic non-linearity. Relation between Young's Modulus  $E$  and measured reduced elastic Modulus  $Er$  is given by:

$$E = \frac{1-\vartheta_s^2}{\frac{1}{Er} - \frac{1-\vartheta_i^2}{Ei}} \quad (6)$$

$$Er = \frac{\sqrt{\pi}}{2C\sqrt{A}} \quad (7)$$

where  $\vartheta_s$  is Poisson's ratio of the specimen,  $\vartheta_i$  and  $Ei$  are Poisson's ratio and the elastic modulus of the diamond indenter, respectively,  $C$  is derivative of the unloading curve,  $A$  is the cross area of the indenter prism at maximal penetration. The elastic modulus of the indenter ( $Ei$ ) is 1140 GPa, and Poisson's ratio of the indenter ( $\vartheta_i$ ) is 0.07. At room temperature, the Poisson's ratio of a Zry-4 is about 0.4 [26].

The plastic part of the deformation energies are calculated by integrating the area between the loading and unloading curve, while the area between the maximum load and the unloading curve represents the elastic deformation energy. Details of the evaluation are described elsewhere [27].

The test conduction was based on the ISO 14577-1 Norm and performed on a FISCHER-SCOPE HM2000. A Vickers indenter, a four-sided diamond pyramid with a square base and

a standard apex angle of  $136^\circ$ , was used for the measurements. Probes were cut from the rods and properly prepared; care must be taken to produce a flat probe, any irregularity on the bottom side may lead to wrong readings, as the probe bounces under the applied load. Longitudinal and radial profiles were collected from rods #3 and #8. The load applied of 500 g is reached within 10 s, then held for 15 s, which led to indentations of the order of  $190 \mu\text{m}^2$ . The points were set approximately  $300 \mu\text{m}$  apart from each other and covered a range of 80 mm.

## 5.7.2 Results

Figs. 111 and 113 show the longitudinal distribution of microhardness and the reduced elastic modulus at the vicinity of the bursts for rods #3 and #8, correspondingly. Clearly both parameters were altered significantly at the positions where the hydrogen rich band is located. An increased hardness of the Zry-4 from 220 HV to the maximums of 315 HV and 360 HV were observed for rods #3 and #8, respectively. The width of the portion where changes of mechanical properties were observed, are about 17 mm wide for rod #3 and 12 mm for rod #8. This is somewhat larger than seen on the neutron radiographies on Figs. 99 and 102, however this only a graphical matter with the contrast of pictures. The microhardness outside the bands, around 220 HV, is a little higher compared to that of fresh Zry-4 (typical value for the as-received cladding is 210 HV [28]). The measurements at cross sections showed a radial homogeneous distribution of mechanical properties within of the former  $\beta$ -Zr phase and are in a good accordance with the values measured longitudinally.

The reduced elastic modulus on the other hand shows a sharp decrease within of hydrogen containing zones, reaching minimums of 55 GPa and 62 GPa for rods #3 and #8 respectively. Outside of the hydrogen affected zones the elastic modulus is essentially comparable to the values of fresh Zry-4 which are around 98~101 GPa [28]. The decrease of elastic modulus is accompanied with increase of the elastic deformation part, what illustrated by Figs. 112 and 114.

The maximum of hardness and the minimum of elastic modulus do not coincide perfectly, a cause for this is not known. The reduction of the elastic modulus and simultaneous increasing of hardness seem to be incoherent at first. The substantial increasing of hardness is not reported by the consulted literature because ranges of hydrogen concentration in solution are usually lower than 500 wppm [27], whereas according to the neutron radiography the rods show concentration up to 2560 wppm. However, optical measurements of indentation mark sizes confirm the increased hardness in hydrogen rich zones of the bursts too. A reduction of the elastic modulus of hydrogenated Zircaloy was reported by some prior works, among them [29] and [26]. The decrease of elastic modulus for cladding, hydrogenated at  $800^\circ\text{C}$ , was also observed during the tensile tests with specially prepared single probes [30].

The increase of microhardness and decrease of the elastic modulus within the hydrogenated regions, detected with the neutron radiography, should have strong influence on results of tension and compression mechanical tests with rod claddings.

## 5.8 Mechanical Tests

To determine the residual strength and ductility of QUENCH-LOCA tested claddings, in particular to identify the embrittlement in dependence of the different quench test conditions, tensile tests on relevantly long cladding sections were performed. Additionally, standard ring compression tests were conducted in order to compare the results with results from similar former investigations.

### 5.8.1 Tensile Tests

#### Test set-up

The tensile tests were carried out using a universal testing machine from INSTRON (type 4505, 50 kN load cell), equipped with specially developed grip holders ([Fig. 115](#)). The experiments were performed displacement-controlled with a displacement rate of 4 mm/min. To clamp the tubes without deforming their end sections, exact fitting end plugs were mounted. Since a quench tested cladding usually shows an inhomogeneous  $ZrO_2/\alpha-Zr(O)$  layer thickness along the main tube axis, the specimens were optically subdivided with paint markers to determine both the global and the local axial elongation ([Fig. 116](#)) during a test by using a CCD-camera measurement system. The initial gauge length  $l_0$  of a specimen in general was 500 mm and a sample was prepared in that way, that the ballooning section was positioned in the axial center. To increase the resolution of the optical measurement device, two cameras were used for the tests. However, with respect to a central position of the ballooning section, some specimens which were used in previous investigations, such as neutron radiography/tomography investigations (chapter 5.5), had to be cut to a measuring length of 250 mm (#01, #04, #05, and #07). For these samples, only one camera was used during an experiment. The strain was calculated from the captured pictures by using the Digital Image Correlation and Tracing program provided by MATLAB [31] and the stress was calculated by using average values of the measured initial inner and outer diameters from the ends of a tube.

#### Results

The experiments showed, that the failure behaviour of the single claddings is mainly influenced by the morphology of the related pre-cracks inside the ballooning section. If the burst geometry shows a discontinuity like a buckle or a small cross-crack, failure occurs at these positions, based on stress concentrations. If the burst shape is free from discontinuities, in general failure occurs in dependence of the position of a cladding within the bundle. Based on higher degrees of oxidation/hydrogenation, claddings of the inner rod group of the bundle (rods #01 - #09) fail mainly within the region of the hydrogen affected zones (compare 5.5.4), whereas claddings of the outer rod group of the bundle fail after necking with significant distances from the ballooning sections ([Fig. 117](#), [Fig. 118](#) and [Fig. 119](#)). In general it can be observed, that in particular the specimens from the inner group of the bundle show low strength and strain values at fracture. Only one specimen of inner group (rod #09) failed after distinctive plastic deformation. In contrast, single claddings from the outer group partly show high plastic deformations up to fracture, even when they failed within the burst region ([Fig. 120](#) and [Fig. 121](#), [Table 12](#)). However, one anomaly was observed at

cladding #17. Based on a constraint caused by a stuck pellet, failure was forced due to increasing stress concentrations close to the pellets edges with increasing plastic deformation and occurred obviously too early after slight necking (Fig. 122). A significant dependency of the failure behaviour on the length of a specimen, as well as from the pre-pressure in the quench test, could not be observed.

## 5.8.2 Ring Compression Tests

### Test set-up

The ring compression tests were also carried out using the INSTRON universal testing machine 4505. To measure the exact displacement during a test, the rings were compressed between two SiC-disks (very high stiffness) within the machine, which are connected via Al<sub>2</sub>O<sub>3</sub>-plates with a high resolution LVDT (linear variable differential transformer) position sensor (Fig. 123). The experiments were performed displacement controlled with a displacement rate of 1 mm/min. In order to protect the testing machine against overloads, the displacement was limited to a maximum value of 8.5 mm. Since the rings need a cylindrical shape in order to carry out accurate tests with a linear load application at the beginning, 10 mm rings were cut from the upper and the lower part of the specimens which were used later on for the tensile tests (i.e. in general enough far away from the ballooning region to have an almost ideal cylindrical geometry).

### Results

Due to the axial gradient of the oxidation degree along an entire cladding, the less oxidized rings from the upper section in general showed clearly better mechanical properties than the more oxidized rings from the lower section. All samples from above the burst region failed ductile, based on plastic instability (buckling). In contrast, half of the specimens from below the ballooning section failed by fracture and half of the specimens failed ductile also based on plastic instability (Fig. 124, Fig. 125 and Fig. 126). Like buckling, fracture always occurred within the region of highest stresses on the left or right hand side of a specimen. A dependency of the failure behaviour from the position of a cladding inside the bundle, as well as from the pre-pressure in the quench test, could not be seen. However, in contrast to the tensile tests it was observed, that the rings prepared from shorter (tensile) specimens, i.e. rings with a higher degree of oxidation based on a lower distance to the burst position (#01, #04, #05 and #07; marked with \*), showed clearly lower values of the load and displacement at fracture, in particular the upper rings (Table 13).

## 6 Summary and Conclusions

The conduct of the QUENCH-L0 test at KIT proved that the QUENCH facility is suitable for LOCA bundle tests. Two shortcomings turned out during the conduct of this commissioning experiment: 1) The intended heat-up rates during the transient of 8 K/s were not reached due to current limitations of the DC generator. This will be improved for the next test by a modified heater design and/or the purchase of a more powerful DC generator; 2) Rapid cool-down already occurred with initiation of increased steam flow (50 g/s) due to entrained water droplets. This has already been smoothed out by the installation of improved trace heating.

The data evaluation showed typical ballooning and burst processes for all 20 pressurized rods (pressure values 35, 40, 45, 50 and 55 bar). All burst cases took place during the transient heating phase at peak bundle temperatures between 1053 and 1133 K. Burst opening lengths between 8 and 20 mm were measured.

A recently installed laser profilometer allowed very precise and detailed measurement of cladding strain. Measured maximal circumferential strains are between 20 and 40% at hottest bundle elevations between 850 and 1050 mm. Maximal blockage of cooling channel is 21% at elevation of 995 mm.

The investigation of the outer surface of cladding upwards and downwards from burst showed the development of longitudinal oxidized micro cracks, which were formed during ductile extension of metallic substrate.

Oxide layers were developed on outer and inner cladding surface near to burst elevations. Only external oxide layer was observed outside away from burst positions. A maximal oxide layer thickness  $\delta_{ox} \approx 15 \mu\text{m}$  (ECR  $\approx 2\%$ ) was measured.

Neutron radiography showed the formation of banded, not axial symmetric hydrogen containing bands with a width of about 10 mm at the boundary of cladding inner oxidized area. Formation of these hydrogen bands was observed for rods with time interval between burst and quench initiation of more than 70 s. A hydrogen content up to 2550 wppm at band locations was measured by means of neutron tomography.

Measurements of microhardness showed increased hardness values within the hydrogenated regions (360 HV; to comparison: as produced Zry-4 has 210 HV).

No hydride formation was observed by means of optical microscopy. X-ray diffractometry gave also no indication of zirconium hydride precipitates, but showed at least partial hydrogen solution in lattice. However these both methods are not suitable to exclude the presence of very fine hydrides of nano-meter size.

During ring compression tests it was observed, that the rings with a higher degree of oxidation showed clearly lower values of the load and displacement at fracture.

The cladding tensile tests showed that the specimens of the inner rod group of the bundle (rods #01 - #09) fail mainly within the region of the hydrogen affected zones, whereas



claddings of the outer rod group of the bundle fail after necking at significant distances from the ballooning sections.

## Acknowledgments

The QUENCH-LOCA experiments are supported and partly sponsored by the association of the German utilities (VGB).

The broad support needed for preparation, execution, and evaluation of the QUENCH-L0 experiment is gratefully acknowledged. In particular, the authors would like to thank Mr. J. Moch for the assembly including instrumentation as well as disassembly of the test bundle, Mr. H. Leiste for the X-ray diffractometry measurements, Mrs. U. Peters for the metallographic examinations and the photographic documentation, Mrs. M. Heck for her very detailed draft review and corrections.

The determination of the test protocol was based on numerous calculations with SCDAP/RELAP5 and SCDAPSIM performed by Dr. J. Birchley, Paul Scherrer Institute (PSI), Switzerland.

## References

- [1] Atomic Energy Commission Rule-Making Hearing, Opinion of the Commission, Docket RM-50-1, 28 December, 1973.
- [2] G. Hache and H. M. Chung, "The History of LOCA Embrittlement Criteria," NUREG/CP-0172, May 2001, pp. 205-237.
- [3] RSK-Leitlinien für Druckwasserreaktoren. Ursprungsfassung (3. Ausgabe vom 14. Oktober 1981) mit Änderungen vom 15.11.1996.  
<http://www.rskonline.de/downloads/8110dwr.pdf>
- [4] P. Hofmann, S. Raff. Verformungsverhalten von Zircaloy-4-Hüllrohren unter Schutzgas im Temperaturbereich zwischen 600 und 1200°C. Wissenschaftliche Berichte, KFK-3973, Karlsruhe, 1981.  
<http://bibliothek.fzk.de/zb/kfk-berichte/KFK3168.pdf>
- [5] L. Schmidt, H. Lehning, D. Piel. Berstversuche an Zircaloy-Huellrohren unter kombinierter mechanisch-chemischer Beanspruchung (FABIOLA). In: Projekt Nukleare Sicherheit. Jahresbericht 1982. Kfk-3350 (Juli 83) S.4200/69-4200/70.
- [6] M. E. Markiewicz, F. J. Erbacher. Experiments on Ballooning in Pressurized and Transiently Heated Zircaloy-4 Tubes. Wissenschaftliche Berichte, KFK-4343, Karlsruhe, 1988.  
<http://bibliothek.fzk.de/zb/kfk-berichte/KFK4343.pdf>
- [7] E. H. Karb, M. Prüßmann, L. Sepold, P. Hofmann, G. Schanz. LWR Fuel Rod Behavior in the FR2 In-pile Tests Simulating the Heatup Phase of a LOCA. Final Report. Wissenschaftliche Berichte, KFK-3346, Karlsruhe, 1983.  
<http://bibliothek.fzk.de/zb/kfk-berichte/KFK3346.pdf>

- [8] K. Wiehr. REBEKA-Bündelversuche Untersuchungen zur Wechselwirkung zwischen aufblähenden Zircaloyhüllen und einsetzender Kernnotkühlung. Abschlußbericht. Wissenschaftliche Berichte, KFK-4407, Karlsruhe, 1988.
- <http://bibliothek.fzk.de/zb/kfk-berichte/KFK4407.pdf>
- [9] F. J. Erbacher, H. J. Neitzel, K. Wiehr. Cladding Deformation and Emergency Core Cooling of a Pressurized Water Reactor in a LOCA. Summary Description of the REBEKA Program. Wissenschaftliche Berichte, KFK-4781, Karlsruhe, 1990.
- <http://bibliothek.fzk.de/zb/kfk-berichte/KFK4781.pdf>
- [10] F. J. Erbacher, S. Leistikow. A Review of Zircaloy Fuel Cladding Behavior in a Loss-of-Coolant Accident. Wissenschaftliche Berichte, KFK-3973, Karlsruhe, 1985.
- <http://bibliothek.fzk.de/zb/kfk-berichte/KFK3973.pdf>
- [11] J.-C. Brachet, V. Vandenberghe-Maillot, L. Portier, D. Gilbon, A. Lesbros, N. Waeckel, and J.-P. Mardon, Hydrogen Content, Preoxidation, and Cooling Scenario Effects on Post-Quench Microstructure and Mechanical Properties of Zircaloy-4 and M5® Alloys in LOCA Conditions. J. ASTM Intl., Vol. 5, No. 5 (2008). Available online as JAI101116 at [www.astm.org](http://www.astm.org).
- [12] T. Chuto, F. Nagase and T. Fuketa. High Temperature Oxidation of Nb-containing Zr Alloy Cladding in LOCA Conditions. Nuclear Engineering and Technology, Vol.41, No.2, March 2009.
- [13] Hee M. Chung. Fuel Behavior under Loss-of-Coolant Accident Situations. Nuclear Engineering and Technology, Vol.37 No.4, August 2005.
- [14] H. Uetsuka, T. Furuta and S. Kawasaki. Zircaloy-4 Cladding Embrittlement due to Inner Surface Oxidation under Simulated Loss-of-Coolant Condition. Journal of Nuclear Science and Technology, 18[9], pp. 705~717 (September 1981).
- [15] M. Billone, Y. Yan, T. Burtseva, R. Daum. Cladding Embrittlement During Postulated Loss-of-Coolant Accidents, NUREG/CR-6967, July 2008.
- [16] OECD SCIP-2 Project:
- <http://www.oecd-nea.org/jointproj/scip-2.html>
- [17] M. Grosse, E. Lehmann, P. Vontobel, M. Steinbrueck: "Quantitative determination of absorbed hydrogen in oxidised zircaloy by means of neutron radiography", Nucl. Instr. & Methods in Phys. Res. A 566 (2006), 739
- [18] M. Große, G. Kühne, M. Steinbrück, E. Lehmann, P. Vontobel, J. Stuckert: „Determination of the hydrogen uptake of steam-oxidised zirconium alloys by means of quantitative analysis of neutron radiographs”, J. Phys.: Condens. Matter 20 (2008), 104263
- [19] M. Grosse, E. Lehmann, M. Steinbrueck, G. Kühne, J. Stuckert: „Influence of oxide layer morphology on hydrogen concentration in tin and niobium containing zirconium alloys after high temperature steam oxidation”, J. Nucl. Mater. 385 (2009), 339

- [20] J. Stuckert, J. Birchley, M. Grosse, B. Jaeckel, M. Steinbrück: „Experimental and calculation results of the integral reflood test QUENCH-14 with M5 cladding tubes.”, *Annals of Nuclear Energy*, 37(2010) S.1036-47, DOI:10.1016/j.anucene.2010.04.015
- [21] M. Grosse, M. Van den Berg, C. Goulet: „In-situ neutron radiography investigations of hydrogen diffusion and absorption in zirconium alloys”, accepted from *Nucl. Instr. & Methods in Phys. Res. A*
- [22] Yang-Soon Park, Yeong-Keong Ha, Sun-Ho Han, Kwang-Yong Jee, Won-Ho Kim. Changes in chemical structure of oxidation reaction layers of Zircaloy-4 and Ti by micro X-ray diffractometry. *Journal of Nuclear Materials* 372 (2008) 59–65
- [23] M.R. Warren, D.K. Bhattacharya.  $\gamma$  Zr-Hydride precipitate in irradiated massive  $\delta$  Zr-Hydride. *Journal of Nuclear Materials* 56 (1975) 121-123
- [24] M. Kuroda, D. Setoyama, M. Uno, S. Yamanaka. Nanoindentation studies of zirconium hydride. *Journal of Alloys and Compounds* 368 (2004) 211–214
- [25] K. Sangwal. On the reverse indentation size effect and microhardness measurement of solids. *Materials Chemistry and Physics* 63 (2000) 145–152
- [26] JiuJun Xu, San-Qiang Shi. Investigation of mechanical properties of  $\epsilon$ -zirconium hydride using micro- and nano-indentation techniques *Journal of Nuclear Materials* 327 (2004) 165–170
- [27] Shinsuke Yamanaka, Daigo Setoyama, Characteristics of zirconium hydrogen solid solution. *Journal of Alloys and Compounds* 372 (2004) 129–135
- [28] Sung-Joon Lee, Hyuk-Sang Kwon and Joung-Soo Kim. Analysis of Microstructure and Corrosion Behavior of Laser Surface. Alloyed Zircaloy-4 with Niobium. *Metals and Materials*, Vol. 6, No. 2 (2000), pp. 145-149
- [29] G. Bertolino, G. Meyera, J. Perez Ipina. Degradation of the mechanical properties of Zircaloy-4 due to hydrogen embrittlement. *Journal of Alloys and Compounds* 330–332 (2002) 408–413
- [30] J. Stuckert, M. Große, M. Walter. Mechanical properties of pre-hydrogenated (600 – 5000 wppm) cladding segments. 16<sup>th</sup> International QUENCH-Workshop, Karlsruhe, November 2010, ISBN 978-3-923704-74-3.
- [31] C. Eberl, D.S. Gianola, K. J. Hemker, *Experimental Mechanics*, DOI: 10.1007/s11340-008-9187-4

**Table 1: QUENCH Test Matrix 1997 – 2009 (tests on severe accidents)**

Test	Quench medium and injection rate	Temp. at onset of flooding <sup>1)</sup>	Max. ZrO <sub>2</sub> before transient <sup>2)</sup>	Max. ZrO <sub>2</sub> (X s) before flooding <sup>2)</sup>	Posttest average ZrO <sub>2</sub> thickness <sup>3)</sup>	H <sub>2</sub> production before / during cooldown	Remarks, objectives
<b>QUENCH-00</b> Oct. 9 - 16, 97	Water 80 g/s	≈ 1800 K			completely oxidized		Commissioning tests.
<b>QUENCH-01</b> Febr 26, 98	Water 52 g/s	≈ 1830 K	312 μm		500 μm at 913 mm	36 / 3	COBE Project; partial fragmentation of pre-oxidized cladding.
<b>QUENCH-02</b> July 7, 98	Water 47 g/s	≈ 2400 K			completely oxidized	20 / 140	COBE Project; no additional pre-oxidation; quenching from high temperatures.
<b>QUENCH-03</b> January 20, 99	Water 40 g/s	≈ 2350 K			completely oxidized	18 / 120	No additional pre-oxidation, quenching from high temperatures.
<b>QUENCH-04</b> June 30, 99	Steam 50 g/s	≈ 2160 K	82 μm		280 μm	10 / 2	Cool-down behavior of slightly pre-oxidized cladding by cold steam injection.
<b>QUENCH-05</b> March 29, 2000	Steam 48 g/s	≈ 2020 K	160 μm		420 μm	25 / 2	Cool-down behavior of pre-oxidized cladding by cold steam injection.
<b>QUENCH-06</b> Dec 13 2000	Water 42 g/s	≈ 2060 K	207 μm <sup>5)</sup>	300 μm, (60 s), SVECHA modeling	670 μm <sup>4)</sup> (60% metal converted to outer ZrO <sub>2</sub> )	32 / 4	OECD-ISP 45; prediction of H <sub>2</sub> source term by different code systems.
<b>QUENCH-07</b> July 25, 2001	Steam 15 g/s	≈ 2100 K	230 μm		completely oxidized	66 / 120	COLOSS Project; impact of B <sub>4</sub> C absorber rod failure on H <sub>2</sub> , CO, CO <sub>2</sub> , and CH <sub>4</sub> generation.

Test	Quench medium and injection rate	Temp. at onset of flooding <sup>1)</sup>	Max. ZrO <sub>2</sub> before transient <sup>2)</sup>	Max. ZrO <sub>2</sub> (X s) before flooding <sup>2)</sup>	Posttest average ZrO <sub>2</sub> thickness <sup>3)</sup>	H <sub>2</sub> production before / during cooldown	Remarks, objectives
<b>QUENCH-09</b> July 3, 2002	Steam 49 g/s	≈ 2100 K			completely oxidized	60 / 400	As QUENCH-07, steam-starved conditions prior to cooldown.
<b>QUENCH-08</b> July 24, 2003	Steam 15 g/s	≈ 2090 K	274 μm		completely oxidized	46 / 38	As QUENCH-07, no absorber rod
<b>QUENCH-10</b> July 21, 2004	Water 50 g/s	≈ 2200 K	514 μm	613 μm (at 850 mm)	completely oxidized	48 / 5	LACOMERA Project; Air ingress.
<b>QUENCH-11</b> Dec 08, 2005	Water 18 g/s	≈ 2040 K		170 μm	completely oxidized	9 / 132	LACOMERA Project; Boil-off.
<b>QUENCH-12</b> Sept 27, 2006	Water 48 g/s	≈ 2100 K	160 μm, breakaway	300 μm, (110 s), breakaway	completely oxidized	34 / 24	ISTC Project No. 1648.2; VVER bundle with E110 claddings
<b>QUENCH-13</b> Nov 7, 2007	Water 52 g/s	≈ 1820 K		400 μm, after AgInCd rod failure	750 μm	42 / 1	SARNET; impact of AgInCd absorber rod failure on aerosol generation.
<b>QUENCH-14</b> July 2, 2008	Water 41 g/s	≈ 2100 K	170 μm <sup>6)</sup>	470 μm <sup>6)</sup> , (30 s)	840 μm <sup>4)</sup> (74% metal converted to outer ZrO <sub>2</sub> )	34 / 6	ACM series: M5 <sup>®</sup> cladding
<b>QUENCH-15</b> May 27, 2009	Water 48 g/s	≈ 2100 K	145 μm <sup>6)</sup>	380 μm <sup>6)</sup> , (30 s)	630 μm <sup>4)</sup> (70% metal converted to outer ZrO <sub>2</sub> )	41 / 7	ACM series: ZIRLO <sup>™</sup> cladding

<sup>1)</sup> Maximum measured bundle temperature at 950 mm elevation.

<sup>2)</sup> Measured at the withdrawn corner rod at 950 mm elevation.

<sup>3)</sup> Measured posttest at the bundle elevation of maximum temperature, i.e. 950 mm. <sup>4)</sup> Some claddings were completely oxidized at 950 mm elevation.

<sup>5)</sup> Oxide thickness during transient phase.

<sup>6)</sup> Zircaloy-4 corner rods.

Revised: March 2011

**Table 2: Design characteristics of the QUENCH-L0 test bundle**

Bundle type		PWR
Bundle size		21 heated rods
Effective number of rods	(considering surface of heated rods, shroud and corner rods)	37 rods (21 + 13.8 from shroud + 2.2 from corner rods)
Pitch		14.3 mm
Coolant channel area		29.65 cm <sup>2</sup>
Hydraulic diameter		11.5 mm
Rod outside diameter		10.75 mm
Cladding material		Zircaloy-4
Cladding thickness		0.725 mm
Rod length	(elevations)	2480 mm (-690 to 1790 mm)
Internal rod pressure	(gas)	3.5 - 5.5 MPa abs.; rod#15: 0.3 MPa; (Kr)
Heater material		Tungsten (W)
Heater length		1024 mm
Heater diameter		6 mm
Annular pellet	material dimensions	ZrO <sub>2</sub> ;Y <sub>2</sub> O <sub>3</sub> -stabilized Ø 9.15/6.15 mm; L=11 mm
Pellet stack		0 mm to ~1020 mm
Corner rod (4)	material instrumented (A, C, D)  not instrumented (B)	Zircaloy-4 tube Ø 6x0.9 (bottom: -1140 mm) rod Ø 6 mm (top: +1300 mm) rod Ø 6 mm (-1350 to +1155 mm)
Grid spacer	material length sheet thickness elevation of lower edge	Zircaloy-4, Inconel 718 Zircaloy: 42 mm, Inconel: 38 mm 0.5 mm Inc: -100 mm; Zry: 150, 550, 1050, 1410 mm
Shroud	material wall thickness outside diameter length (extension)	Zirconium 702 (flange: Zry-4) 3.17 mm 86.0 mm 1600 mm (-300 mm to 1300 mm)
Shroud insulation	material insulation thickness elevation	ZrO <sub>2</sub> fiber ~ 37 mm -300 to ~1000 mm
Molybdenum-copper electrodes	length of upper electrodes length of lower electrodes outer diameter: prior to coating after coating with ZrO <sub>2</sub> borehole of Cu-electrodes	766 mm (576 Mo, 190 mm Cu) 690 mm (300 Mo, 390 mm Cu)  8.6 mm 9.0 mm diameter 2 mm, length 96 mm
Cooling jacket	Material: inner/outer tube inner tube outer tube	Inconel 600 (2.4816) / SS (1.4571) Ø 158.3 / 168.3 mm Ø 181.7 / 193.7 mm

### **Table 3: Properties of Zircaloy-4 cladding tubes**

**Table 3.1. Chemical Composition of Zircaloy-4 in Weight-%**

Element	Symbol	Specified Value
Tin	Sn	1.20-1.40
Iron	Fe	0.21-0.24
Chromium	Cr	0.07-0.13
Oxygen	O	0.10-0.15
Silicon	Si	0.005-0.012

**Table 3.2. Mechanical Properties at Tensile Test on finished Tube at 400°C ± 3°C**

Element	Specified Value
0.2 Yield strength Rp 0.2	200-300 N/mm <sup>2</sup>
Tensile strength Rm	≥ 270 N/mm <sup>2</sup>
Breaking elongation A <sub>50</sub> mm	≥ 10 %

**Table 3.3. Microstructure**

<b>Grain size: 6.7 μm</b>	according to ASTM-E 112-96: <b>Nr. 11.5</b> (for final size tubing; samples are recrystallized; magnification x500)
<b>Surface Conditions:</b> Roughness (inside): <b>Ra ≤ 1.0 μm</b> Roughness (outside): <b>Ra ≤ 0.7 μm</b>	

**Table 4: Main characteristics of the ZrO<sub>2</sub> pellet material, yttria-stabilized (type FZY) \***

Property		Data
Density		5.5-5.8 g/cm <sup>3</sup>
Open porosity		0
Mean grain size		50 μm
Hardness (Knoop, 100 g)		17000 N/mm <sup>2</sup>
Yield strength under compression		2000 N/mm <sup>2</sup>
Bending strength		350 N/mm <sup>2</sup>
Elastic modulus		165 GPa
Specific heat at 20 °C		400 J/kg K
Thermal conductivity at 100 °C		2.5 W/m K
Linear expansion, 20-1000 °C		10.5 x 10 <sup>-6</sup> /K
Specific electric resistance	at 20 °C	10 <sup>10</sup> Ω cm
	at 500 °C	5000 Ω cm
	at 1000 °C	50 Ω cm

\*According to FRIATEC, Mannheim



**Table 5: QUENCH-L0; Electrical resistances of rods [mΩ] at 20 C**

**Table 5.1. Internal circuit with 9+1 rods**

rod	1	2	3	4	5	6	7	8	9	16	Ave- rage	10 rods parallel
pre- test	4.3	3.8	3.8	3.8	3.5	3.6	3.4	3.5	3.4	3.3	3.6	0.36
post- test	3.3	3.3	3.2	3.2	3.3	3.3	3.3	3.3	3.2	3.3	3.3	0.33

Note: Measured values include the resistance of slide contacts  $R_s=0.75$  mΩ

**Table 5.2. External circuit with 11 rods**

rod	10	11	12	13	14	15	17	18	19	20	21	ave- rage	11 rods parallel
pre- test	3.4	3.3	3.3	3.5	3.4	3.5	3.3	3.3	3.3	3.3	3.5	3.4	0.31
post- test	3.3	3.2	3.2	3.6	3.3	3.2	3.3	3.2	3.3	3.3	3.3	3.3	0.30

Note: Measured values include the resistance of slide contacts  $R_s=0.75$  mΩ

Each circuit connected to the DC generator with 4 parallel bonded cables. The resistance of each cable is  $R_c=1.2$  mΩ. Therefore, the external (outside) resistance corresponding to each heated rod (indicated by SCDAP/RELAP as **fxwid**) is  $R_{ie}=R_s+10*R_c/4=3.75$  mΩ for the inner rod group and  $R_{oe}=R_s+11*R_c/4=4.05$  mΩ for the outer rod group.

**Table 6 :** Properties of zirconia fiber insulating boards\***Table 6.1.** Chemical composition

Oxide	ZrO <sub>2</sub>	Y <sub>2</sub> O <sub>3</sub>	HfO <sub>2</sub>	TiO <sub>2</sub>	SiO <sub>2</sub>	CaO	MgO	Fe <sub>2</sub> O <sub>3</sub>	Al <sub>2</sub> O <sub>3</sub>	Na <sub>2</sub> O
typical wt%	88	10	2	0.14	0.12	0.09	0.03	0.04	0.01	0.01

**Table 6.2.** Physical properties

bulk density	Porosity	shrinkage		thermal expansion coefficient @298-1453K	melting point	max. service temperature	flexural strength	Compressive strength @10% compression
		(1 hour @1925 K)	(24 hours @1925 K)					
g/cm <sup>3</sup>	%	%		1/K	K	K	MPa	MPa
0.48	92	1.2	2.8	10.7*10 <sup>-6</sup>	2866	2500	0.59	0.29

**Table 6.3.** Thermal conductivity

temperature, K	673	1073	1373	1673	1923
conductivity, W/(m*K)	0.08	0.11	0.14	0.19	0.24

**Table 6.4.** Specific heat capacity

temperature, K	366	2644
specific heat capacity, J/(kg*K)	544	754

\*According to specifications of manufacturer ZIRCAR PRODUCTS on the ZYFB3 material

**Table 7: List of instrumentation for the QUENCH-L0 test**

Chan	Designation	Instrument, Location	Unit
0	P rod 15	Internal pressure of rod #15	bar
1	P rod 14	Internal pressure of rod #14	bar
2	P rod 13	Internal pressure of rod #13	bar
3	P rod 16	Internal pressure of rod #16	bar
4	P rod 05	Internal pressure of rod #05	bar
5	P rod 04	Internal pressure of rod #04	bar
6	P rod 03	Internal pressure of rod #03	bar
7	P rod 12	Internal pressure of rod #12	bar
8	P rod 17	Internal pressure of rod #17	bar
9	P rod 06	Internal pressure of rod #06	bar
10	P rod 01	Internal pressure of rod #01	bar
11	P rod 02	Internal pressure of rod #02	bar
12	P rod 11	Internal pressure of rod #11	bar
13	P rod 18	Internal pressure of rod #18	bar
14	P rod 07	Internal pressure of rod #07	bar
15	P rod 08	Internal pressure of rod #08	bar
16	P rod 09	Internal pressure of rod #09	bar
17	P rod 10	Internal pressure of rod #10	bar
18	P rod 19	Internal pressure of rod #19	bar
19	P rod 20	Internal pressure of rod #20	bar
20	P rod 21	Internal pressure of rod #21	bar
21..23		20 mA, Reserve	
24	P 511 top	Absolute pressure at bottom of L 501 long leg	bar
25	Fm 401	Argon gas mass flow rate, (20 mA)	g/s
26..31		20 mA, Reserve	
32..34		TC (W/Re), Reserve	
35	TSH 15/0	TC (NiCr/Ni), shroud outer surface, 1150 mm, 21°	K

Chan	Designation	Instrument, Location	Unit
36	TSH 14/270	TC (NiCr/Ni), shroud outer surface, 1050 mm, 289°, behind shroud isolation	K
<b>37</b>		TC (W/Re)	K
38	TFS 15/13	TC (NiCr/Ni), surface of fuel rod simulator 15, group 5, 950 mm	K
39	TFS 19/12	TC (NiCr/Ni), surface of fuel rod simulator 19, group 5, 850 mm	K
<b>40</b>		TC (W/Re)	
<b>41</b>		TC (W/Re)	K
42	TFS 7/12	TC (NiCr/Ni), surface of fuel rod simulator 7, group 3, 850 mm	K
43	TFS 15/12	TC (NiCr/Ni), surface of fuel rod simulator 15, group 5, 850 mm	K
44	TFS 2/12	TC (NiCr/Ni), surface of fuel rod simulator 2, group 2, 850 mm	K
45	TFS 4/12	TC (NiCr/Ni), surface of fuel rod simulator 4, group 2, 850 mm	K
46	TFS 19/13	TC (NiCr/Ni), surface of fuel rod simulator 19, group 5, 950 mm	K
<b>47..57</b>		TC (W/Re)	K
58	TFS 7/10	TC (NiCr/Ni), surface of fuel rod simulator 7, group 3, 650 mm	K
<b>59</b>		TC (W/Re)	K
<b>60</b>		TC (W/Re)	K
61	TFS 11/12	TC (NiCr/Ni), surface of fuel rod simulator 11, group 4, 850 mm	K
62	P 206	Reserve	
63	F 206	Reserve	
64	T 402 b	TC (NiCr/Ni), Ar super heater	K
<b>65..67</b>		TC (W/Re)	K
68	T 512	TC (NiCr/Ni), gas temperature bundle outlet	K
<b>69</b>		TC (W/Re)	K
<b>70</b>		TC (W/Re)	K
71	<i>Ref. T01</i>	<i>Temperature of measuring crate 1 (reference temperature)</i>	K
72	TFS 11/13	TC (NiCr/Ni) surface of fuel rod simulator 11, group 4, 950 mm	
73	TFS 7/13	TC (NiCr/Ni), surface of fuel rod simulator 7, group 3, 950 mm	K
74	TFS 2/13	TC (NiCr/Ni), surface of fuel rod simulator 2, group 2, 950 mm	K

Chan	Designation	Instrument, Location	Unit
75	TFS 4/13	TC (NiCr/Ni), surface of fuel rod simulator 4, group 2, 950 mm	K
76	TFS 15/11	TC (NiCr/Ni), surface of fuel rod simulator 15, group 5, 750 mm	K
77	TFS 19/11	TC (NiCr/Ni), surface of fuel rod simulator 19, group 5, 750 mm	K
78	TFS 11/11	TC (NiCr/Ni) surface of fuel rod simulator 11, group 4, 750 mm	K
79	TFS 7/11	TC (NiCr/Ni), surface of fuel rod simulator 7, group 3, 750 mm	K
80	TFS 2/11	TC (NiCr/Ni) surface of fuel rod simulator 2, group 2, 750 mm	K
81	TSH 12/90	TC (NiCr/Ni), shroud outer surface, 850 mm, 109°	K
82	TFS 2/10	TC (NiCr/Ni); surface of fuel rod simulator 2, group 2, 650 mm	K
83	TSH 10/270	TC (NiCr/Ni), shroud outer surface, 650 mm, 289°	K
84	TSH 9/180	TC (NiCr/Ni), shroud outer surface, 550 mm, 191°	K
85	TSH 8/90	TC (NiCr/Ni), shroud outer surface, 450 mm, 109°	K
86	TSH 7/0	TC (NiCr/Ni), shroud outer surface, 350 mm, 11°	K
87	TSH 6/270	TC (NiCr/Ni) shroud outer surface, 250 mm, 281°	K
88	TSH 5/180	TC (NiCr/Ni), shroud outer surface, 150 mm, 191°	K
89	TSH 4/90	TC (NiCr/Ni), shroud outer surface, 50 mm, 109°	K
90	TSH 11/0	TC (NiCr/Ni), shroud outer surface, 750 mm, 11°, behind shroud isolation	K
91	TCI 9/270	TC (NiCr/Ni), cooling jacket inner tube wall, 550 mm, 270°	K
92	TCI 10/270	TC (NiCr/Ni), cooling jacket inner tube wall, 650 mm, 270°	K
93	TCI 11/270	TC (NiCr/Ni), cooling jacket inner tube wall, 750 mm, 270°	K
94	TCI 13/270	TC (NiCr/Ni), cooling jacket inner tube wall, 950 mm, 270°	K
95	TFS 4/11	TC (NiCr/Ni), surface of fuel rod simulator 4, group 2, 750 mm	K
96	TFS 15/10	TC (NiCr/Ni), surface of fuel rod simulator 15, group 5, 650 mm	K
97	TFS 19/10	TC (NiCr/Ni), surface of fuel rod simulator 19, group 4, 650 mm	K
98	TFS 11/10	TC (NiCr/Ni), surface of fuel rod simulator 11, group 2, 650 mm	K
99	TSH 13/180	TC (NiCr/Ni), shroud outer surface, 950 mm, 191°	K
100	TSH 3/0	TC (NiCr/Ni), shroud outer surface, -50 mm, 11°	K

Chan	Designation	Instrument, Location	Unit
101	TFS 4/10	TC (NiCr/Ni), surface of fuel rod simulator 4, group 2, 650 mm	K
102	TFS 15/14	TC (NiCr/Ni), surface of fuel rod simulator 15, group 5, 1050 mm	K
103	TFS 19/14	TC (NiCr/Ni), surface of fuel rod simulator 19, group 4, 1050 mm	K
104	TFS 11/14	TC (NiCr/Ni), surface of fuel rod simulator 11, group 4, 1050 mm	K
105	TFS 7/14	TC (NiCr/Ni), surface of fuel rod simulator 7, group 3, 1050 mm	K
106	TFS 2/14	TC (NiCr/Ni), surface of fuel rod simulator 2, group 2, 1050 mm	K
107	TFS 4/14	TC (NiCr/Ni), surface of fuel rod simulator 4, group 2, 1050 mm	K
108	TFS 15/9	TC (NiCr/Ni), surface of fuel rod simulator 15, group 5, 550 mm	K
109	TFS 11/9	TC (NiCr/Ni), surface of fuel rod simulator 11, group 4, 550 mm	K
110	TFS 7/9	TC (NiCr/Ni), surface of fuel rod simulator 7, group 3, 550 mm	K
111	TFS 4/9	TC (NiCr/Ni), surface of fuel rod simulator 4, group 2, 550 mm	K
112	TFS 15/15	TC (NiCr/Ni), surface of fuel rod simulator 15, group 5, 1150 mm	K
113	TFS 19/15	TC (NiCr/Ni), surface of fuel rod simulator 19, group 5, 1150 mm	K
114	TFS 11/15	TC (NiCr/Ni), surface of fuel rod simulator 11, group 4, 1150 mm	K
115	TFS 7/15	TC (NiCr/Ni), surface of fuel rod simulator 7, group 3, 1150 mm	K
116	TFS 2/15	TC (NiCr/Ni), surface of fuel rod simulator 2, group 2, 1150 mm	K
117	TFS 4/15	TC (NiCr/Ni), surface of fuel rod simulator 4, group 2, 1150 mm	K
118	TFS 11/8	TC (NiCr/Ni), surface of fuel rod simulator 11, group 4, 450 mm	K
119	TFS 7/8	TC (NiCr/Ni), surface of fuel rod simulator 7, group 3, 450 mm	K
120	TFS 4/8	TC (NiCr/Ni), surface of fuel rod simulator 4 group 2, 450 mm	K
121	TFS 11/16	TC (NiCr/Ni), surface of fuel rod simulator 11, group 4, 1250 mm	K
122	TFS 7/16	TC (NiCr/Ni), surface of fuel rod simulator 7, group 3, 1250 mm	K
123	T 601	Temperature off-gas, 2660 mm from test section outlet (flange)	K
124	TFS 11/7	TC (NiCr/Ni), surface of fuel rod simulator 11, group 4, 1350 mm	K
125	T 514	Temperature bundle head, cooling water inlet	K
126	TFS 7/7	TC (NiCr/Ni), surface of fuel rod simulator 7, group 3, 350 mm	K
127	TFS 4/7	TC (NiCr/Ni), surface of fuel rod simulator 4, group 2, 350 mm	K
128	T 104	Temperature quench water	K

Chan	Designation	Instrument, Location	Unit
129	T 201	Temperature steam generator heating pipe	K
130	TIT C/12	TC (NiCr/Ni), center line of corner rod C, 850 mm	K
131	T 205	Temperature upstream steam flow instrument location 10 g/s	K
132	T 301A	Temperature downstream superheater	K
133	T 302	Temperature superheater heating pipe	K
134	T 303	Temperature upstream total flow instrument location	K
135	T 401	Temperature upstream Ar flow instrument (orifice) location	K
136	T 403	Temperature of Ar at inlet cooling jacket	K
137	T 404	Temperature of Ar at outlet cooling jacket	K
138	T 501	Temperature in containment (near from bundle head)	K
139	TFS 7/6	TC (NiCr/Ni), surface of fuel rod simulator 7, group 3, 250 mm	K
140	TFS 4/6	TC (NiCr/Ni), surface of fuel rod simulator 4, group 2, 250 mm	K
141	TFS 7/17	TC (NiCr/Ni), surface of fuel rod simulator 7, group 3, 1350 mm	K
142	TFS 7/5	TC (NiCr/Ni), surface of fuel rod simulator 7, group 3, 150 mm	K
143	TFS 7/4	TC (NiCr/Ni), surface of fuel rod simulator 7, group 3, 50 mm	K
144	TFS 7/3	TC (NiCr/Ni), surface of fuel rod simulator 7, group 3, -50 mm	K
145	TFS 7/2	TC (NiCr/Ni), surface of fuel rod simulator 7, group 3, -150 mm	K
146	TFS 7/1	TC (NiCr/Ni), surface of fuel rod simulator 7, group 3, -250 mm	K
147	T 510	Temperature at outer surface of containment, 270°, 4.4 m	K
148	T 511	Gas temperature at bundle inlet	K
149	TIT D/11	TC (NiCr/Ni), center line of corner rod D, 750 mm	K
150	TIT A/13	TC (NiCr/Ni), center line of corner rod A, 950 mm	K
151	<i>Ref. T02</i>	<i>Temperature of measuring crate 2 (reference temperature)</i>	K
152	P 201	Pressure steam generator	bar
153	P 204	Pressure at steam flow instrument location 50 g/s	bar
154	P 205	Pressure at steam flow instrument location 10 g/s	bar
155	P 303	Pressure upstream total flow instrument (orifice) location	bar
156	P 401	Pressure upstream gas flow instrument location	bar

Chan	Designation	Instrument, Location	Unit
157	P 511	Pressure at bundle inlet	bar
158	P 512	Pressure at bundle outlet	bar
159	P 601	Pressure upstream off-gas flow instrument (orifice) F 601	bar
160	P 901	Pressure He supply for unheated rods	bar
161	L 201	Liquid level steam generator	mm
162	L 501	Liquid level quench water	mm
163	L 701	Liquid level condensation vessel	mm
164	Fm 401B	Argon flow rate (Bronkhorst device)	g/s
165	P 411	Pressure Kr supply for heated rods, Reserve	bar
166	P 403	Pressure Ar cooling of cooling jacket	bar
167	P 406	Pressure insulation shroud/cooling jacket	bar
168	Fm 104	Flow rate quench water	g/s
169	Fm 204	Flow rate steam 50 g/s	g/s
170	Fm 205	Flow rate steam 10 g/s	g/s
171	F 303	Flow rate at bundle inlet (steam + argon), orifice	mbar
172	F 401	Reserve	
173	Fm 403	Flow rate cooling gas (Ar)	g/s
174	F 601	Flow rate off-gas (orifice), 2000 mm from test section outlet (flange)	mbar
175	Fm 406	Flow rate argon into room between shroud and cooling jacket	g/s
176	E 201	Electric current steam generator	A
177	E 301	Electric current superheater	A
178	E 501	Electric current of inner group of fuel rod simulators	A
179	E 502	Electric current of outer group of fuel rod simulators	A
180	E 503	Electric voltage of inner group of fuel rod simulators	V
181	E 504	Electric voltage of outer group of fuel rod simulators	V
182	Hub_V302	Gas supply valve lift	%
183	Ref. T03	Temperature of buffer amplifier (reference temperature)	K




Chan	Designation	Instrument, Location	Unit
184.... .199		Binary inputs	
200.... .215		Analog outputs	
250	E 505	Electric power inner ring of fuel rod simulators	W
251	E 506	Electric power outer ring of fuel rod simulators	W
252	EP	Gross electrical power	kW

**Indications:**

TFS - TC at the rod surface;

TCR - TC at the rod surface;

TSH - TC at outer surface of shroud;

 - gauge outside of containment.

**Groups of the rods for modeling:**

group 1: rods 1;

group 2: rods 2, 4, 6, 8;

group 3: rods 3, 5, 7, 9;

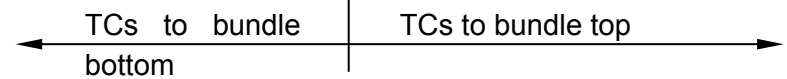
group 4: rods 11, 14, 17, 20;

group 5: rods 10, 12, 13, 15, 16, 18, 19, 21.

**Table 8: QUENCH-L0; Bundle thermocouple positions**

Elevation, mm	-250	-150	-50	50	150	250	350	450	550	650	750	850	950	1050	1150	1250	1350
Rod/Elevation	1	2	3	4	5	6	7	8	9	10	11	12	13	14	15	16	17
1																	
2										X	X	X	X	X	X		
3																	
4						X	X	X	X	X	X	X	X	X	X		
5																	
6																	
7	X	X	X	X	X	X	X	X	X	X	X	X	X	X	X	X	X
8																	
9																	
10																	
11							X	X	X	X	X	X	X	X	X	X	
12																	
13																	
14																	
15									X	X	X	X	X	X	X		
16																	
17																	
18																	
19										X	X	X	X	X	X		
20																	
21																	

Number per elevation    1    1    1    1    1    2    3    3    4    6    6    6    6    6    6    2    1



<b>TFS (rod surface), indicated in table above</b>	<b>56</b>
<b>TIT (inside corner rods)</b>	<b>3</b>
<b>TSH (outer shroud surface)</b>	<b>13</b>
<b>Total quantity of NiCr/Ni thermocouples</b>	<b>72</b>

**Table 9: QUENCH-L0; Sequence of events**

Time [s]	Event
-1405 (11:13:40 h)	Start data recording, $T_{max} = TFS\ 4/13 = 800\ K$ , el. power at 4.62 kW. L701 = 535 mm. L 501 = -396 mm. System pressure 3 bar.
-880; -690; -440; -300; -200	Pressurization of rods to 35 bar (rods 2, 6); 40 bar (rods 5, 9, 11, 17); 45 bar (rods 10, 16, 21); 50 bar (rods 1, 4, 8, 12, 13, 14, 18, 19, 20); 55 bar (3, 7). Reference rod 15 was unpressurised ( $\sim 3$ bar).
0	Start of transient with max electrical power increase rate.
2	Electrical power 27 kW.
<b>70...100</b>	<b>Sequential onset of ballooning for rods pressurized to 55 ... 35 bar.</b>
<b>111...174</b>	<b>Sequential onset of burst for rods from center rod #1 to peripheral rod #10. See burst table (Table 10)</b>
140	Reducing of electrical power increase rate from 100% to 70%. El. power 41 kW; $T_{max} = TFS\ 4/13 = 1143\ K$ .
186.6	Switch of the electrical power to decay heat of 3.4 kW. El. power 43.5 kW; $T_{max} = TFS\ 4/13 = 1317\ K$ .
200	<i>Cladding surface temperature maximum reached (heat transfer from heater and pellet to cladding). <math>T_{max} = TFS\ 4/13 = 1349\ K</math>.</i>
217.8	Initiation of rapid steam supply line (50 g/s) additionally to slow steam supply (2 g/s) and carrier argon (6 g/s)
223...225	Rapid cladding cooling to $\sim 400\ K$ at all elevations by entrainment of water condensed in steam supply tubes.
237...263	Increase of bundle temperatures to $\sim 660\ K$ after evaporation of entrained water.
362	Initiation of quench water supply. Switch-off of steam supply. Switch of argon to bundle top supply.
387	Maximum quench rate (100 g/s) reached.
402...442	Sequential wetting of cladding surface thermocouples (TFS) at elevations between -250 and 1350 mm.
480	Bundle completely filled with water (L 501 = 1307 mm)
528	Electrical power switched off. $T_{max} = TFS\ 15/15 = 333\ K$
1100	End of data recording. L 501 = 1288 mm.

**Table 10: QUENCH-L0; Burst parameters**

rod	initial p, bar	burst p, bar	burst time, s	T@950mm, K	T measurement	burst azimuth. position, °	burst from elevation, mm	burst to elevation, mm	burst length, mm	burst area, mm <sup>2</sup>
1	49.3	48.5	111.2	1069	average T for 3 internal rods	59	973.2	986.2	13	36.02
7	54.6	54.1	114.2	1066	TFS 7/13	338	989	1003	14	40.36
4	49.2	49.5	114.6	1073	TFS 4/13	158	967.8	982	14.2	35.60
3	55	54.4	119.2	1089	average: TFS 2/13 and TFS 4/13	136	954	969	15	41.82
8	47.7	46.8	122.0	1086	TFS 7/13	29	989.5	1007	17.5	60.37
5	38	38.9	129.6	1108	TFS 4/13	192	963	974	11	23.98
6	34.2	34.7	130.4	1106	TFS 7/13	329	1001.2	1008.8	<b>7.6</b>	<b>9.43</b>
9	39.2	40.1	136.2	1133	TFS 2/13	64	995	1004	9	14.59
2	33.8	34.5	136.8	1134	TFS 2/13	116	990	1002	12	39.73
12	49.9	50.2	150.0	1088	average: TFS 2/13 and TFS 11/13	173	948	962.5	14.5	41.07
18	49	48.7	151.2	1103	average: TFS 7/13 and TFS 19/13	7	937	954	17	48.14
17	39.6	40.4	152.0	1127	average: TFS 7/13 and TFS 15/13	280	947.1	955.4	8.3	12.04
20	50.3	50.4	153.2	1049	TFS 19/13	325	967	983	16	53.18
14	49	49.0	153.4	1094	TFS 15/13	223	982	1000.8	<b>18.8</b>	<b>96.54</b>
16	44.6	44.9	155.0	1091	TFS 15/13	206	977	989	12	23.72
19	50	50.0	159.6	1123	average: TFS 7/13 and TFS 19/13	344	994.3	1004.6	10.3	16.30
13	49.4	49.0	162.5	1078	average: TFS 11/13 and TFS 15/13	137	971.2	979.8	8.6	12.92
11	39.8	40.8	167.2	1141	average: TFS 2/13 and TFS 11/13	71	957.8	967.8	10	21.86
21	44.4	44.8	170.6	1068	average: TFS 11/13 and TFS 19/13	41	968	983	15	29.18
10	44.5	45.2	174.4	1064	TFS 11/13	77	958.2	967.8	9.6	13.39

**Table 11: QUENCH-L0; Strain parameters**

rod	initial p, bar	burst p, bar	burst time, s	T@950mm, K	elevation of burst middle, mm	max D, mm	at azimuth, °	min D, mm	at azimuth, °	strain, %
1	49.3	48.5	111.2	1069	980	17.1	59	14.2	137	33.5
7	54.6	54.1	114.2	1066	996	16.4	338	13.9	233	40.0
4	49.2	49.5	114.6	1073	975	15.8	158	13.3	262	33.7
3	55	54.4	119.2	1089	962	16.0	136	13.4	59	37.0
8	47.7	46.8	122.0	1086	998	18.3	29	14.6	112	49.0
5	38	38.9	129.6	1108	969	14.6	192	12.7	267	26.5
6	34.2	34.7	130.4	1106	1005	15.2	329	13.3	231	30.8
9	39.2	40.1	136.2	1133	1000	15.1	64	12.7	146	28.0
2	33.8	34.5	136.8	1134	996	15.7	116	13.2	8	33.8
12	49.9	50.2	150.0	1088	955	16.3	173	13.3	251	36.5
18	49	48.7	151.2	1103	946	16.0	7	13.0	289	34.7
17	39.6	40.4	152.0	1127	951	14.8	280	12.5	184	26.4
20	50.3	50.4	153.2	1049	975	16.0	325	13.1	73	34.1
14	49	49.0	153.4	1094	991	18.2	223	14.2	114	48.0
16	44.6	44.9	155.0	1091	983	15.0	206	12.6	131	28.2
19	50	50.0	159.6	1123	999	14.8	344	12.7	63	27.2
13	49.4	49.0	162.5	1078	976	15.2	137	13.2	226	30.6
11	39.8	40.8	167.2	1141	963	15.7	71	12.5	173	28.5
21	44.4	44.8	170.6	1068	976	14.8	41	12.5	143	26.4
10	44.5	45.2	174.4	1064	963	14.6	77	12.5	160	25.3

**Table 12: QUENCH-L0; Results of tensile tests**

specimen (* : l <sub>0</sub> = 250 mm)	ultimate tensile strength [MPa]	fracture stress [MPa]	elongation at fracture [%]	rupture type
P 01*	254	254	0.38	hydrogen embrittlement
P 02	408	408	0.99	hydrogen embrittlement
P 04*	276	276	0.40	hydrogen embrittlement
P 05*	274	274	0.37	hydrogen embrittlement
P 06	<b>148</b>	<b>148</b>	<b>0.16</b>	stress concentration
P 07*	<b>222</b>	<b>222</b>	<b>0.29</b>	hydrogen embrittlement
P 09	<b>518</b>	433	8.10	plastic deformation
P 10	512	507	10.12	plastic deformation
P 11	509	391	11.67	plastic deformation
P 12	502	499	6.44	stress concentration
P 13	504	<b>504</b>	9.18	stress concentration
P 14	430	430	1.97	stress concentration
P 15 (no burst)	505	450	11.70	plastic deformation
P 16	512	389	10.95	plastic deformation
P 17	501	497	3.83	rupture at stuck pellet
P 18	513	458	10.19	plastic deformation
P 19	489	368	<b>11.80</b>	plastic deformation
P 20	452	447	2.20	stress concentration
P 21	506	498	8.11	stress concentration

**Table 13: QUENCH-L0; Results of ring compression tests**

Specimen (*: elevated O- content)	load at failure [N]		displacement at failure [mm]		failure behaviour	
	upper ring	lower ring	upper ring	lower ring	upper ring	lower ring
P 01*	1178	802	6.35	5.15	plastic instability	rupture
P 02	2477	915	7.96	6.08	plastic instability	rupture
P 04*	<b>1104</b>	932	<b>5.92</b>	6.16	plastic instability	plastic instability
P 05*	1200	793	6.33	4.77	plastic instability	plastic instability
P 06	2378	<b>711</b>	7.97	<b>3.58</b>	plastic instability	rupture
P 07*	1264	859	6.69	5.83	plastic instability	plastic instability
P 09	2542	934	7.99	6.23	plastic instability	plastic instability
P 10	2605	<b>1299</b>	8.10	6.94	plastic instability	plastic instability
P 11	2522	1294	8.08	6.85	plastic instability	plastic instability
P 12	2550	1018	8.04	5.78	plastic instability	rupture
P 13	2473	855	7.94	4.97	plastic instability	rupture
P 14	<b>2829</b>	915	8.06	5.59	plastic instability	rupture
P 15	2503	1256	8.04	5.59	plastic instability	plastic instability
P 16	2576	1193	8.05	6.54	plastic instability	plastic instability
P 17	2538	973	8.08	5.43	plastic instability	rupture
P 18	2480	1197	8.02	6.42	plastic instability	rupture
P 19	2687	1142	8.00	6.64	plastic instability	plastic instability
P 20	1724	945	7.69	5.60	plastic instability	rupture
P 21	2638	1501	<b>8.13</b>	<b>7.35</b>	plastic instability	plastic instability





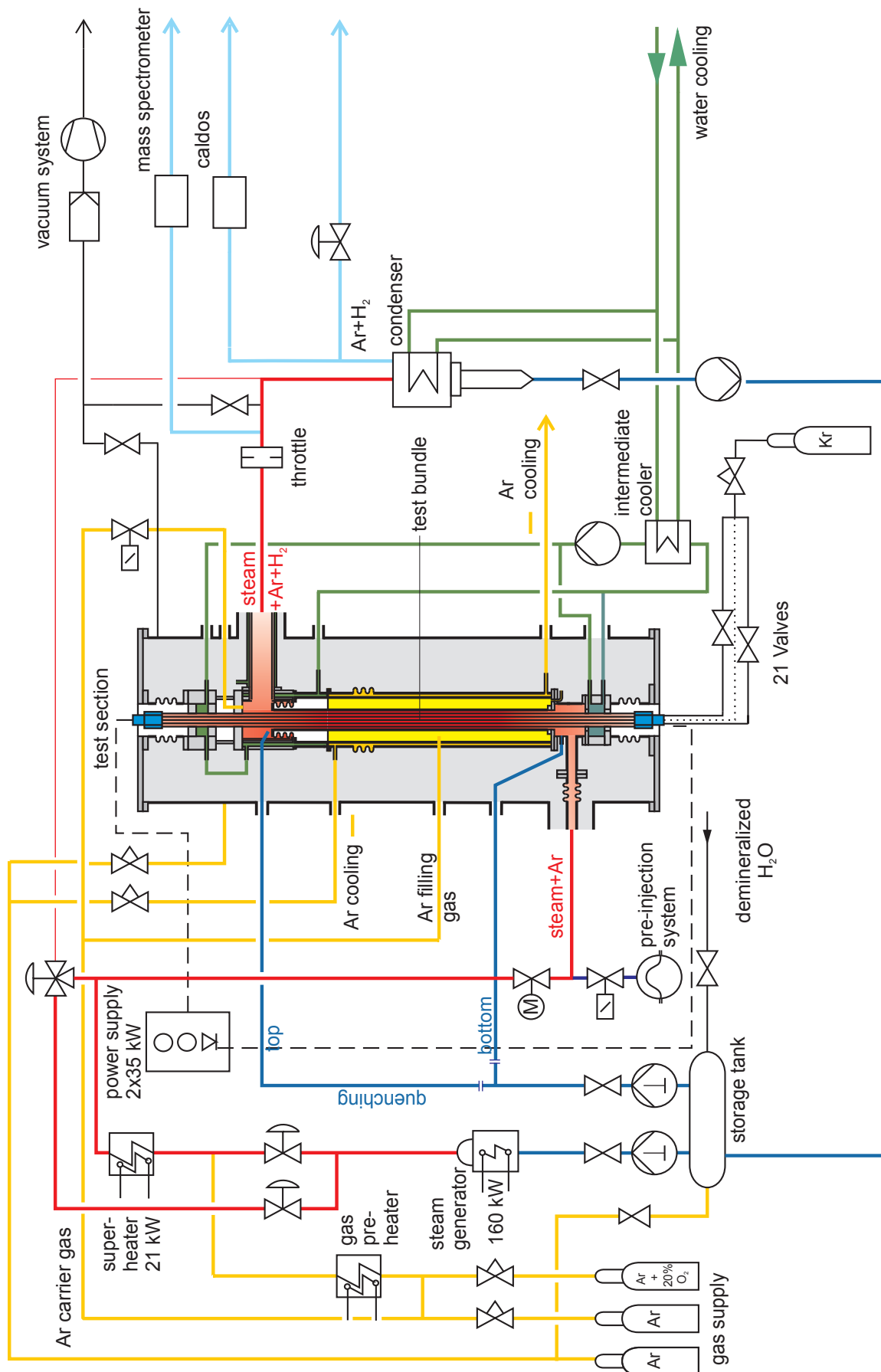


Fig. 1: Flow diagram of the QUENCH test facility.

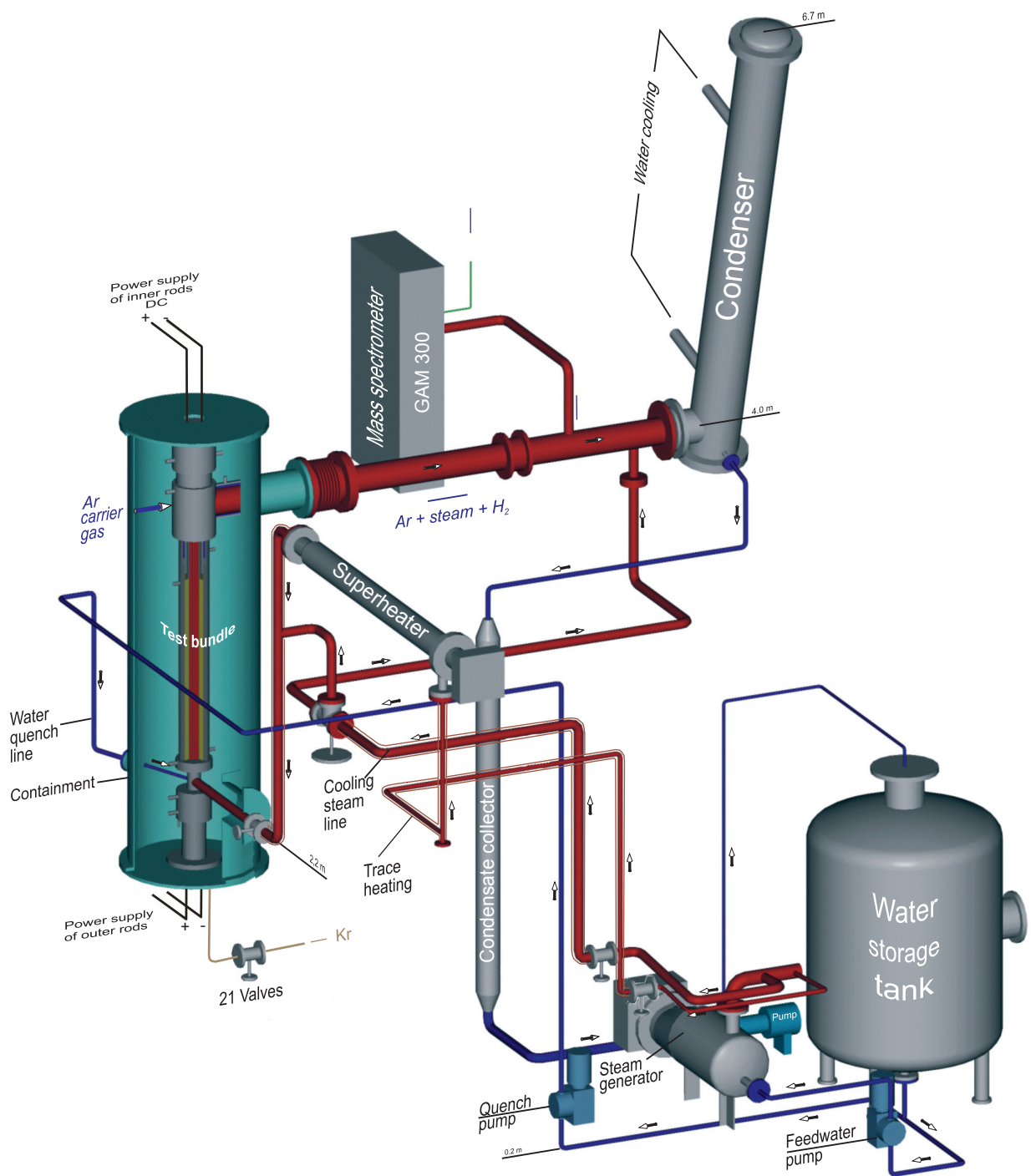


Fig. 2: QUENCH Facility - Main components.

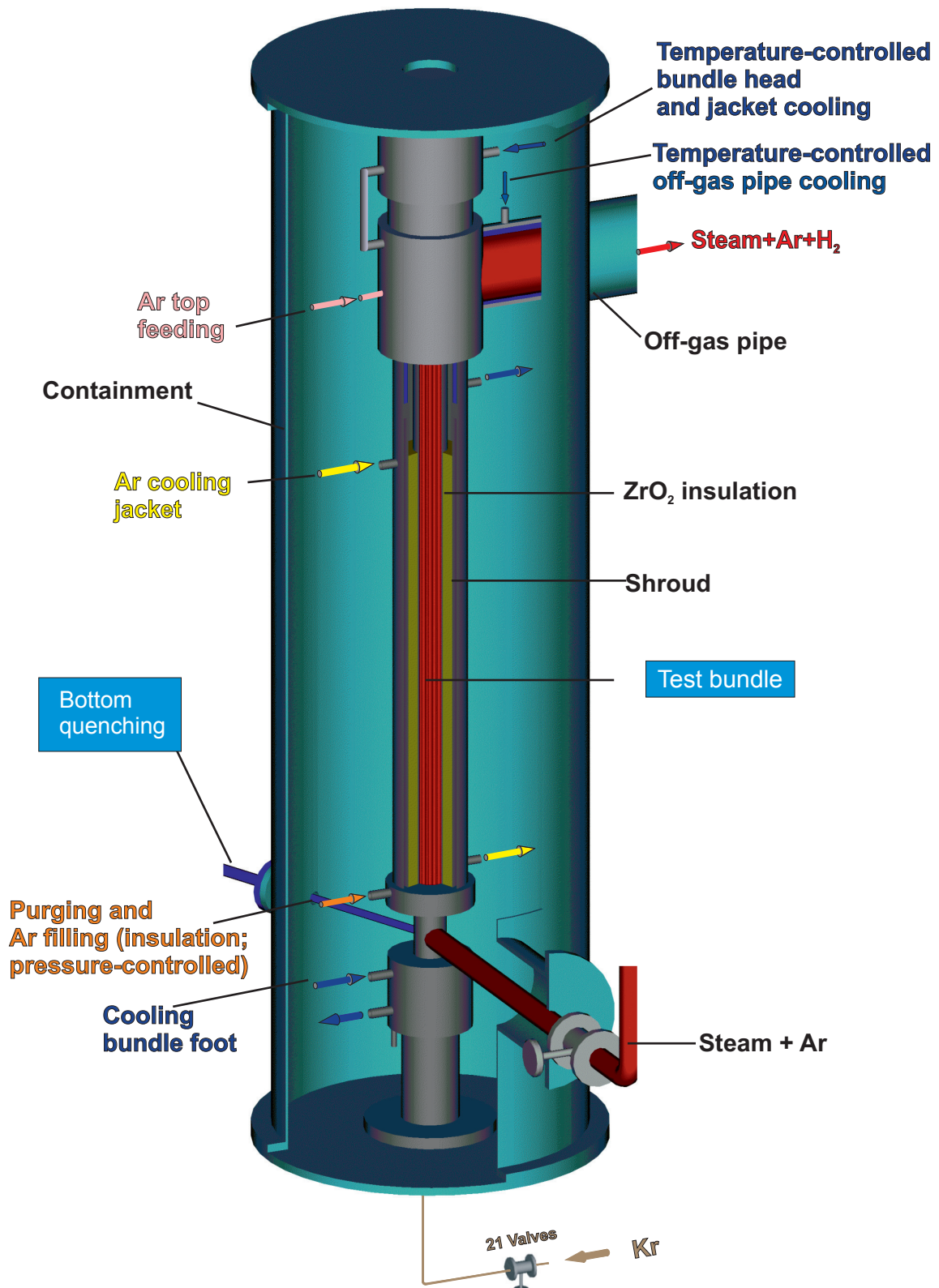


Fig. 3: QUENCH Facility; Containment and test section.

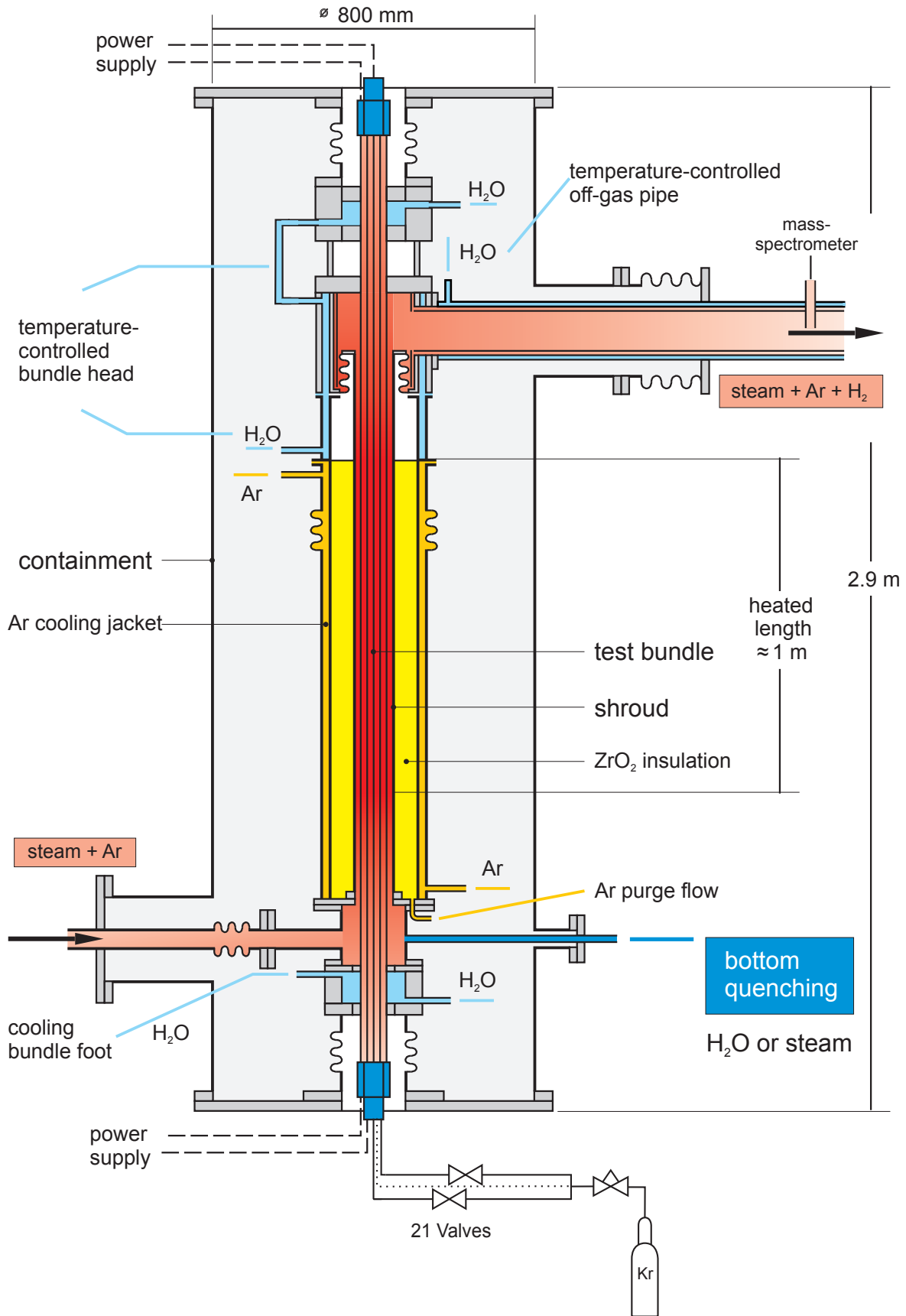


Fig. 4: QUENCH-L0; Test section with flow lines.

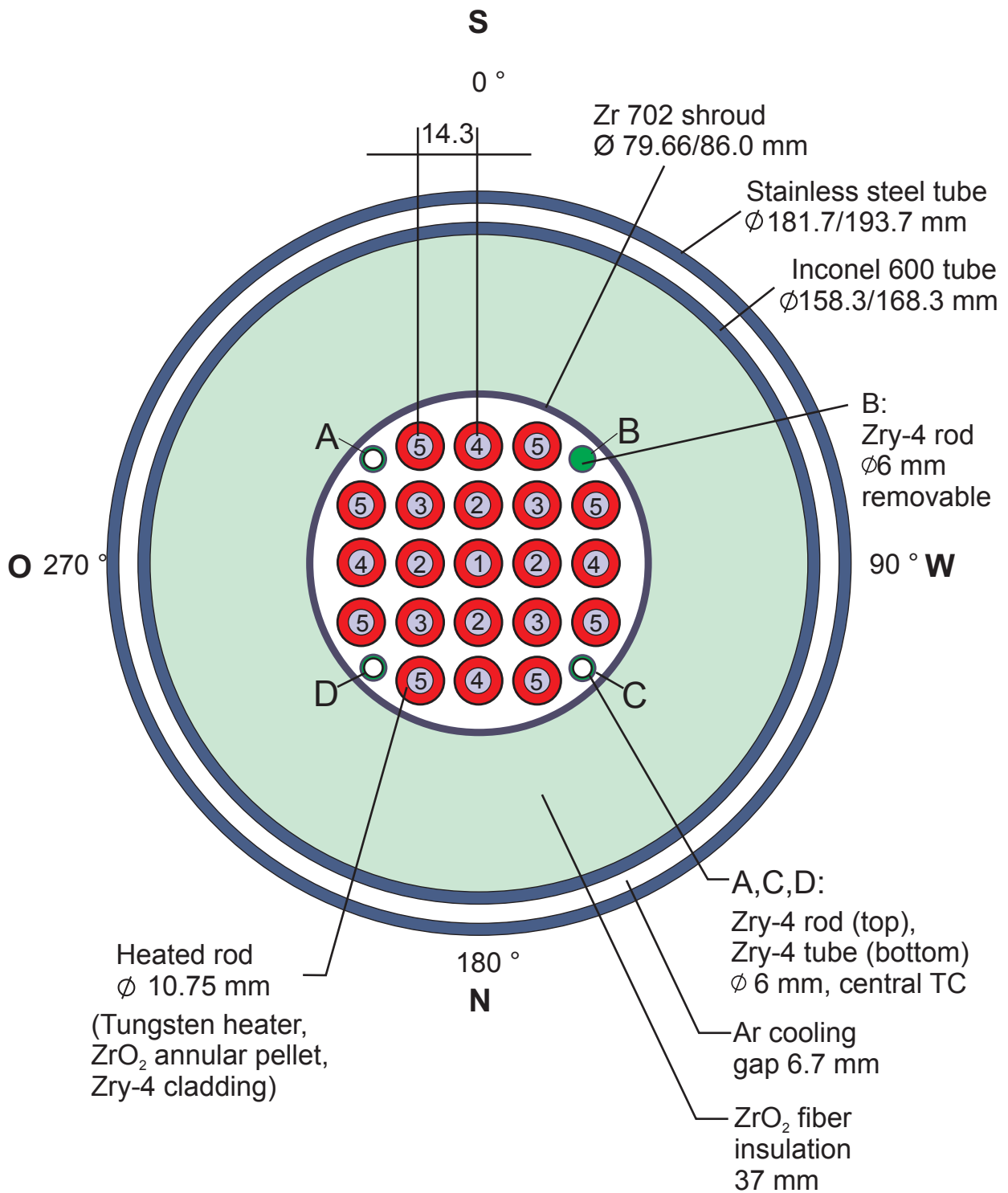


Fig. 5: QUENCH-L0; Fuel rod simulator bundle (cross section, top view) including rod type indications corresponding to table "List of Instrumentation".

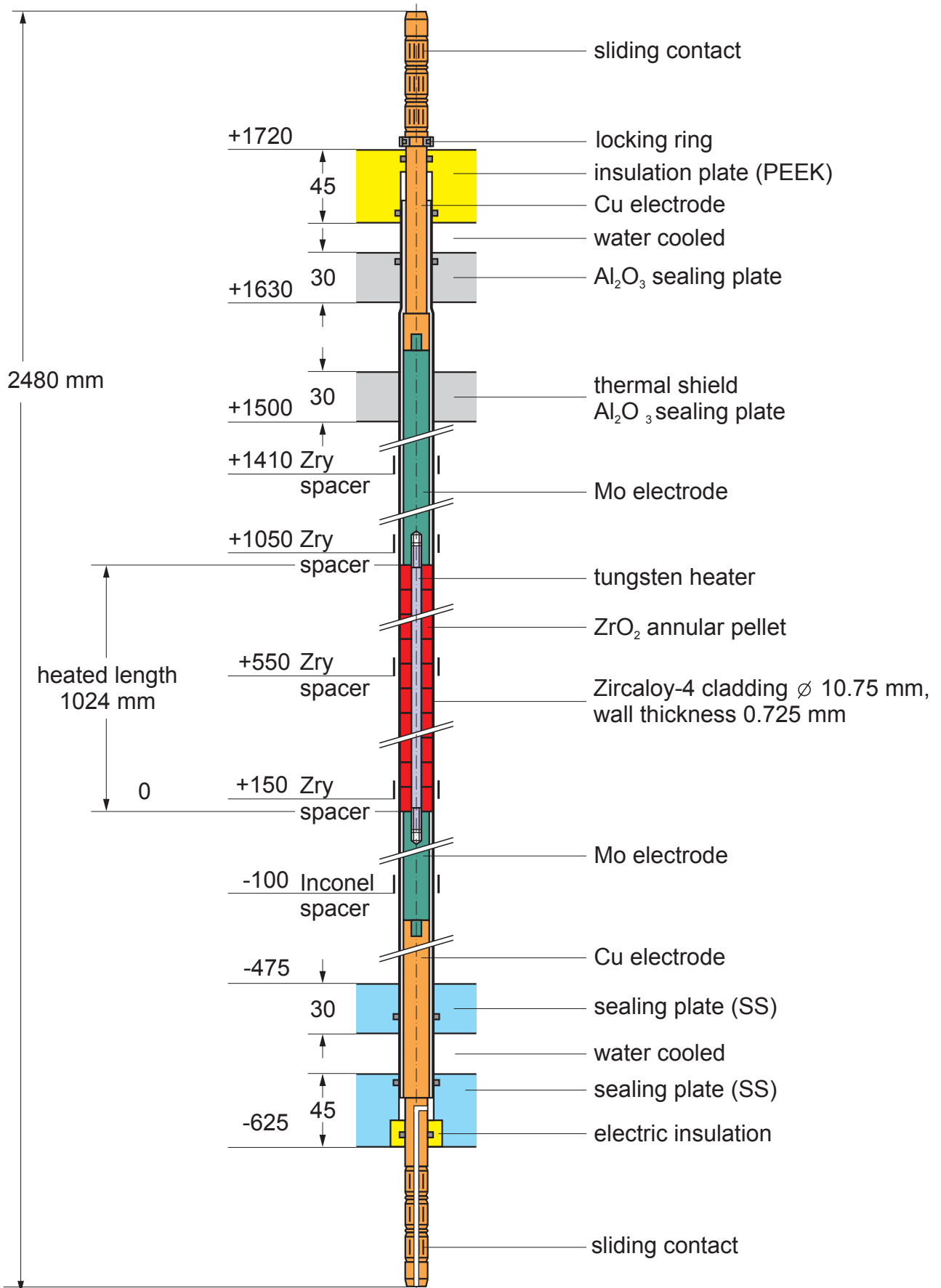
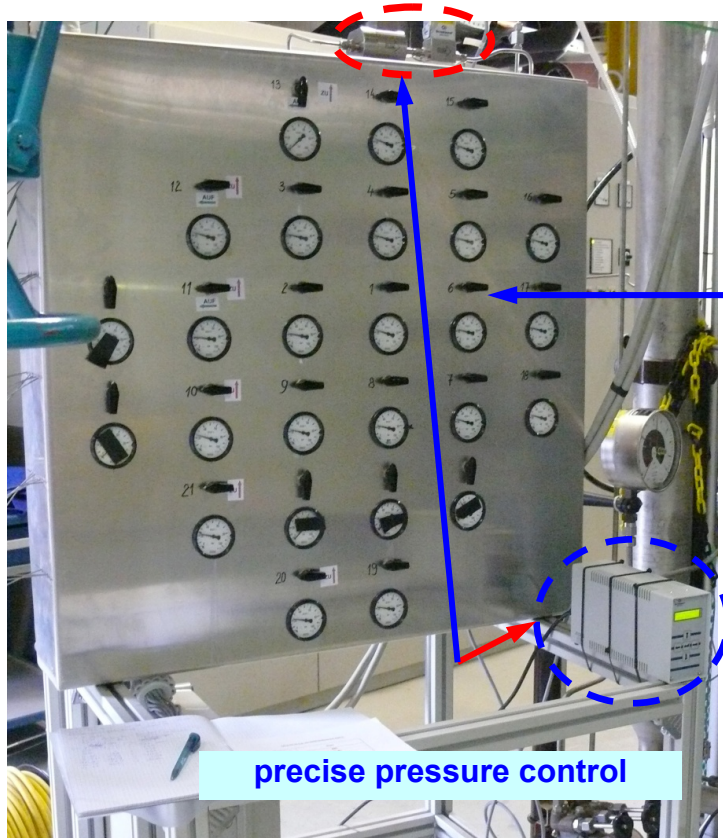


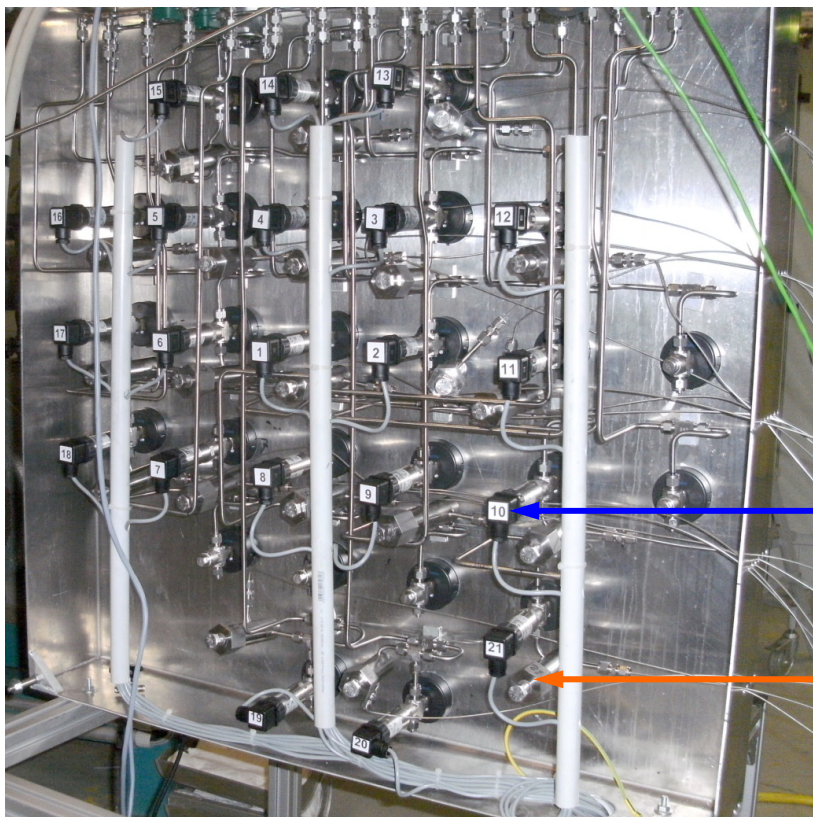
Fig. 6: Heated fuel rod simulator.





Front side with:  
21 pressure valves

precise pressure control



Rear side with :

21 capillary tubes  
to test bundle

21 pressure  
transducers

21 adjustable  
compensation volumes  
to setting of original  
volume value  
of  $31.5 \text{ cm}^3$

Fig. 7: QUENCH-L0; Rod pressure control and measurement panel.

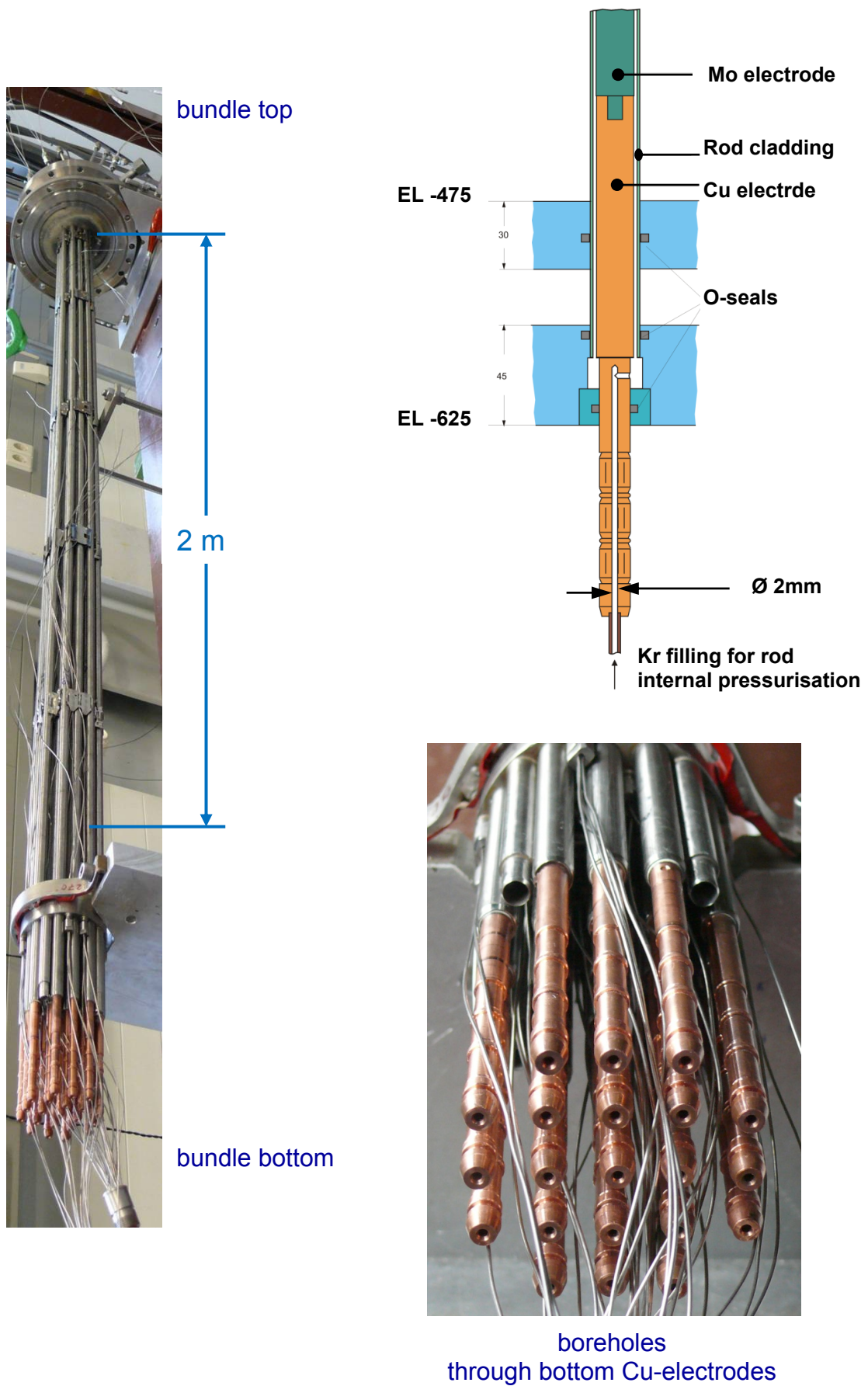
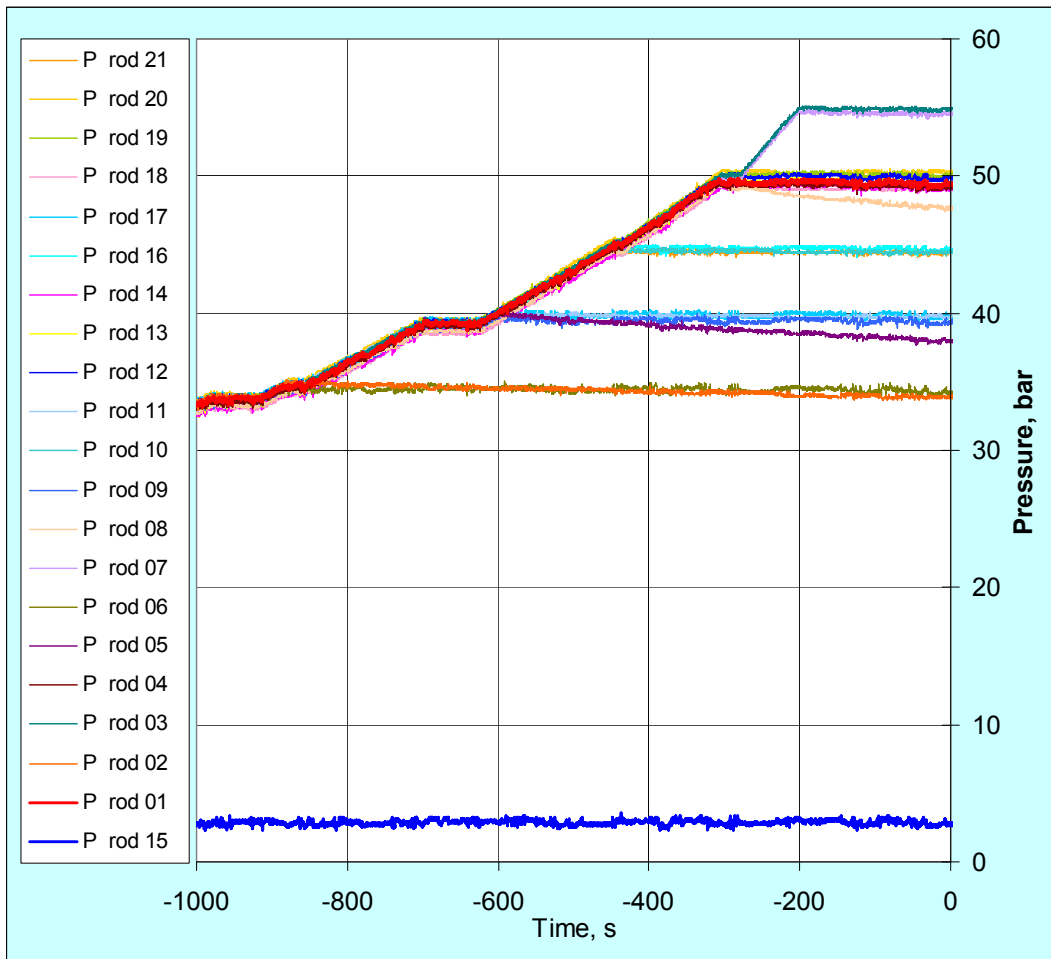


Fig. 8: QUENCH-L0; Rod pressurization.





individual rod pressurization with  $Kr$   
at max cladding temperature  $T_{pct}=520^{\circ}C$



Map of bundle filling

Pressure, bar	Number of rods
3 (system p)	1
35	2
40	4
45	3
50	9
55	2

Fig. 9: QUENCH-L0; Rod pressurization process.

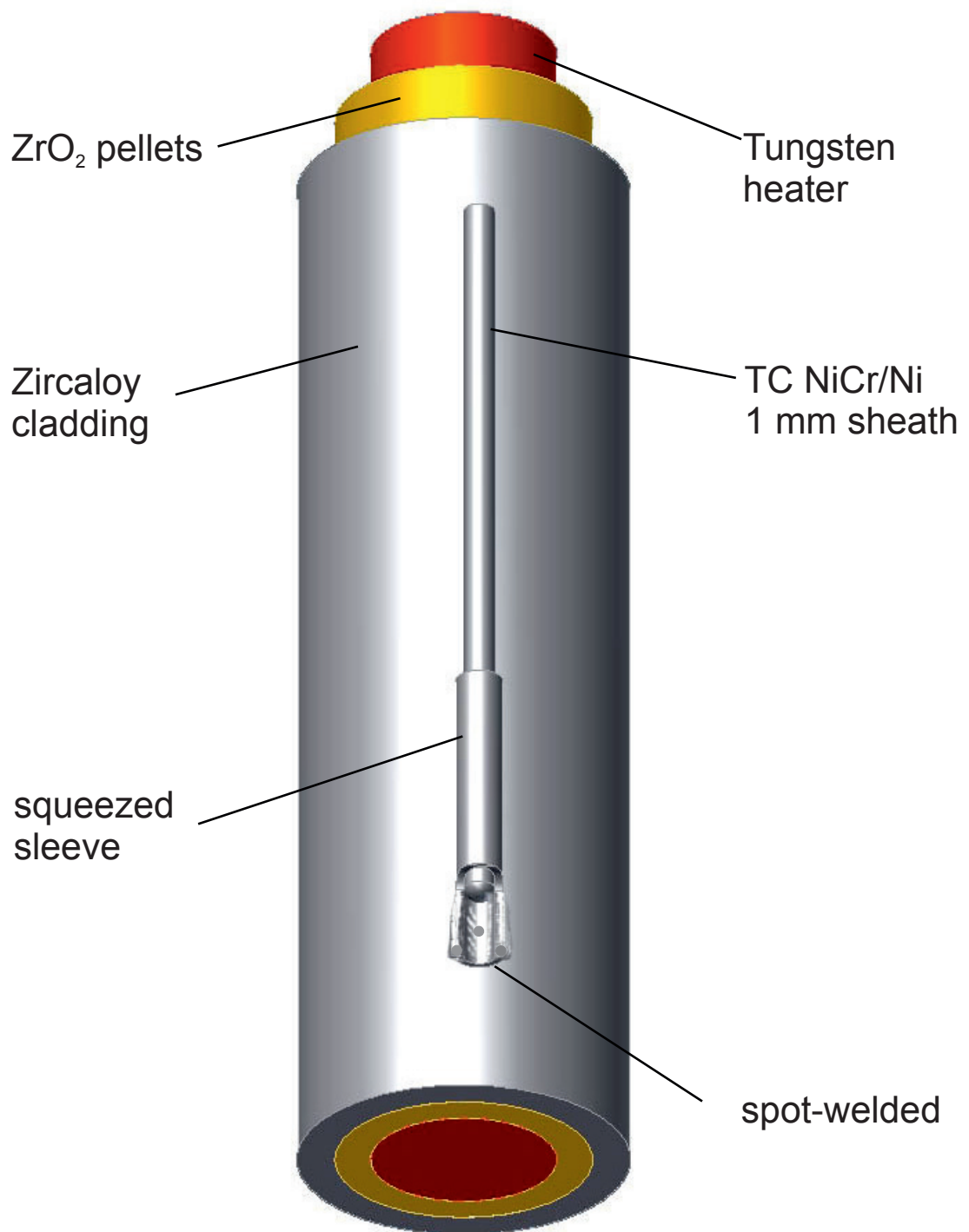


Fig. 10: QUENCH-L0; Concept for TC fastening at the test rod.

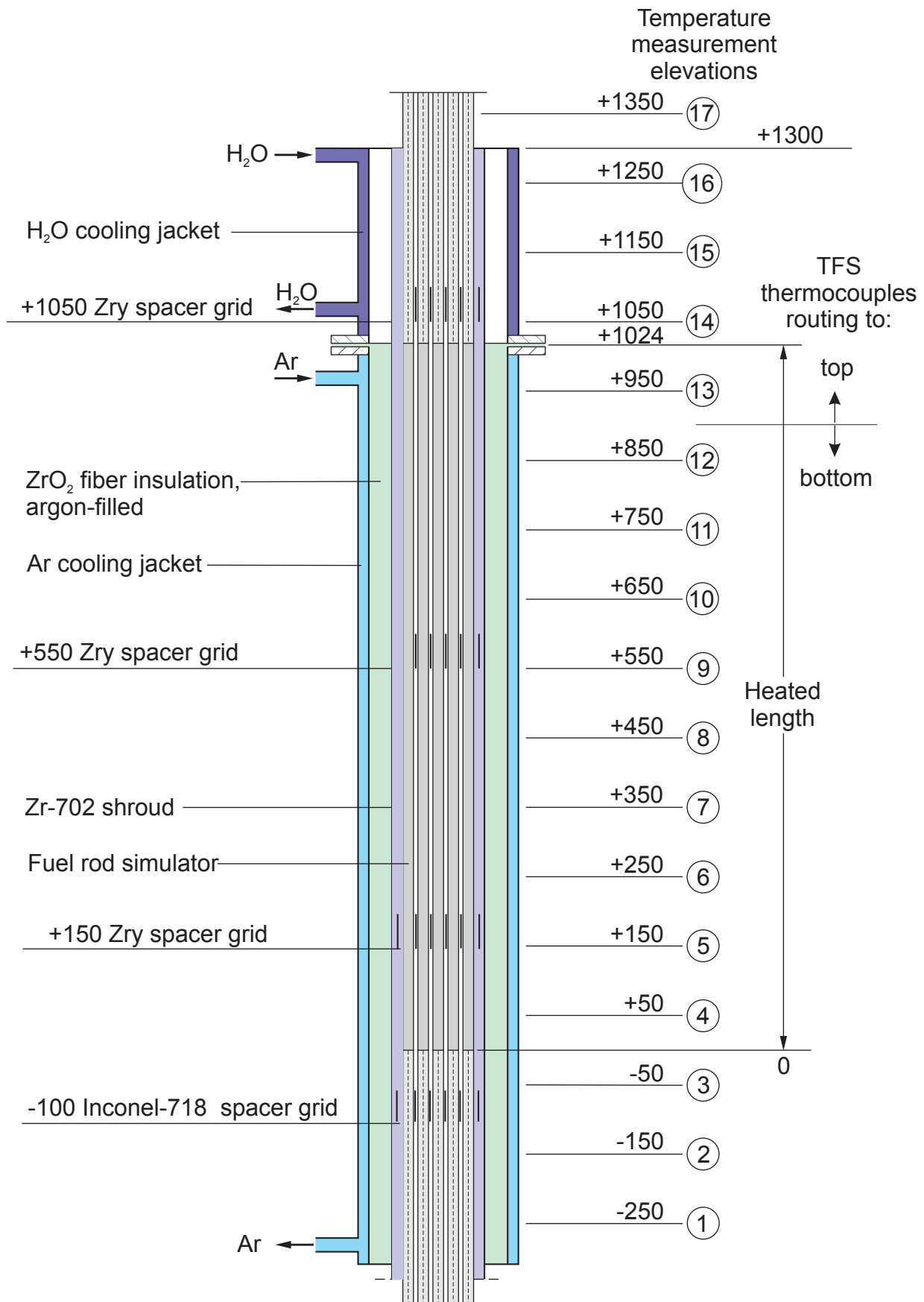


Fig. 11: Axial temperature measurement locations in the QUENCH-L0 test section.

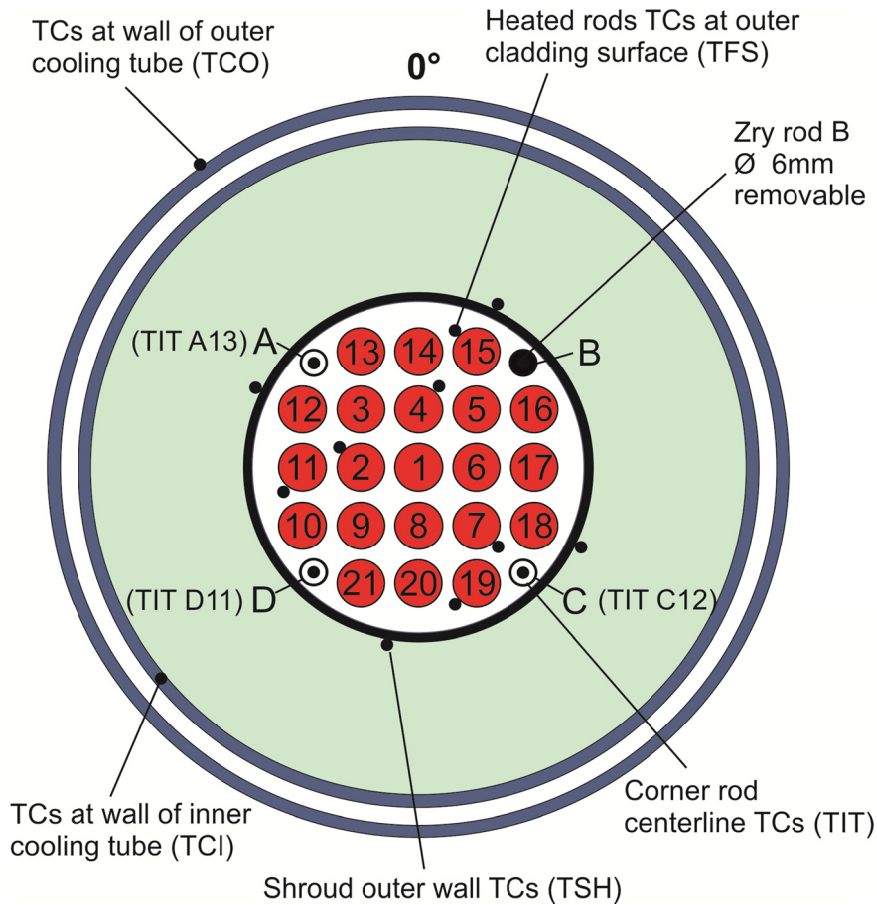
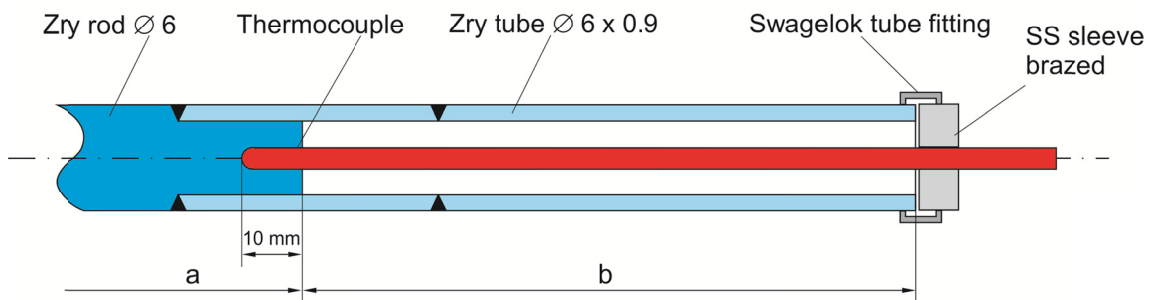


Fig. 12: QUENCH-L0; Test bundle; TC instrumentation and rod designation (top view).

(TIT A13, TIT C12, TIT D11)



Rod A: TIT A13 (950 mm), a = 360 mm, b = 2080 mm  
 Rod C: TIT C12 (850 mm), a = 460 mm, b = 1980 mm  
 Rod D: TIT D11 (750 mm), a = 560 mm, b = 1880 mm  
 (Rod B: Zry-4 rod, Ø 6 mm, removable)

Fig. 13: QUENCH-L0; Arrangement of the thermocouples inside the corner rods.

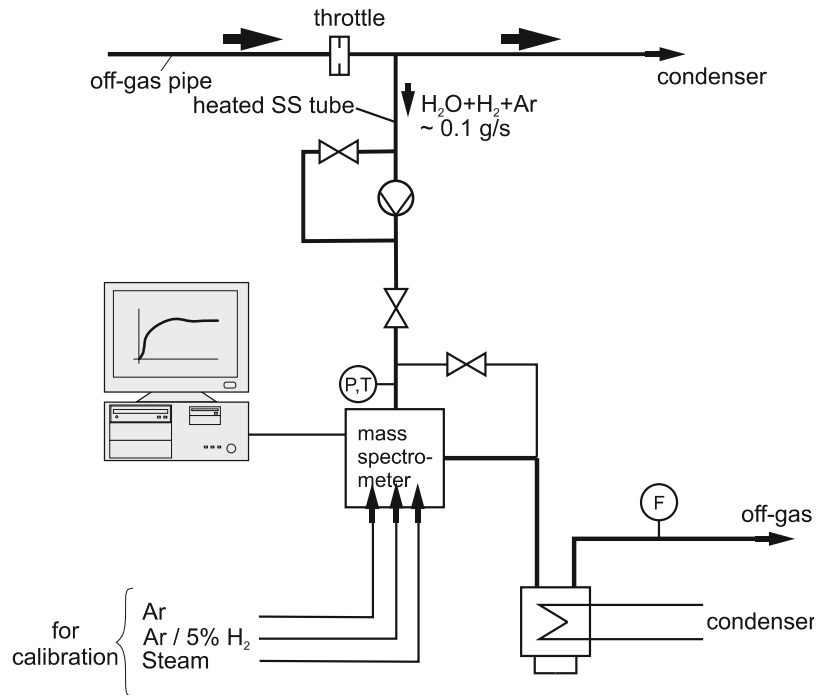


Fig. 14: QUENCH Facility;  $\text{H}_2$  measurement with the GAM 300 mass spectrometer.

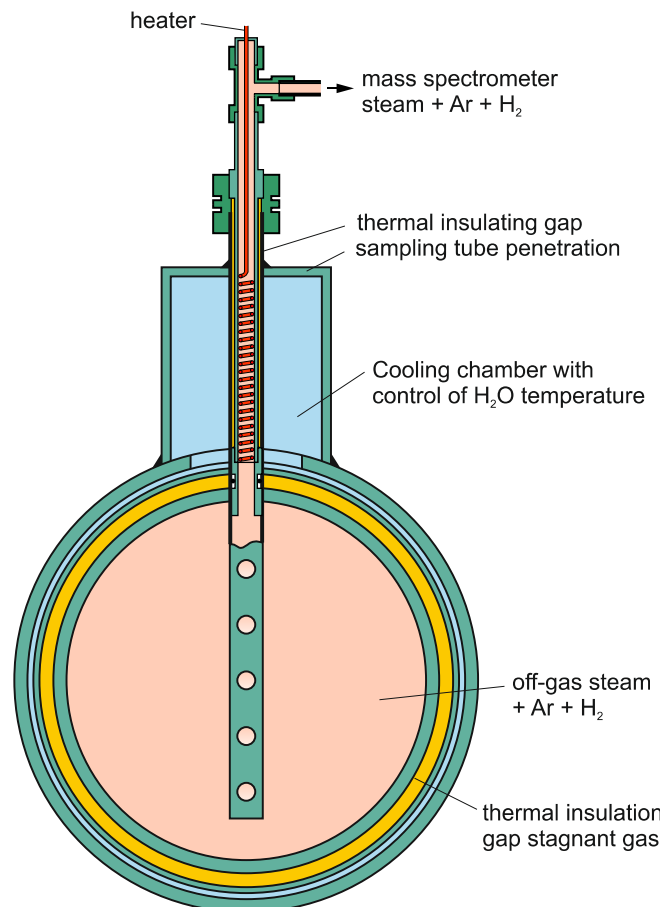


Fig. 15: Mass spectrometer sampling position at the off-gas pipe off the QUENCH test facility

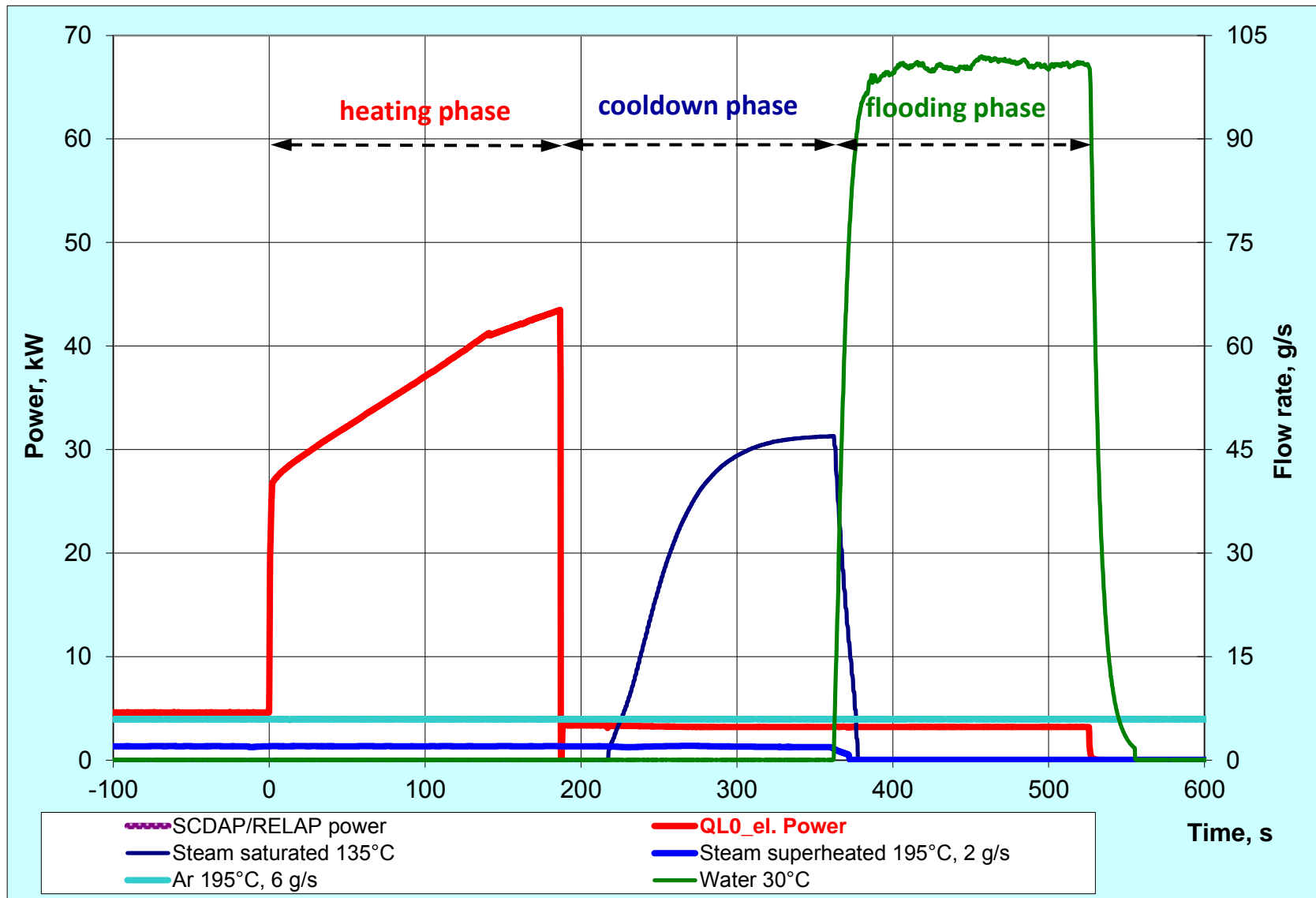


Fig. 16 : QUENCH-L0; QL0 test progression.

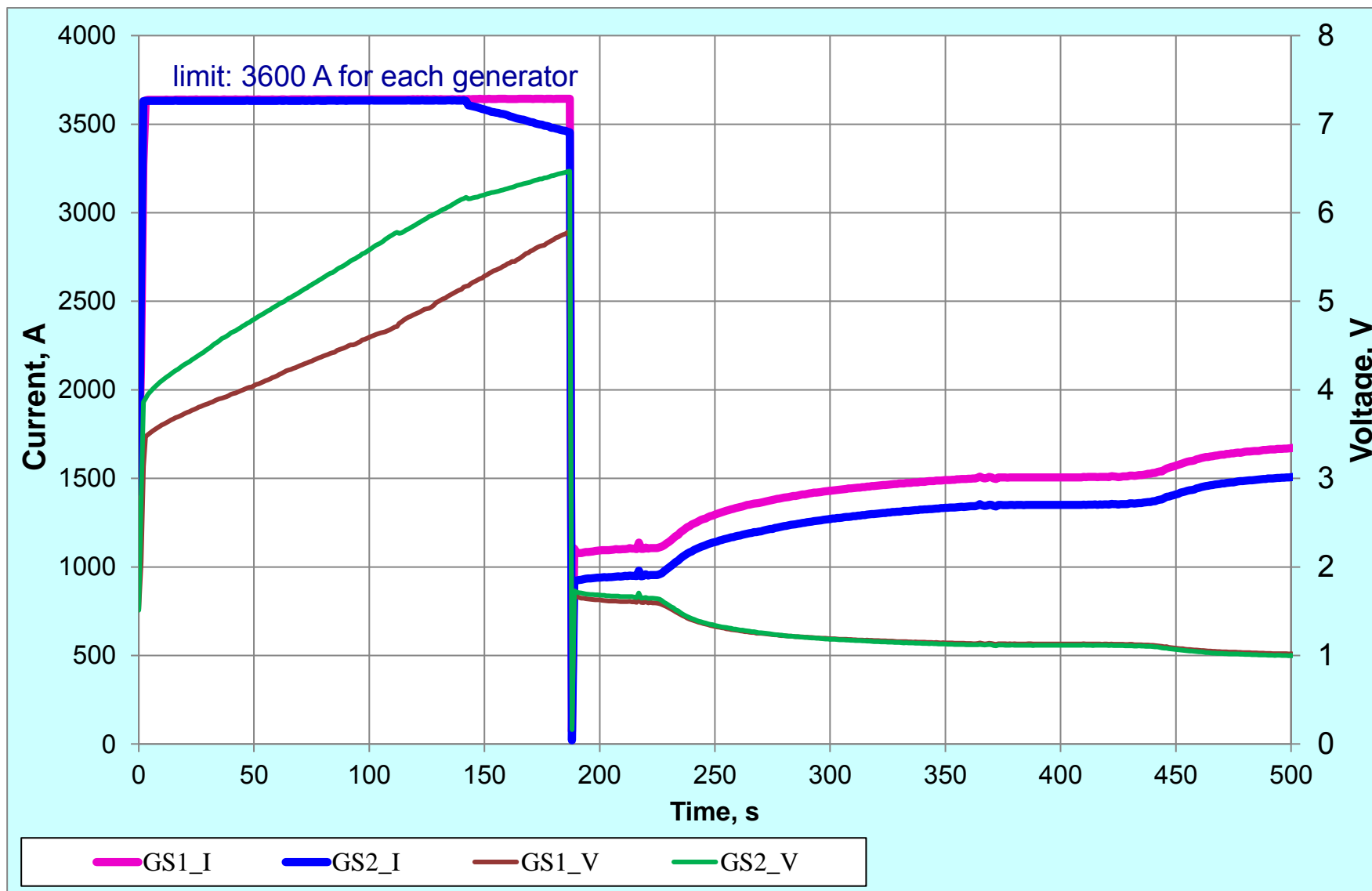


Fig. 17 : QUENCH-L0; current limitation of DC generators.

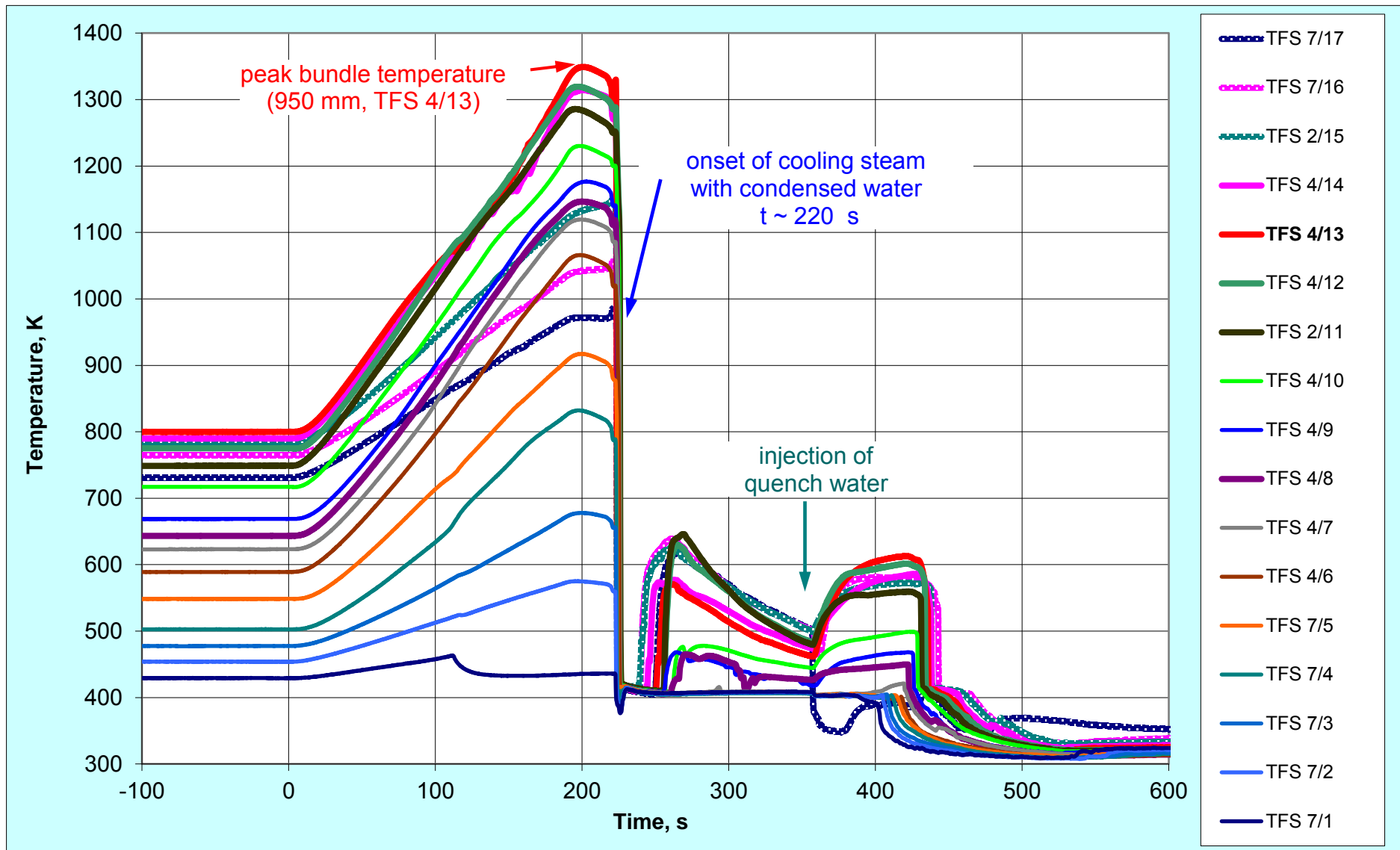


Fig. 18: QUENCH-L0; Rod-surface thermocouple readings at 17 elevations between -250 und 1350 mm.



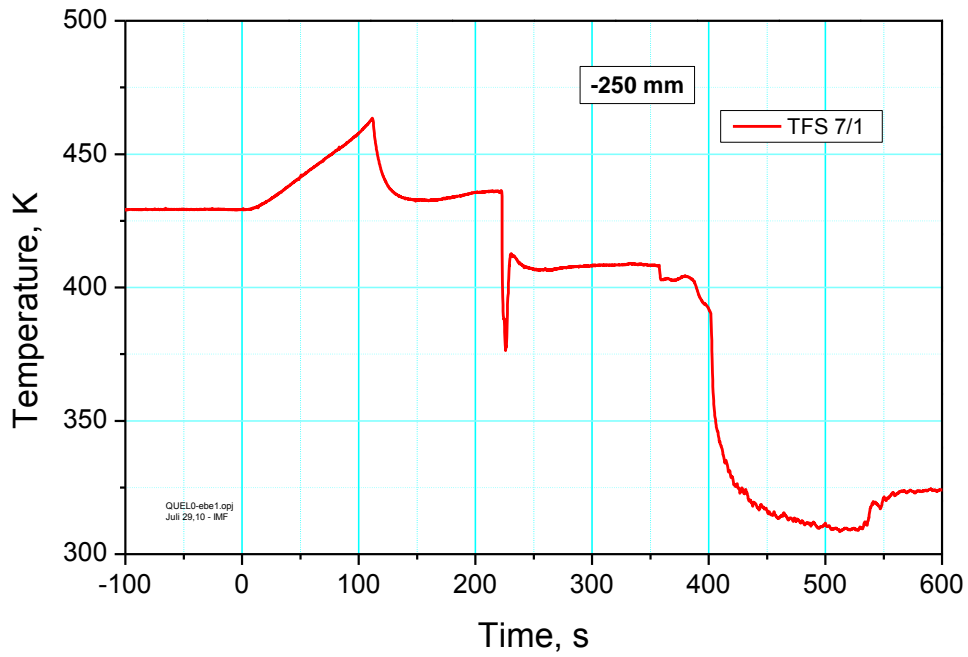


Fig.19: QUENCH-L0; Temperatures measured by rod cladding (TFS 7/1) thermocouple at -250 mm elevation.

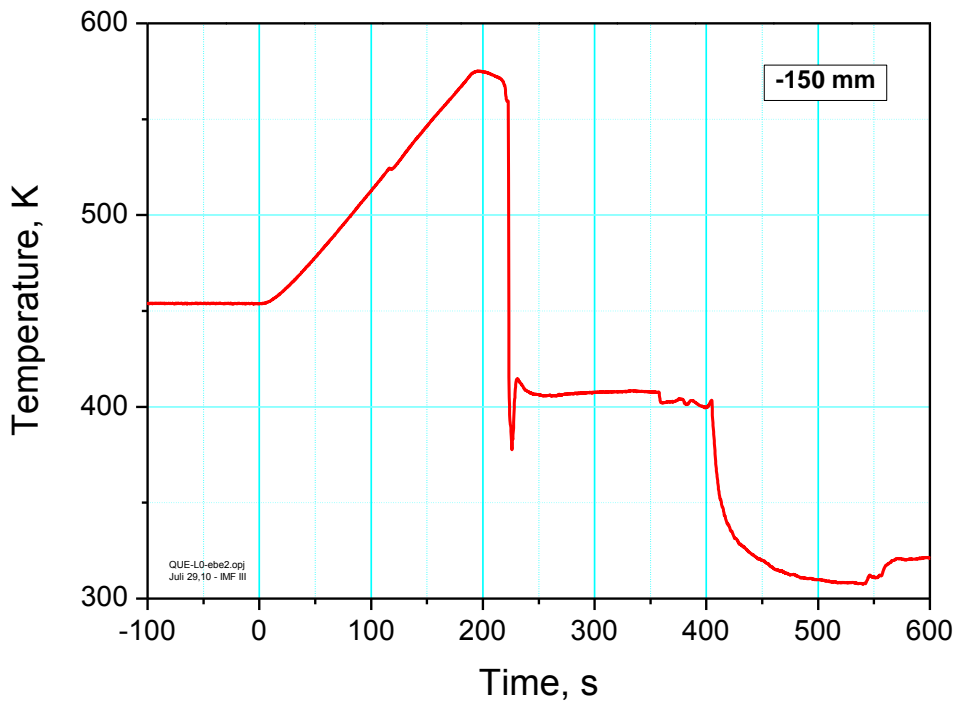


Fig.20: QUENCH-L0; Temperatures measured by rod cladding (TFS 7/2) thermocouple at -150 mm elevation.

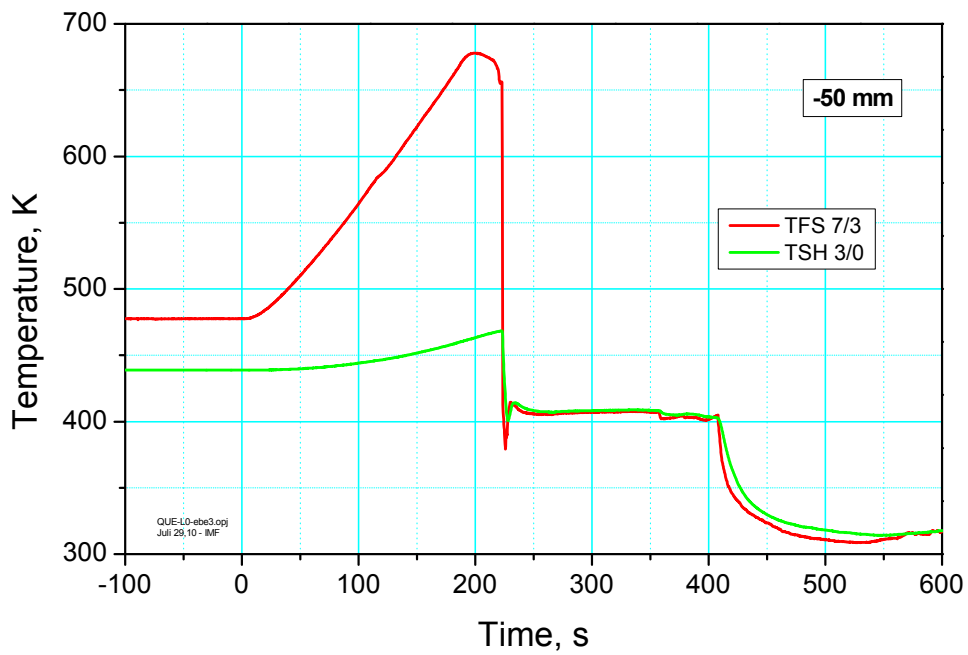


Fig. 21: QUENCH-L0; Temperatures measured by rod cladding (TFS 7/3) and shroud (TSH 3/0) thermocouples at -50 mm elevation.

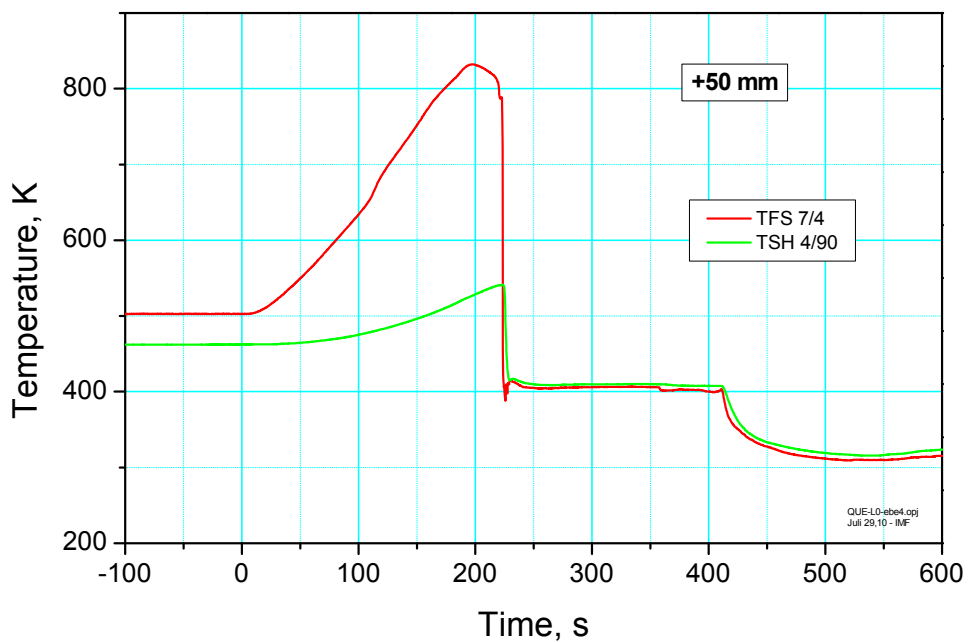


Fig. 22: QUENCH-L0; Temperatures measured by rod cladding (TFS 7/4) and shroud (TSH 4/90) thermocouples at 50 mm elevation.

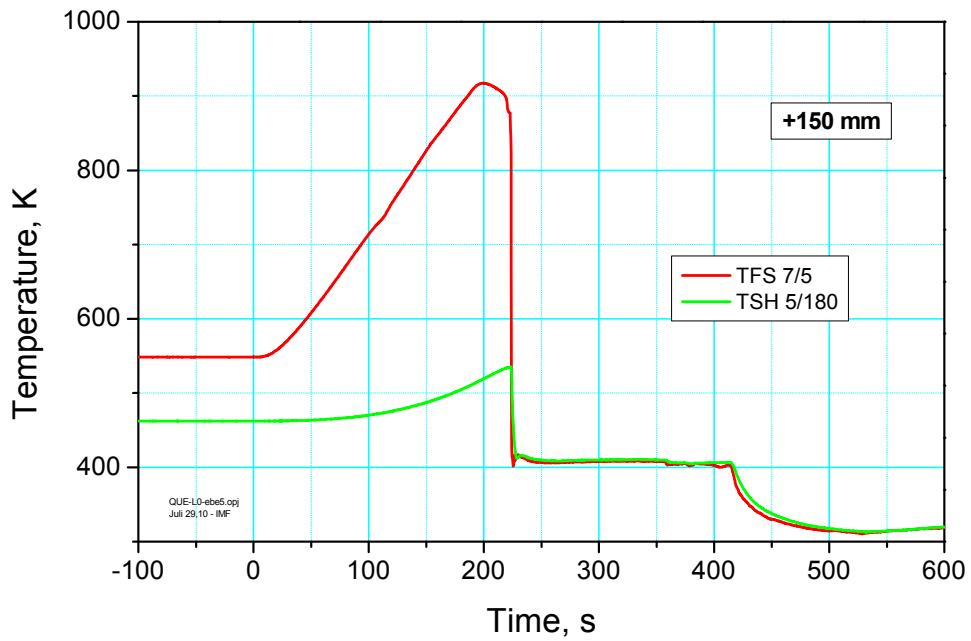


Fig. 23: QUENCH-L0; Temperatures measured by rod cladding (TFS 7/5) and shroud (TSH 5/180) thermocouples at 150 mm elevation.

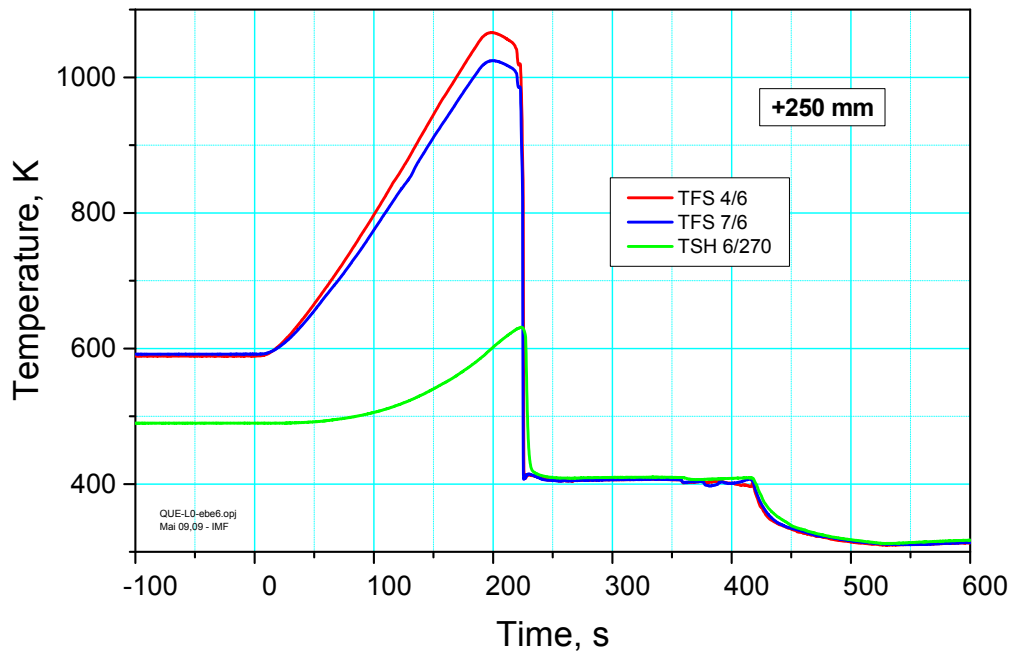


Fig. 24: QUENCH-L0; Temperatures measured by rod cladding (TFS) and shroud (TSH 6/270) thermocouples at 250 mm elevation.

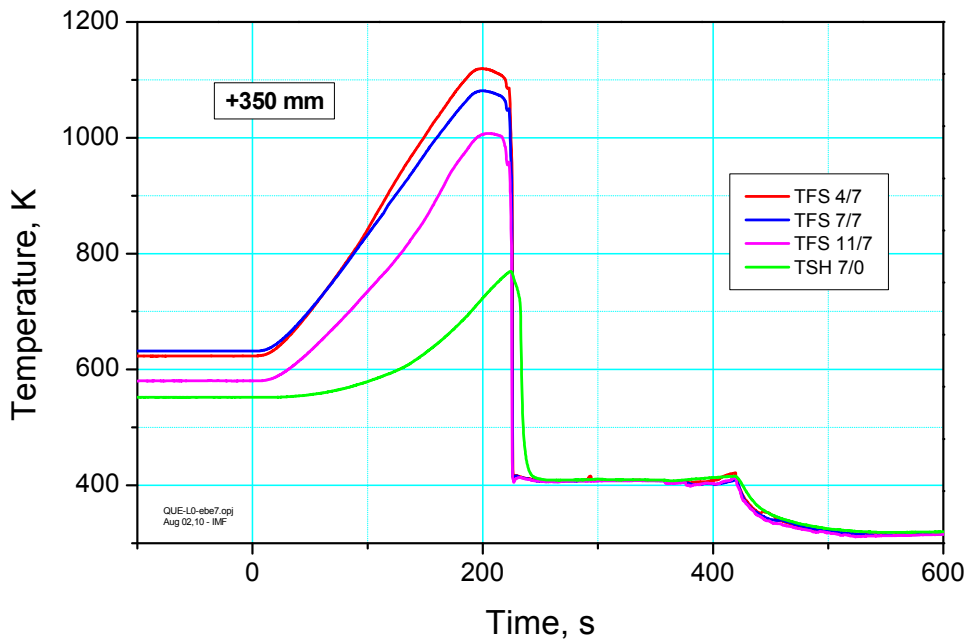


Fig. 25: QUENCH-L0; Temperatures measured by rod cladding (TFS) and shroud (TSH 7/0) thermocouples at 350 mm elevation.

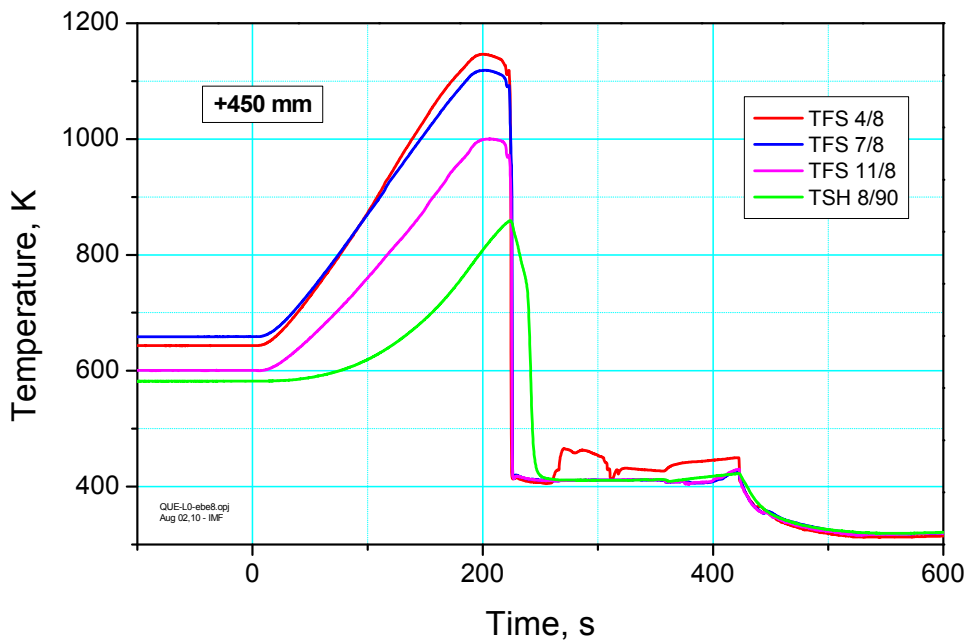


Fig. 26: QUENCH-L0; Temperatures measured by rod cladding (TFS) and shroud (TSH 8/0) thermocouples at 450 mm elevation.

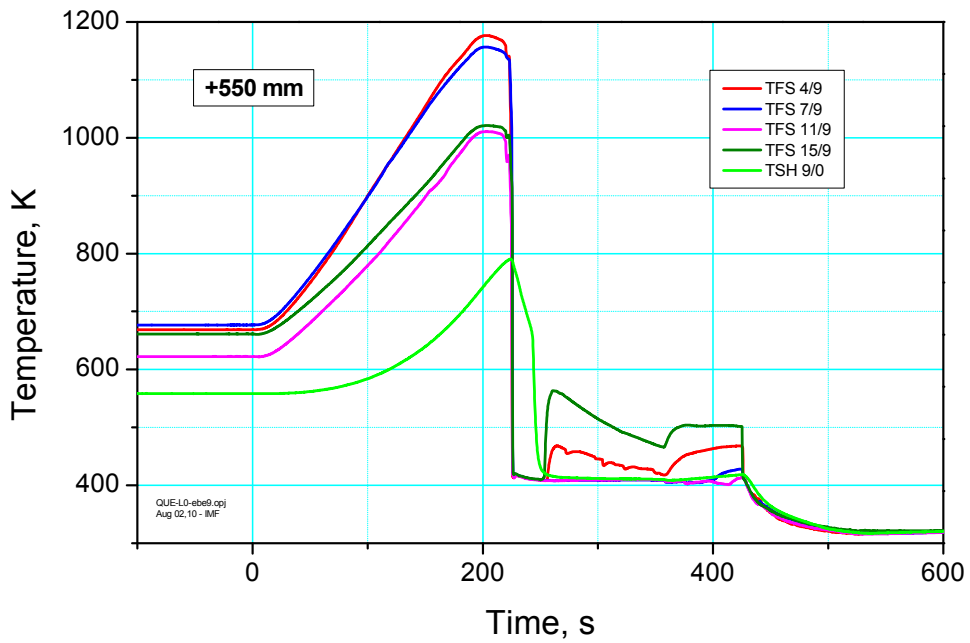


Fig. 27: QUENCH-L0; Temperatures measured by rod cladding (TFS) and shroud (TSH 9/180) thermocouples at 550 mm elevation.

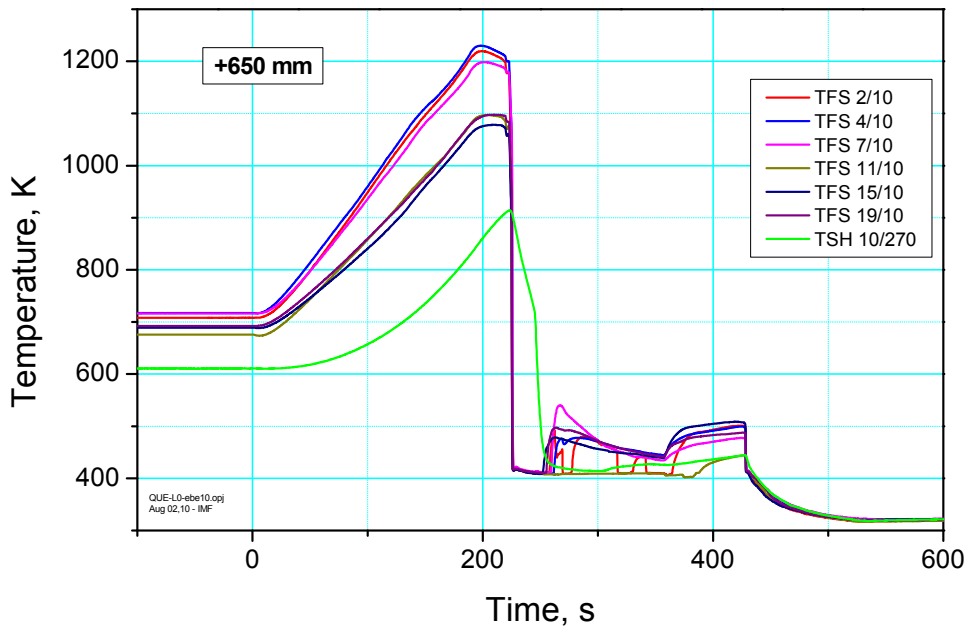


Fig. 28: QUENCH-L0; Temperatures measured by rod cladding (TFS) and shroud (TSH 10/270) thermocouples at 650 mm elevation.

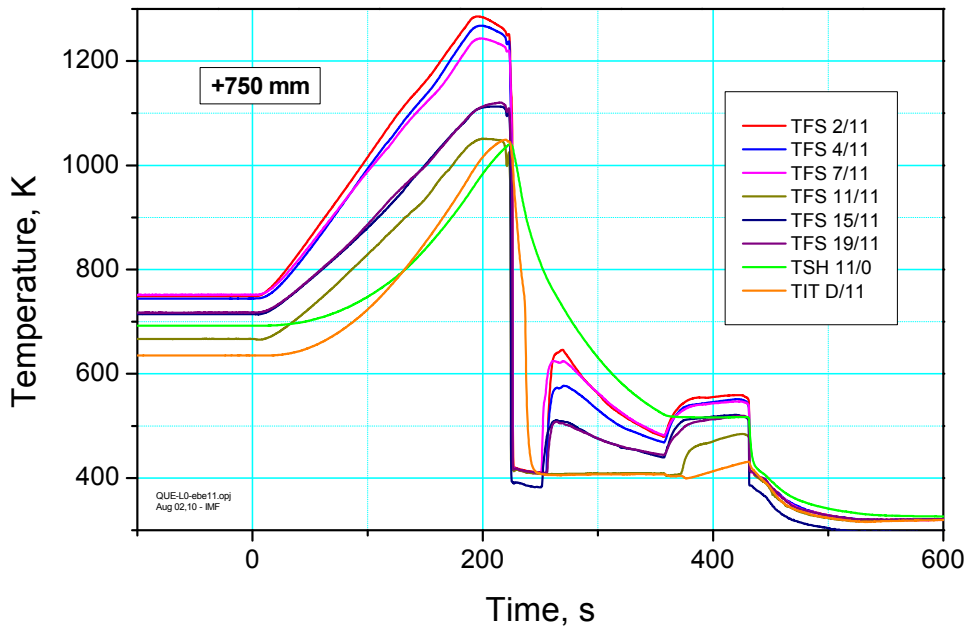


Fig. 29: QUENCH-L0; Temperatures measured by rod cladding (TFS) and shroud (TSH 11/0), and corner rod internal (TIT D/11) thermocouples at 750 mm elevation.

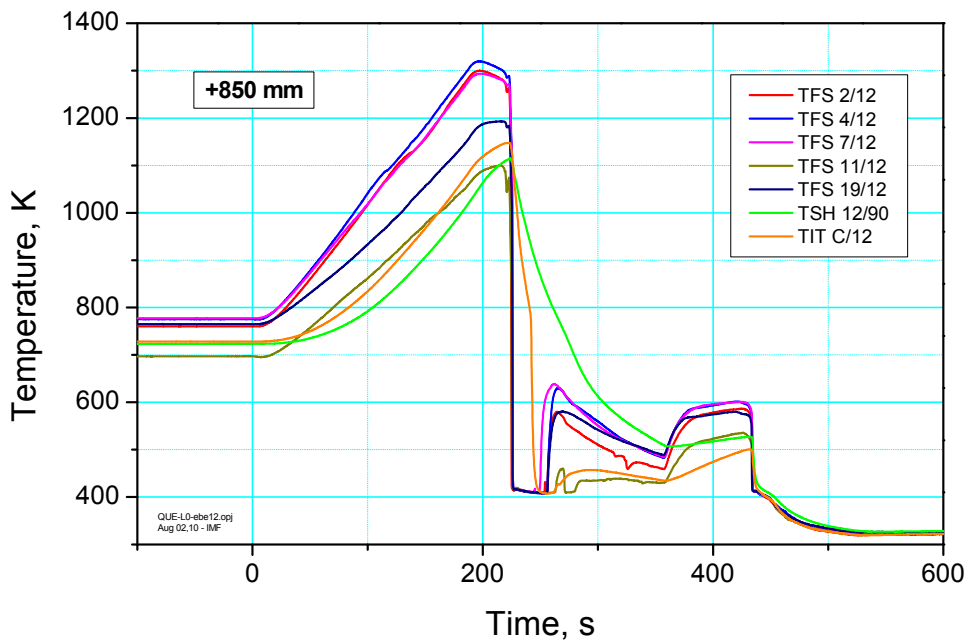


Fig. 30: QUENCH-L0; Temperatures measured by rod cladding (TFS) and shroud (TSH 12/90), and corner rod internal (TIT C/12) thermocouples at 850 mm elevation.

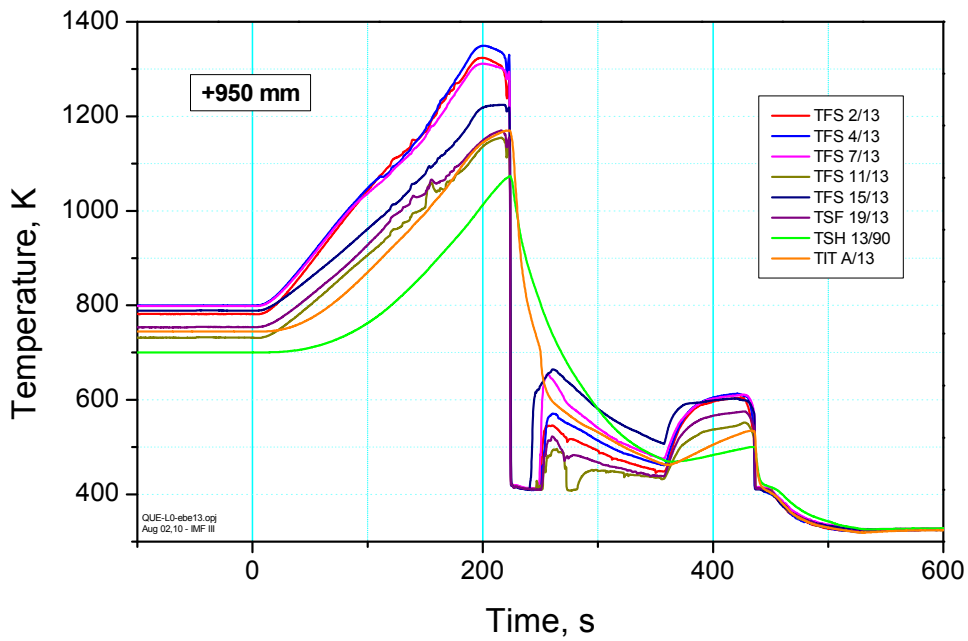


Fig. 31: QUENCH-L0; Temperatures measured by rod cladding (TFS) and shroud (TSH 13/90), and corner rod internal (TIT A/13) thermocouples at 950 mm elevation.

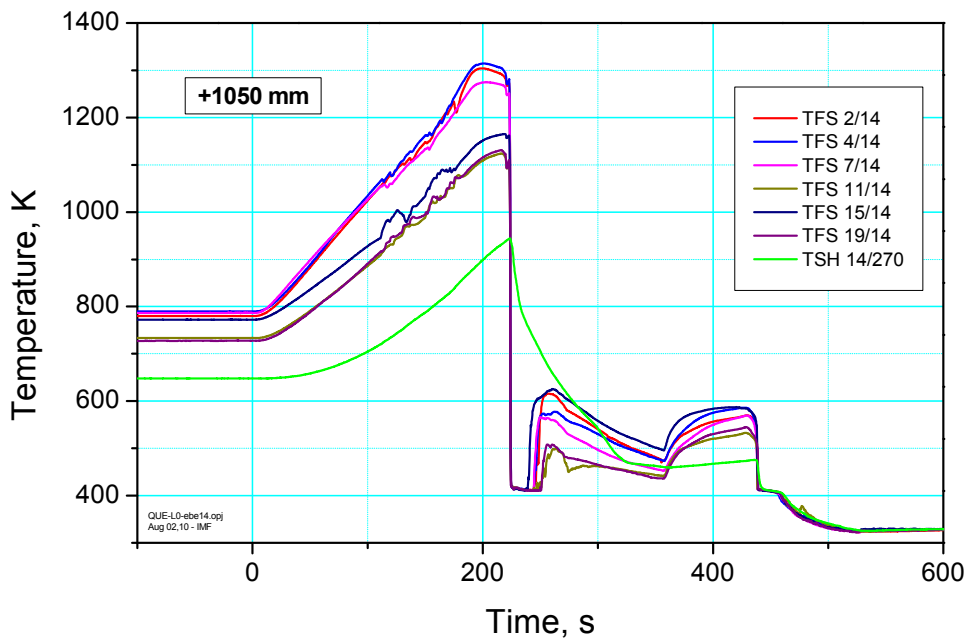


Fig. 32: QUENCH-L0; Temperatures measured by rod cladding (TFS) and shroud (TSH 14/270) thermocouples at 1050 mm elevation.

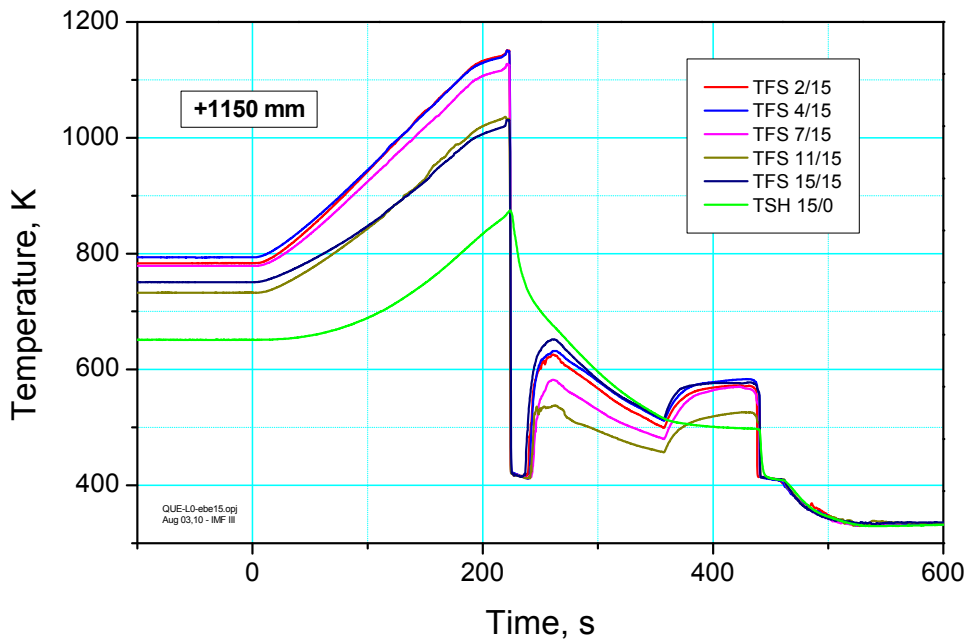


Fig. 33: QUENCH-L0; Temperatures measured by rod cladding (TFS) and shroud (TSH 15/0) thermocouples at 1150 mm elevation.

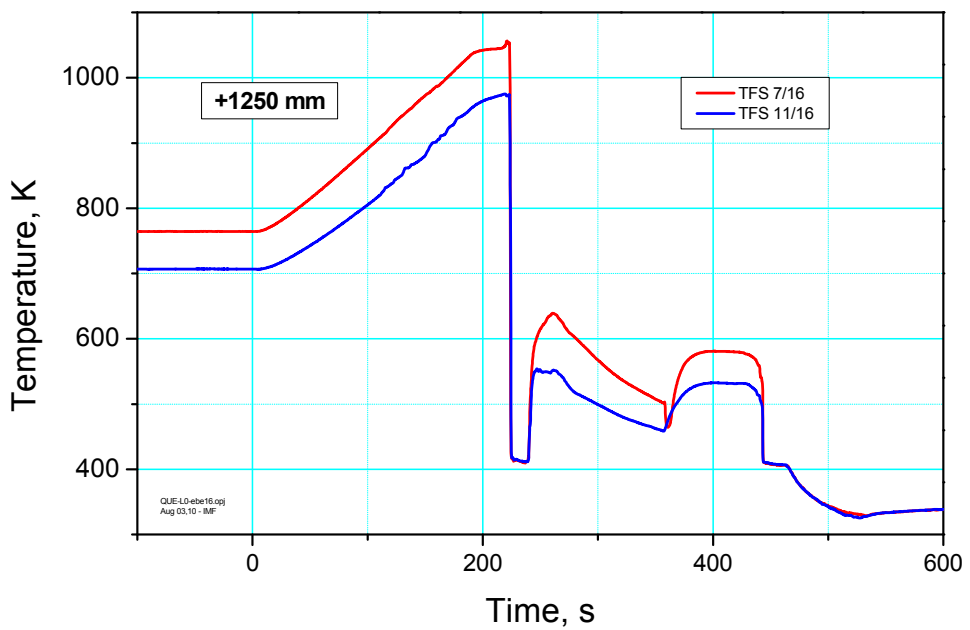


Fig. 34: QUENCH-L0; Temperatures measured by rod cladding (TFS) thermocouples at 1250 mm elevation.



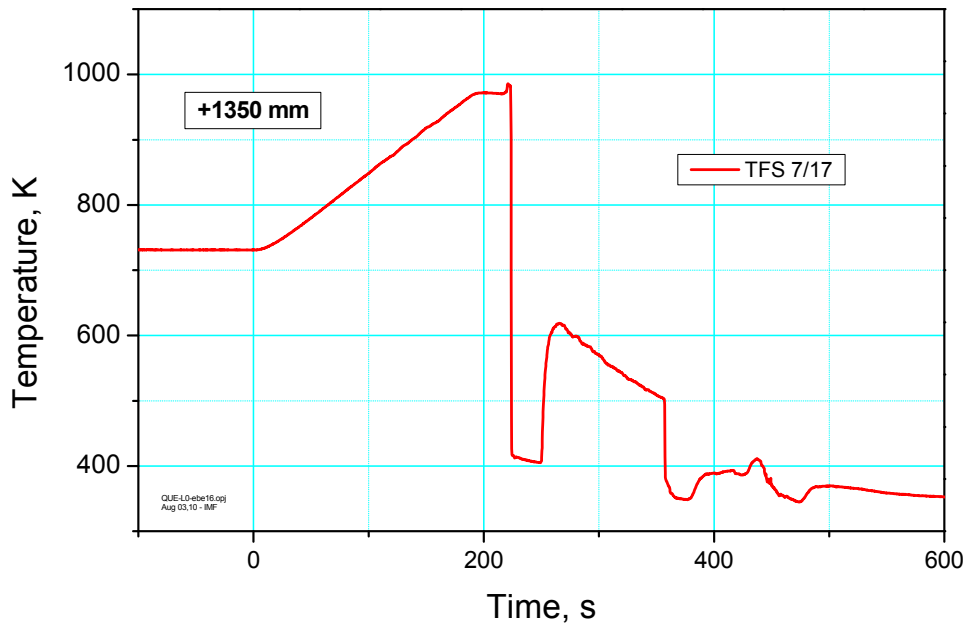


Fig. 35: QUENCH-L0; Temperatures measured by rod cladding (TFS 7/17) thermocouple at 1350 mm elevation.

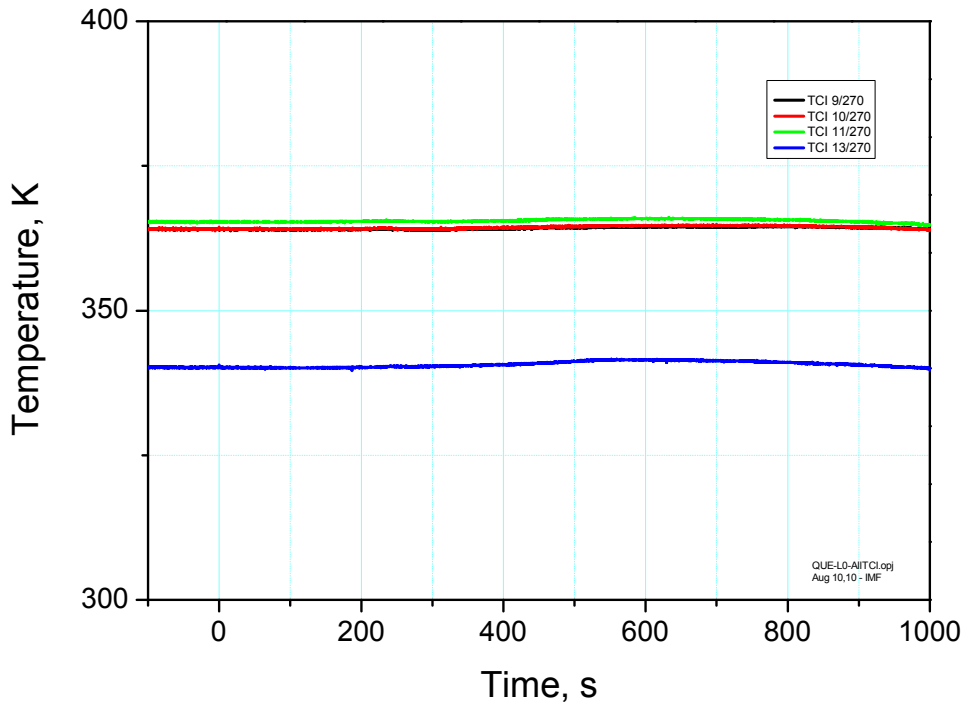


Fig. 36: QUENCH-L0; Overview of the TCI (inner cooling jacket).

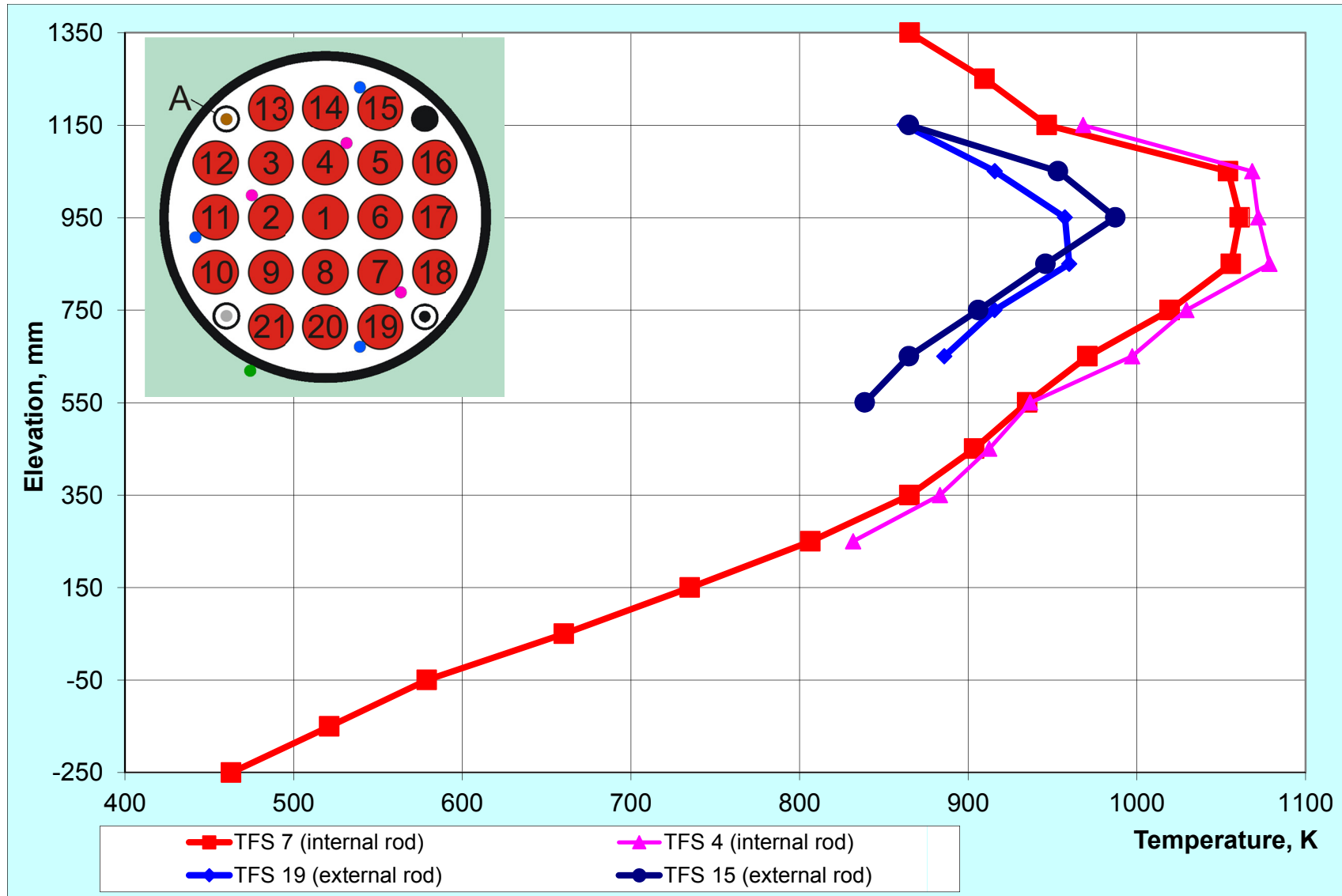


Fig. 37: QUENCH-L0; Axial and radial temperature distribution on time of the first burst case.

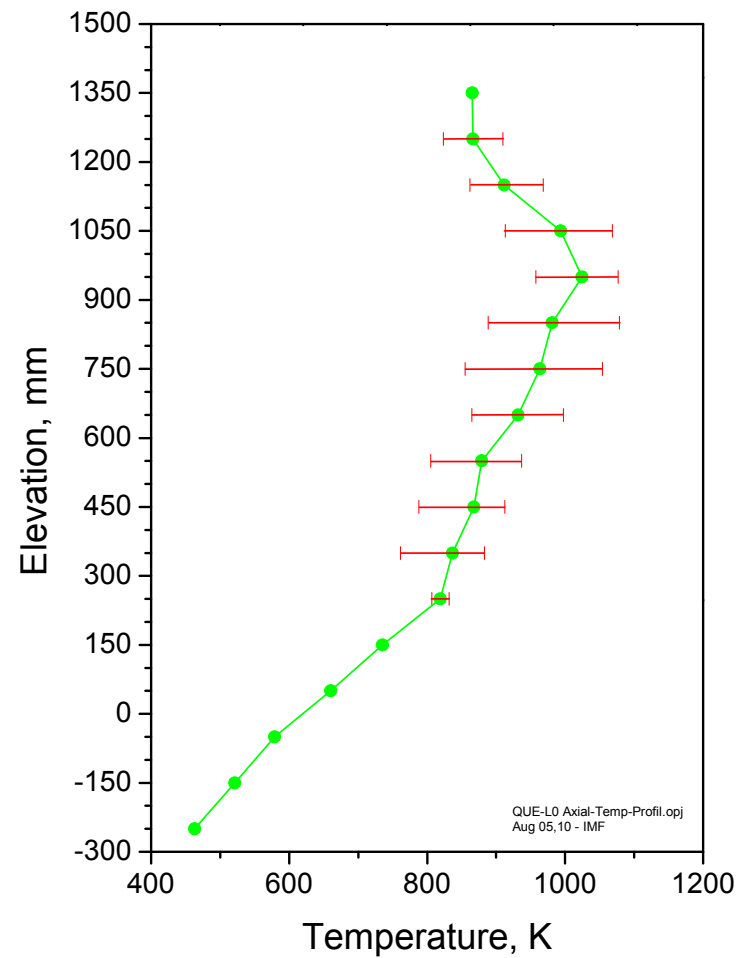
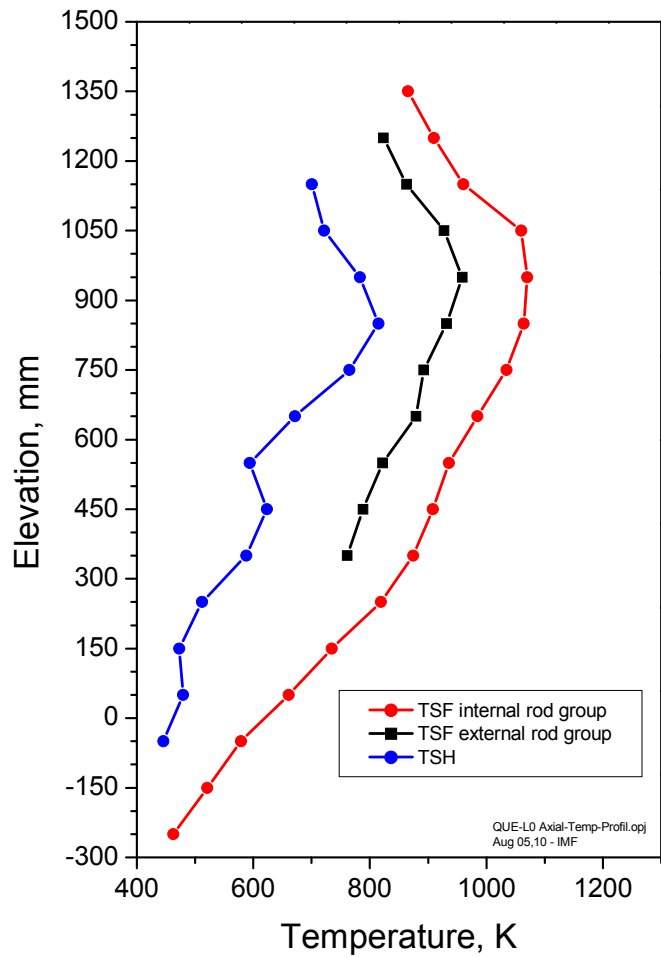


Fig. 38: QUENCH-L0; Axial temperature profile TFS internal and external rod group together with TSH, left, and axial temperature profile of all TFS, right, at 112 s (first cladding burst).

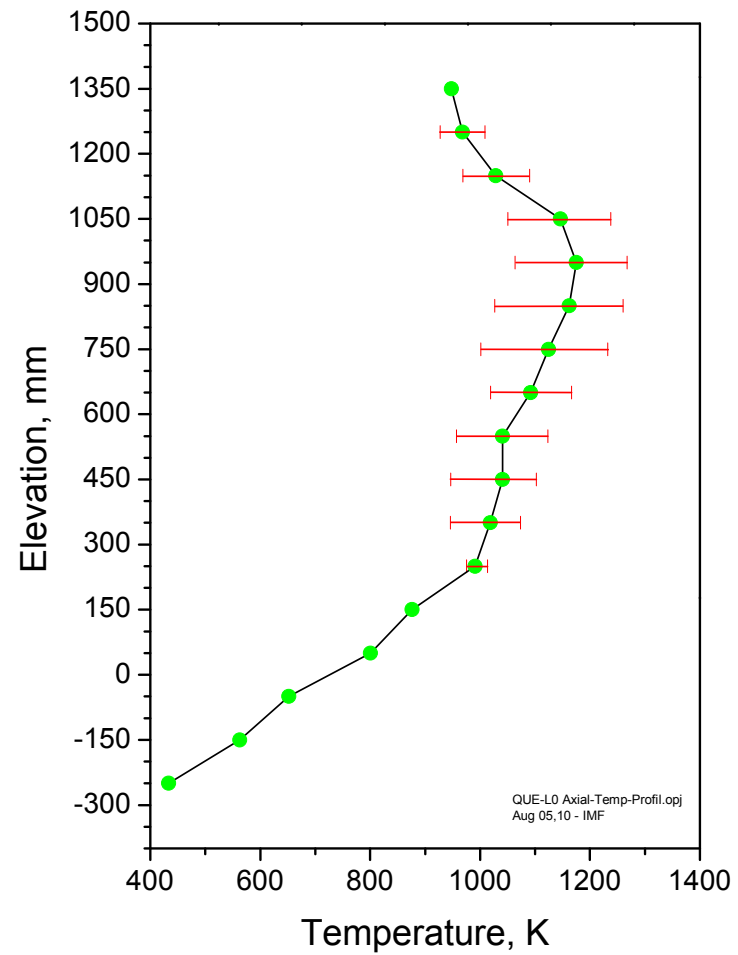
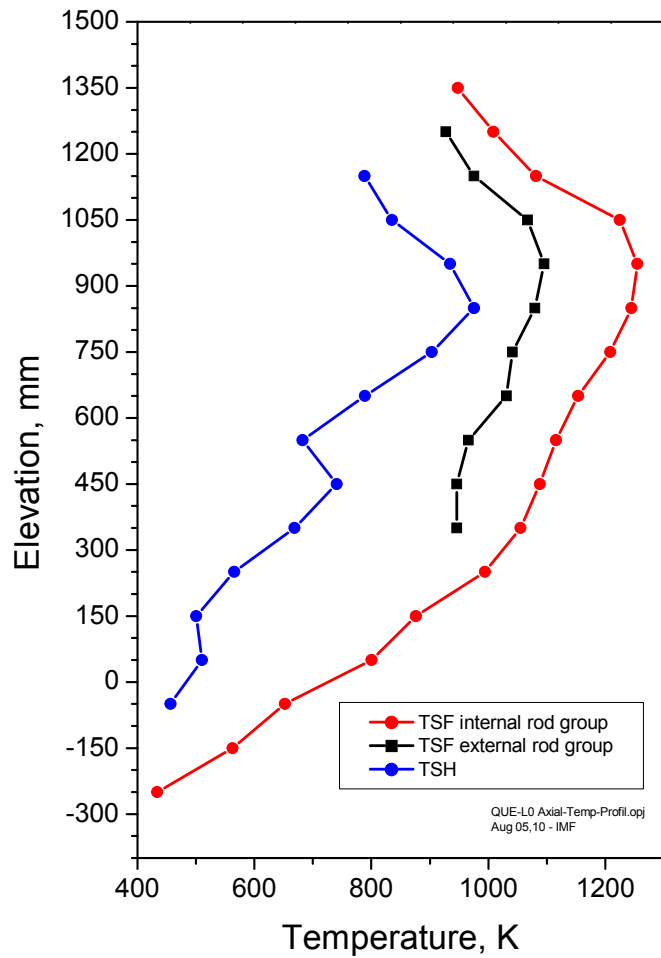


Fig.39: QUENCH-L0; Axial temperature profile TFS internal and external rod group together with TSH, left, and axial temperature profile of all TFS, right, at 174 s (last cladding burst).

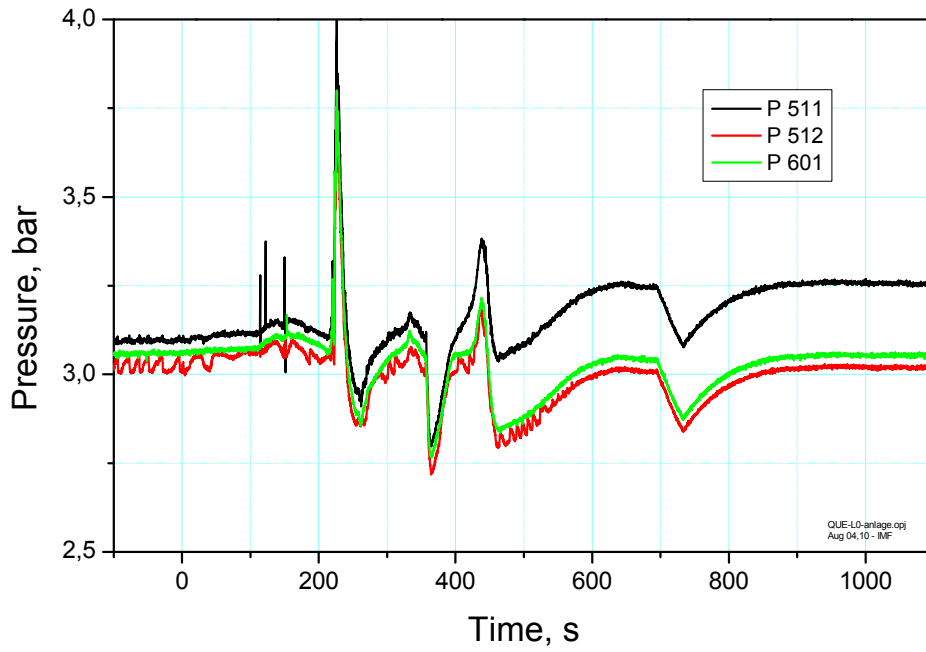


Fig. 40: QUENCH-L0; System pressure measured at test section inlet P 511, at outlet P 512, and in the off-gas pipe P 601.

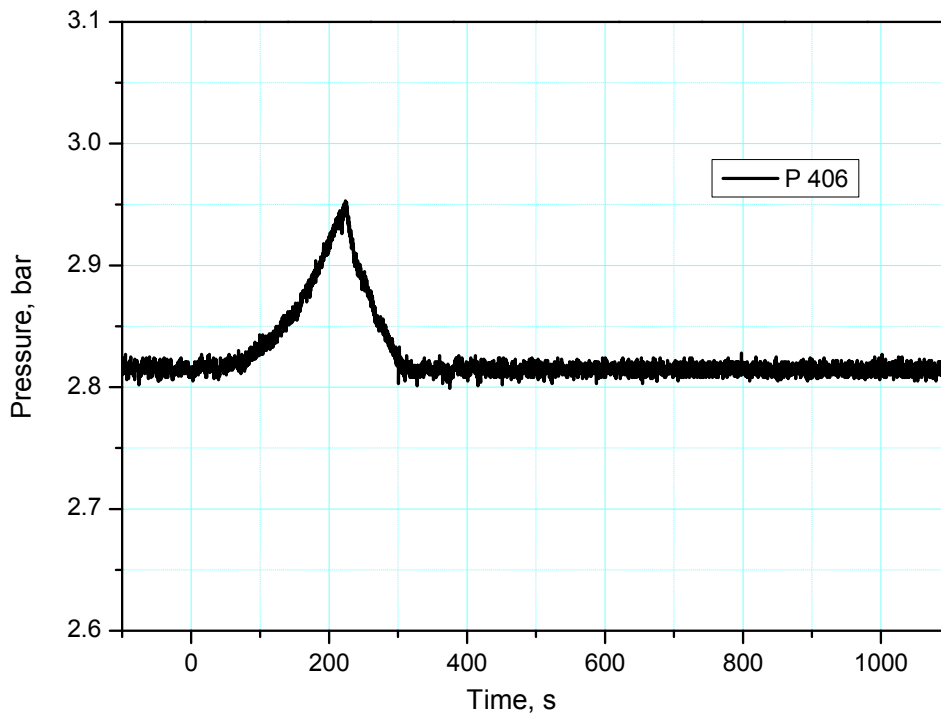


Fig. 41: QUENCH-L0; Argon pressure between shroud and cooling jacket P 406 demonstrates tightness of the shroud.

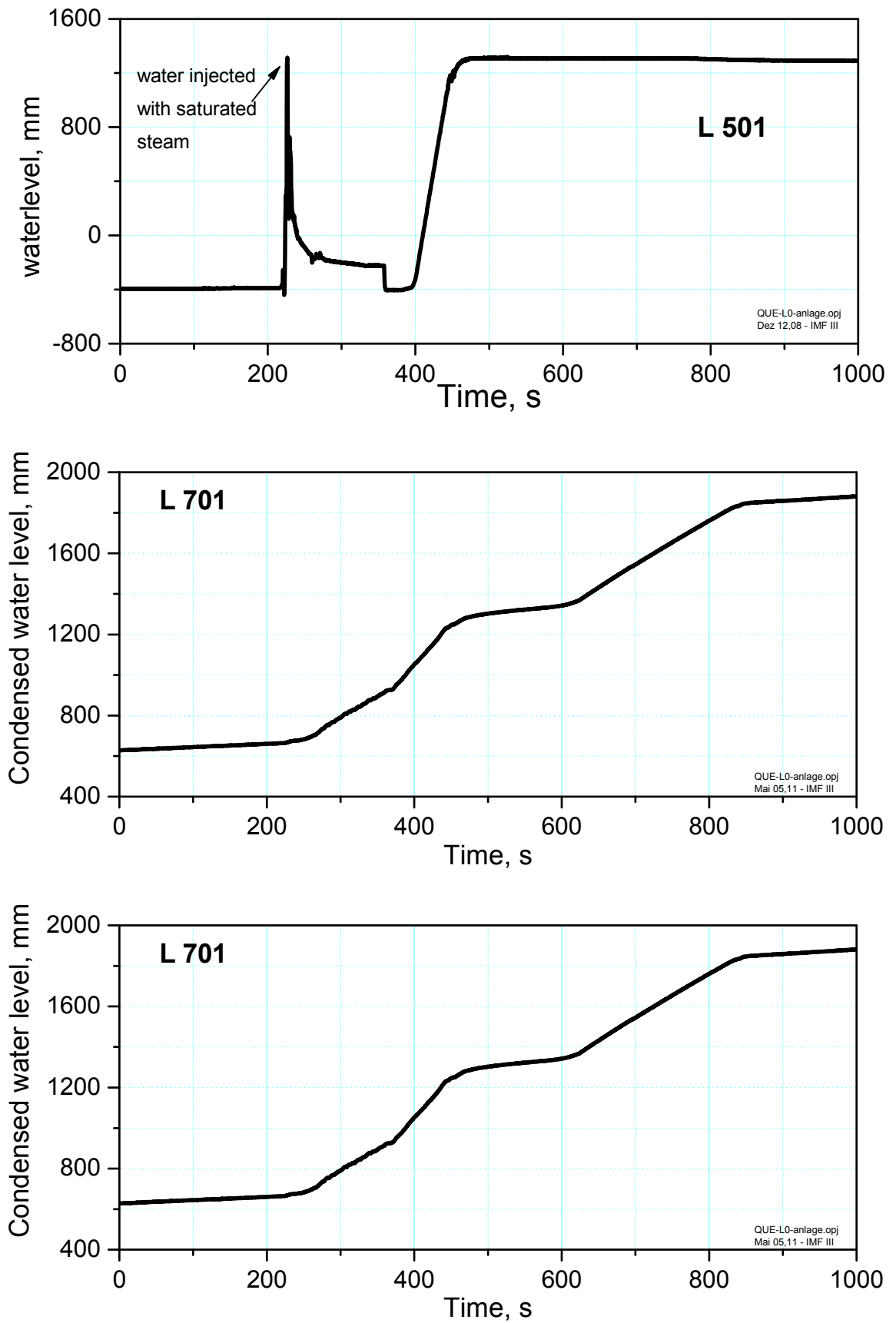


Fig. 42: QUENCH-L0; Quench measurement of collapsed water level (L 501), top, water mass flow rate (F 104), center, condensed water (L 701), bottom.

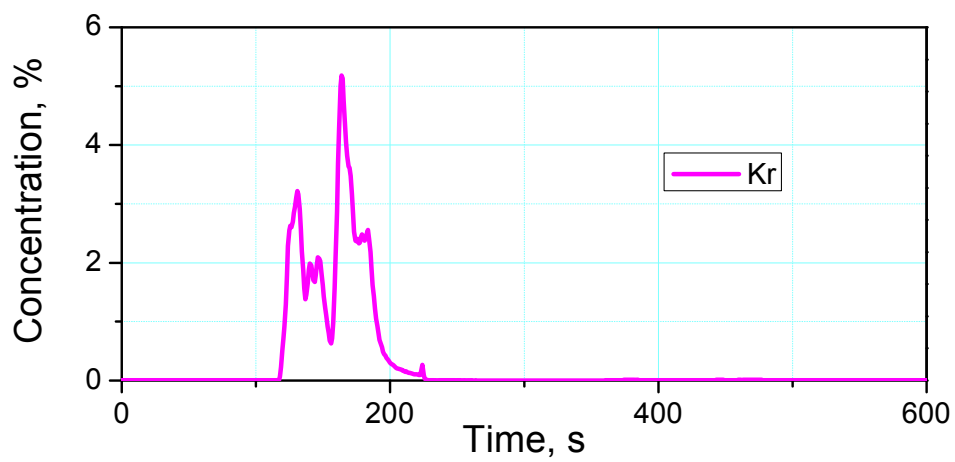
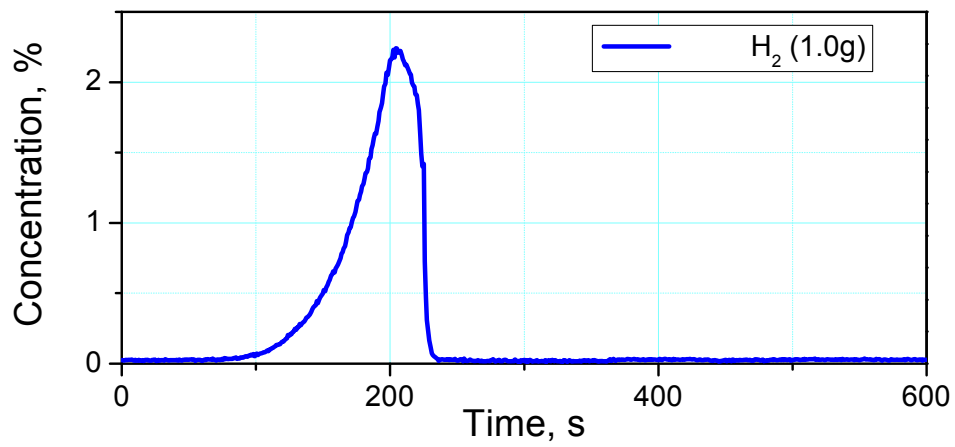
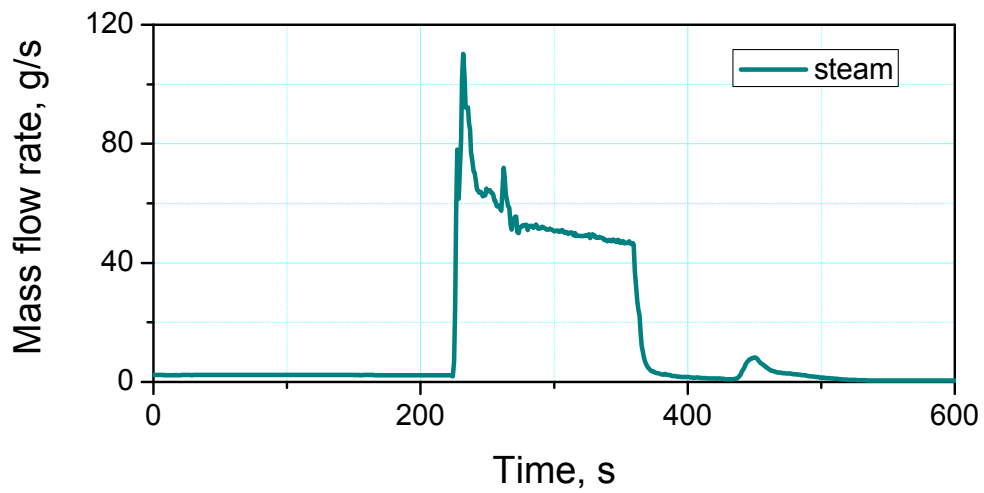


Fig. 43: QUENCH-L0; Steam rate, top, Hydrogen, center, Krypton, bottom, measured by mass spectrometry (MS).

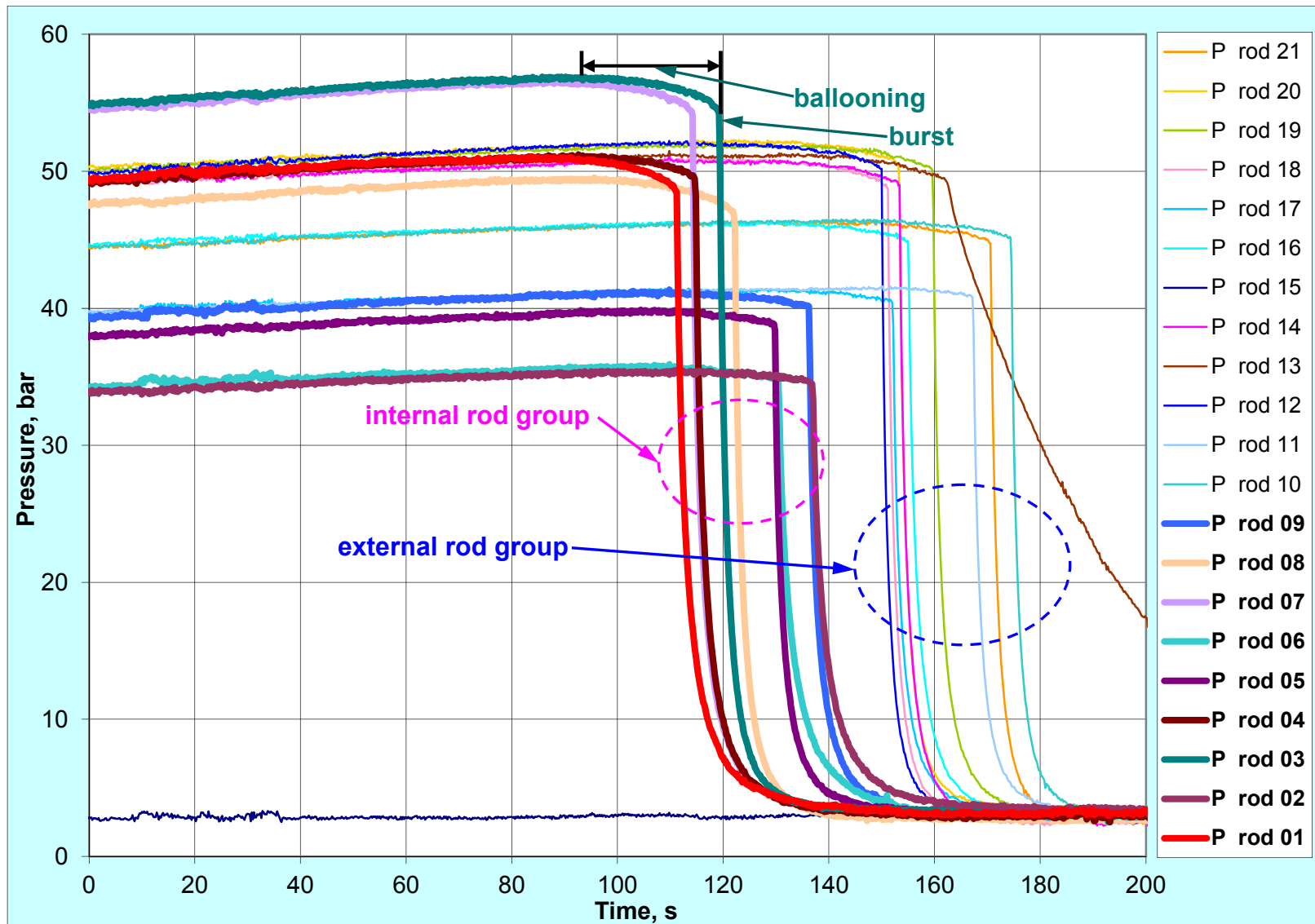


Fig. 44: QUENCH-L0; Pressure changing during heating phase; ballooning and burst.



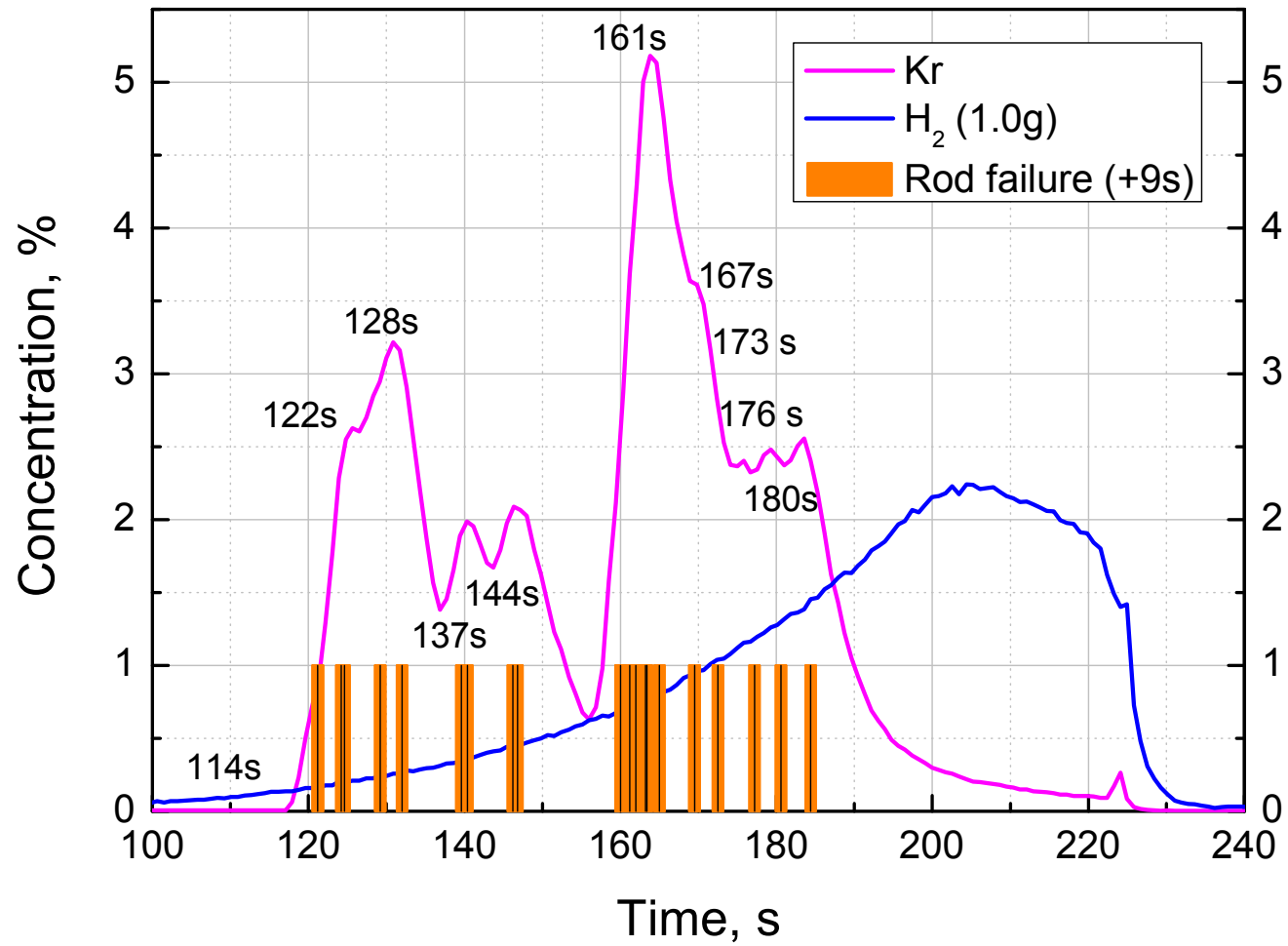
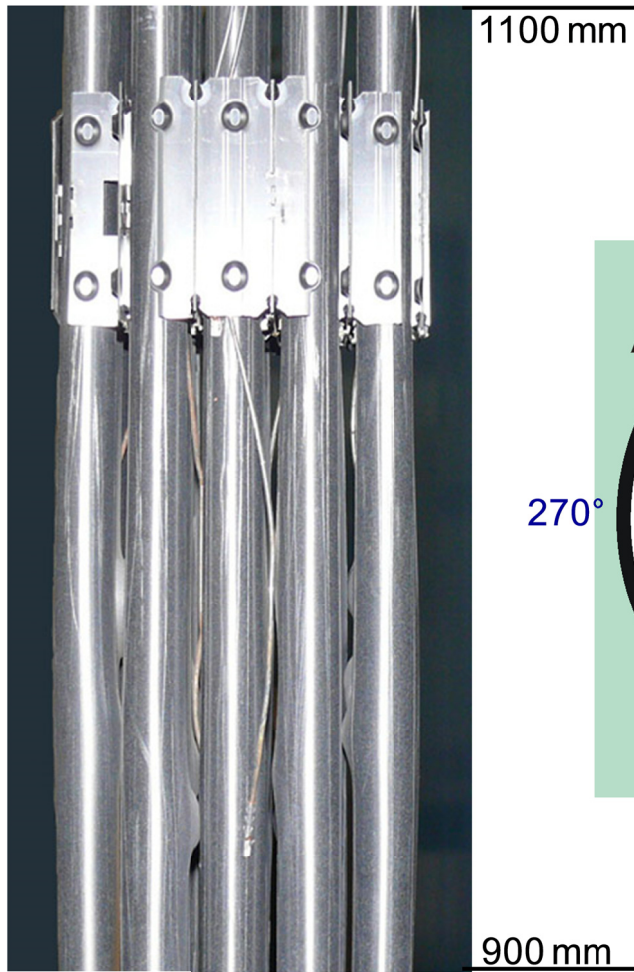


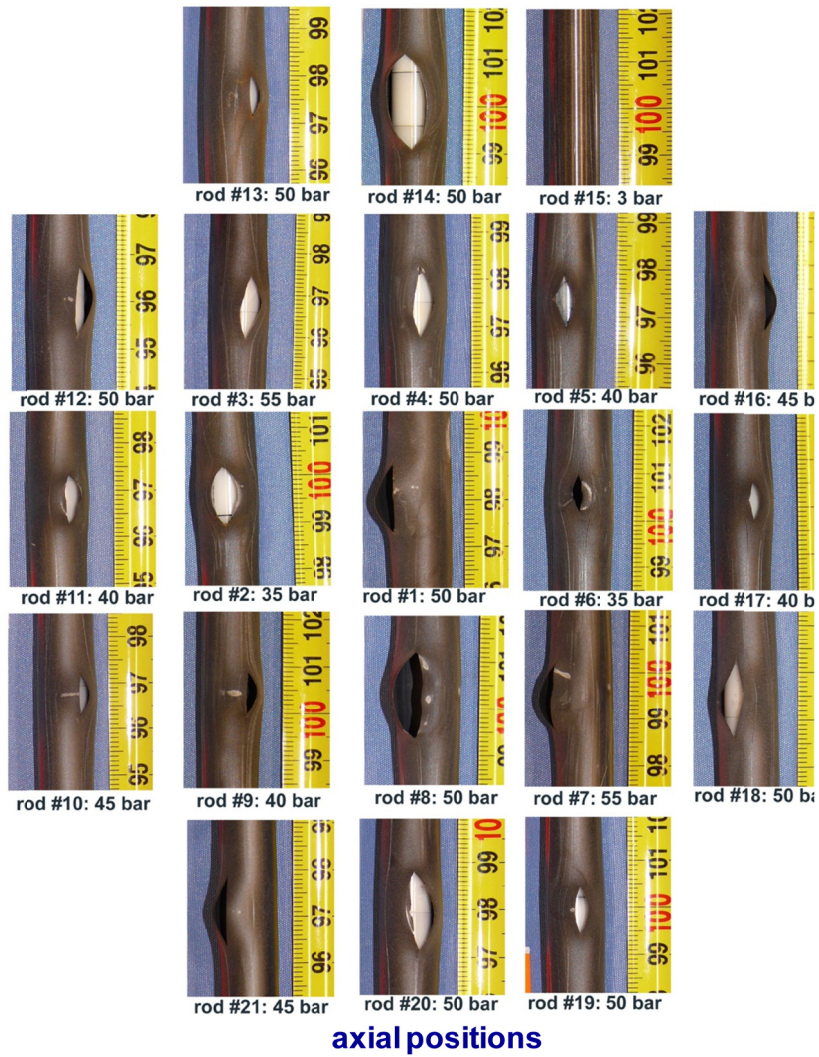
Fig. 45: QUENCH-L0; Mass spectrometer measurements: Krypton as burst indicator.



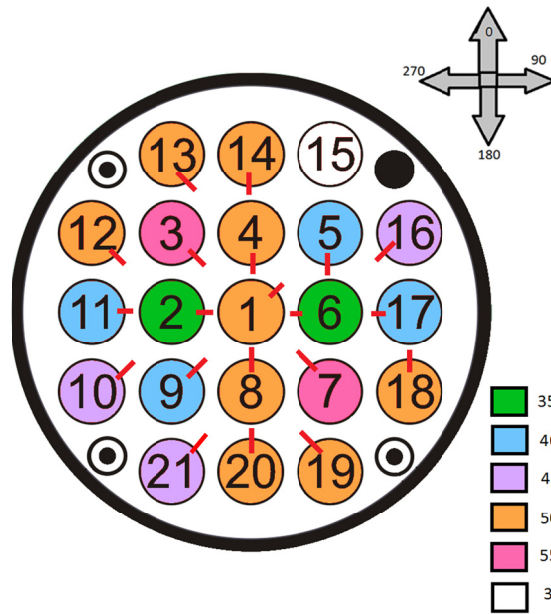
side view at 30°:  
axial shrinkage of claddings  
due to Zry anisotropy



Fig. 46: QUENCH-L0; Consequences of ballooning.



axial positions



circumferential positions

Fig. 47: QUENCH-L0; Burst positions.

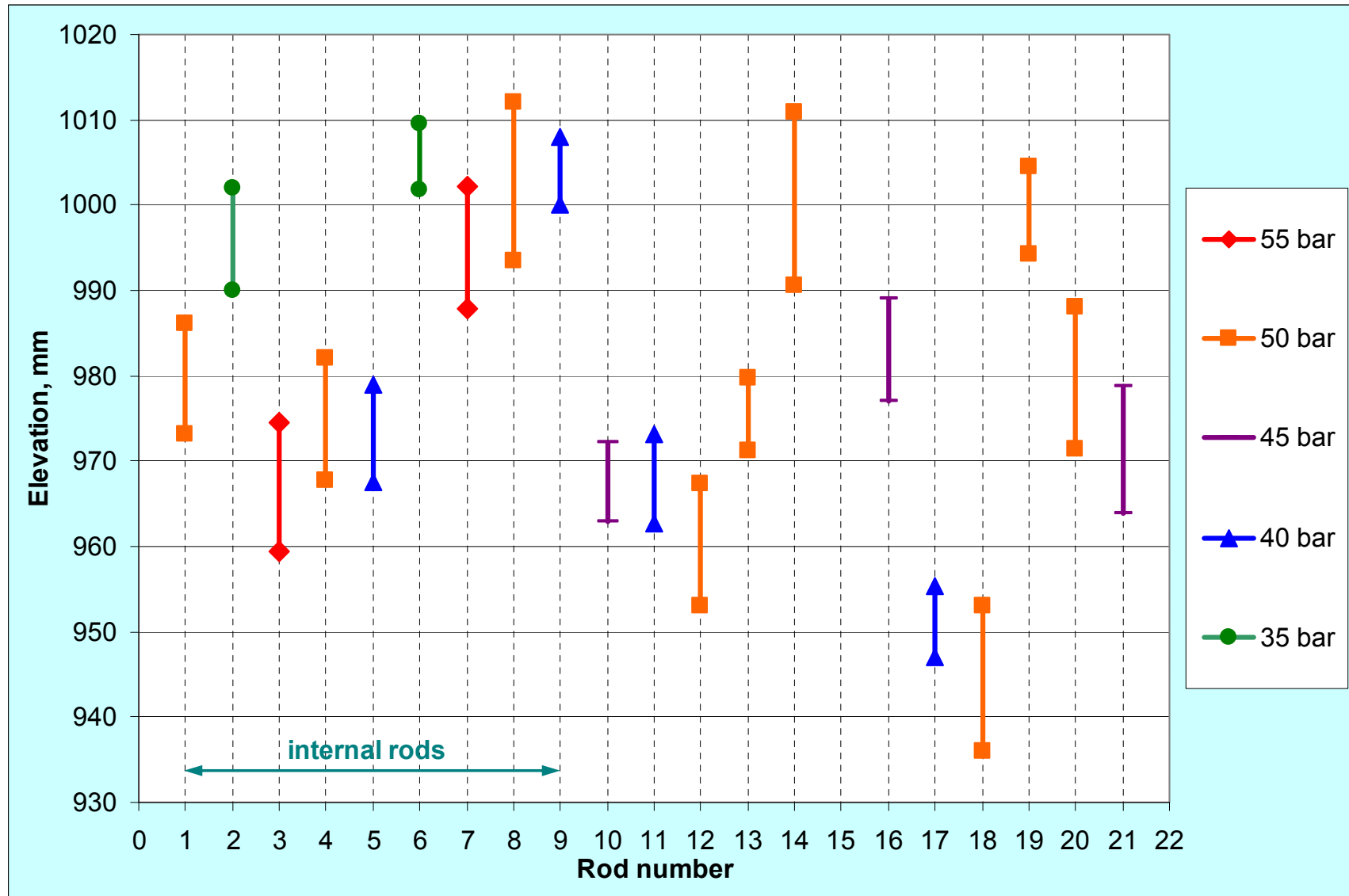
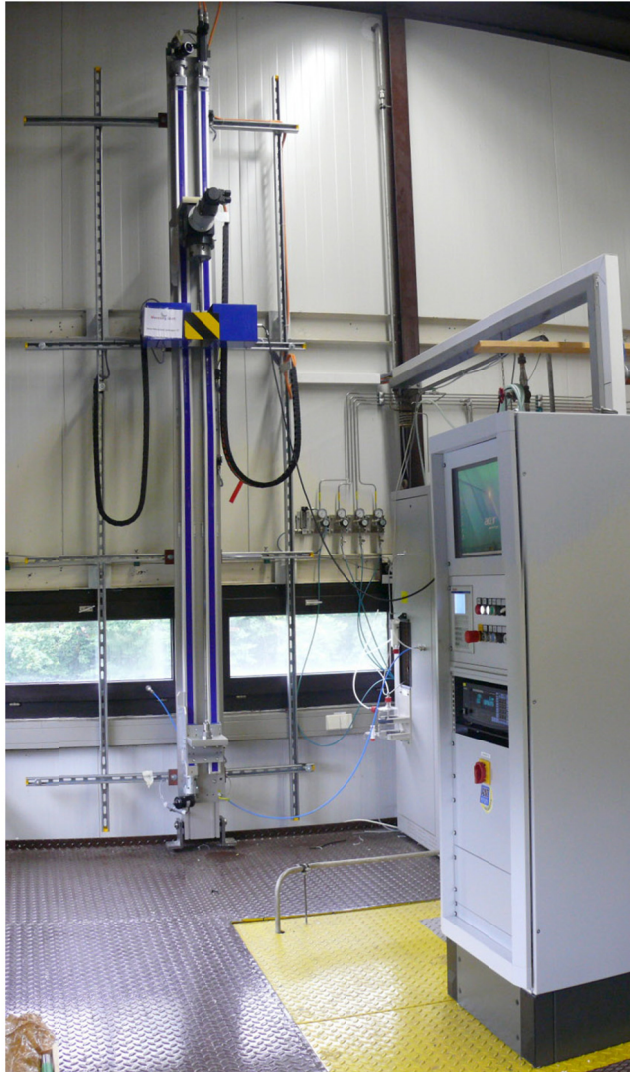
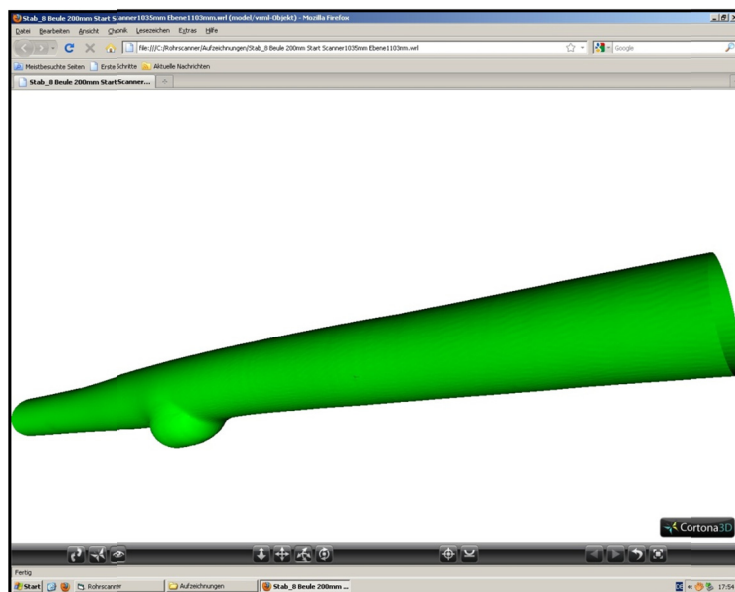


Fig. 48: QUENCH-L0; Axial burst positions.





scanner facility



reconstructed scanned surface of rod #8:  
angle step 1°; axial step 0.5 mm; scanned length 200 mm

Fig. 49: QUENCH-L0; Tube scanner laser profilometry.

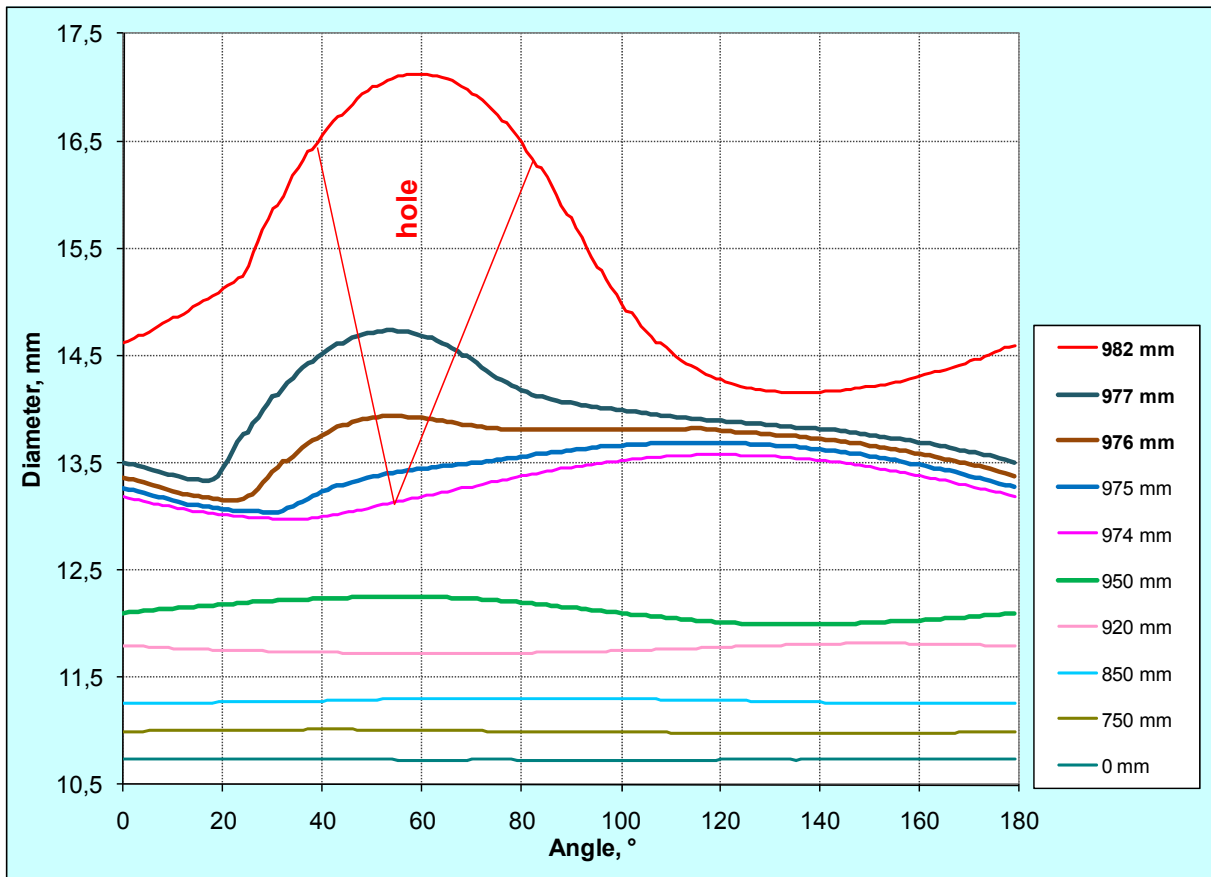
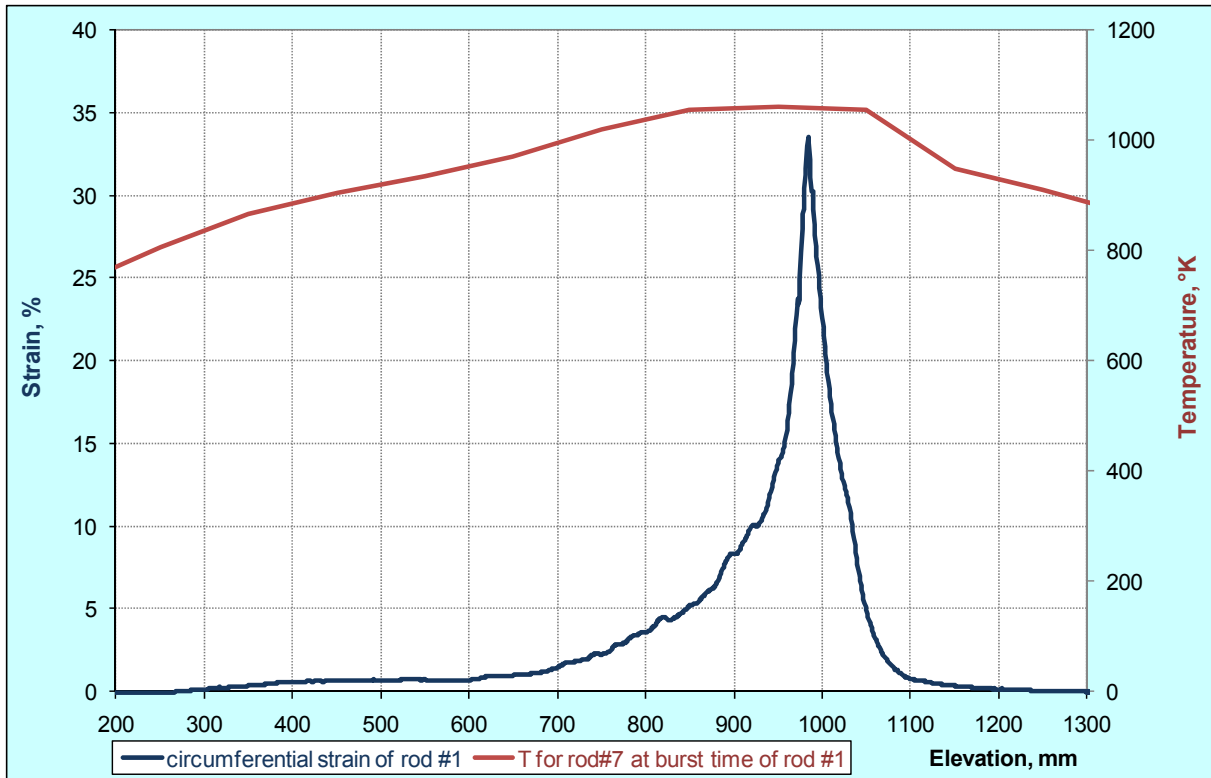


Fig. 50: QUENCH-L0, rod #1; longitudinal circumferential strain changing (top); azimuthal diameter changing downwards from burst (bottom).

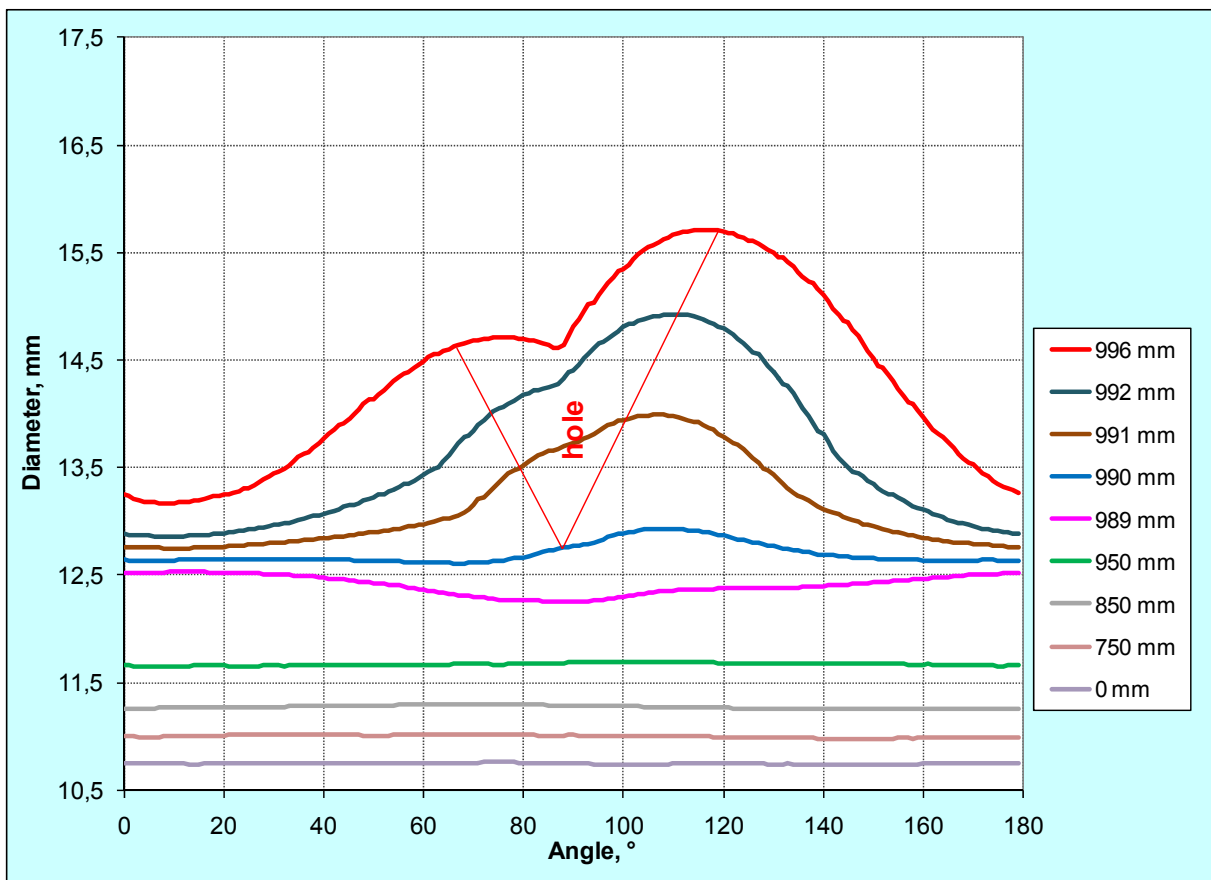
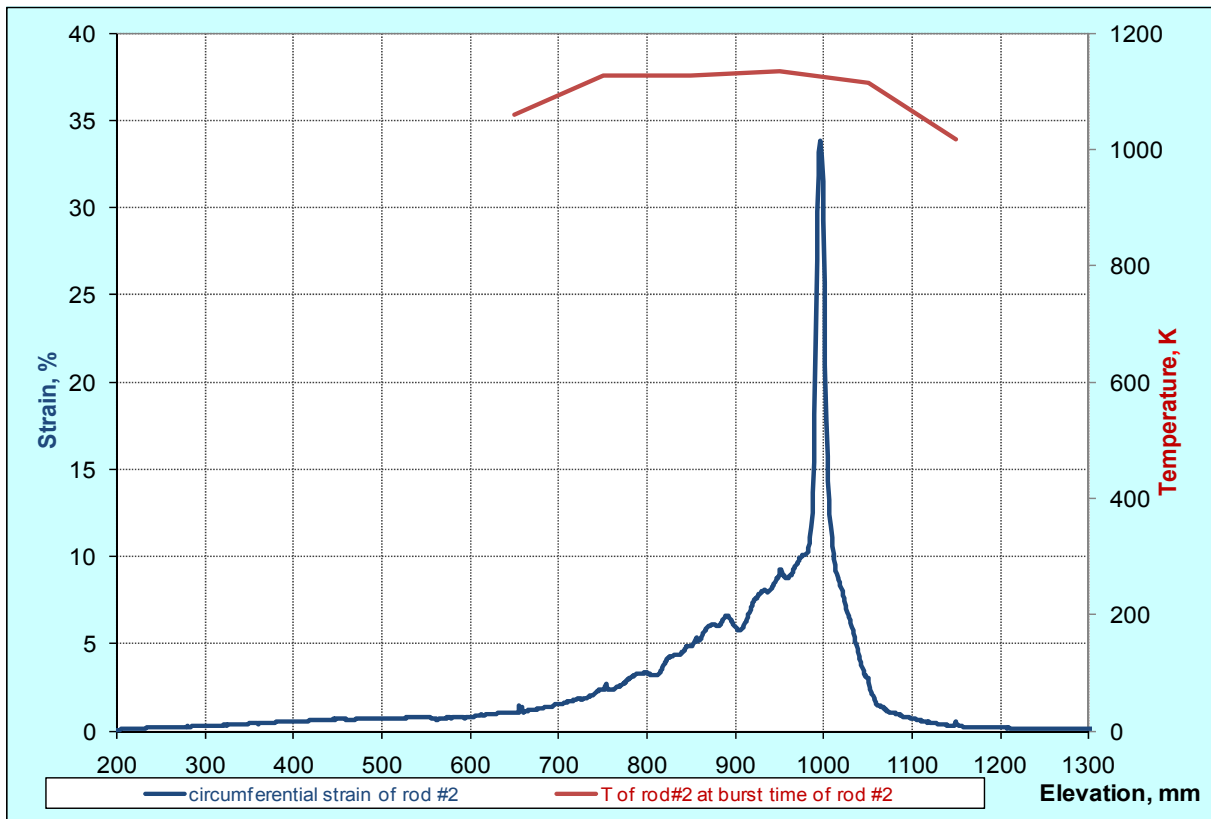


Fig. 51: QUENCH-L0, rod #2; longitudinal circumferential strain changing (top); azimuthal diameter changing downwards from burst (bottom).

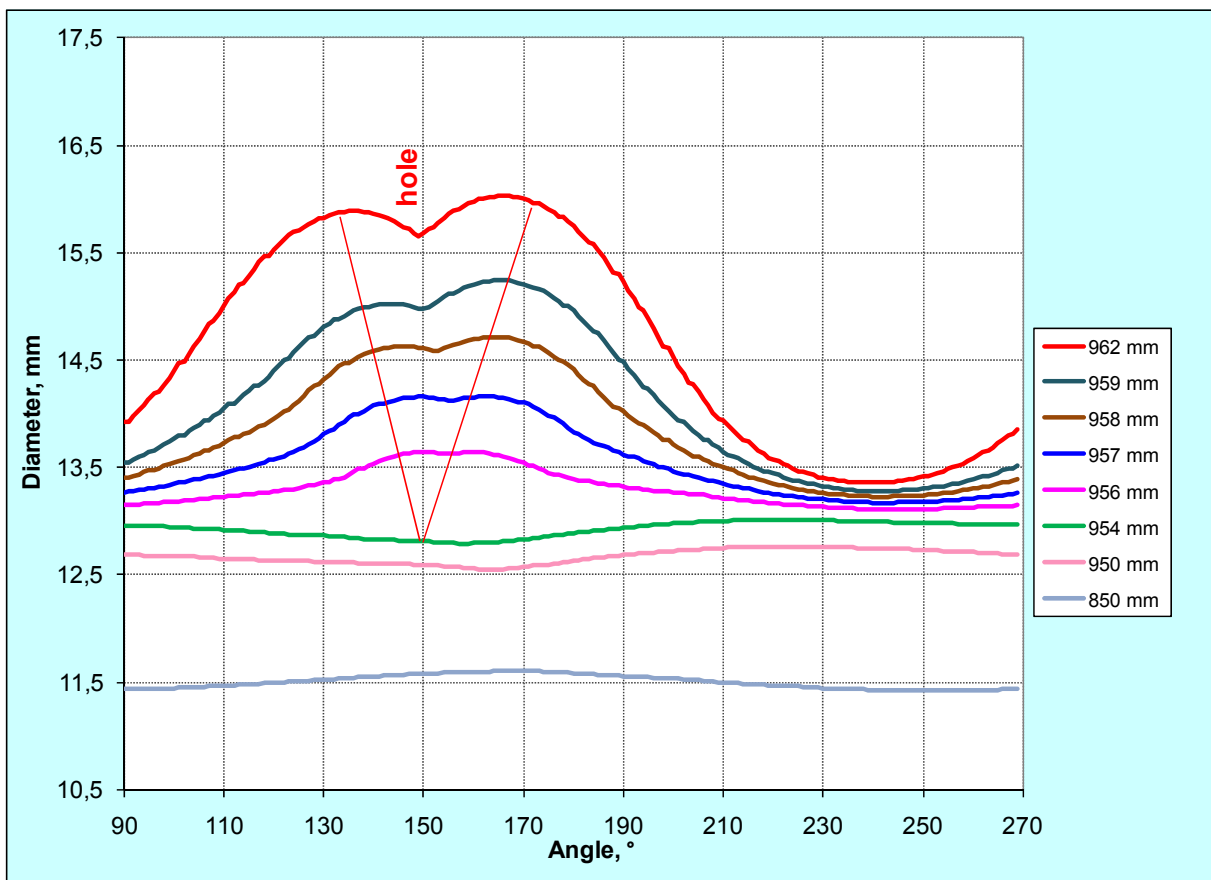
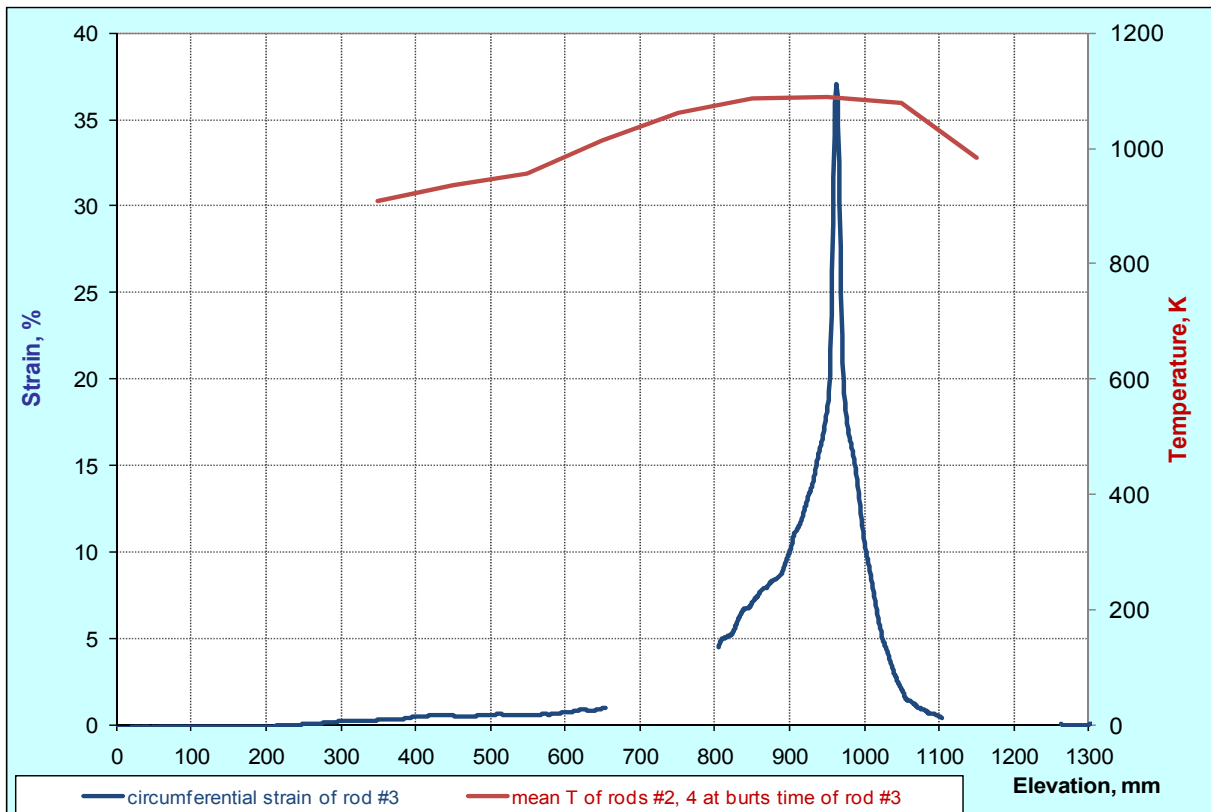


Fig. 52: QUENCH-L0, rod #3; longitudinal circumferential strain changing (top); azimuthal diameter changing downwards from burst (bottom).



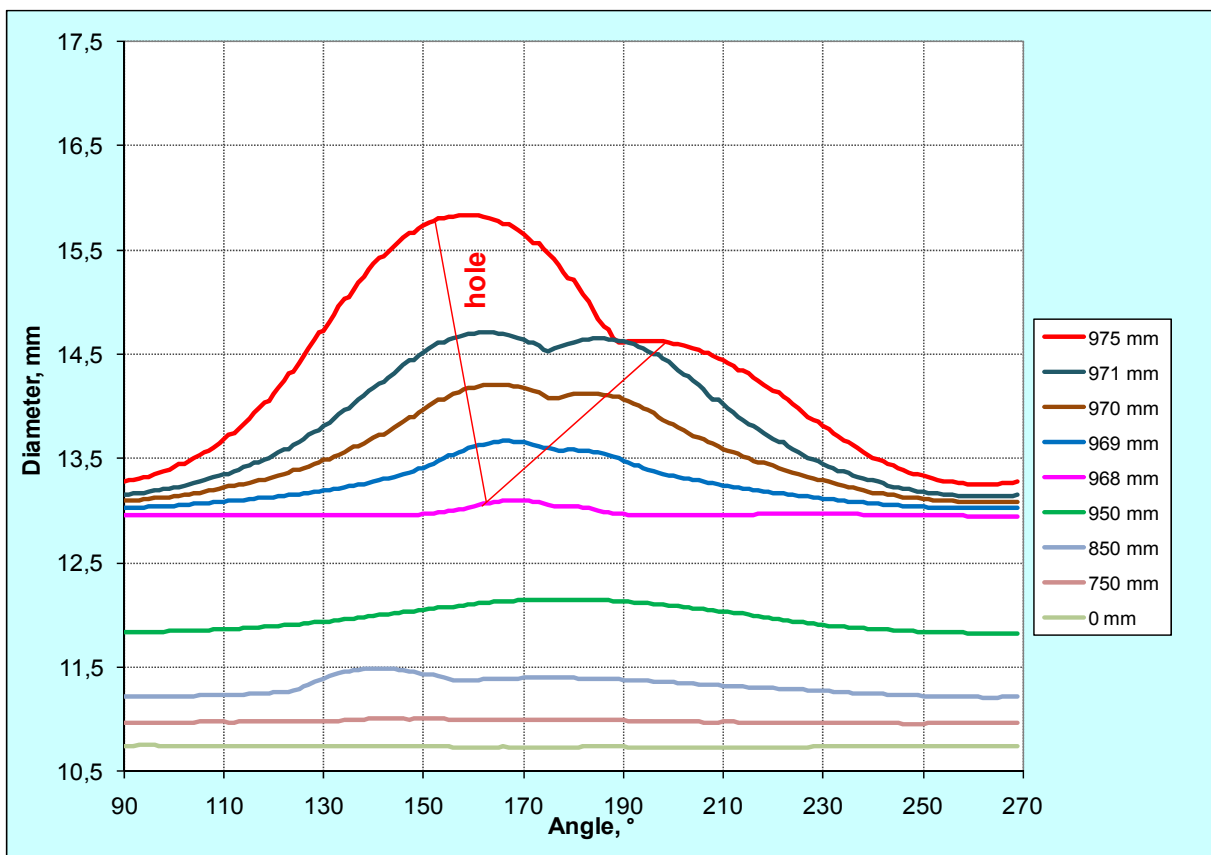
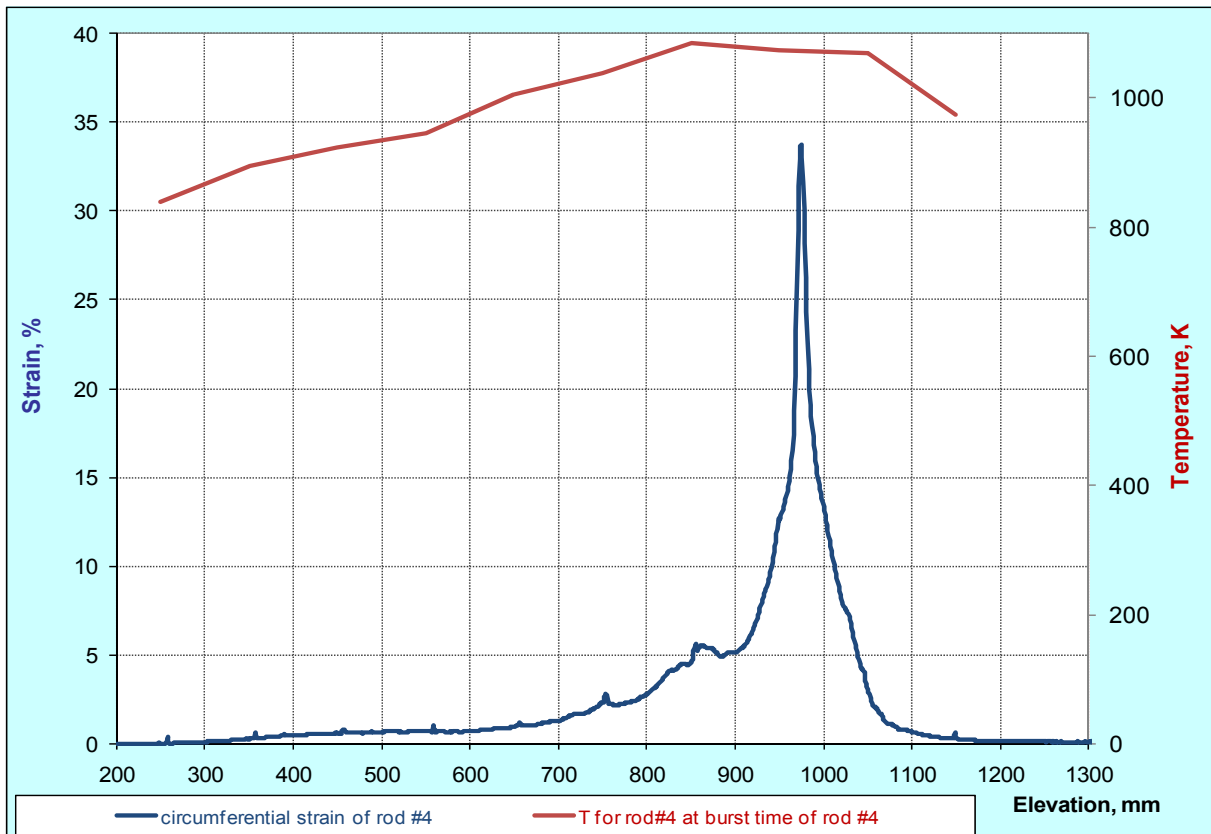


Fig. 53: QUENCH-L0, rod #4; longitudinal circumferential strain changing (top); azimuthal diameter changing downwards from burst (bottom).

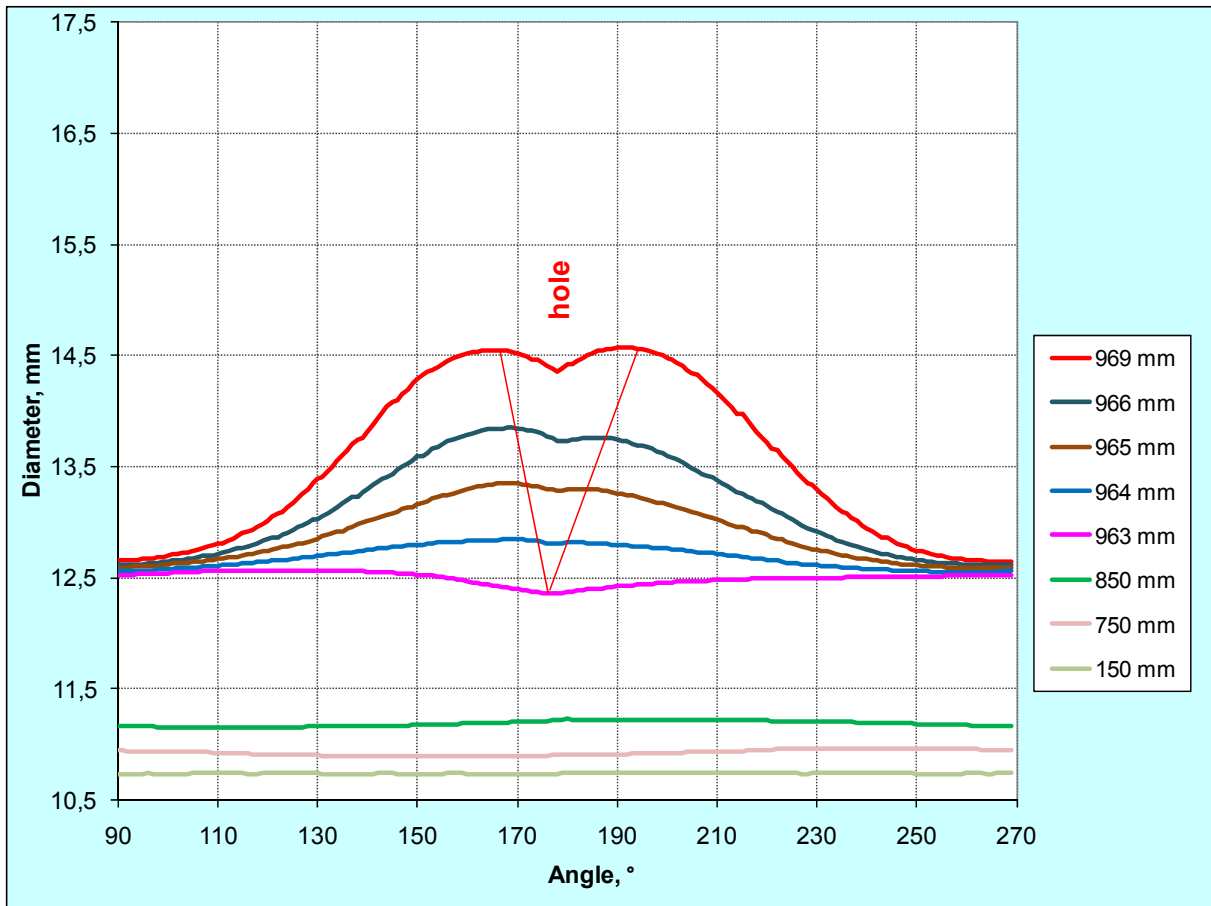
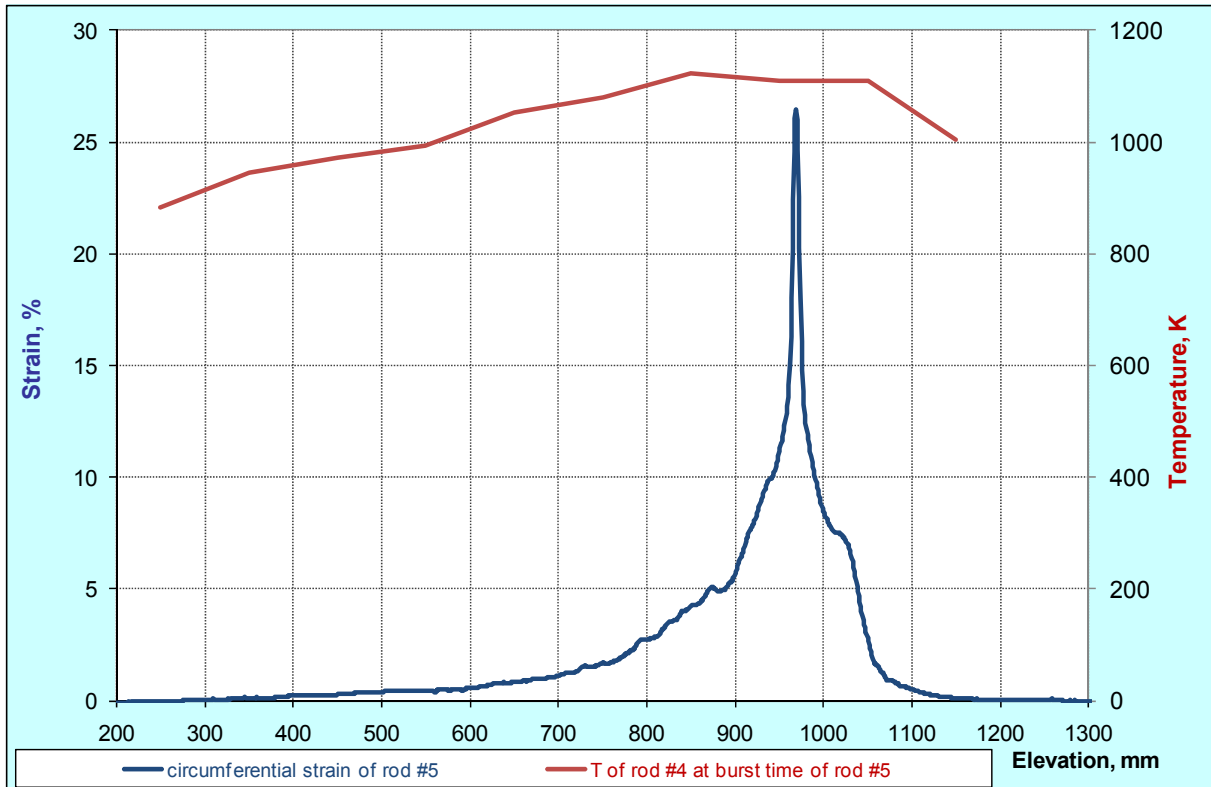


Fig. 54: QUENCH-L0, rod #5; longitudinal circumferential strain changing (top); azimuthal diameter changing downwards from burst (bottom).

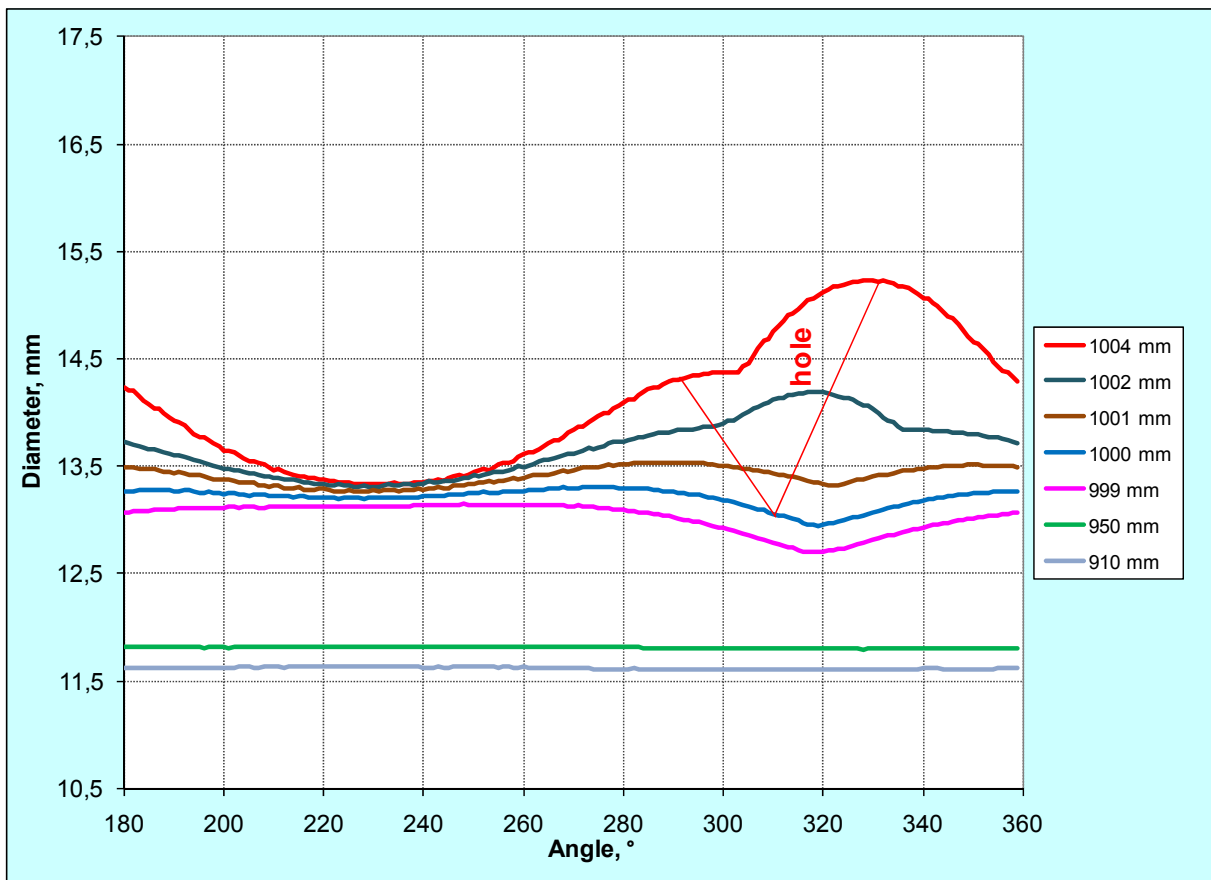
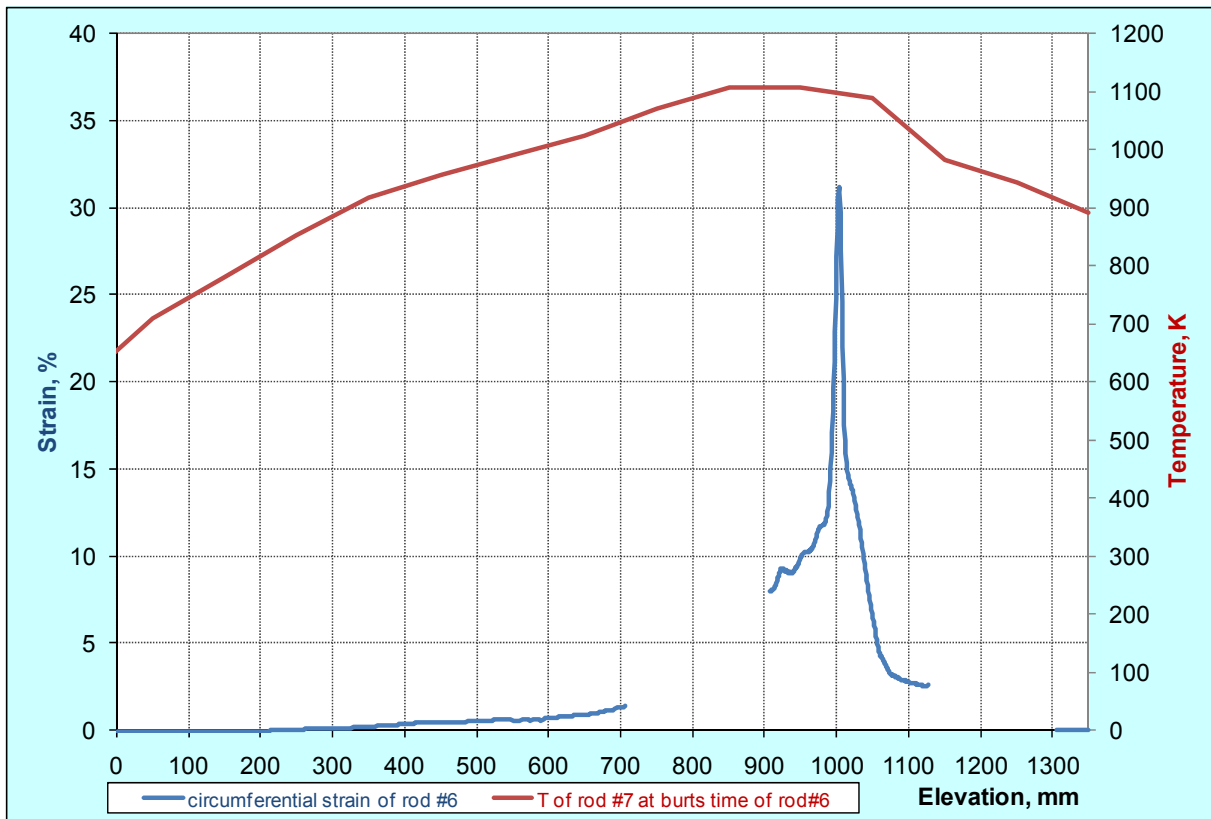


Fig. 55: QUENCH-L0, rod #6; longitudinal circumferential strain changing (top); azimuthal diameter changing downwards from burst (bottom).

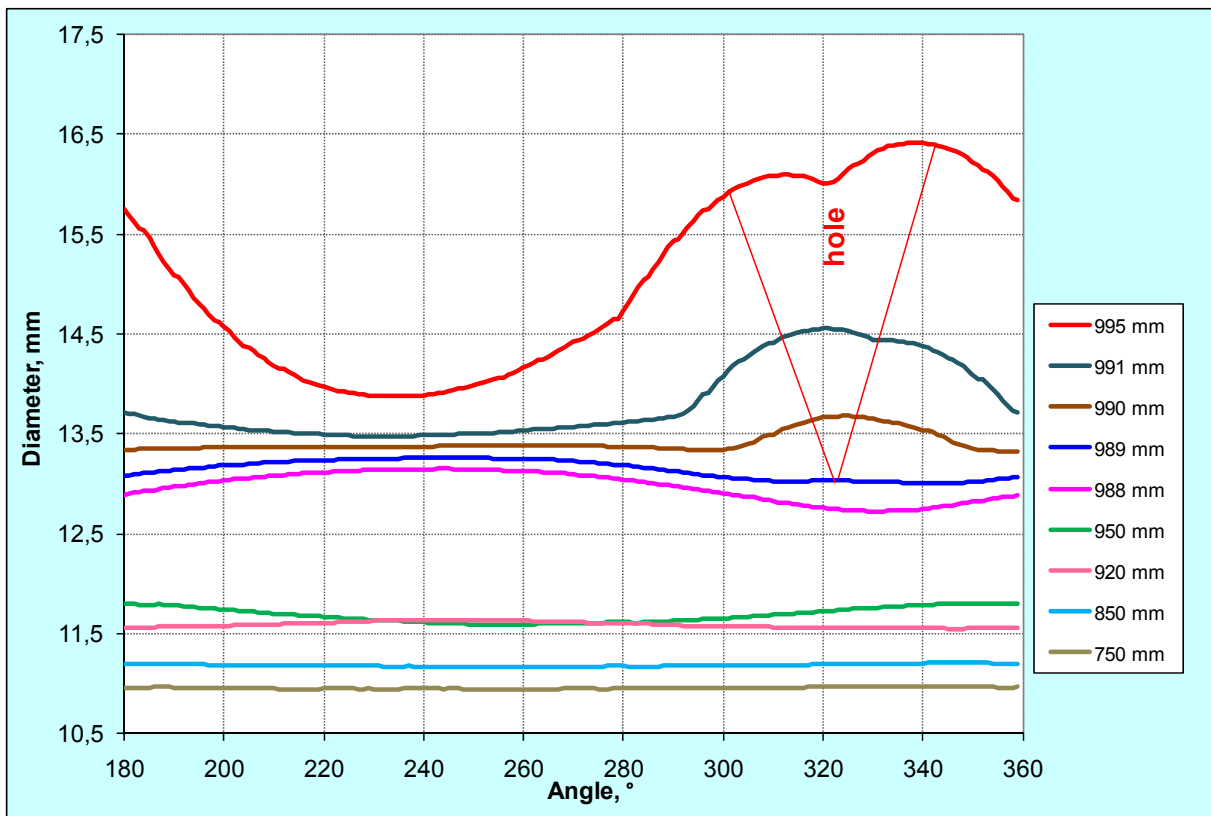
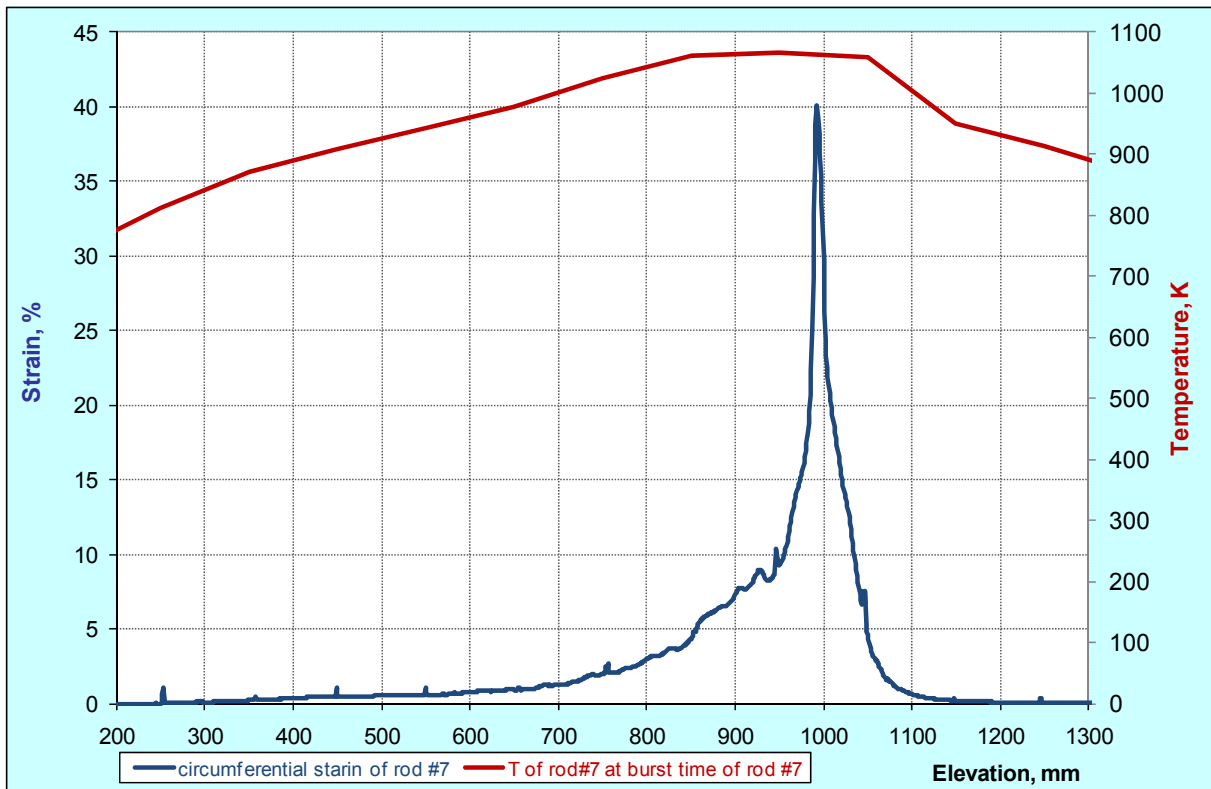


Fig. 56: QUENCH-L0, rod #7; longitudinal circumferential strain changing (top); azimuthal diameter changing downwards from burst (bottom).

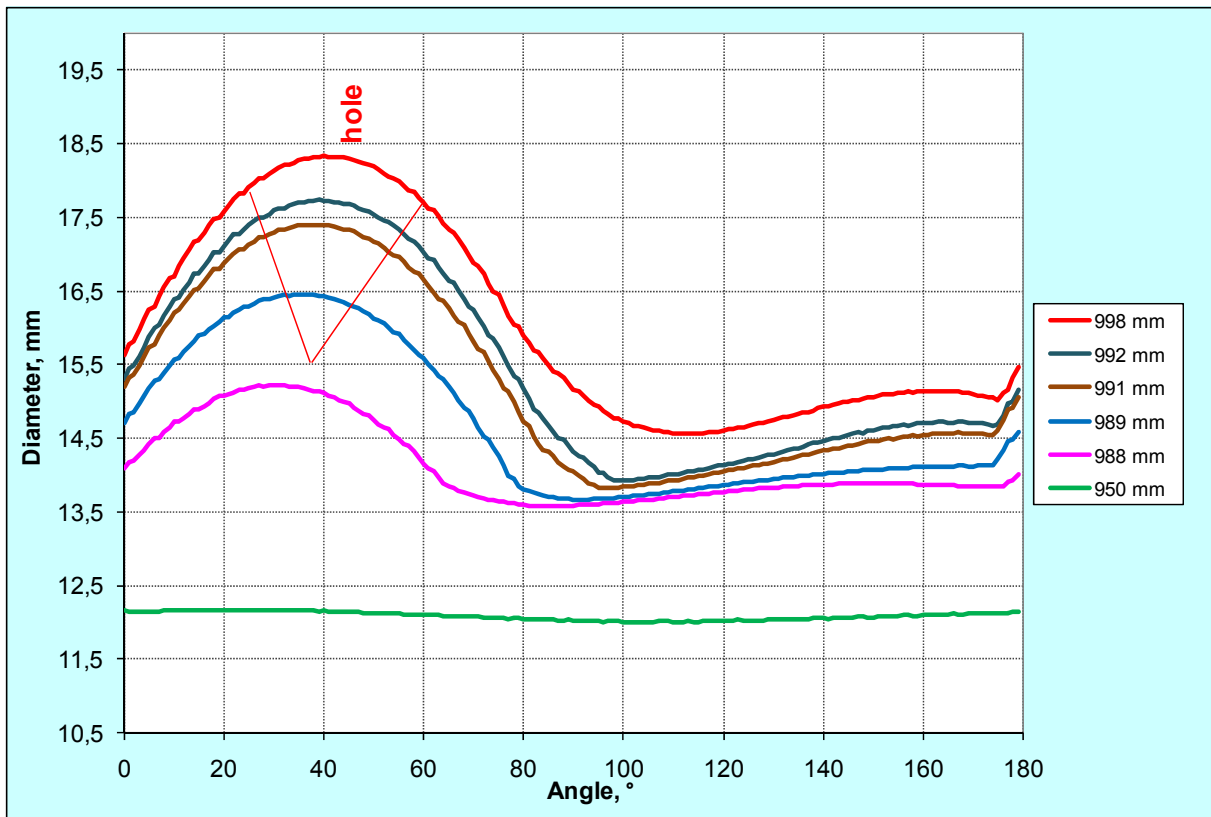
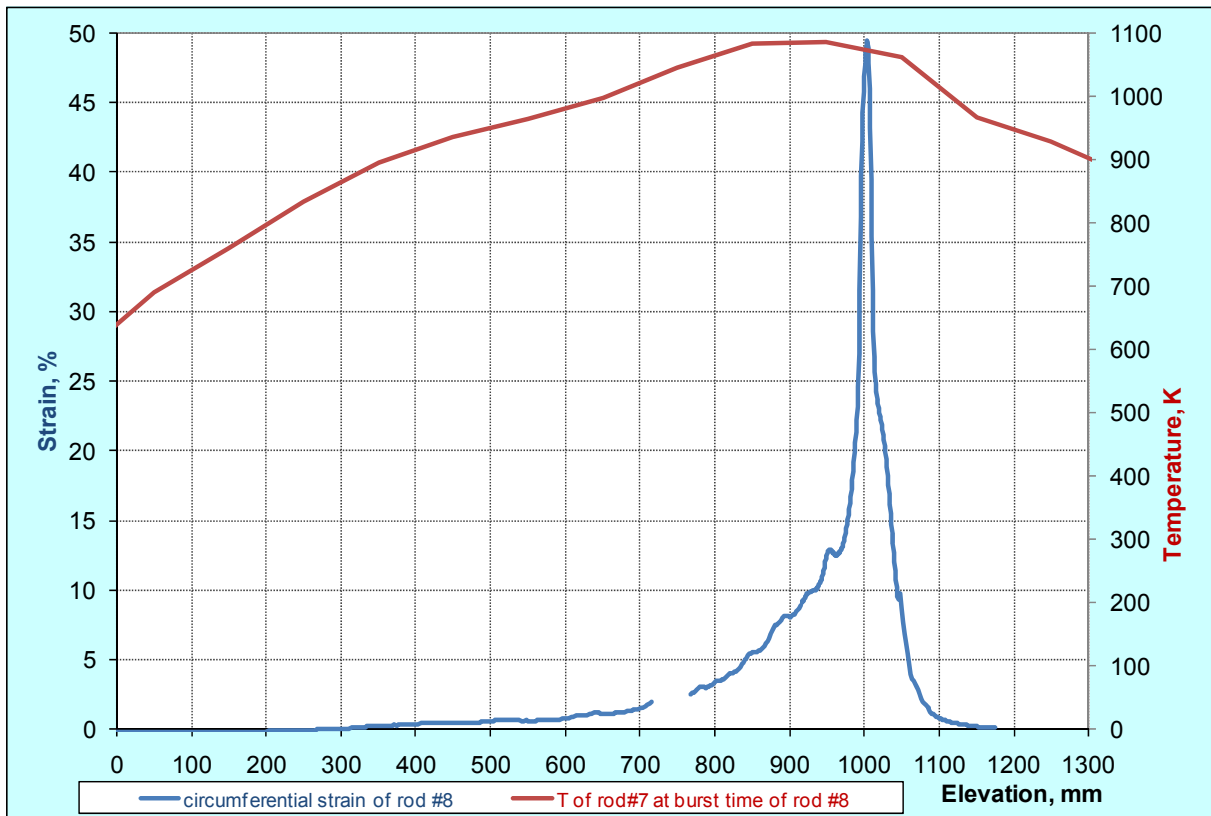


Fig. 57: QUENCH-L0, rod #8; longitudinal circumferential strain changing (top); azimuthal diameter changing downwards from burst (bottom).

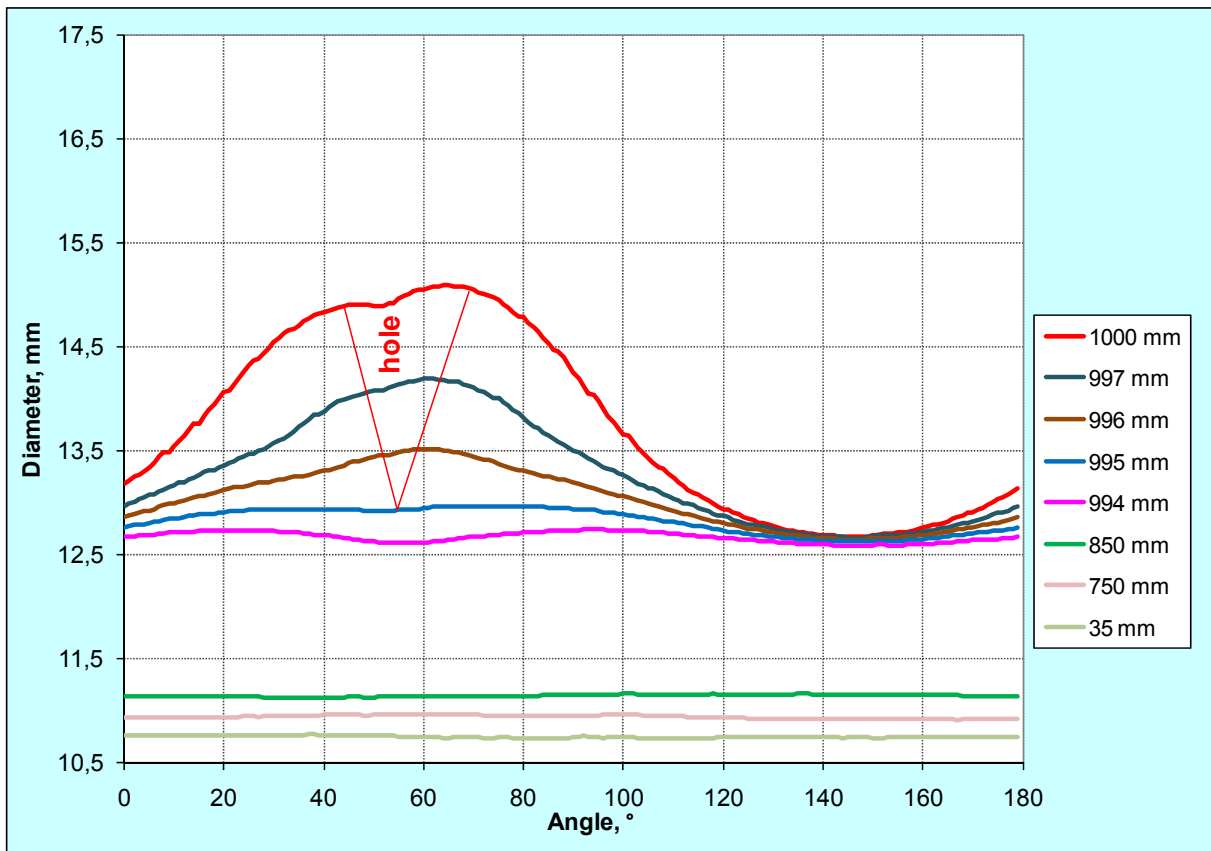
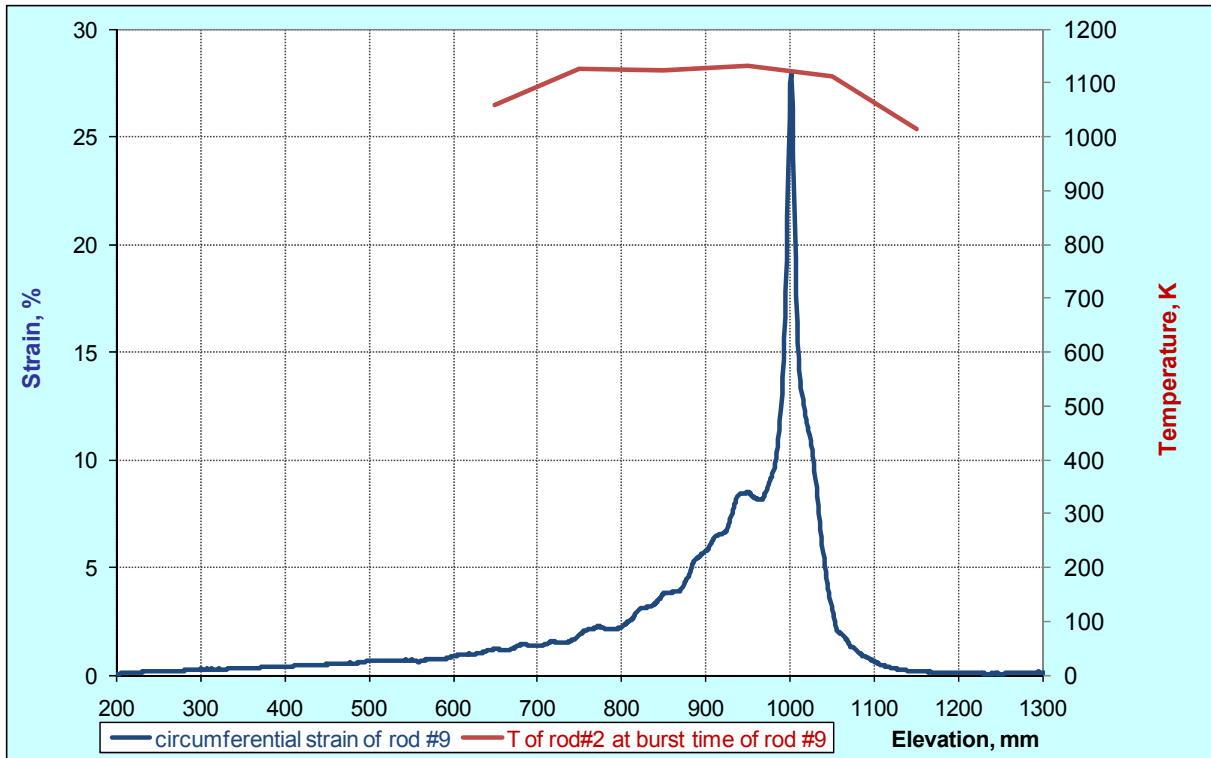


Fig. 58: QUENCH-L0, rod #9; longitudinal circumferential strain changing (top); azimuthal diameter changing downwards from burst (bottom).

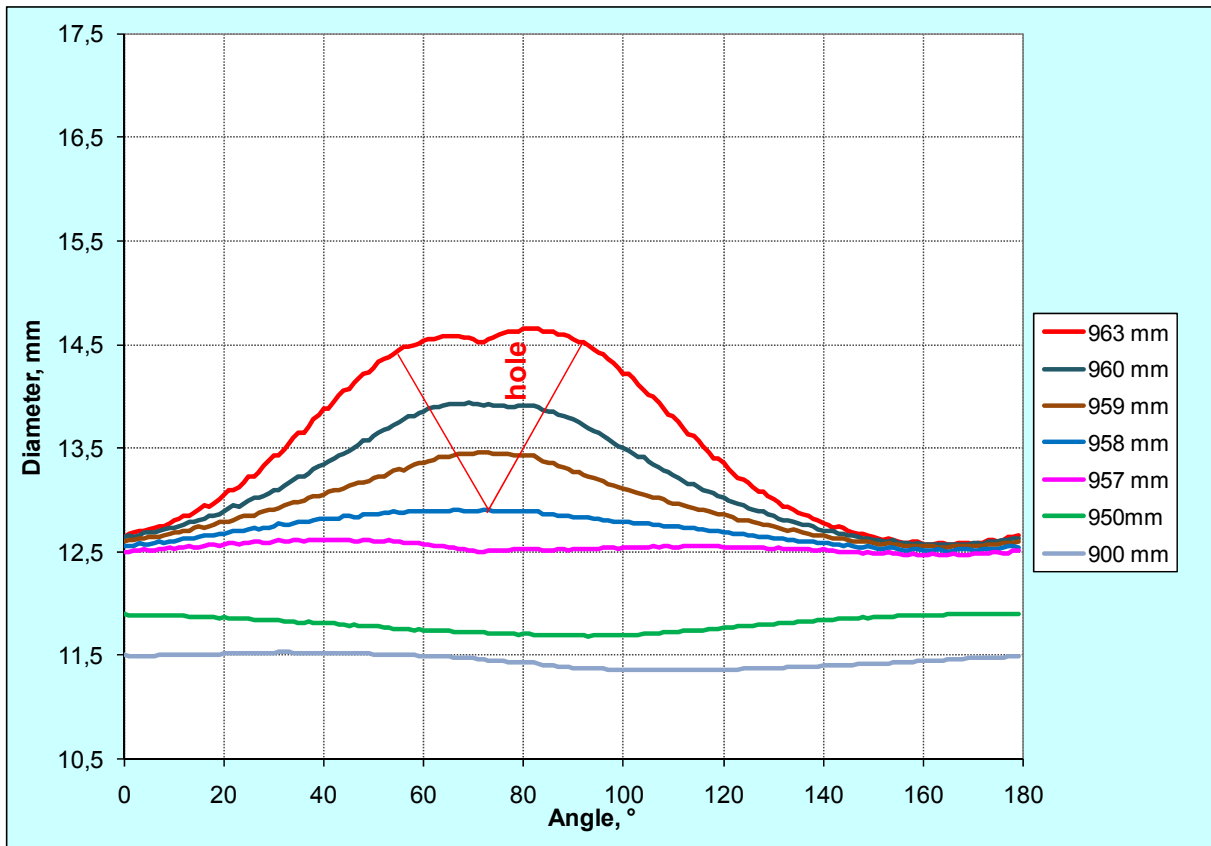
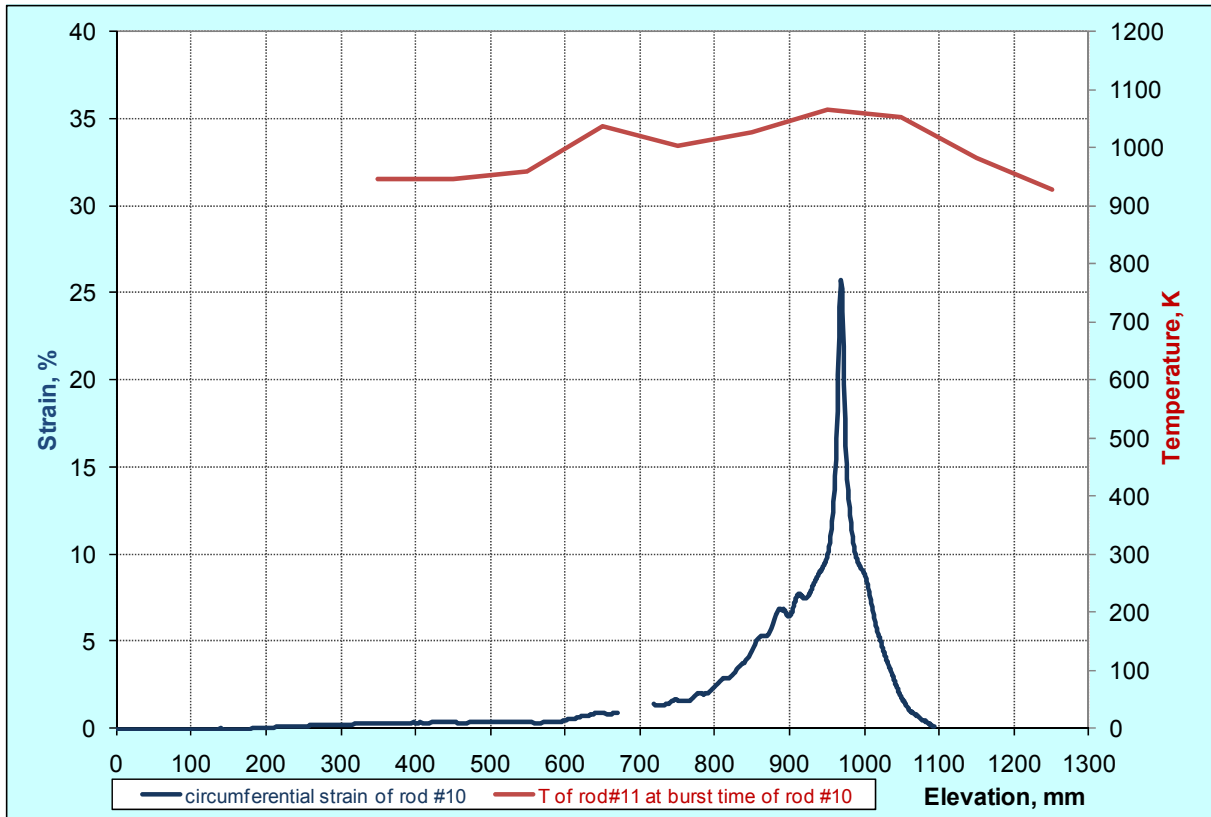


Fig. 59: QUENCH-L0, rod #10; longitudinal circumferential strain changing (top); azimuthal diameter changing downwards from burst (bottom).

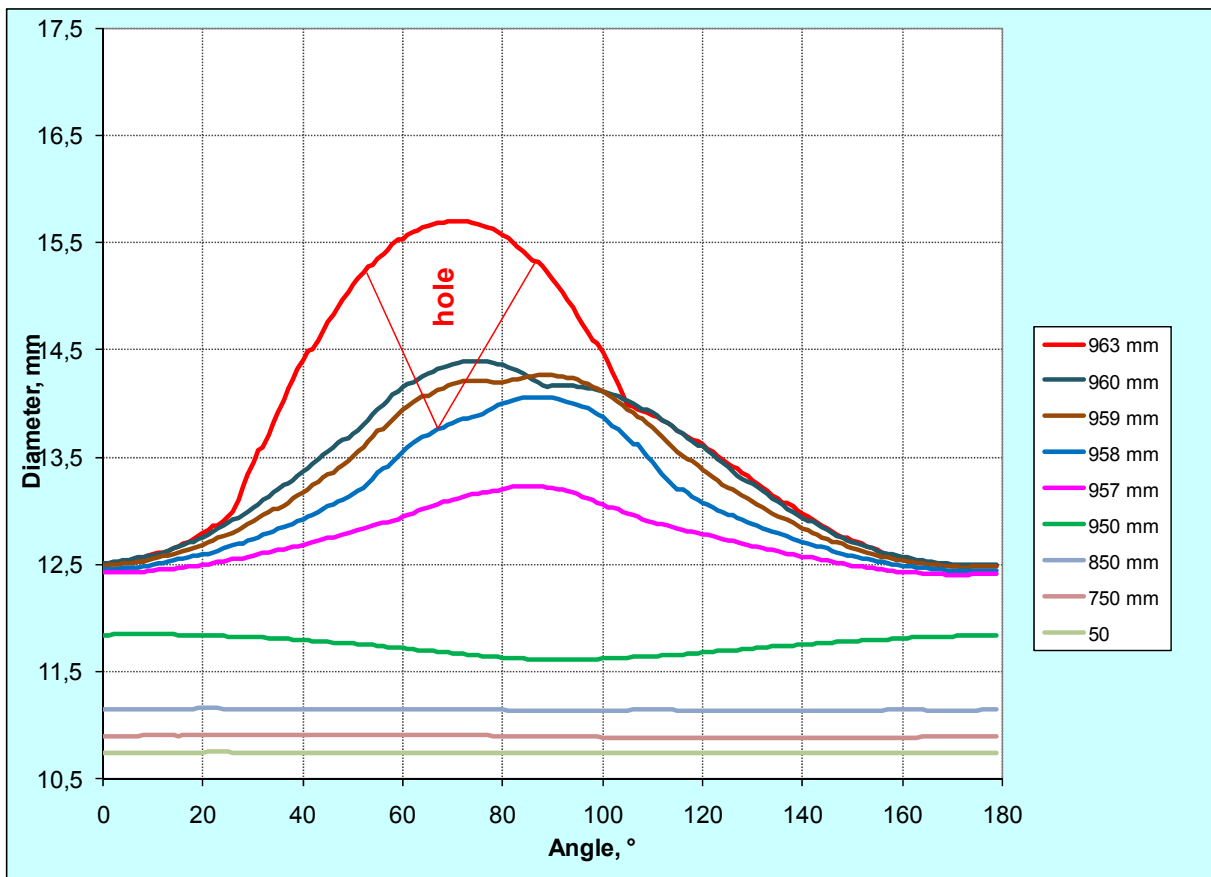
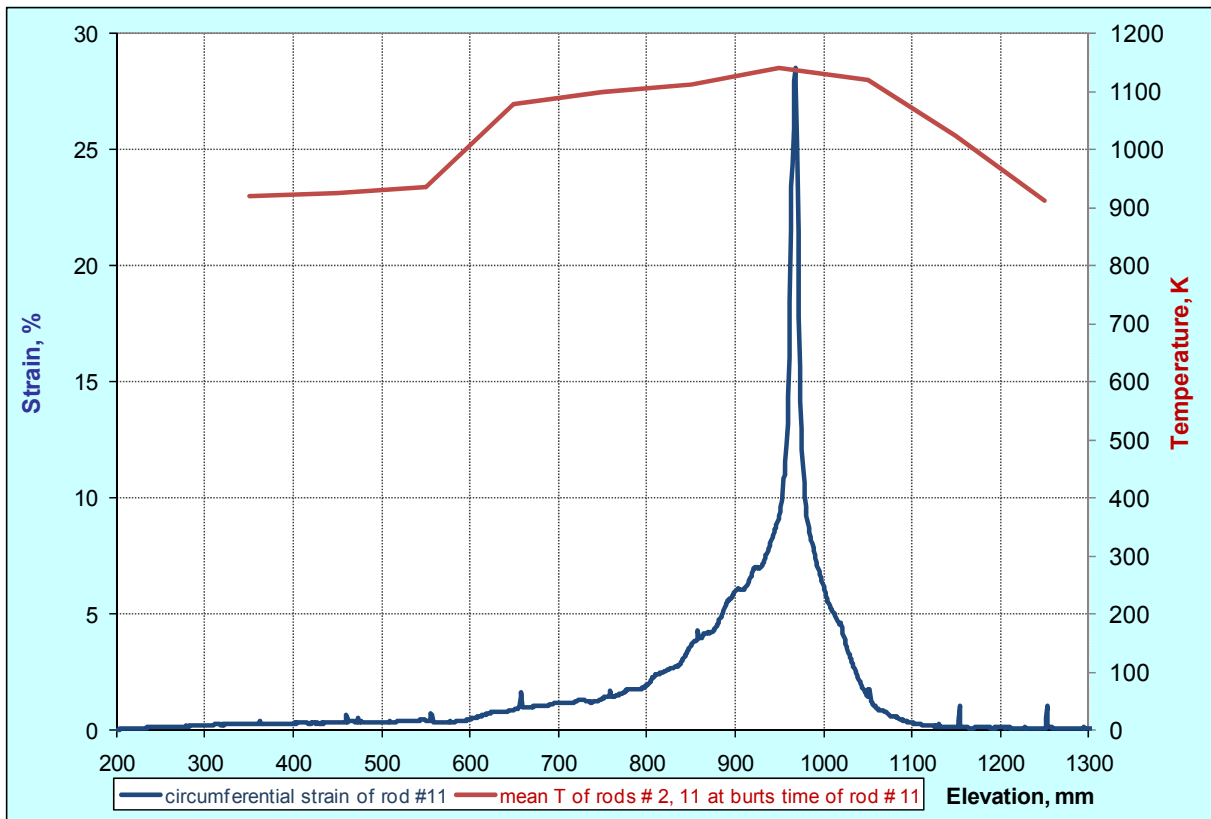


Fig. 60: QUENCH-L0, rod #11; longitudinal circumferential strain changing (top); azimuthal diameter changing downwards from burst (bottom).



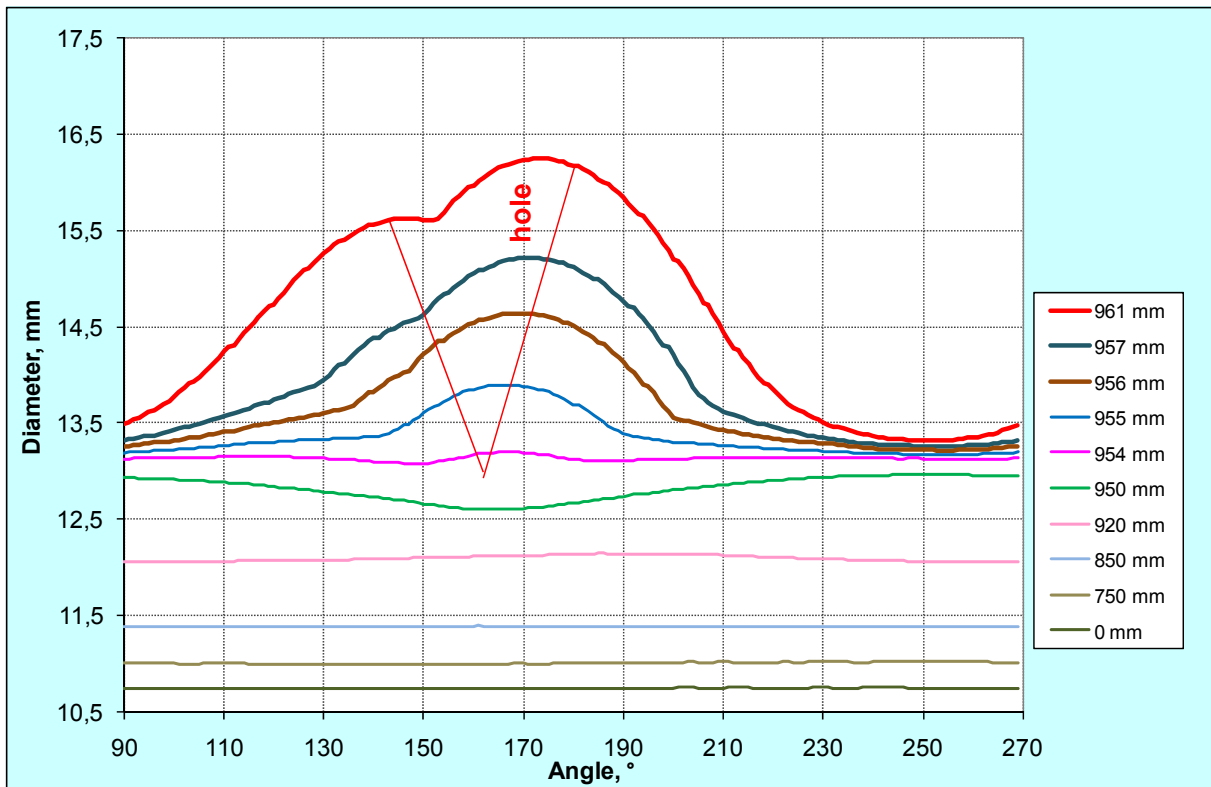
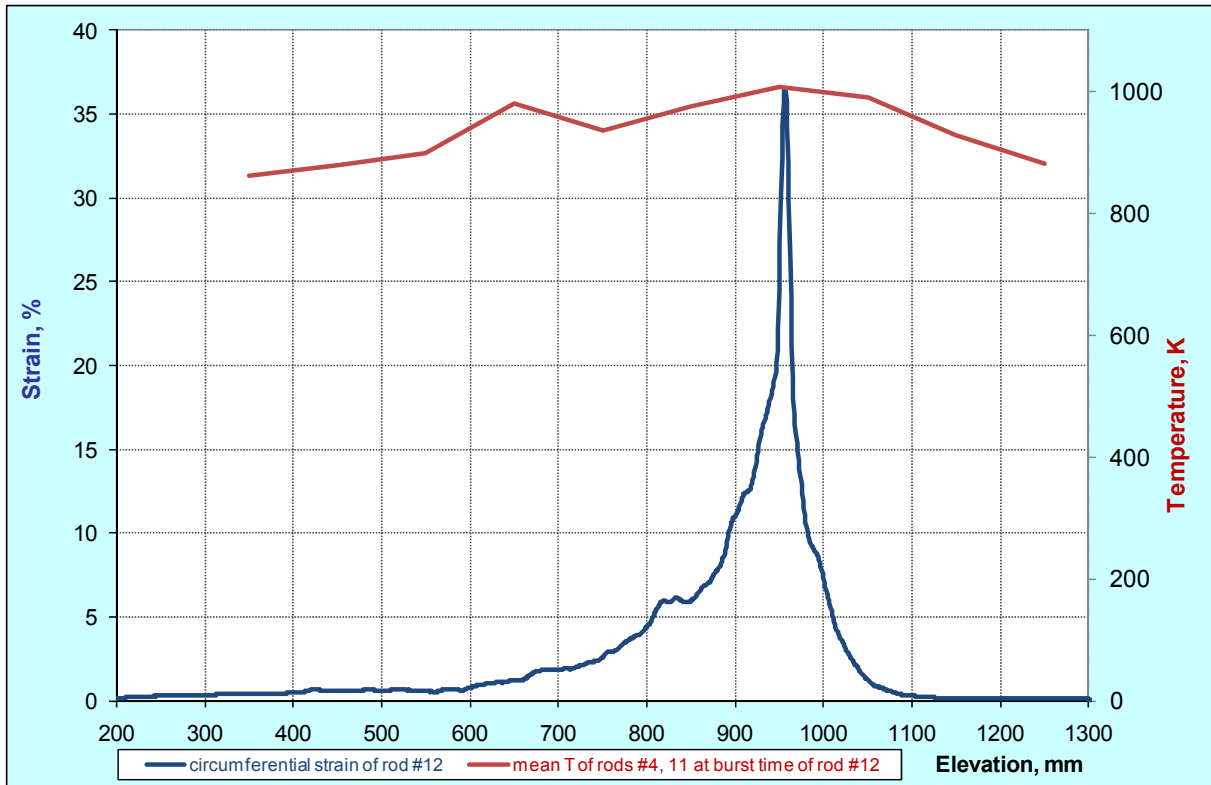


Fig. 61: QUENCH-L0, rod #12; longitudinal circumferential strain changing (top); azimuthal diameter changing downwards from burst (bottom).

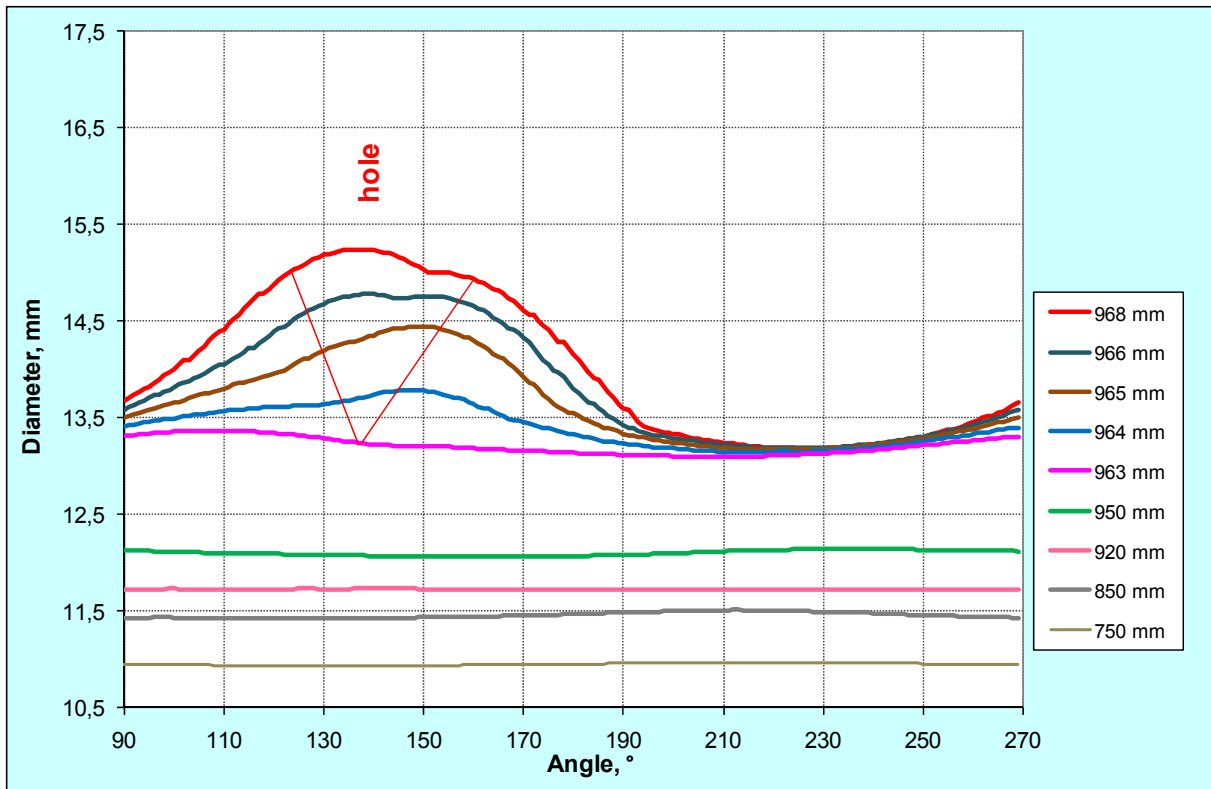
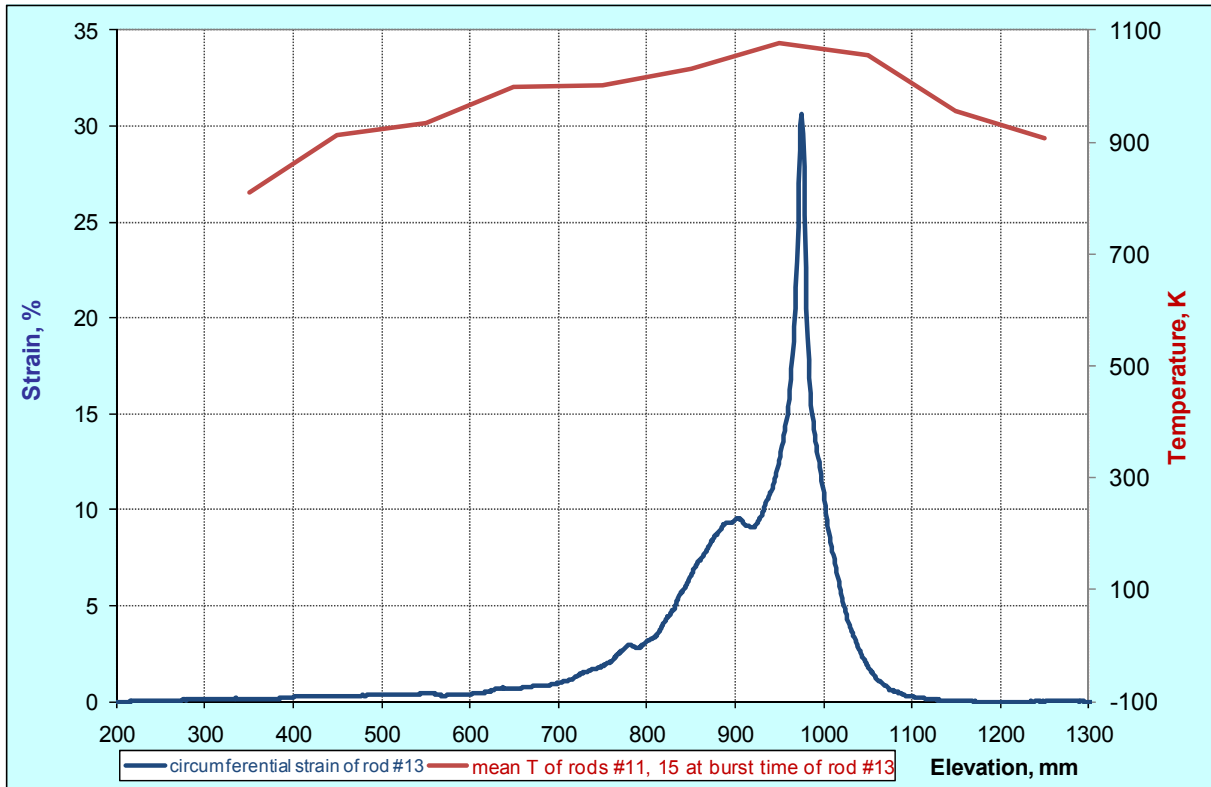


Fig. 62: QUENCH-L0, rod #13; longitudinal circumferential strain changing (top); azimuthal diameter changing downwards from burst (bottom).

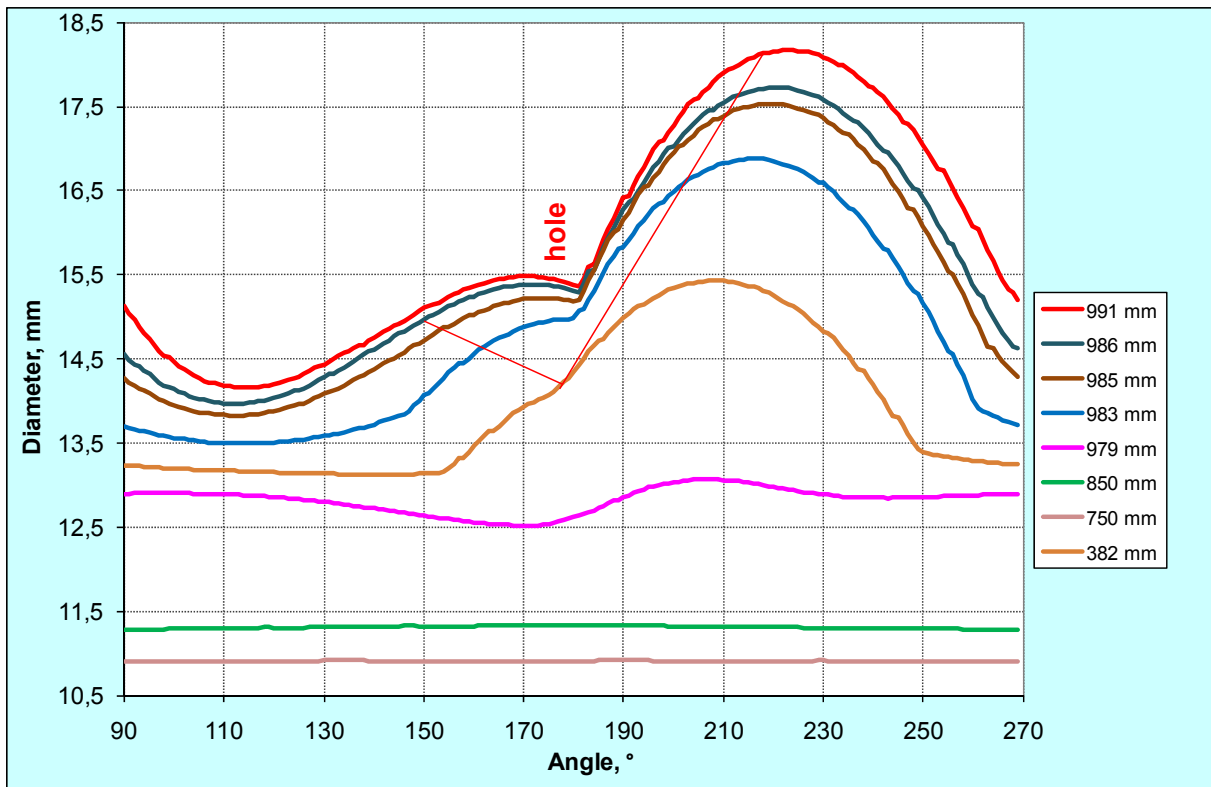
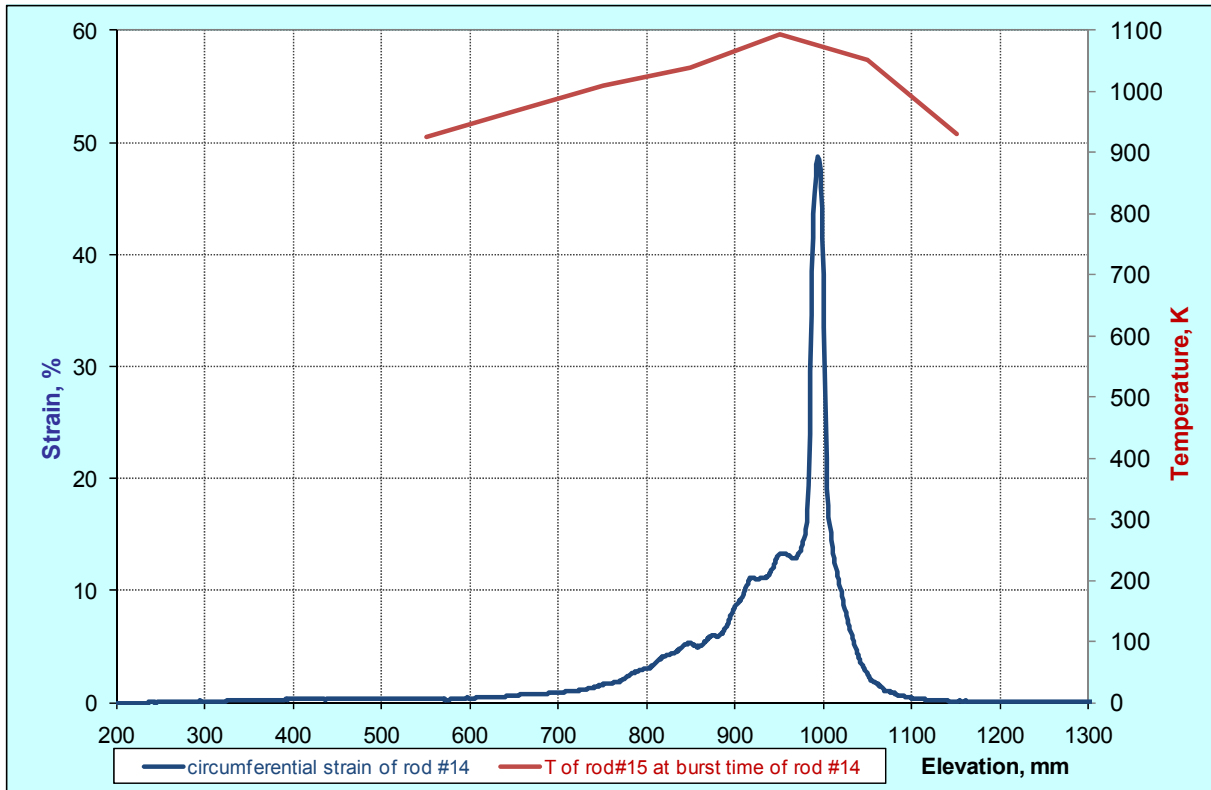


Fig. 63: QUENCH-L0, rod #14; longitudinal circumferential strain changing (top); azimuthal diameter changing downwards from burst (bottom).

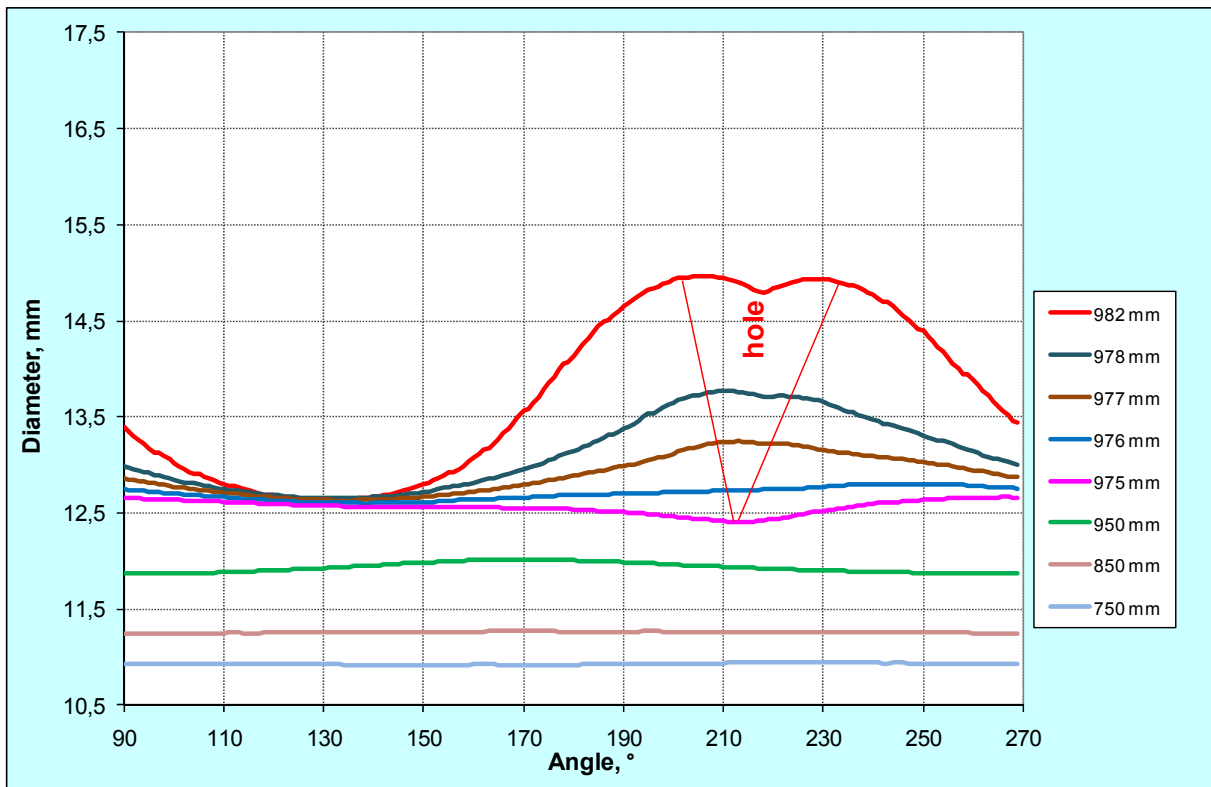
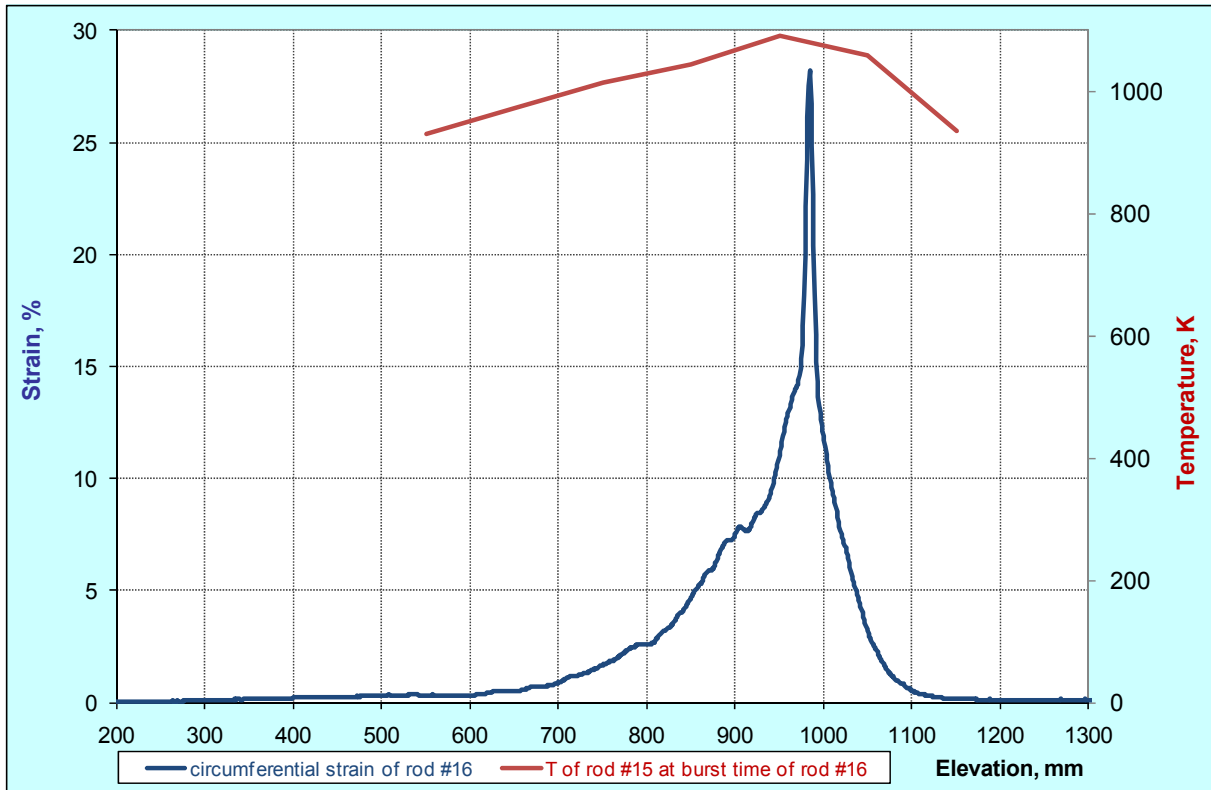


Fig. 64: QUENCH-L0, rod #16; longitudinal circumferential strain changing (top); azimuthal diameter changing downwards from burst (bottom).

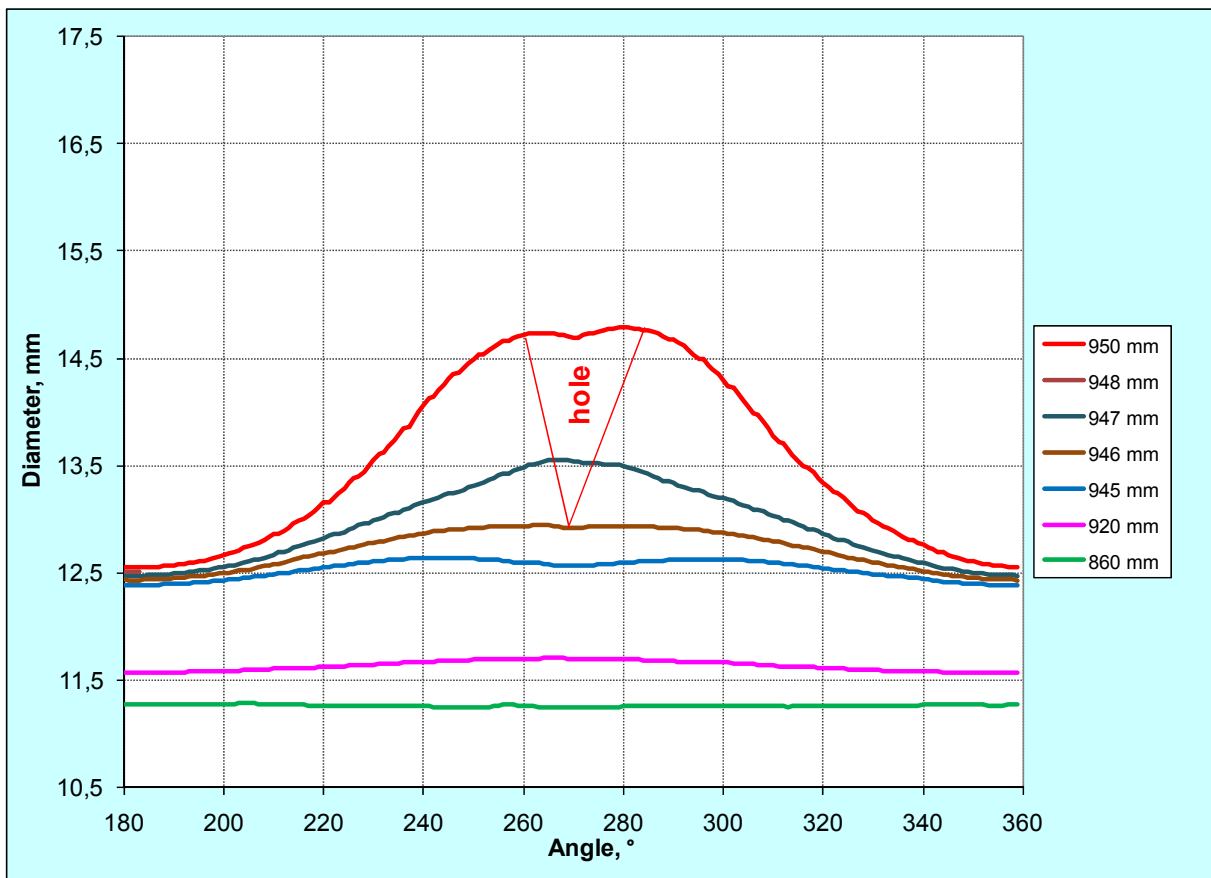
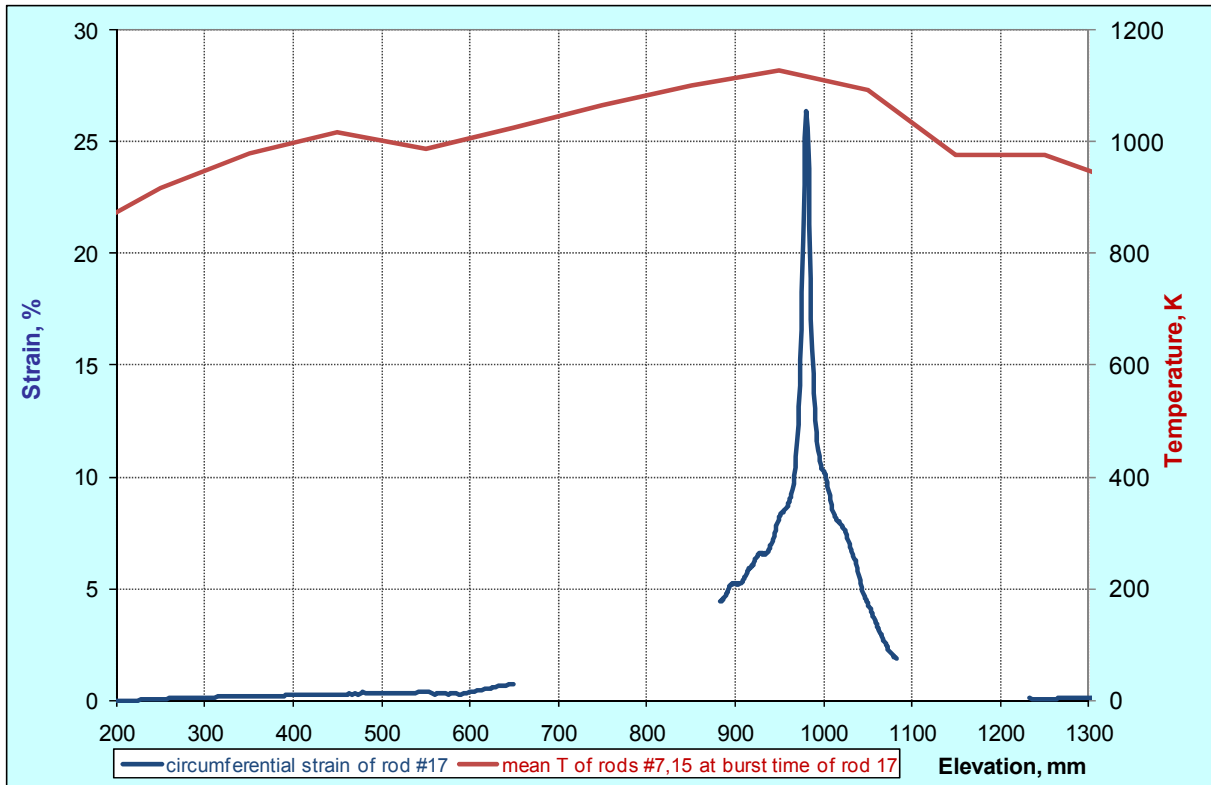


Fig. 65: QUENCH-L0, rod #17; longitudinal circumferential strain changing (top); azimuthal diameter changing downwards from burst (bottom).

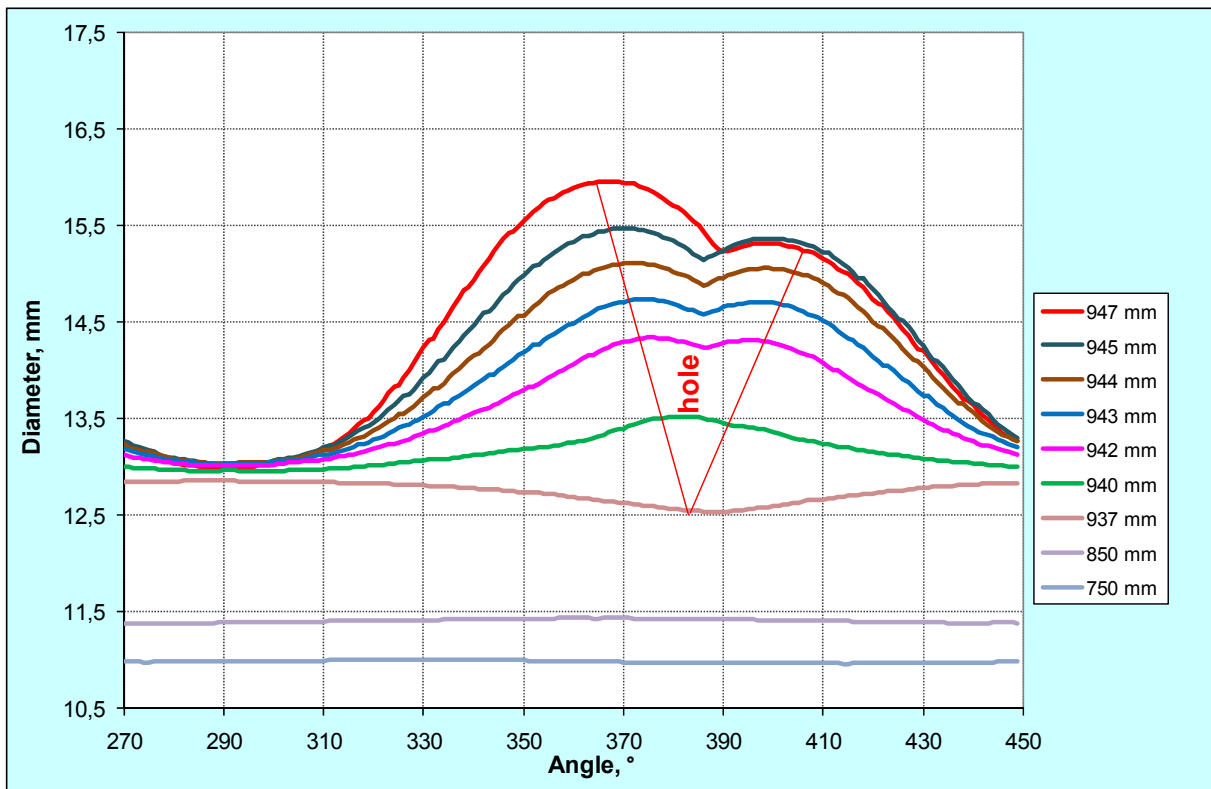
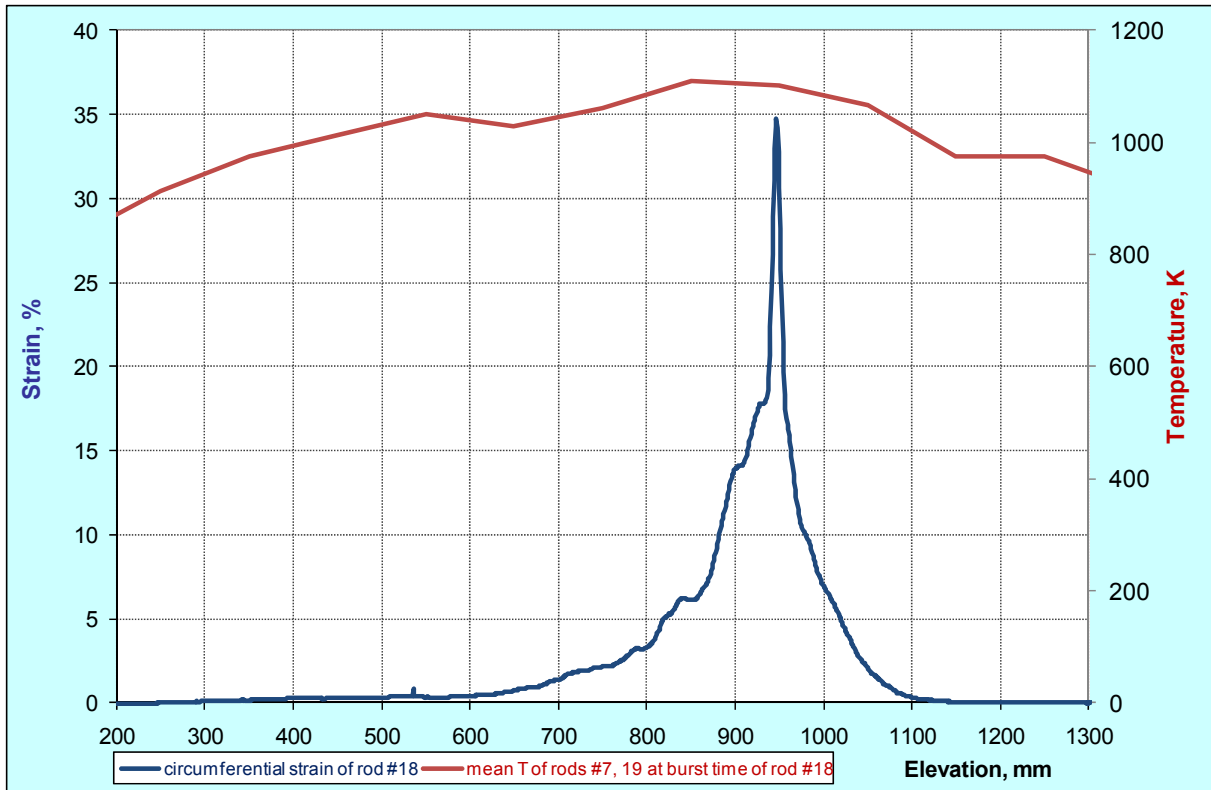


Fig. 66: QUENCH-L0, rod #18; longitudinal circumferential strain changing (top); azimuthal diameter changing downwards from burst (bottom).

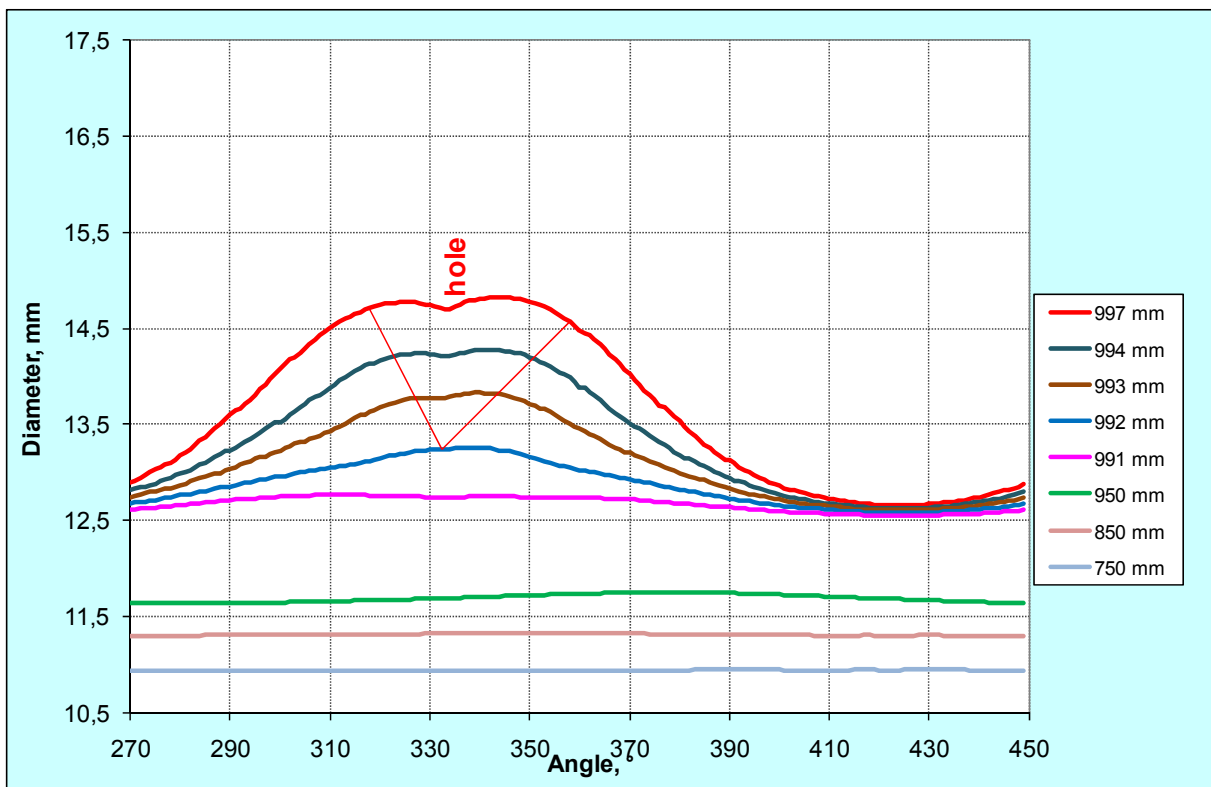
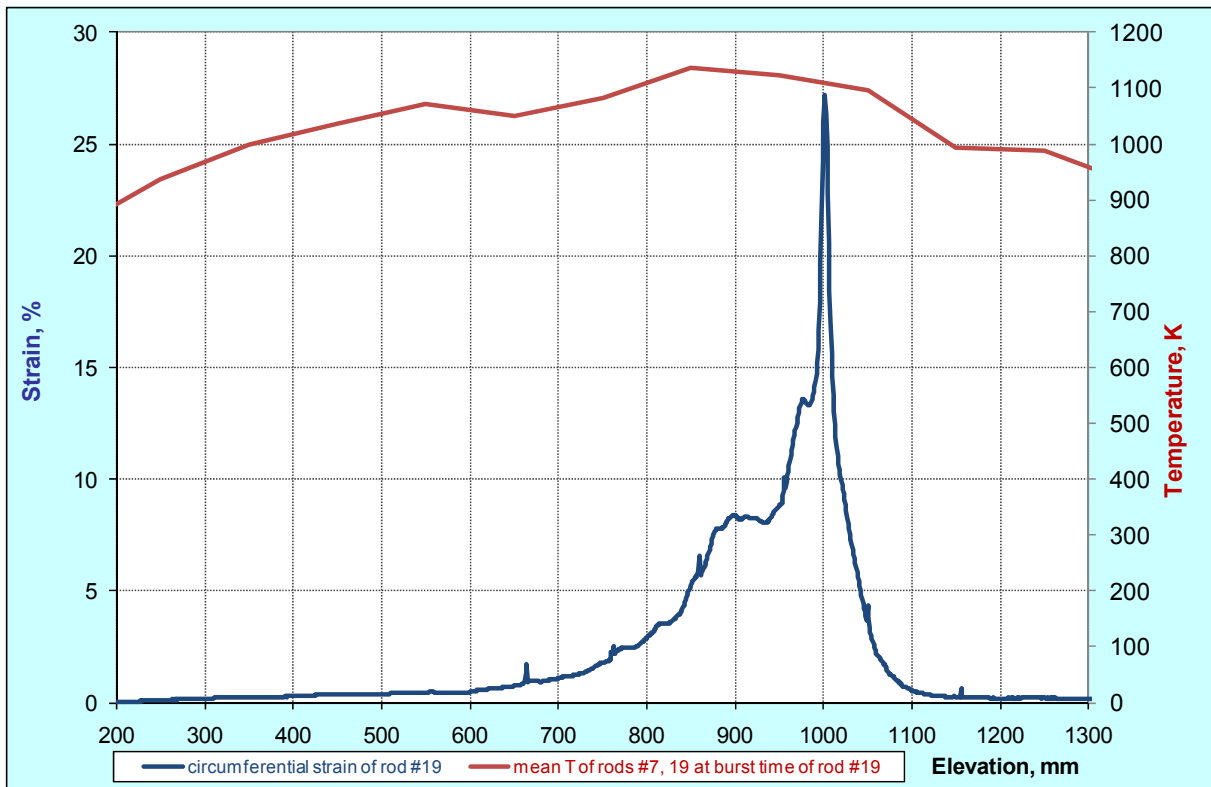


Fig. 67: QUENCH-L0, rod #19; longitudinal circumferential strain changing (top); azimuthal diameter changing downwards from burst (bottom).

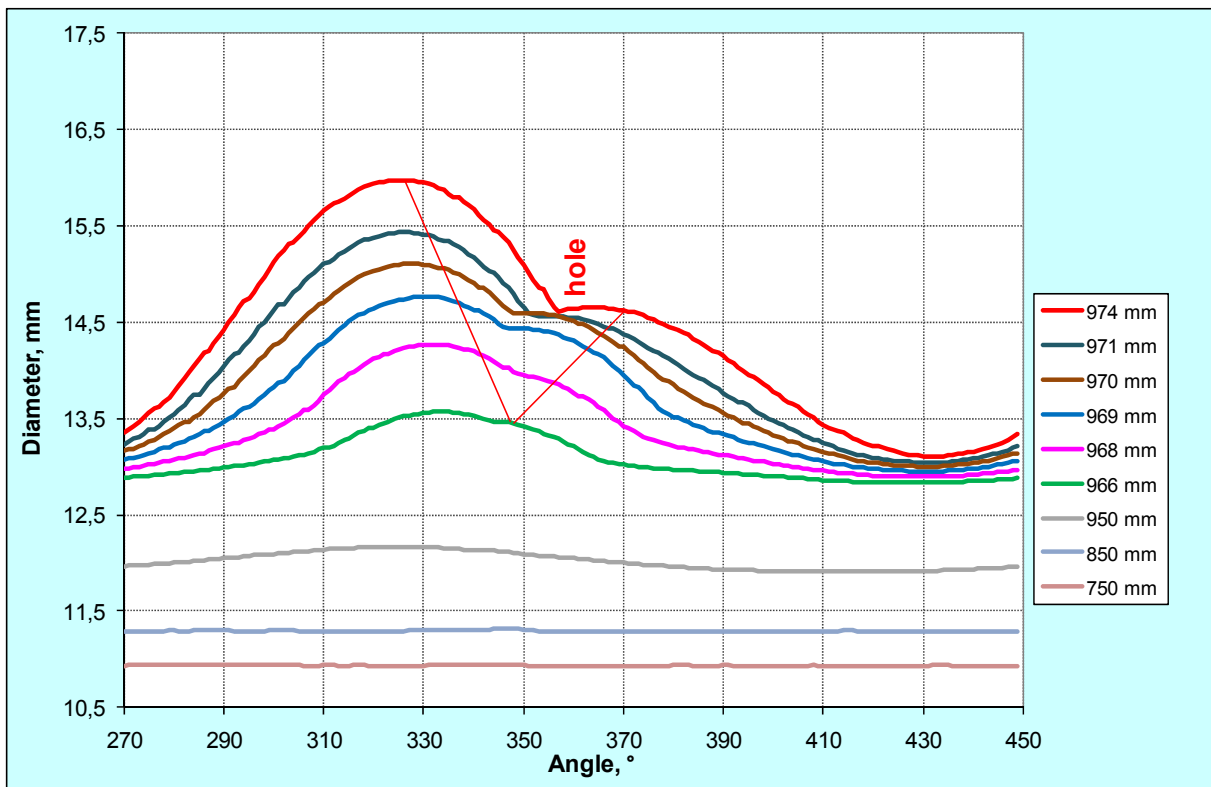
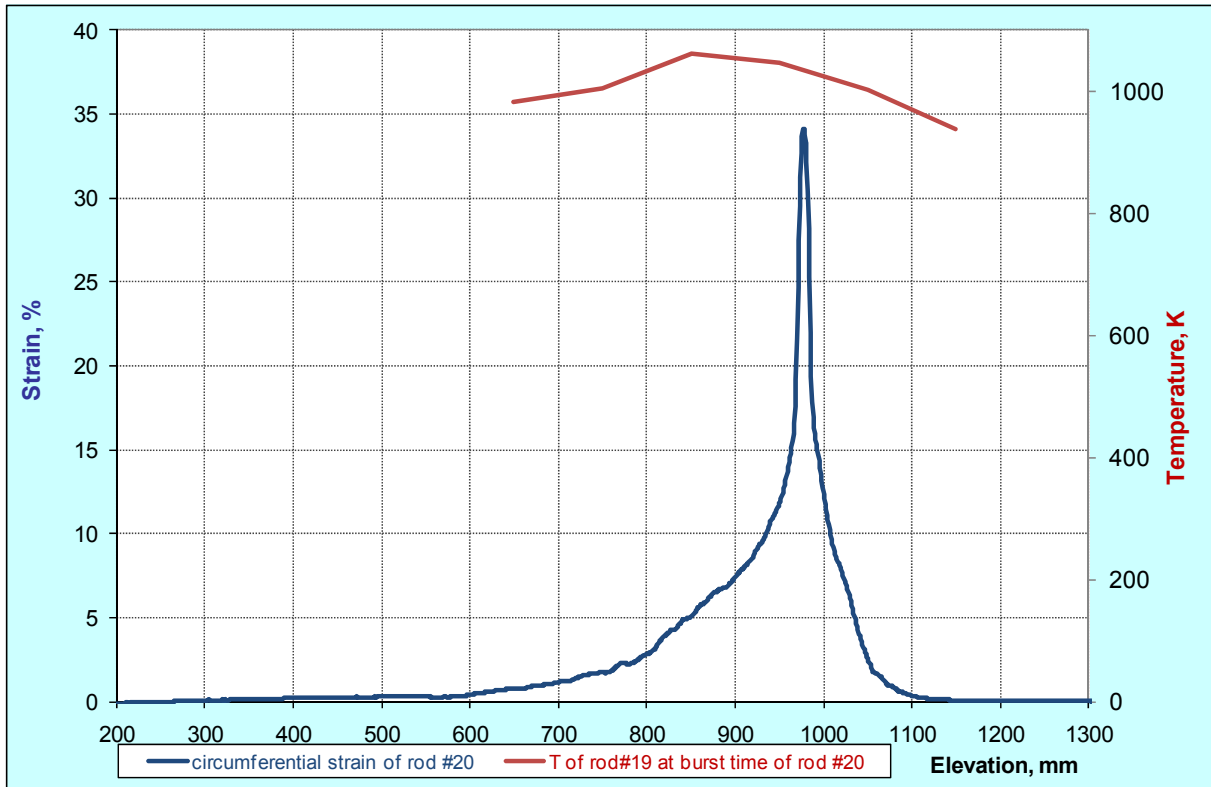


Fig. 68: QUENCH-L0, rod #20; longitudinal circumferential strain changing (top); azimuthal diameter changing downwards from burst (bottom).



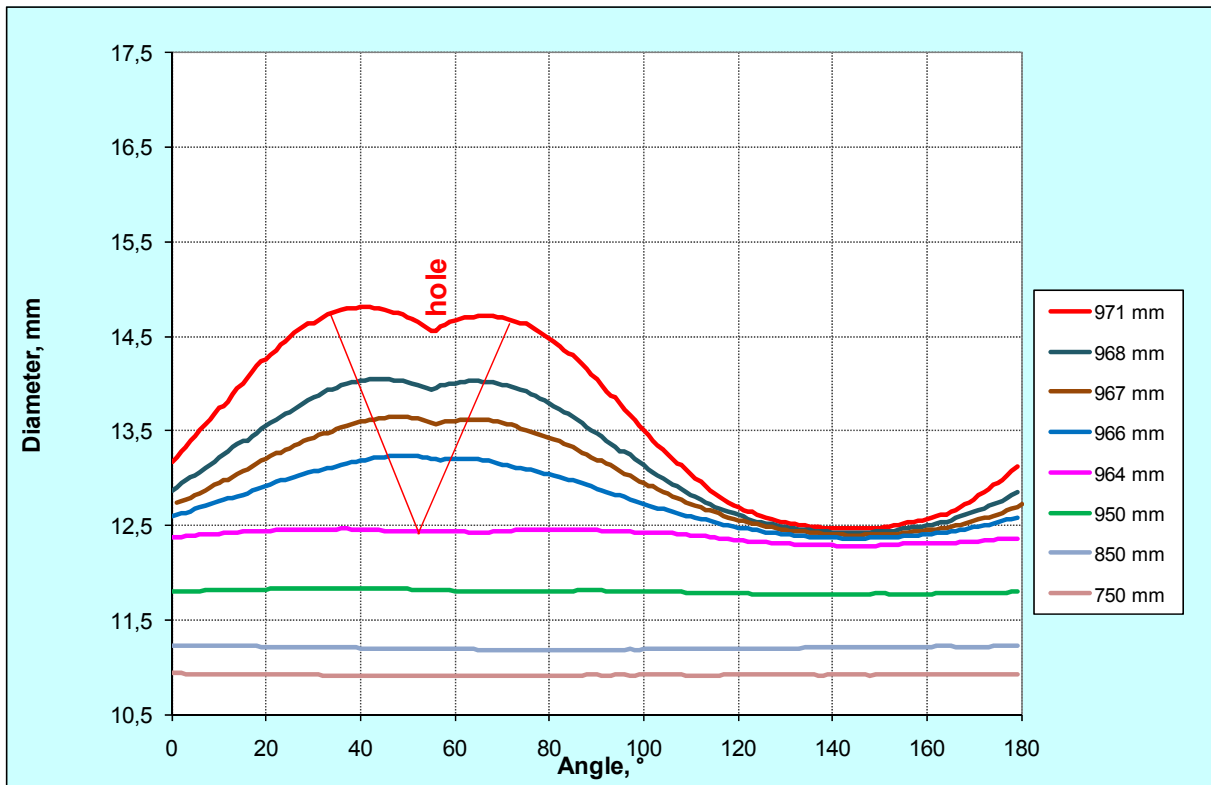
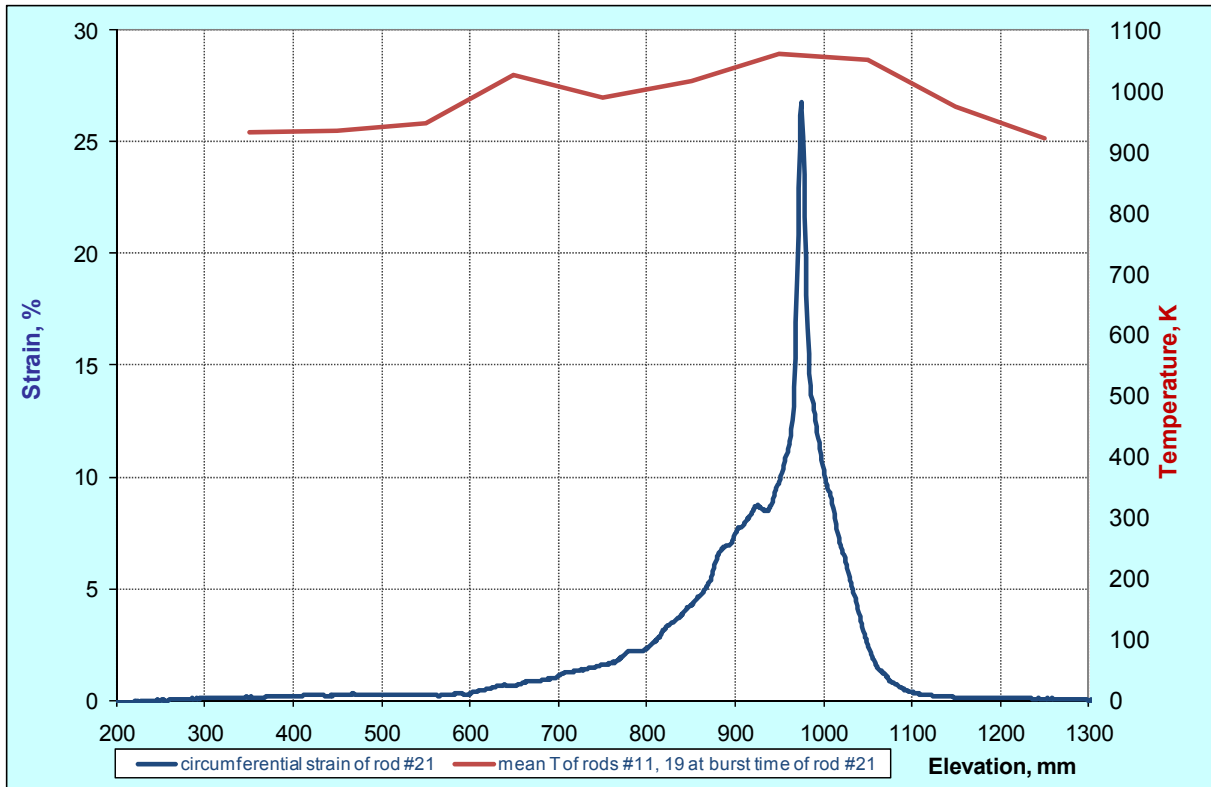


Fig. 69: QUENCH-L0, rod #21; longitudinal circumferential strain changing (top); azimuthal diameter changing downwards from burst (bottom).

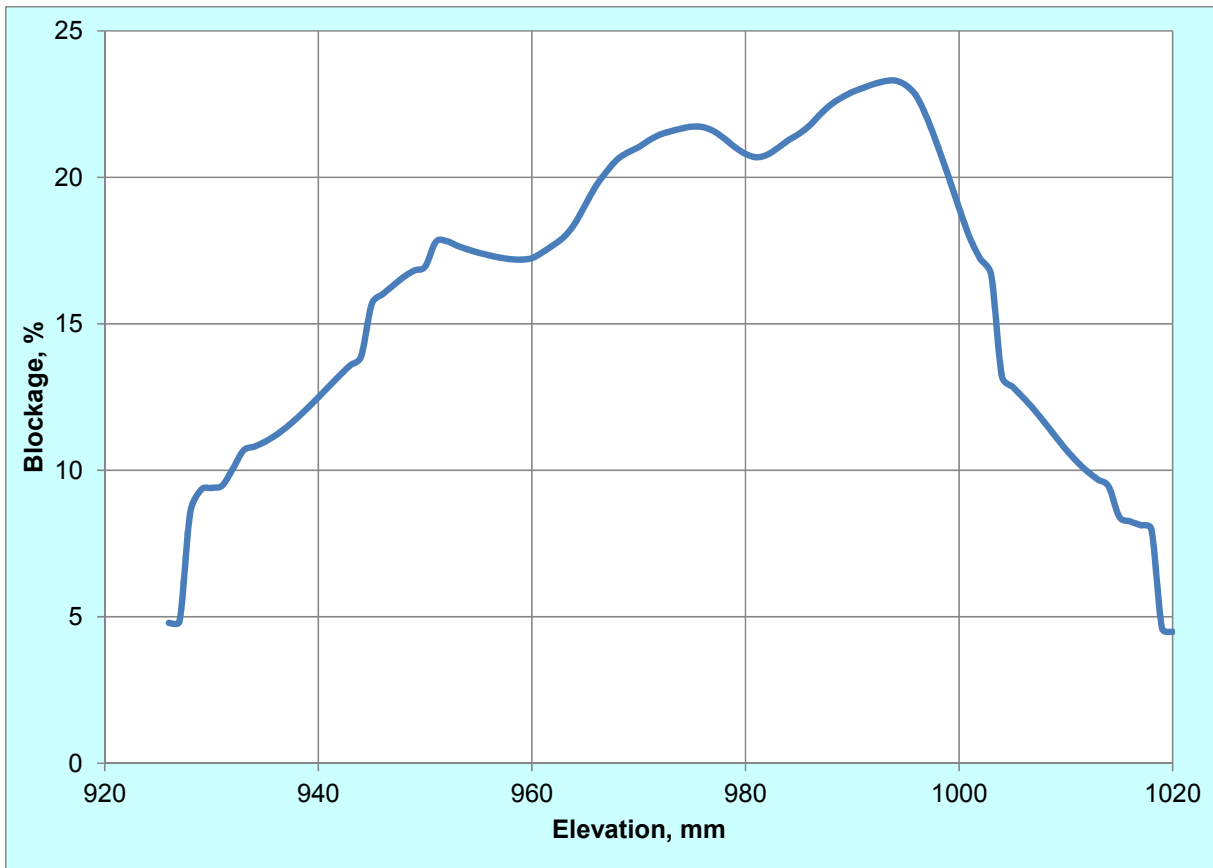


Fig. 70: QUENCH-L0; Blockage of coolant channel.

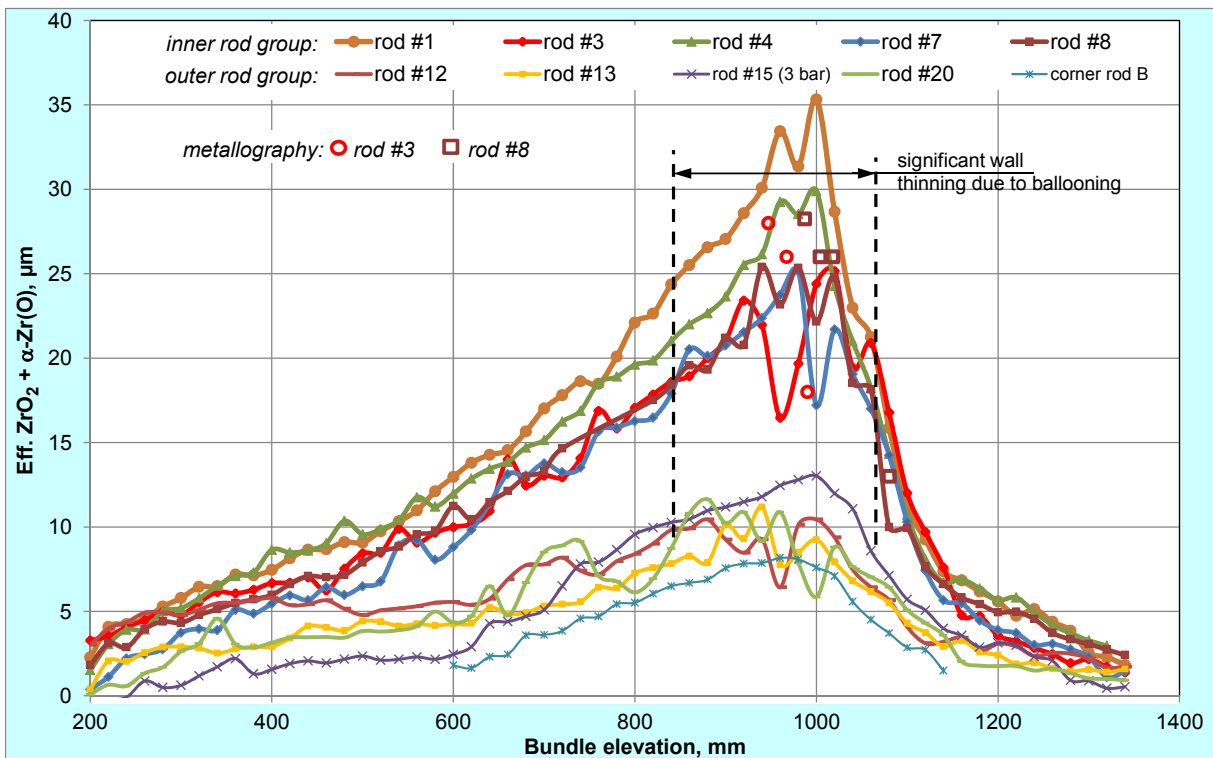
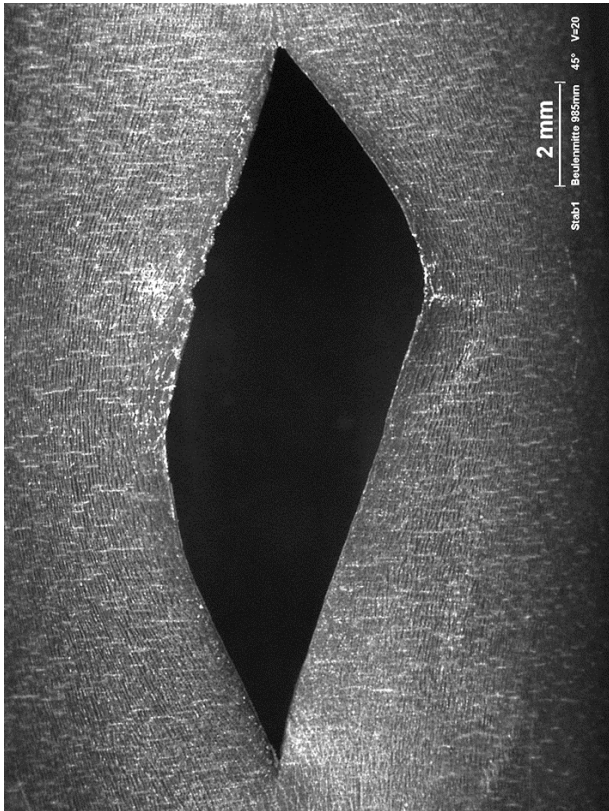
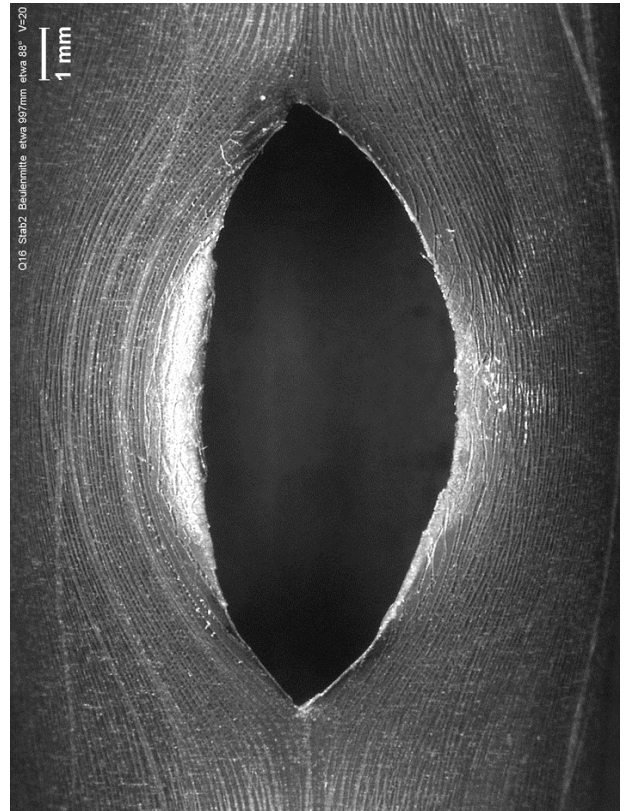


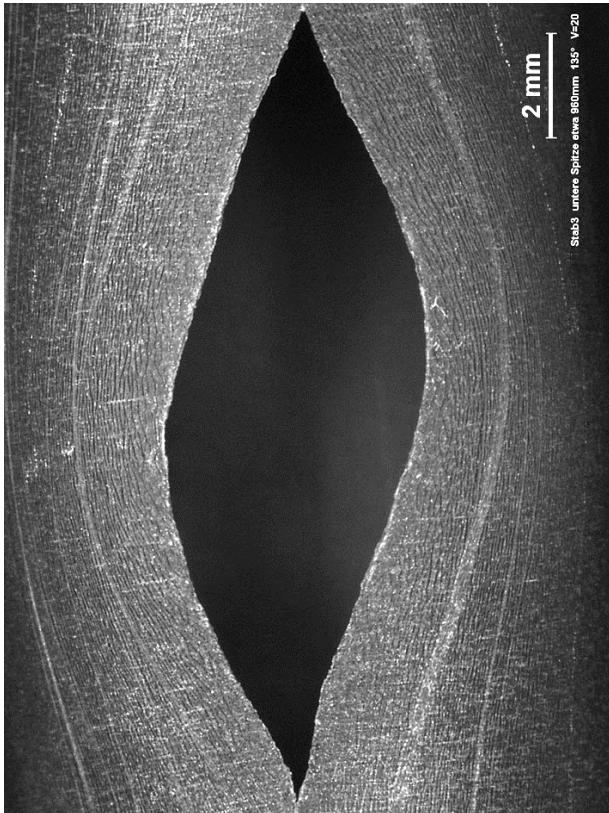
Fig. 71: QUENCH-L0; Eddy current results.



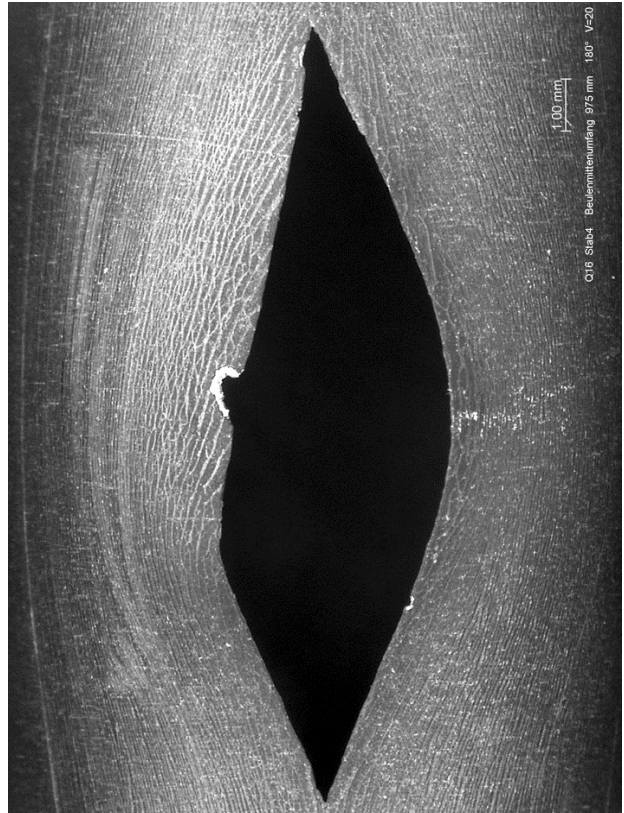
Rod #1 at 59°:  $p=50$  bar,  $A_{burst}=36$  mm<sup>2</sup>



Rod #2 at 116°:  $p=35$  bar,  $A_{burst}=40$  mm<sup>2</sup>

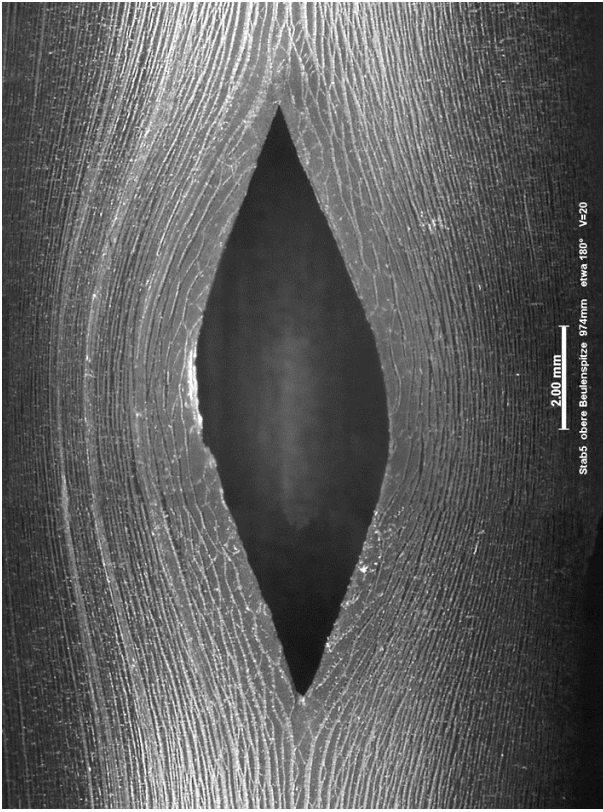


Rod #3 at 136°:  $p=55$  bar,  $A_{burst}=42$  mm<sup>2</sup>

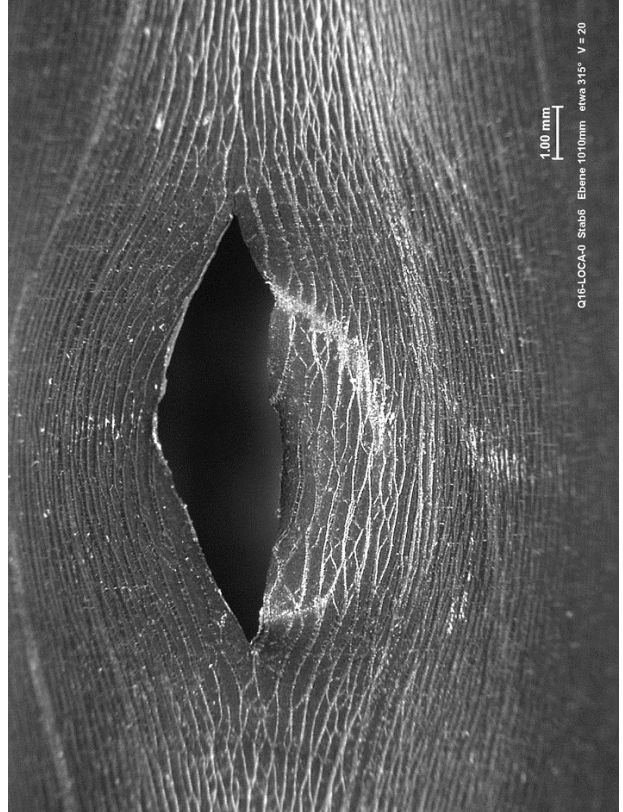


Rod #4 at 158°:  $p=50$  bar,  $A_{burst}=36$  mm<sup>2</sup>

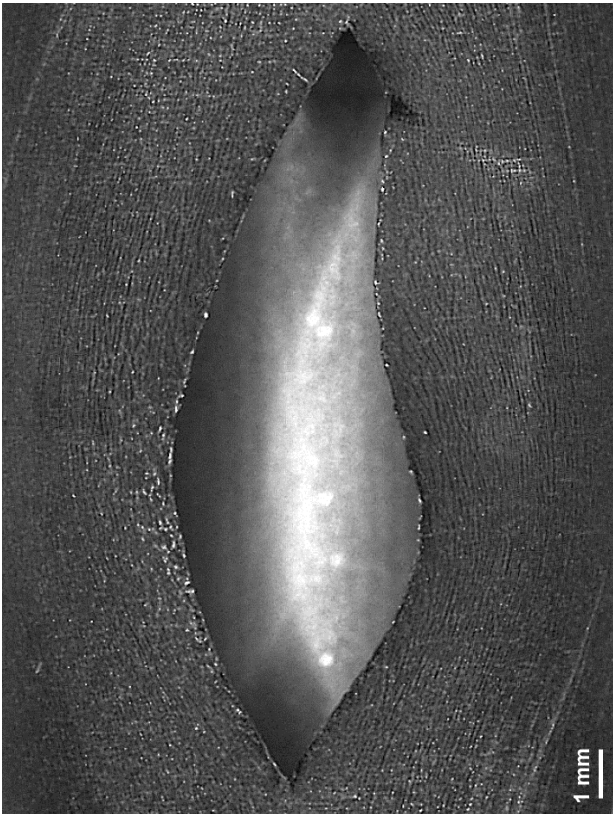
Fig. 72: QUENCH-L0; Overview of burst structures of rods #1 - #4.



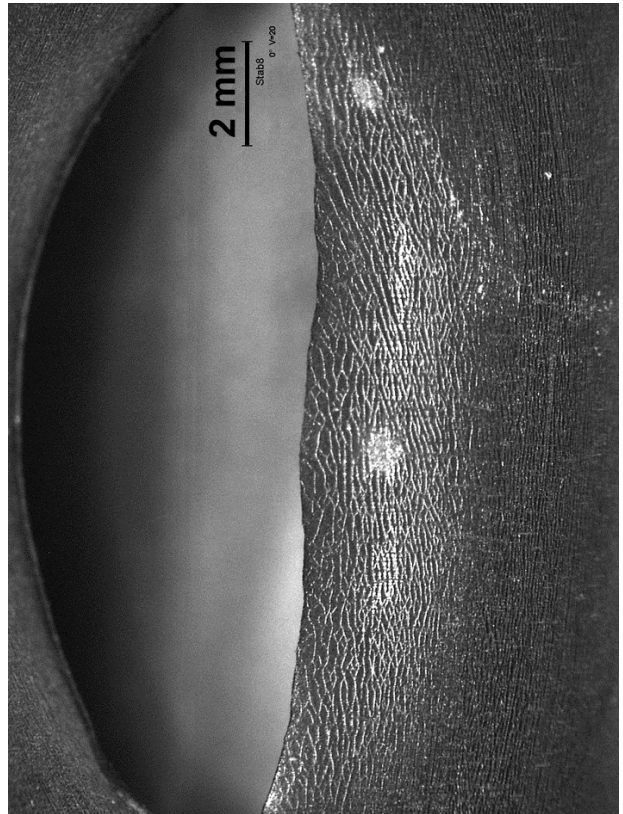
Rod #5 at 192°; p=40 bar,  $A_{burst}=24 \text{ mm}^2$



Rod #6 at 329°; p=35 bar,  $A_{burst}=9 \text{ mm}^2$



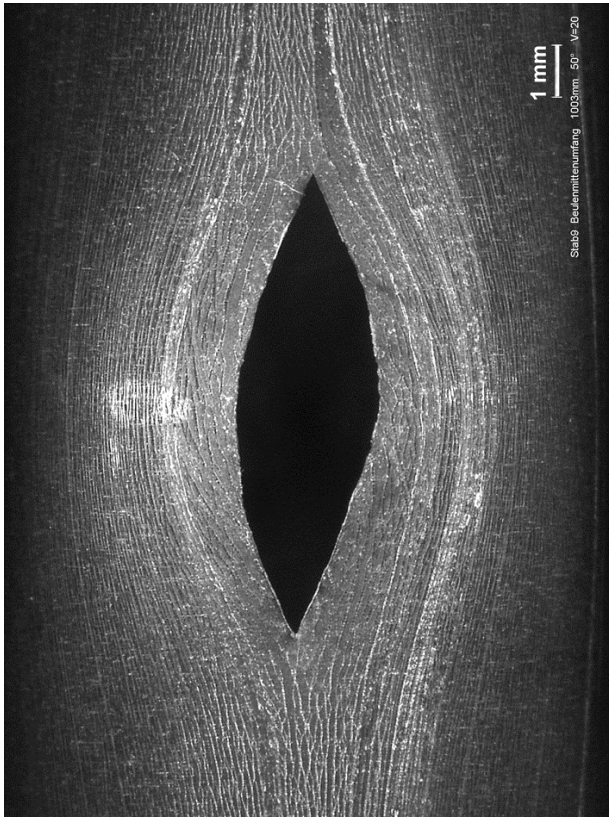
Rod #7 at 338°; p=55 bar,  $A_{burst}=40 \text{ mm}^2$



Rod #8 at 2°; p=50 bar,  $A_{burst}=60 \text{ mm}^2$

Fig. 73: QUENCH-L0; Overview of burst structures of rods #5 - #8.

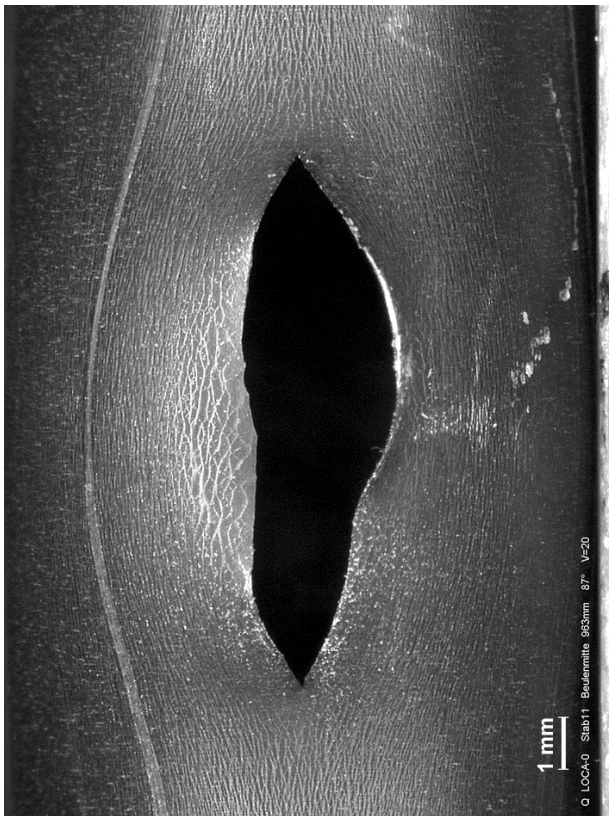




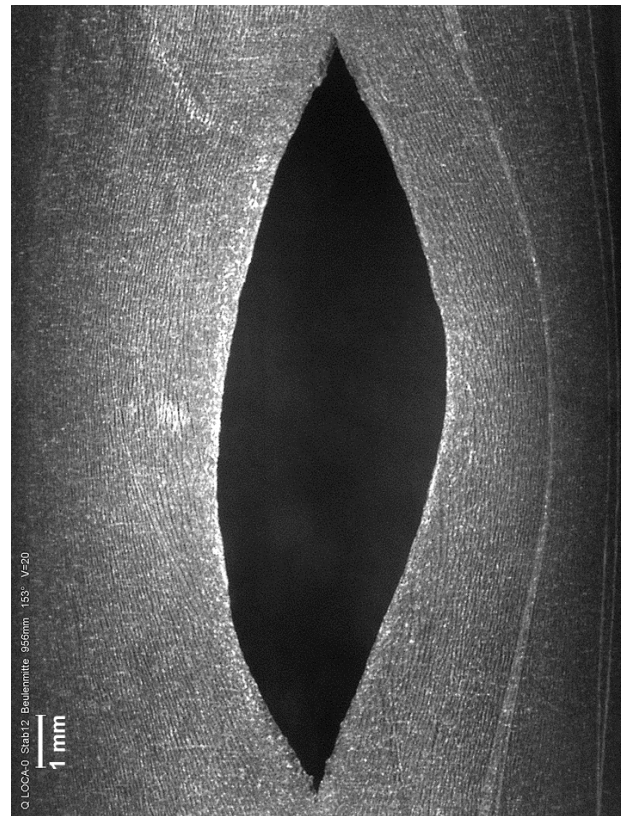
Rod #9 at 64°; p=40 bar,  $A_{burst}=15 \text{ mm}^2$



Rod #10 at 77°; p=45 bar,  $A_{burst}=13 \text{ mm}^2$

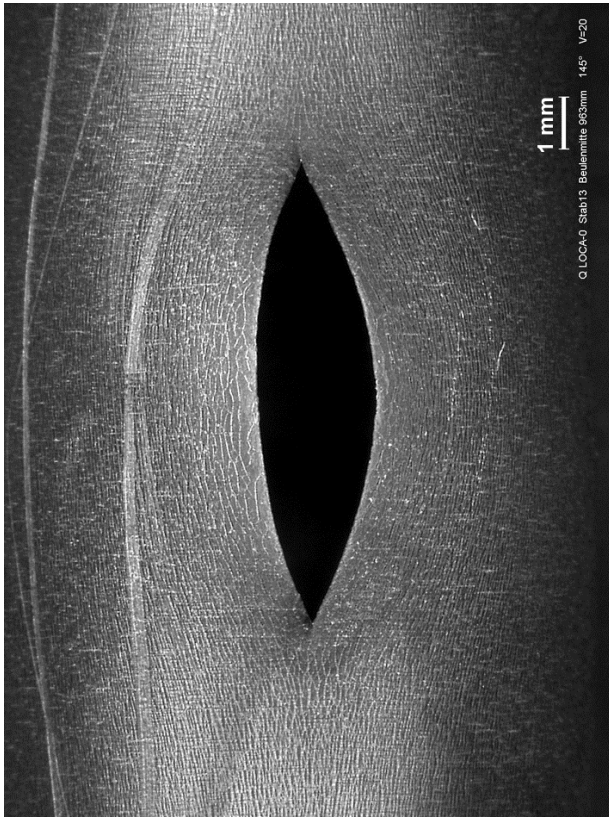


Rod #11 at 71°; p=40 bar,  $A_{burst}=22 \text{ mm}^2$

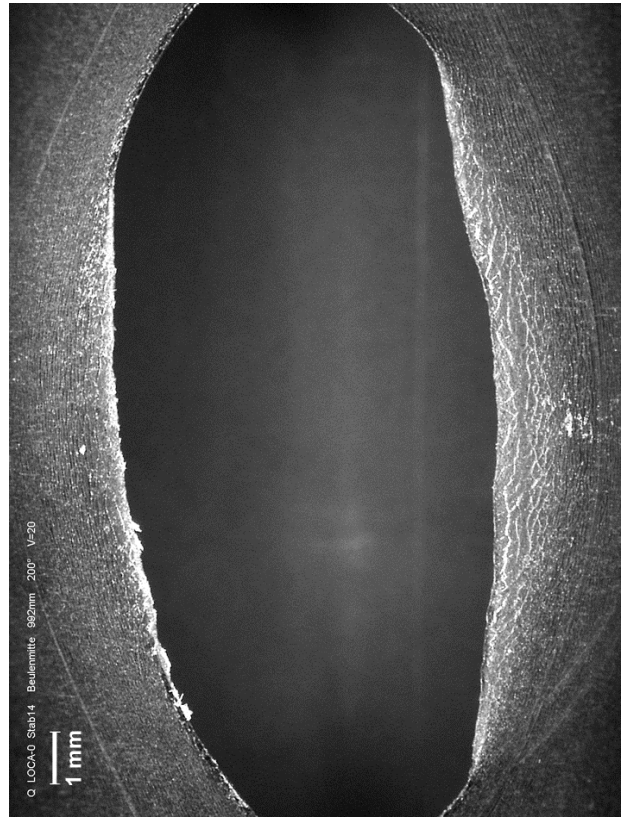


Rod #12 at 173°; p=50 bar,  $A_{burst}=41 \text{ mm}^2$

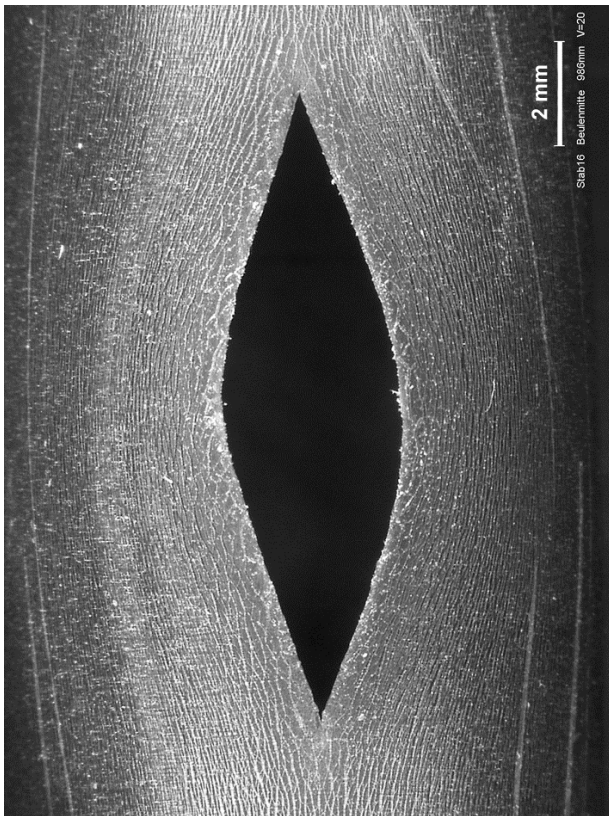
Fig. 74: QUENCH-L0; Overview of burst structures of rods #9 - #12.



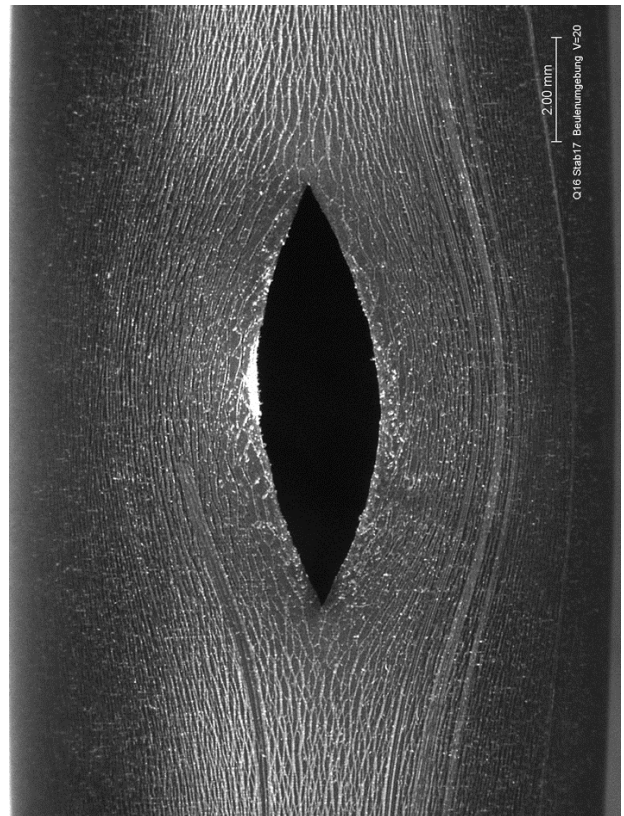
Rod #13 at 137°;  $p=50$  bar,  $A_{burst}=13$  mm<sup>2</sup>



Rod #14 at 223°;  $p=50$  bar,  $A_{burst}=97$  mm<sup>2</sup>



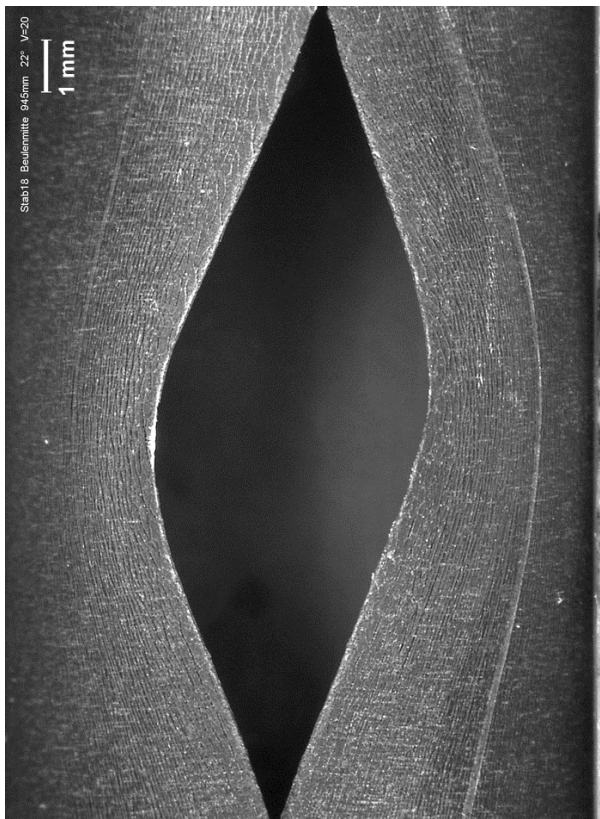
Rod #16 at 206°;  $p=45$  bar,  $A_{burst}=24$  mm<sup>2</sup>



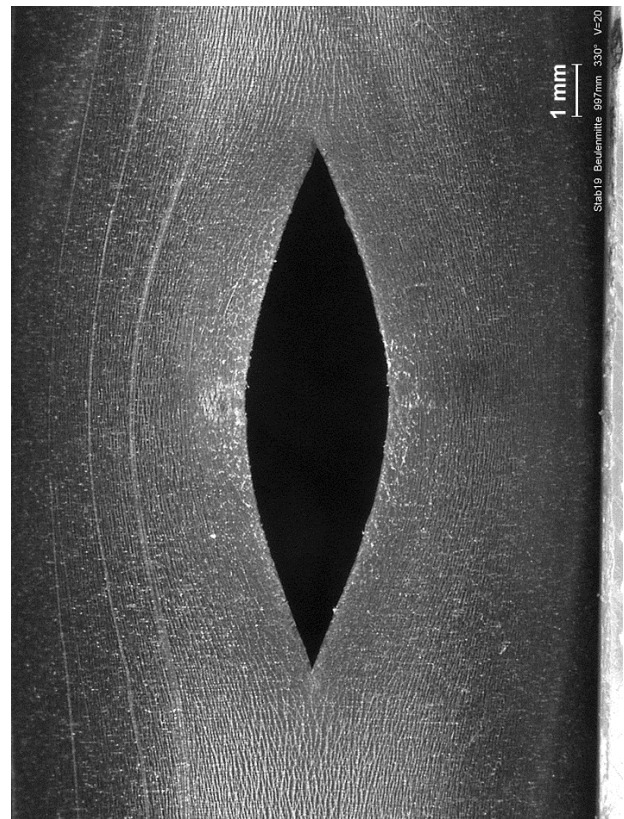
Rod #17 at 280°;  $p=40$  bar,  $A_{burst}=12$  mm<sup>2</sup>

Fig. 75: QUENCH-L0; Overview of burst structures of rods #13 - #17.





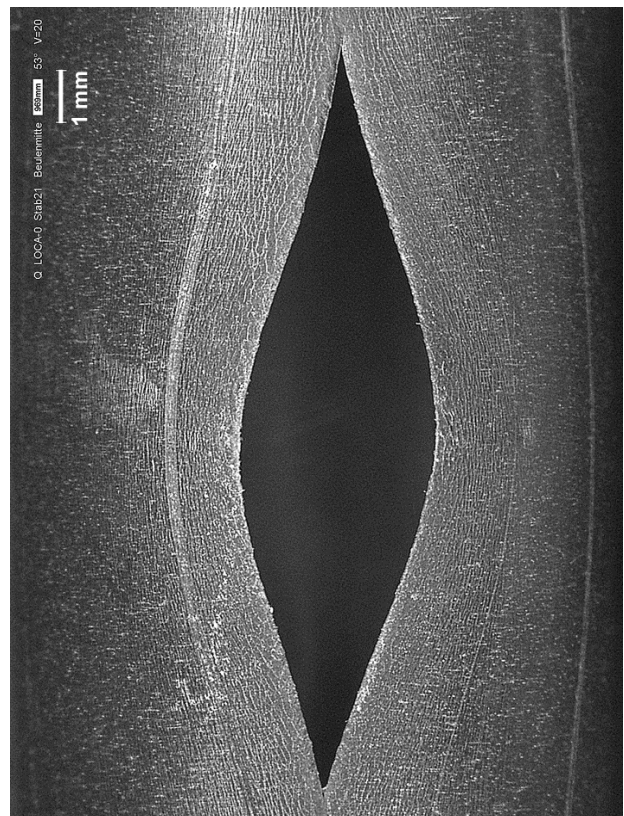
Rod #18 at 7°; p=50 bar,  $A_{burst}=48 \text{ mm}^2$



Rod #19 at 344°; p=50 bar,  $A_{burst}=16 \text{ mm}^2$

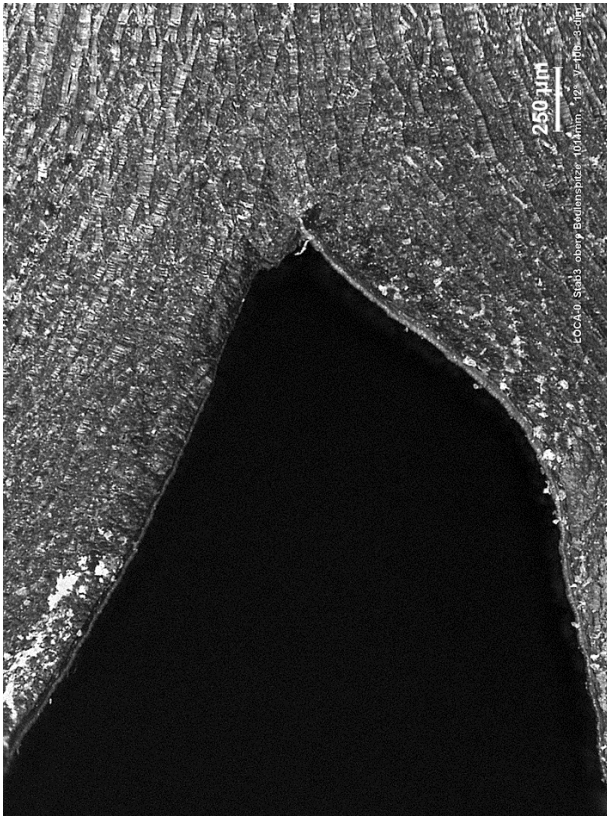


Rod #20 at 325°; p=50 bar,  $A_{burst}=53 \text{ mm}^2$

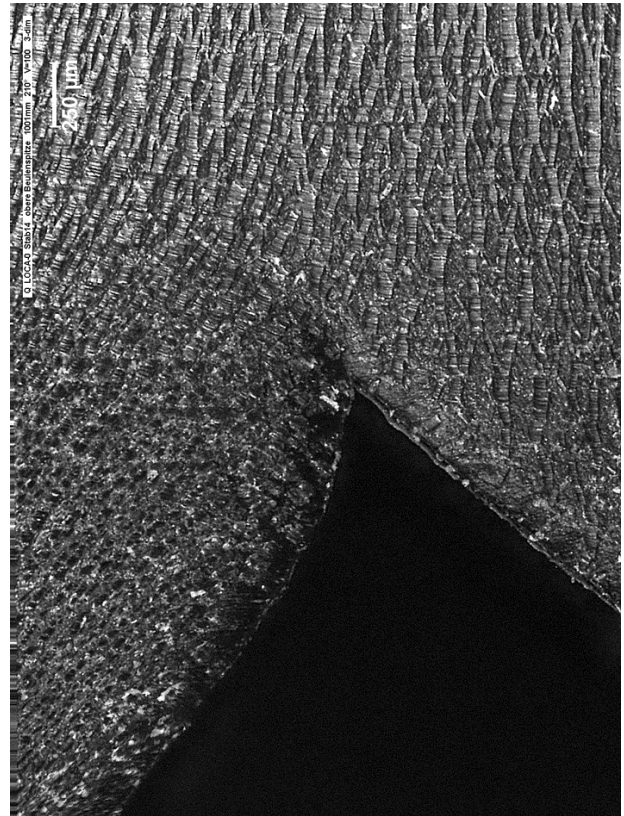


Rod #21 at 41°; p=45 bar,  $A_{burst}=29 \text{ mm}^2$

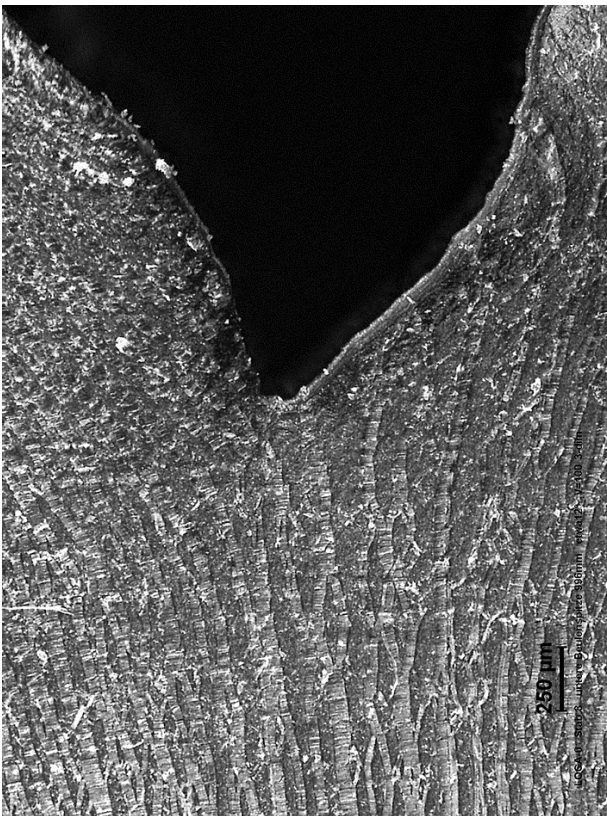
Fig. 76: QUENCH-L0; Overview of burst structures of rods #18 - #21.



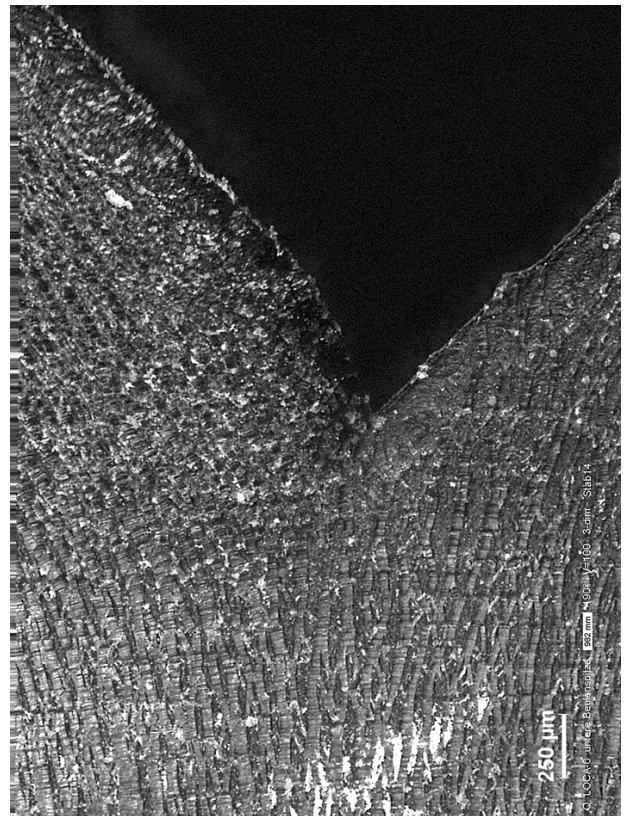
Rod #8: top of burst opening



Rod #14: top of burst opening



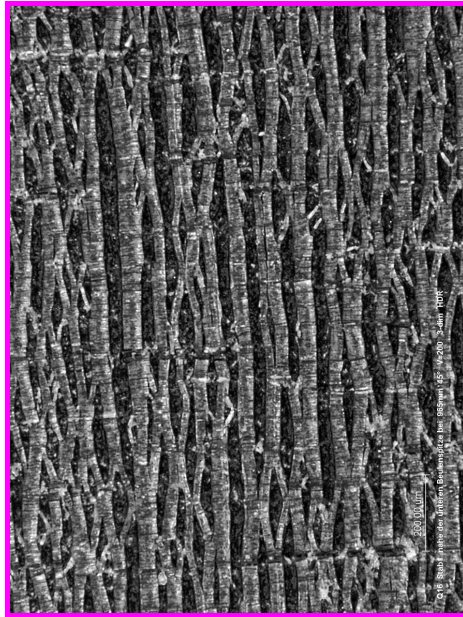
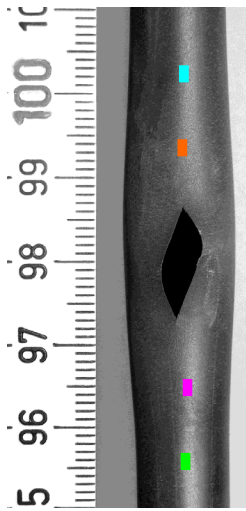
Rod #8: bottom of burst opening



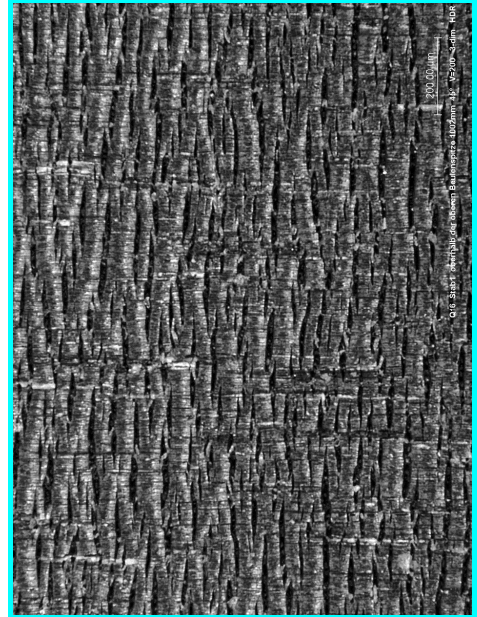
Rod #14: bottom of burst opening

Fig. 77: QUENCH-L0; Upper and low edges of burst opening of rods #8 and #14.

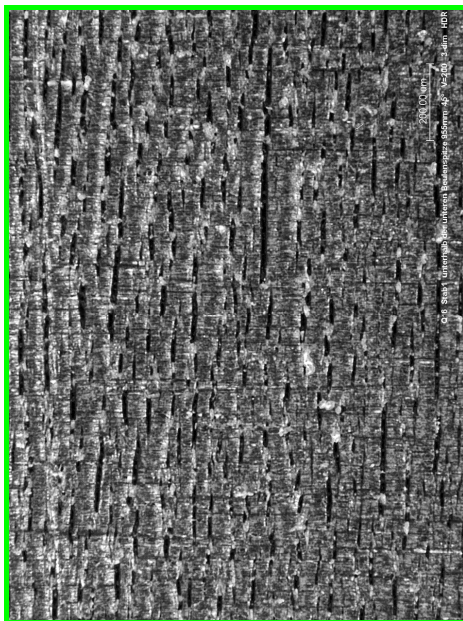




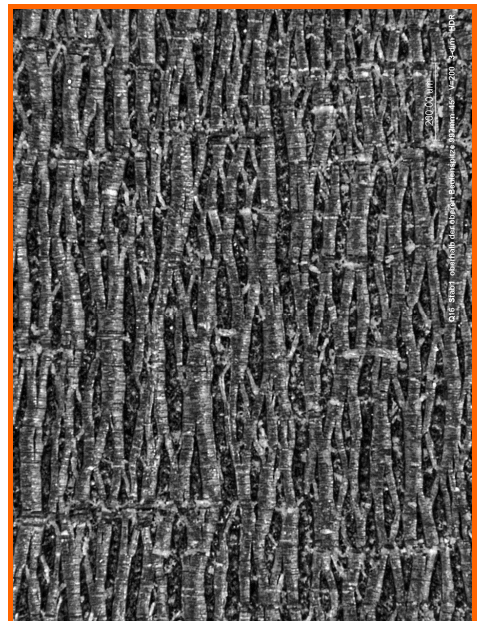
Elevation 965 mm



Elevation 1002 mm

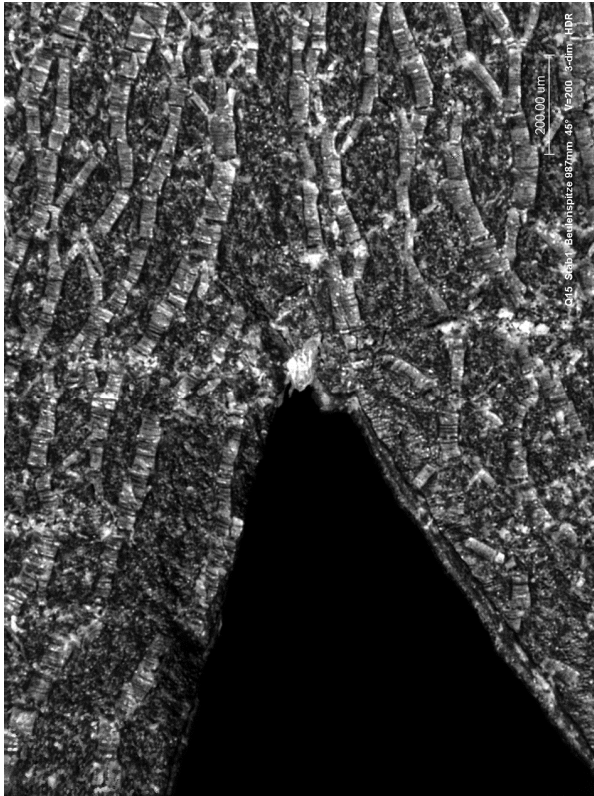


Elevation 955 mm

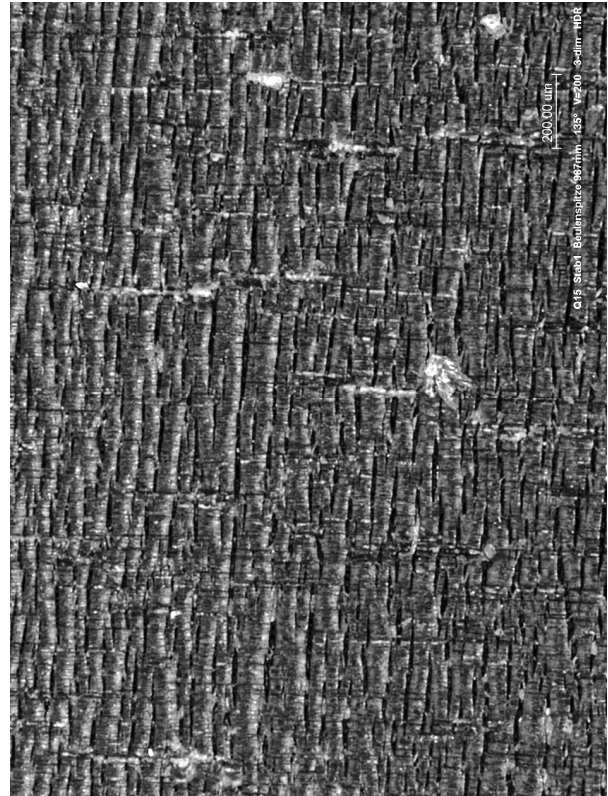


Elevation 992 mm

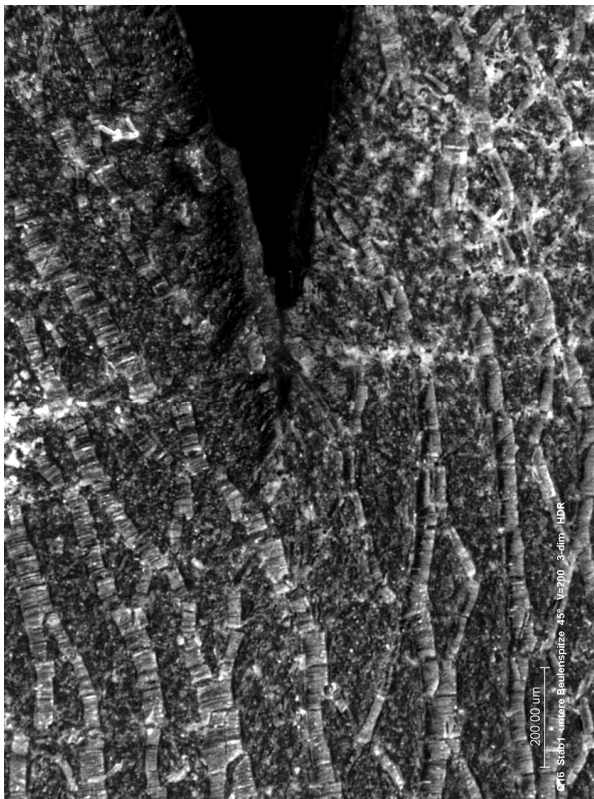
Fig. 78: QUENCH-L0; Overview of cladding surface along burst line (azimuth 60°) of rod #1.



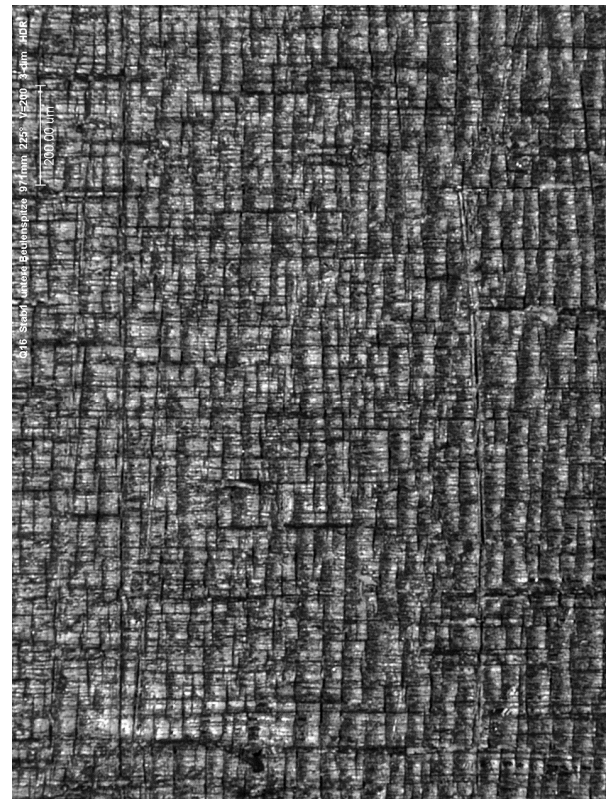
Elevation 987 mm, azimuth 60°



Elevation 987 mm, azimuth 150°



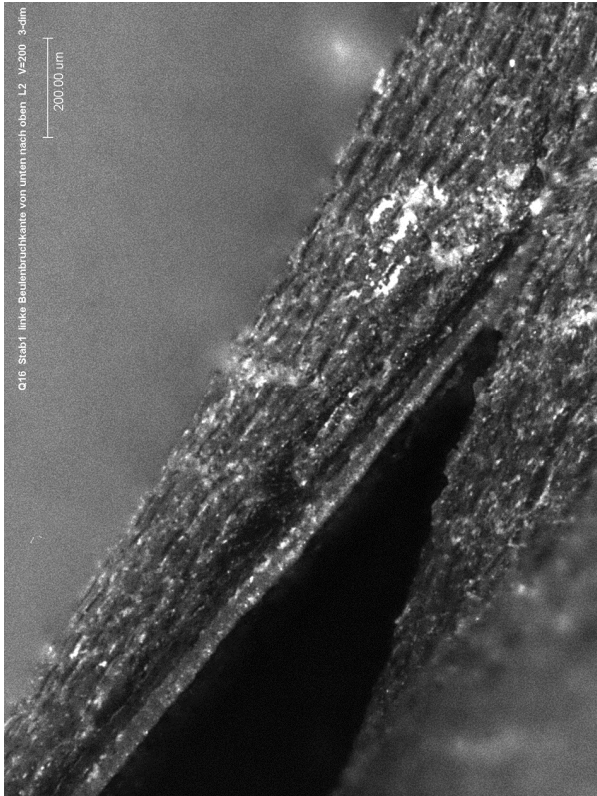
Elevation 971 mm, azimuth 60°



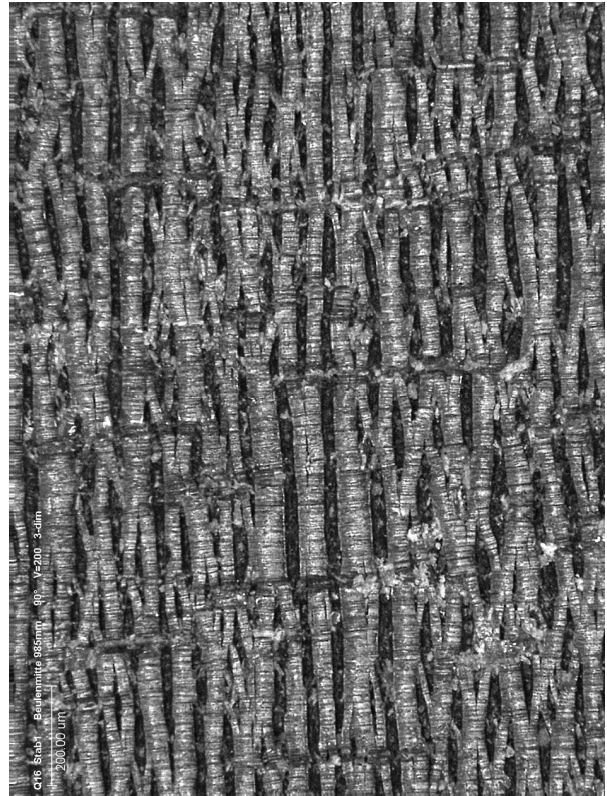
Elevation 971 mm, azimuth 240°

Fig. 79: QUENCH-L0; Overview of cladding surface around burst position of rod #1.

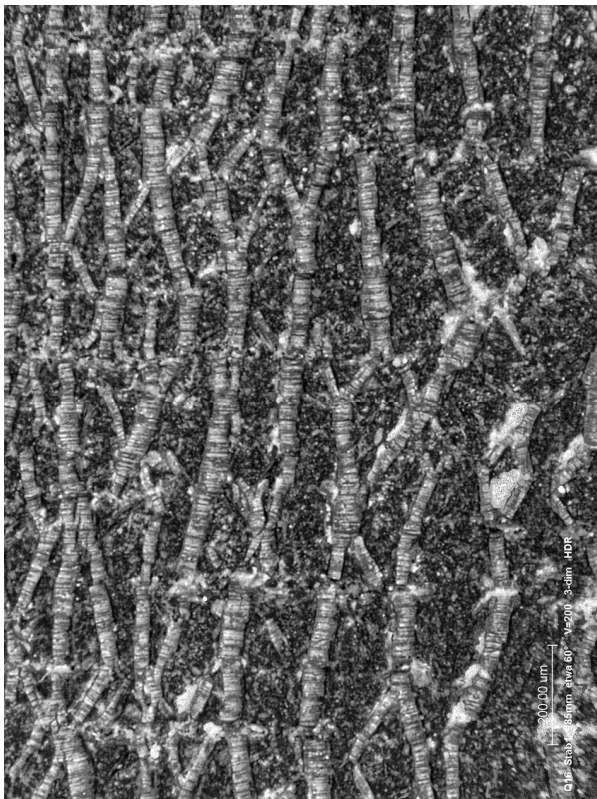




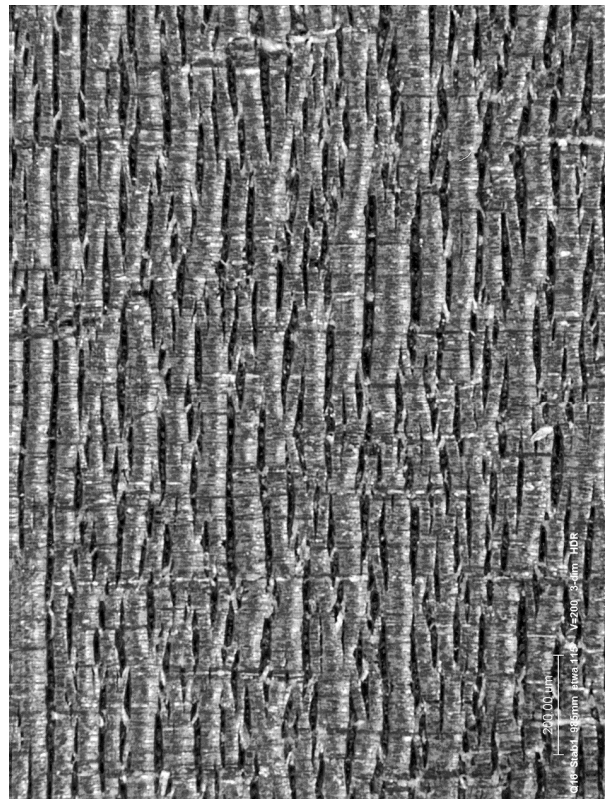
Elevation 985 mm, azimuth 60°, side view



Elevation 985 mm, azimuth 105°

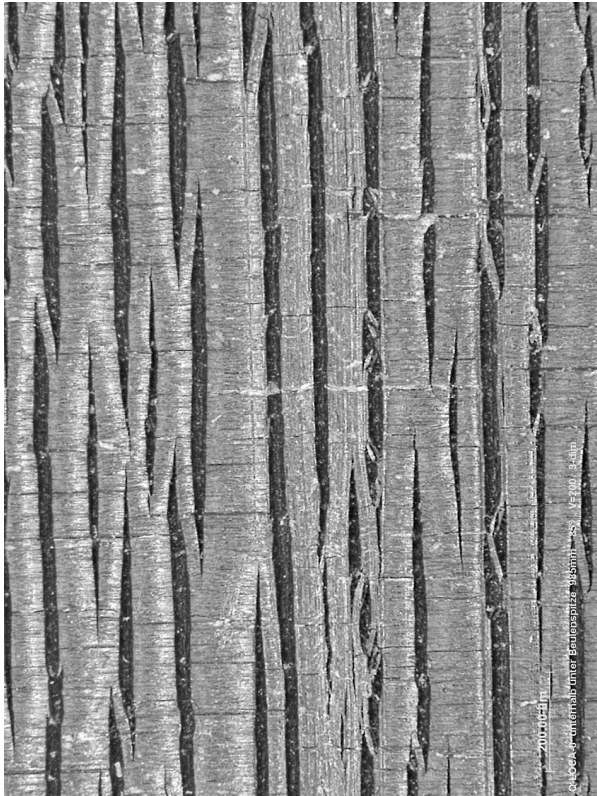


Elevation 985 mm, azimuth 75°

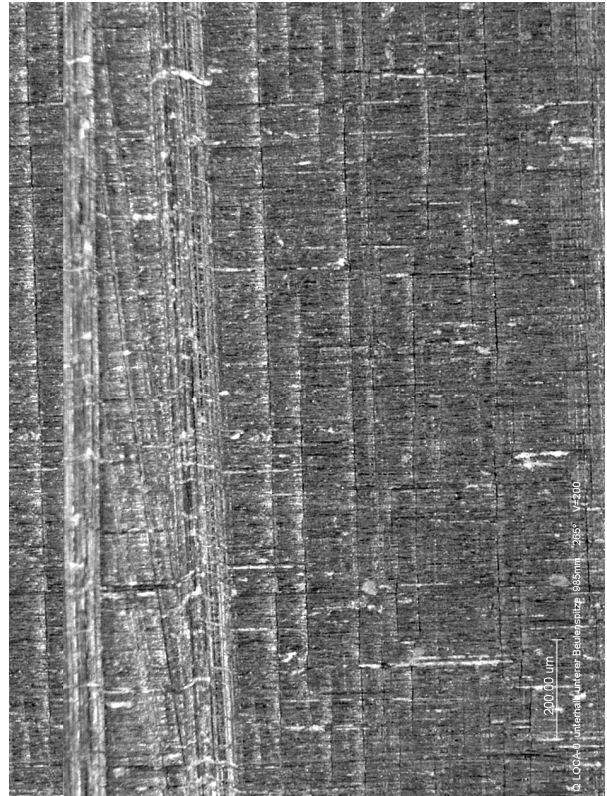


Elevation 985 mm, azimuth 130°

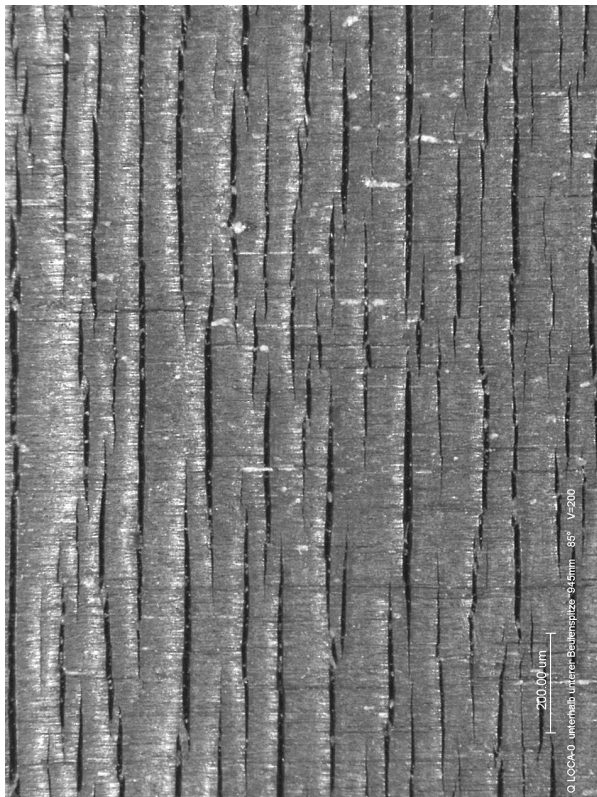
Fig. 80: QUENCH-L0; Overview of cladding surface near to burst position at different azimuths of rod #1.



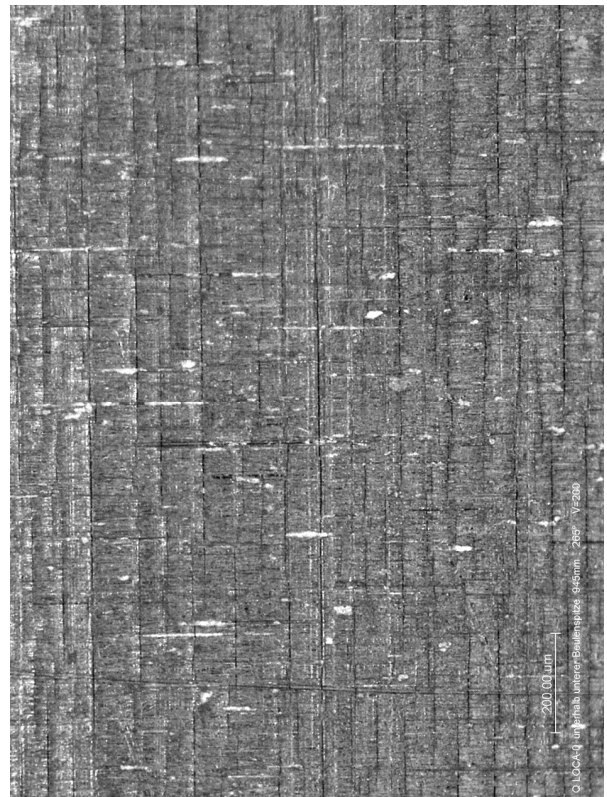
Elevation 985 mm, azimuth 116°



Elevation 985 mm, azimuth 296°

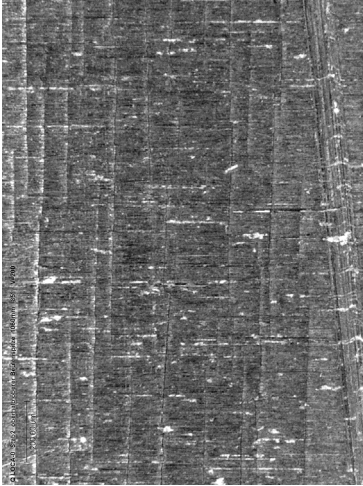


Elevation 945 mm, azimuth 116° (burst side)

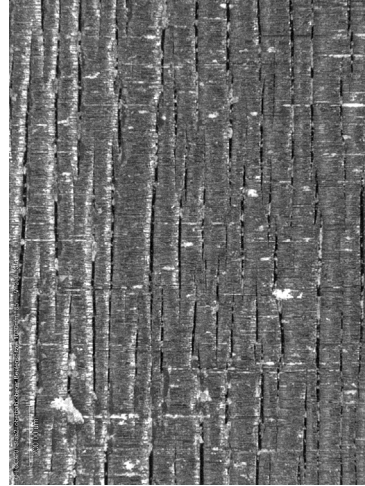


Elevation 945 mm, azimuth 296°

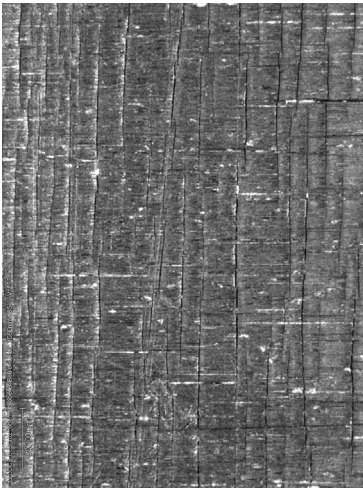
Fig. 81: QUENCH-L0; Overview of cladding surface under burst position of rod #2 at burst azimuth and opposite side.



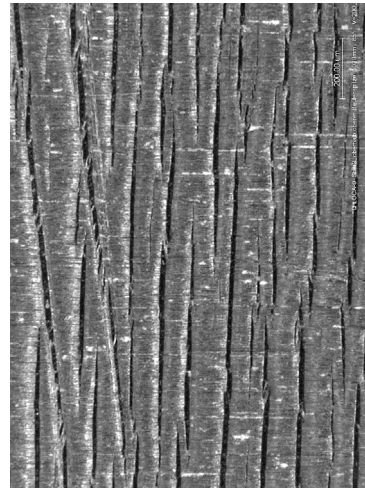
Elevation 1060 mm



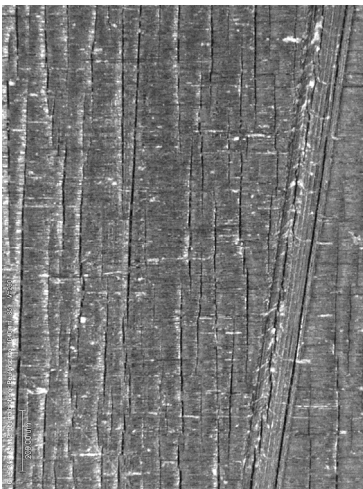
Elevation 1030 mm



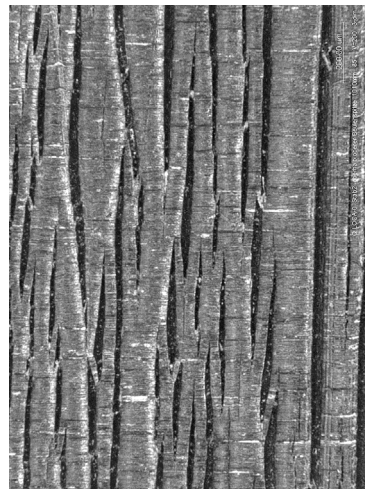
Elevation 1050 mm



Elevation 1020 mm



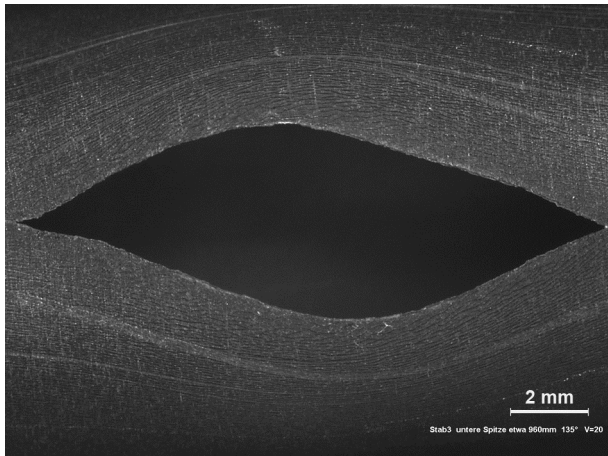
Elevation 1040 mm



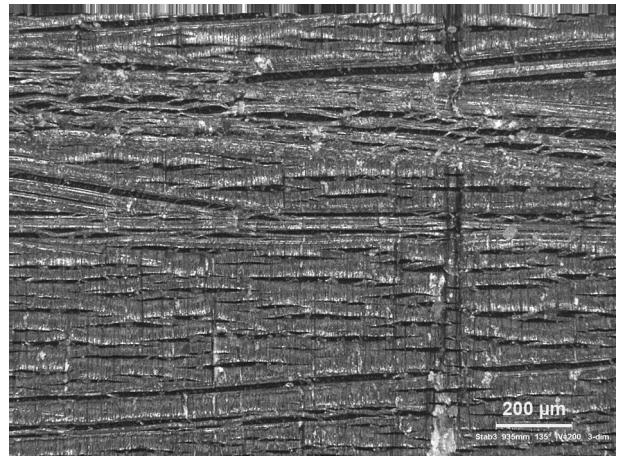
Elevation 1010 mm

Fig. 82: QUENCH-L0; Overview of cladding surface above burst position of rod #2 at burst azimuth of 116°.

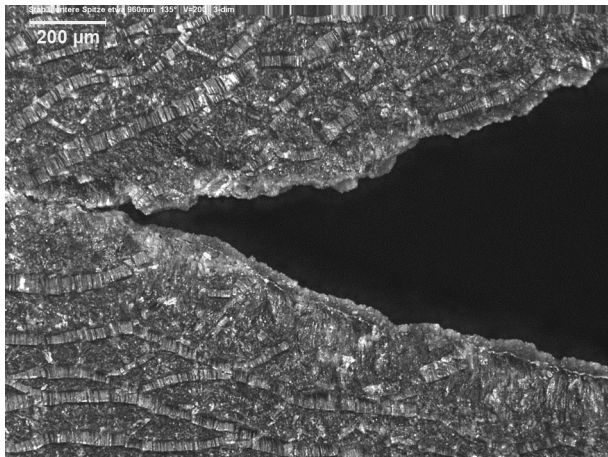




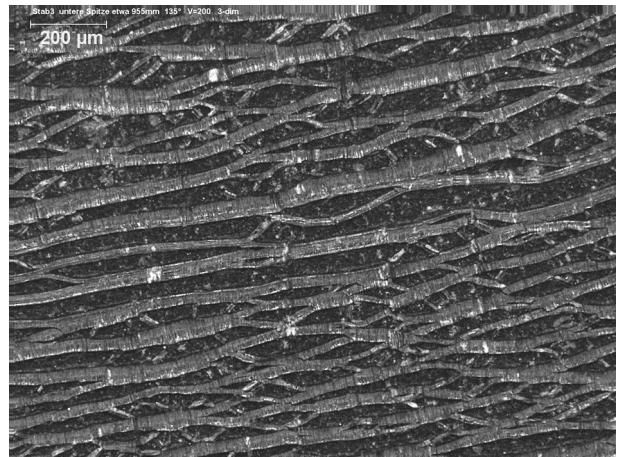
Elevation 960 mm, angle 135°



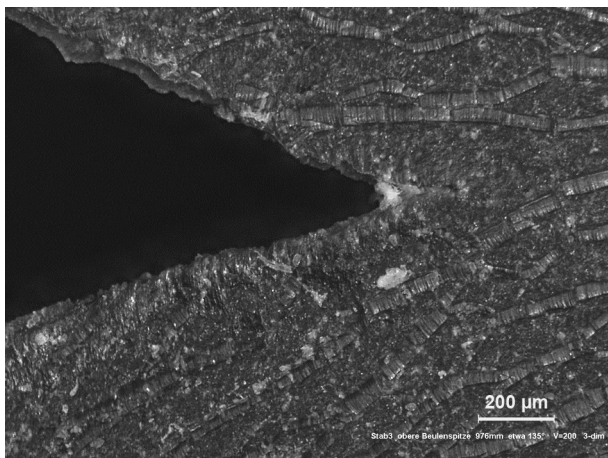
Elevation 935 mm, angle 135°



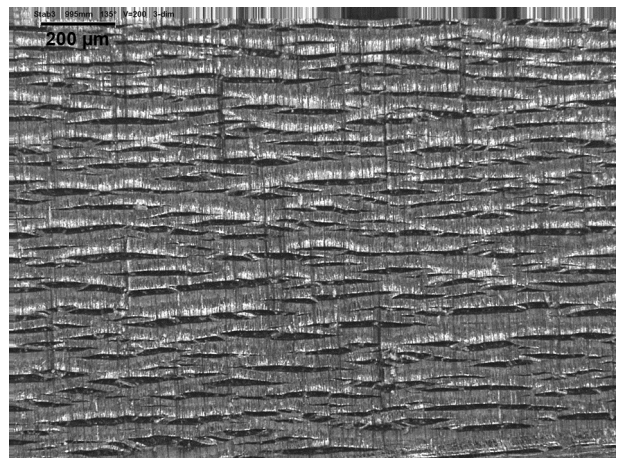
Elevation 960 mm, angle 135°



Elevation 955 mm, angle 135°

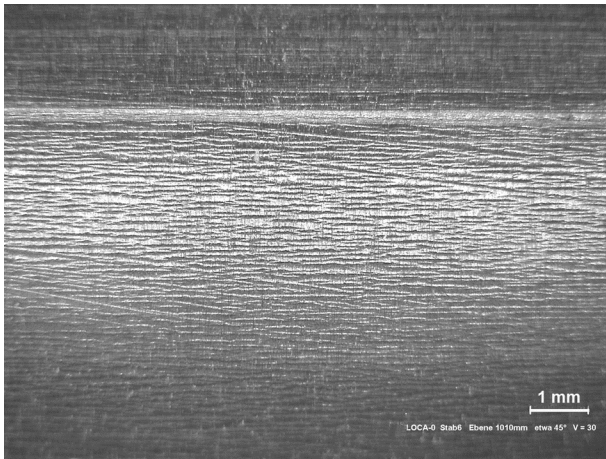


Elevation 976 mm, angle 135°

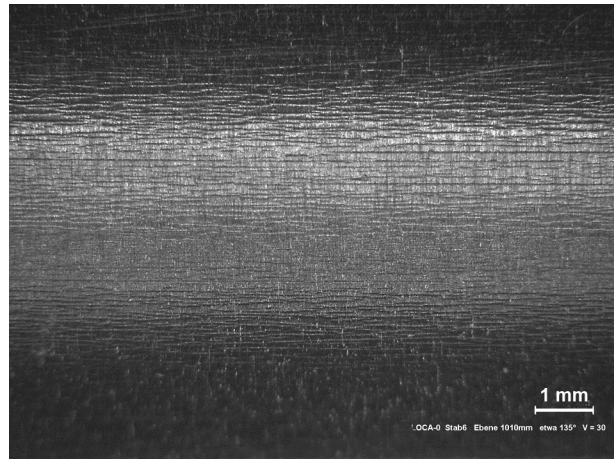


Elevation 995 mm, angle 135°

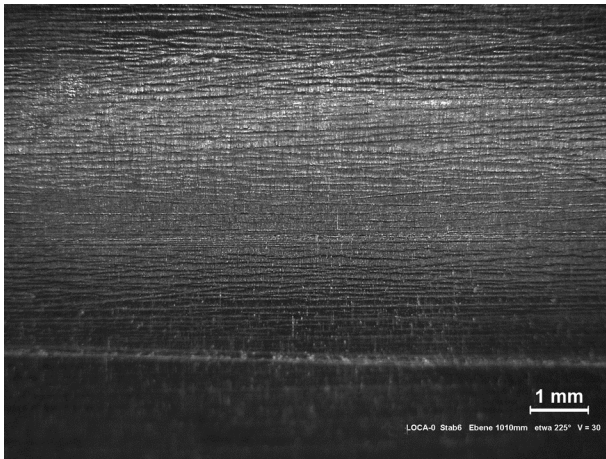
Fig. 83: QUENCH-L0; Overview of cladding surface structure near to burst position for rod No. 3.



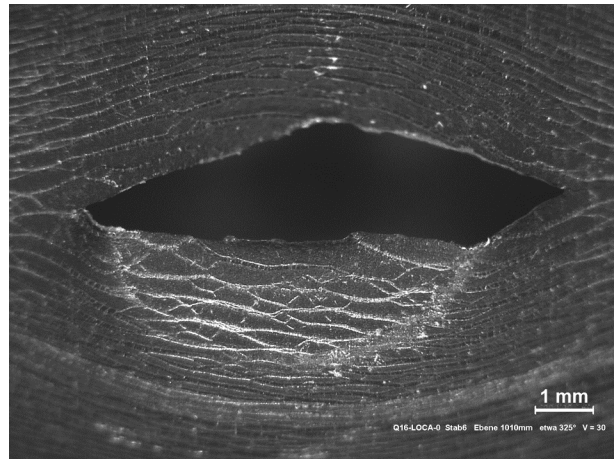
Elevation 1010 mm, angle 45°



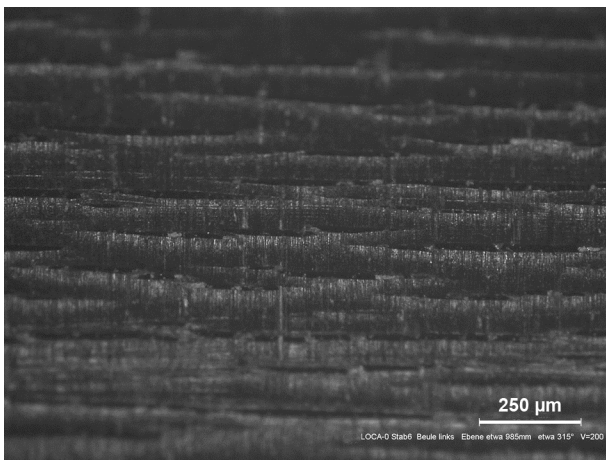
Elevation 1010 mm, angle 135°



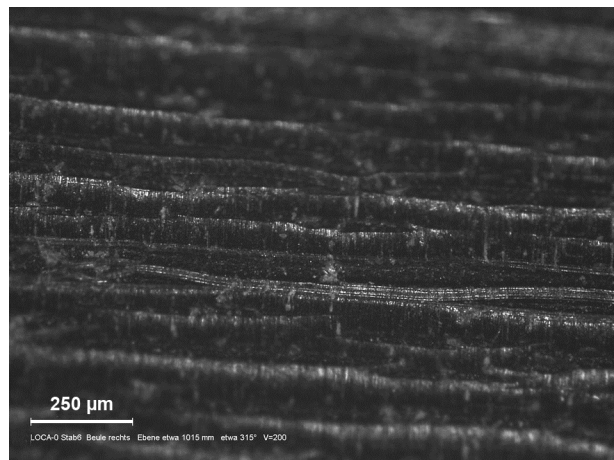
Elevation 1010 mm, angle 225°



Elevation 1010 mm, angle 325°

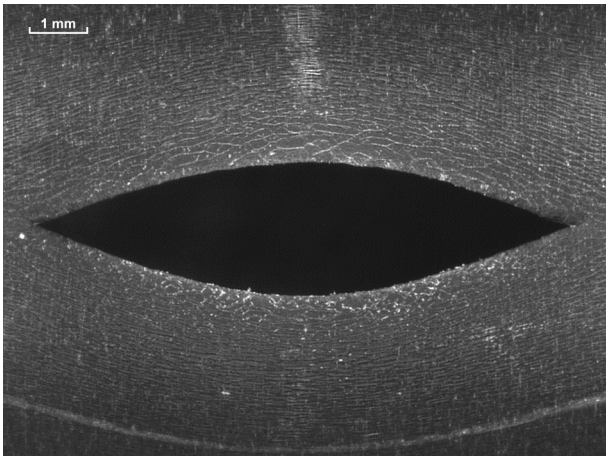


Elevation 985 mm, angle 315°

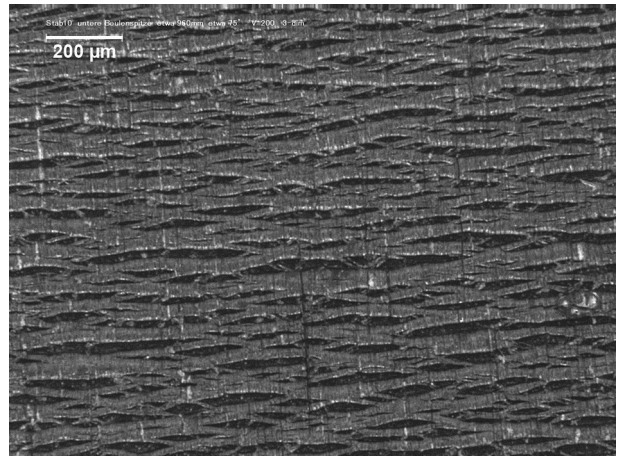


Elevation 1015 mm, angle 315°

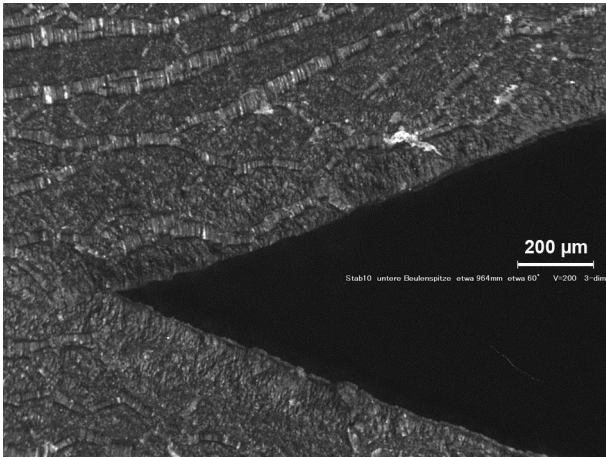
Fig. 84: QUENCH-L0; Overview of cladding surface structure near to burst position for rod No. 6.



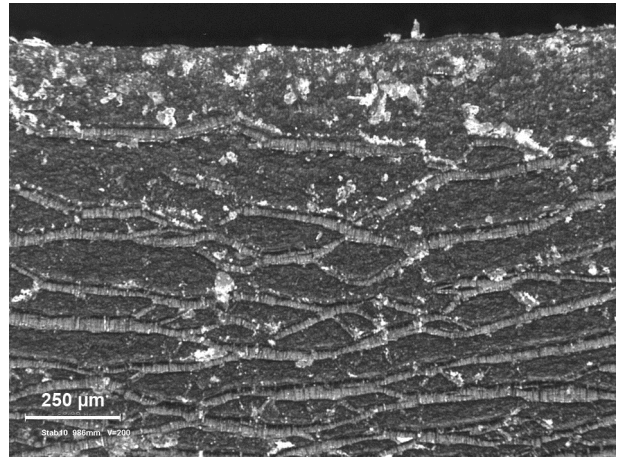
Elevation 968 mm, angle 60°



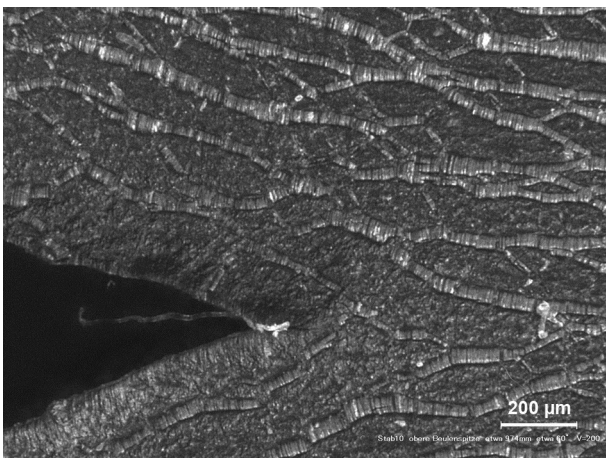
Elevation 960 mm, angle 75°



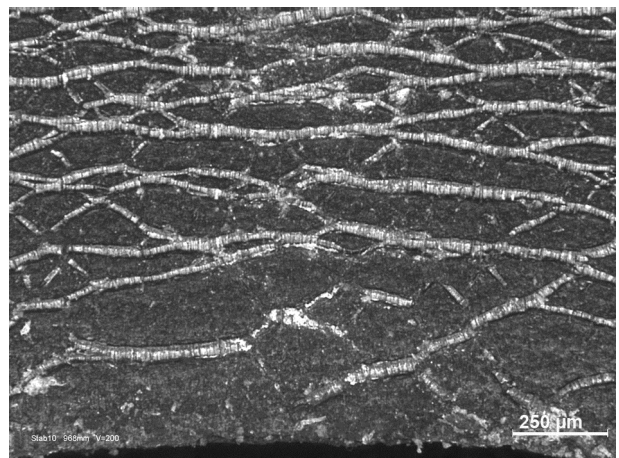
Elevation 964 mm, angle 60°



Elevation 968 mm, angle 40°



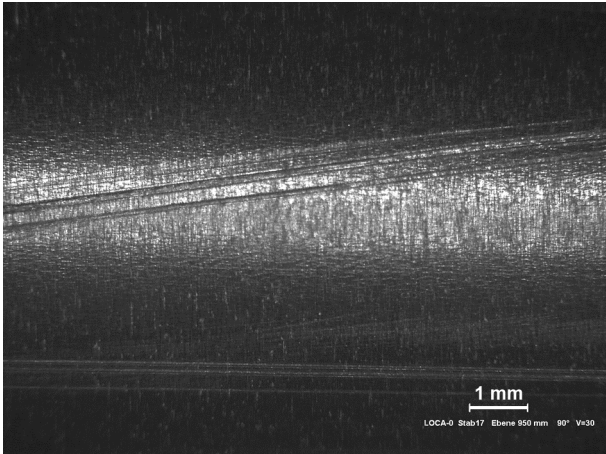
Elevation 974 mm, angle 60°



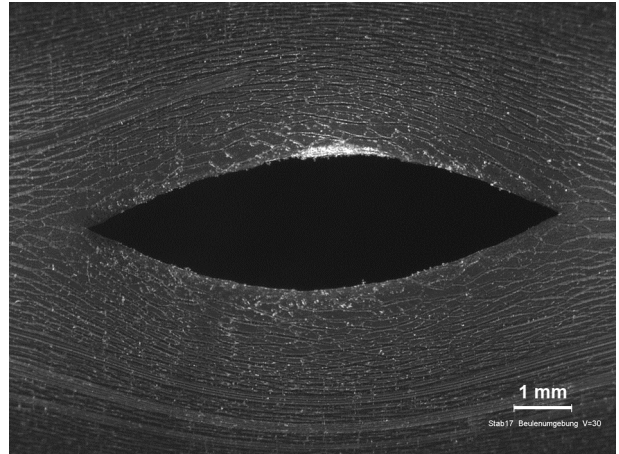
Elevation 968 mm, angle 80°

Fig. 85: QUENCH-L0; Overview of cladding surface structure near to burst position for rod No. 10.

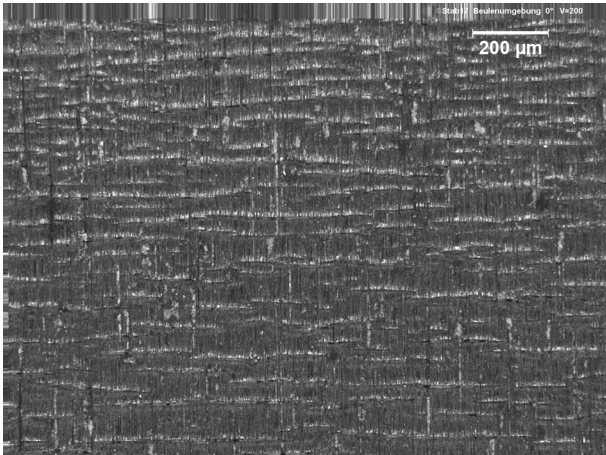




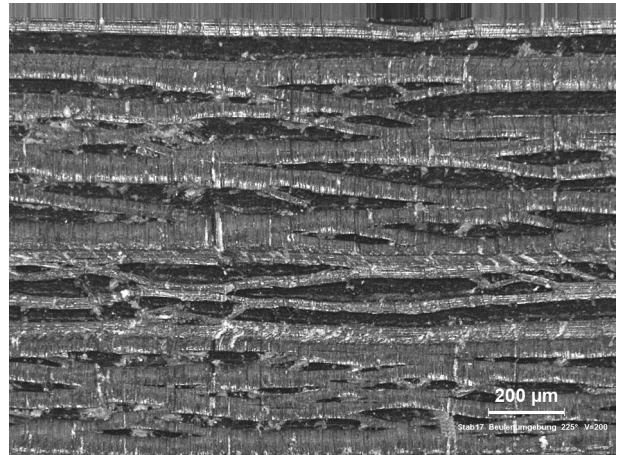
Burst position 950 mm, angle 90°



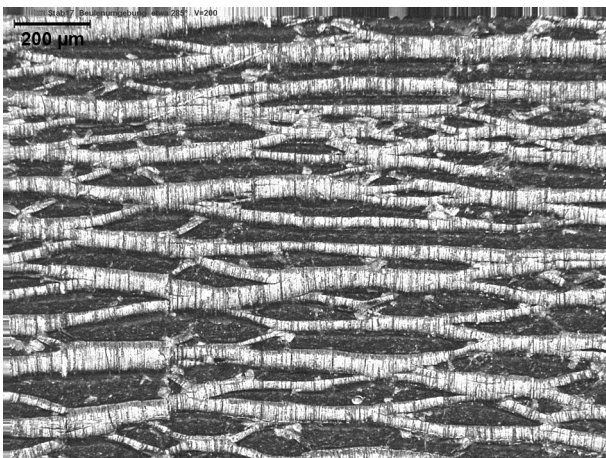
Burst position 951 mm, angle 270°



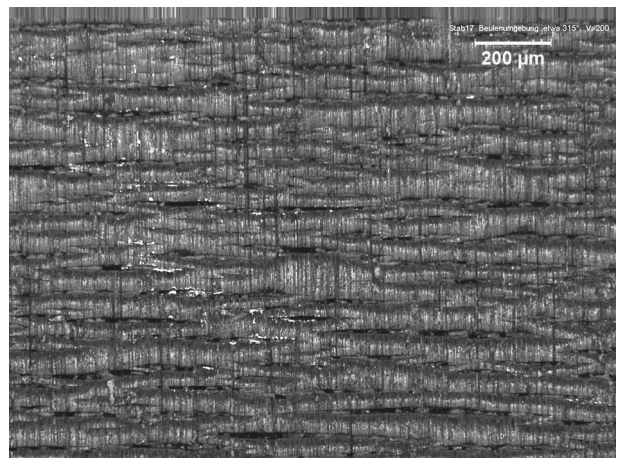
Burst position 951 mm, angle 0°



Burst position 951 mm, angle 225°

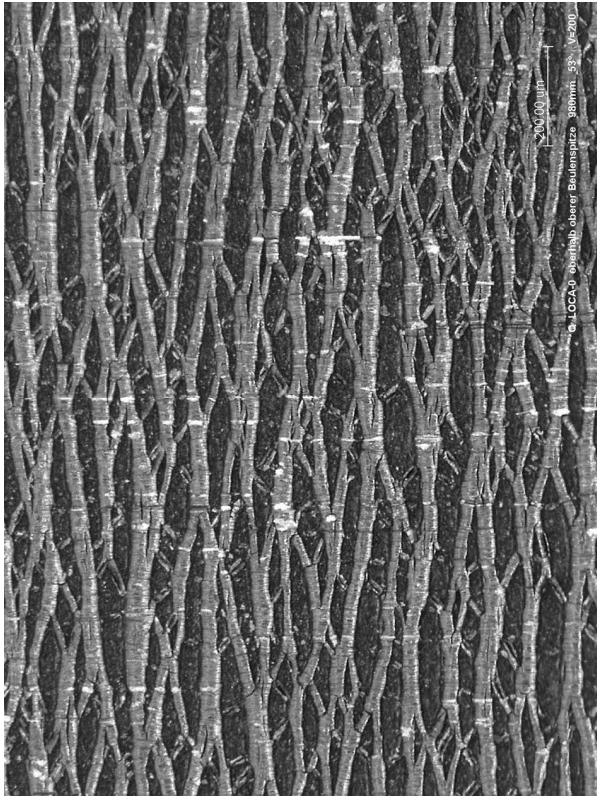


Burst position 951 mm, angle 285°

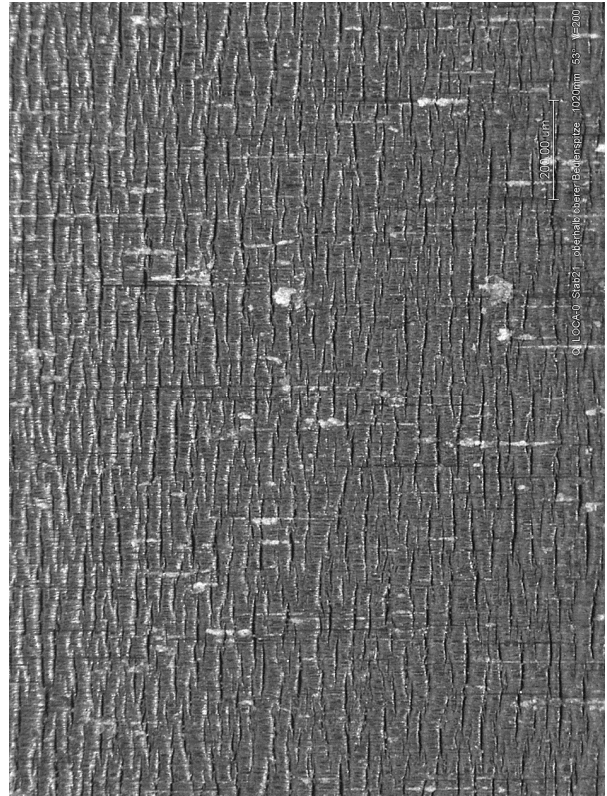


Burst position 951 mm, angle 315°

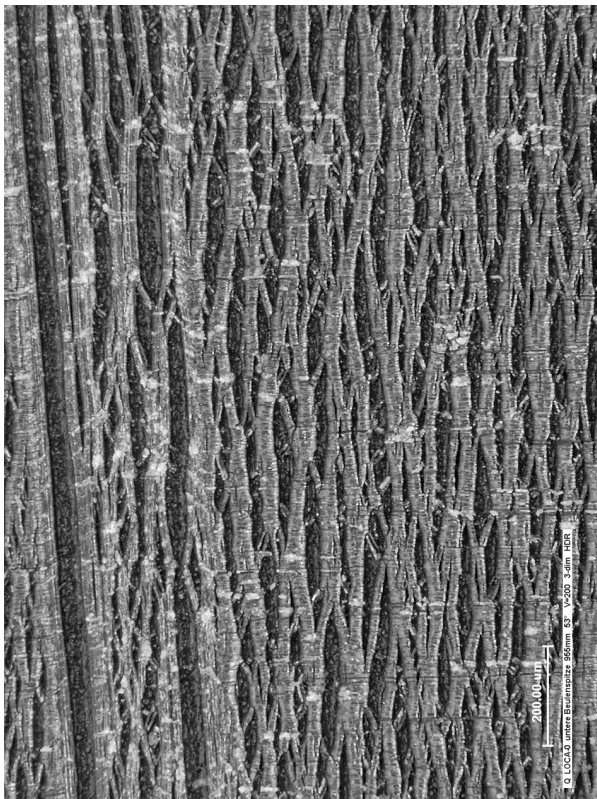
Fig. 86: QUENCH-L0; Overview of cladding surface structure near to burst position for rod No. 17.



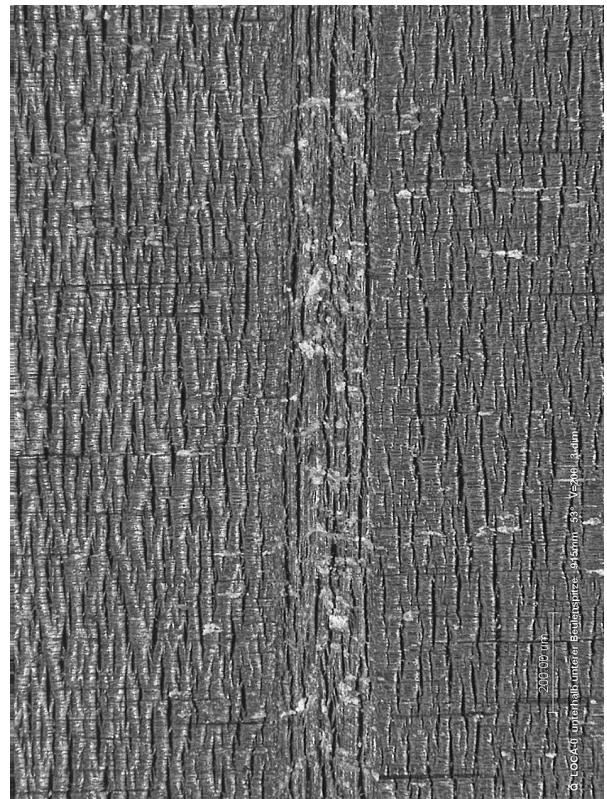
Elevation 985 mm (near to burst top)



Elevation 1025 mm



Elevation 955 mm (near to burst bottom)



Elevation 915 mm

Fig. 87: QUENCH-L0; Overview of cladding surface of rod #21 at burst azimuth of 41°.



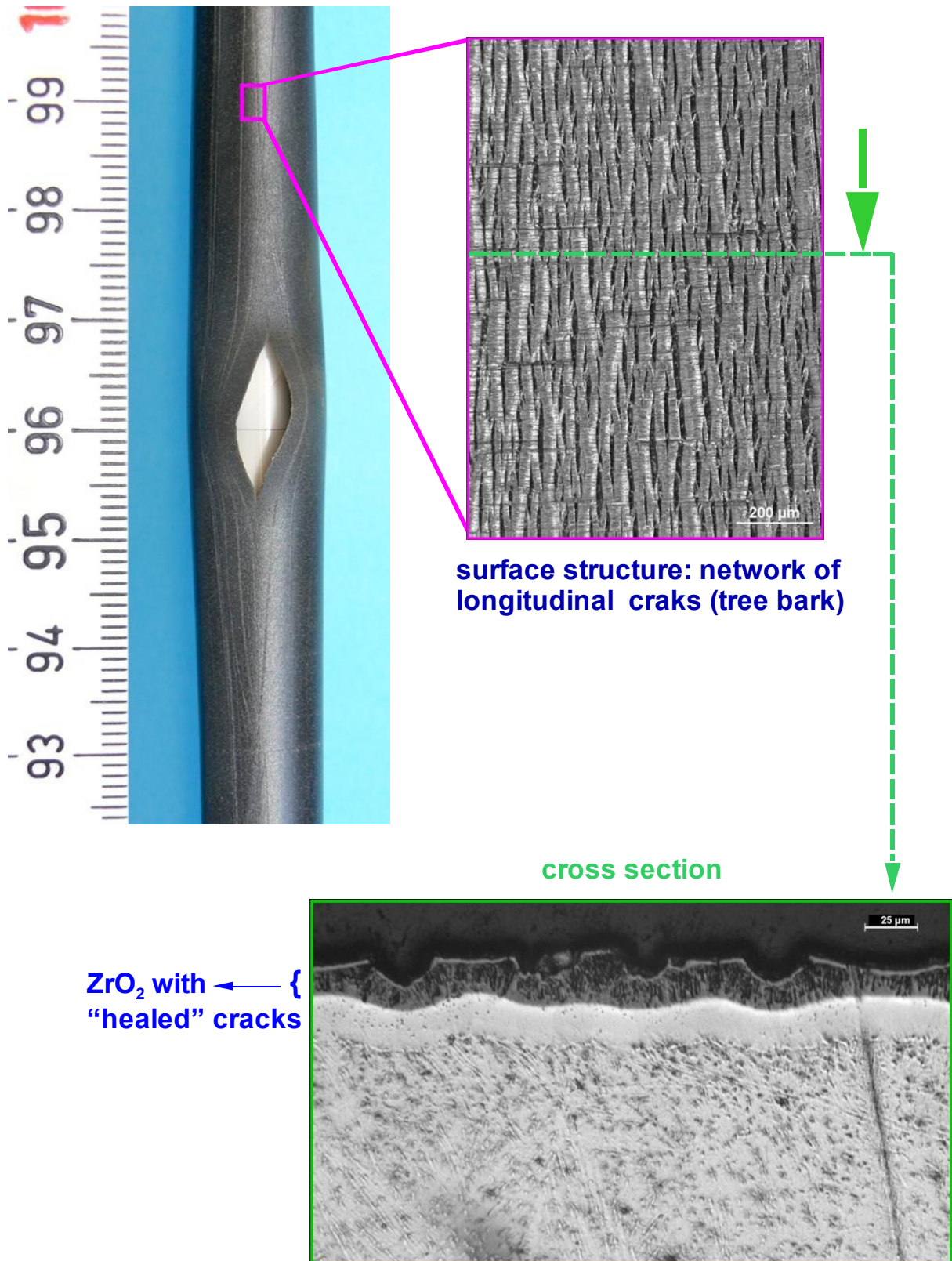


Fig. 88: QUENCH-L0; "Self-healing" surface cracks developed during ballooning rod #3 (55 bar), angle 140°.

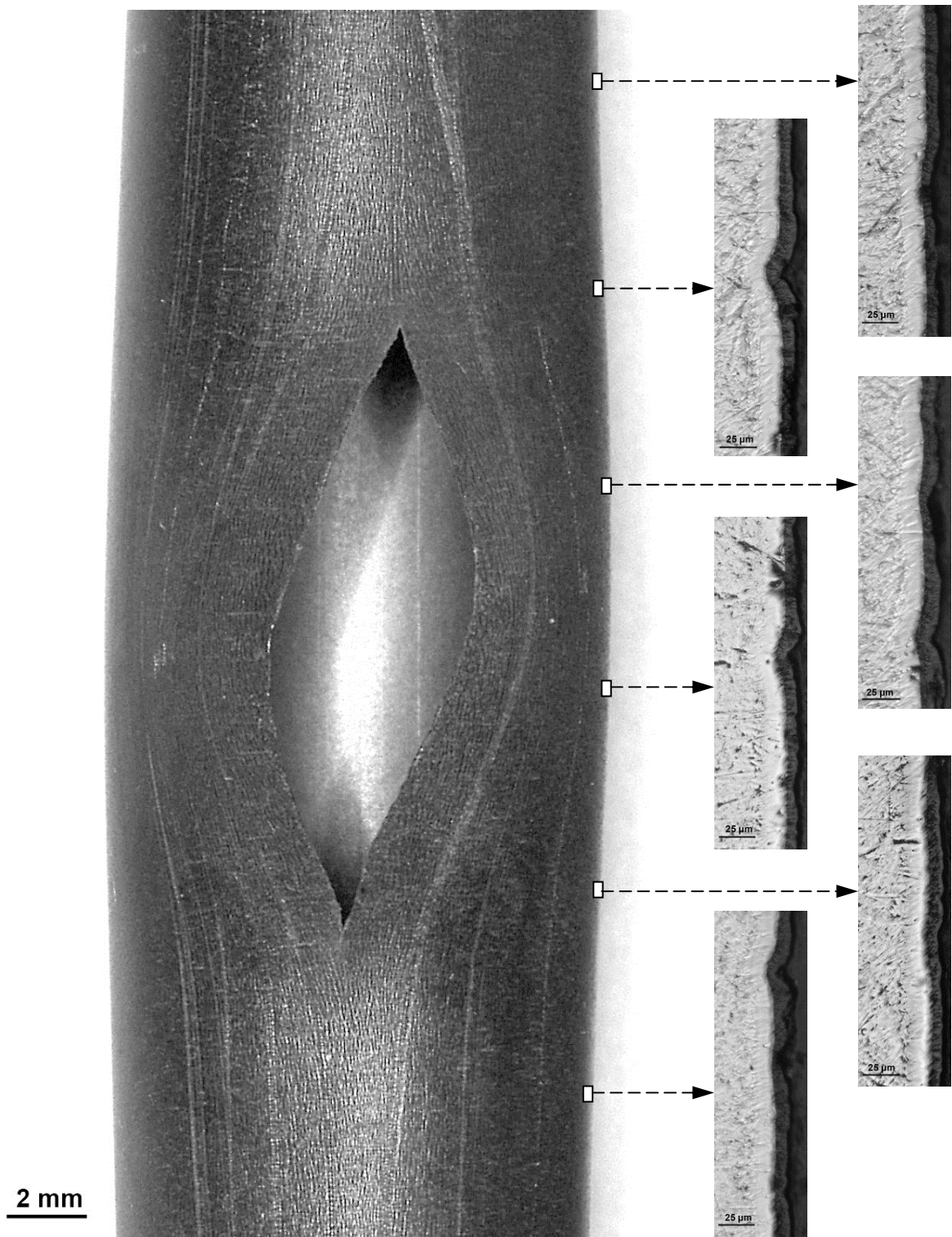


Fig. 89: QUENCH-L0; Longitudinal sections at outer surface of rod #3 at azimuth shifted with 90° to the burst position.

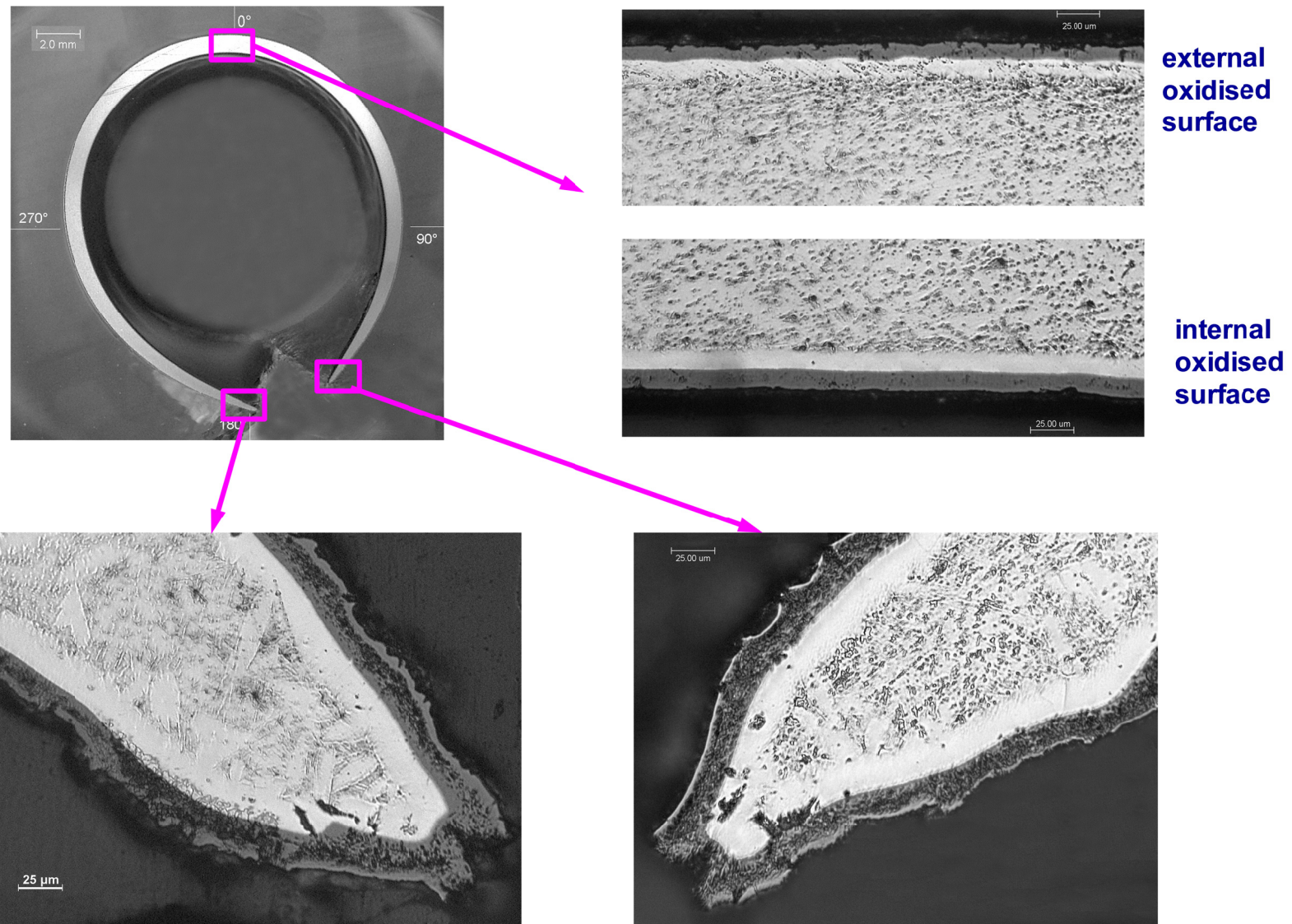


Fig. 90: QUENCH-L0; Similar internal and external oxidation degree at burst elevation rod #3 (55 bar).



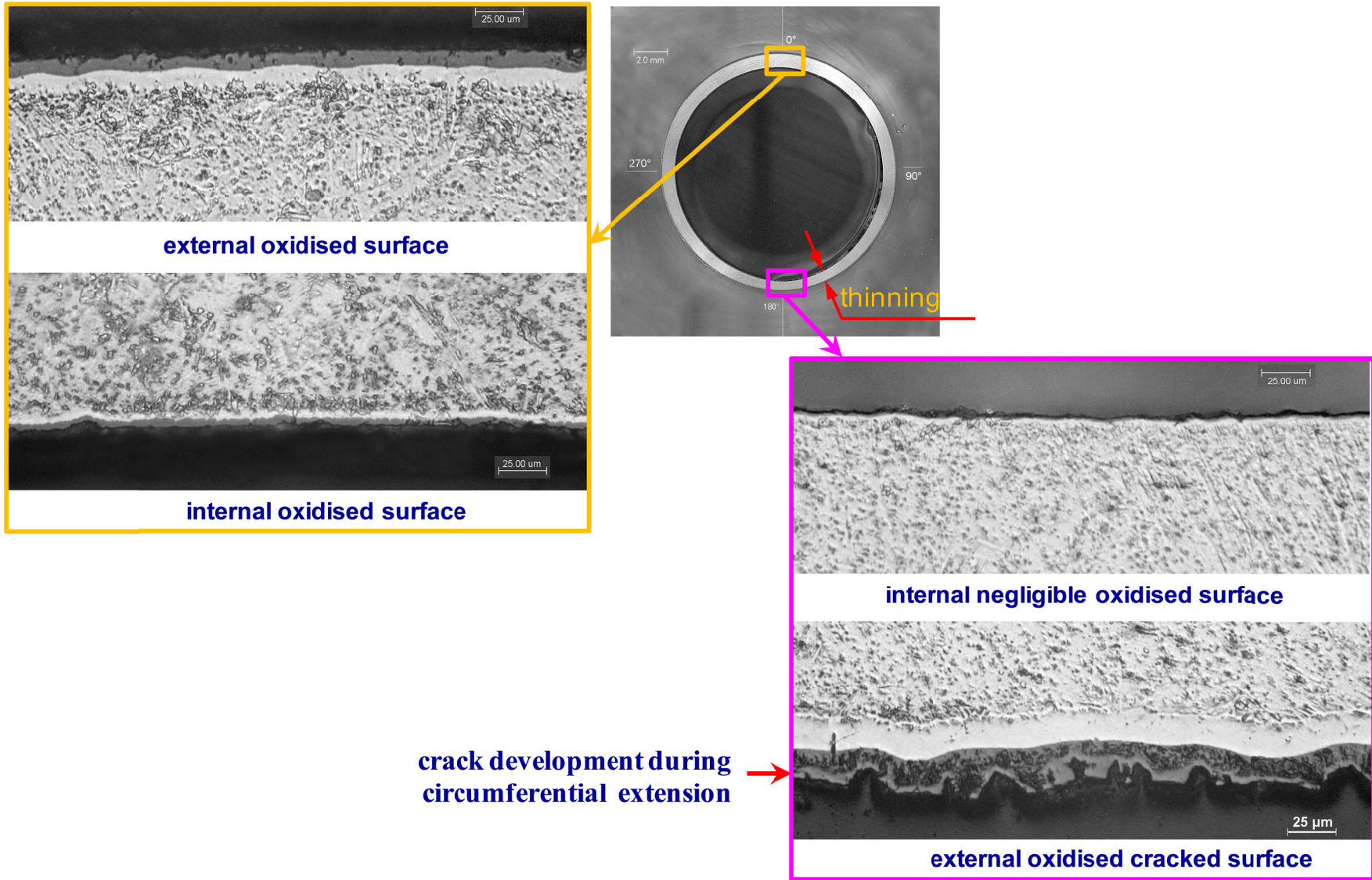


Fig. 91: QUENCH-L0; Different internal and external oxidation degree outside burst elevation rod #3 (55 bar).

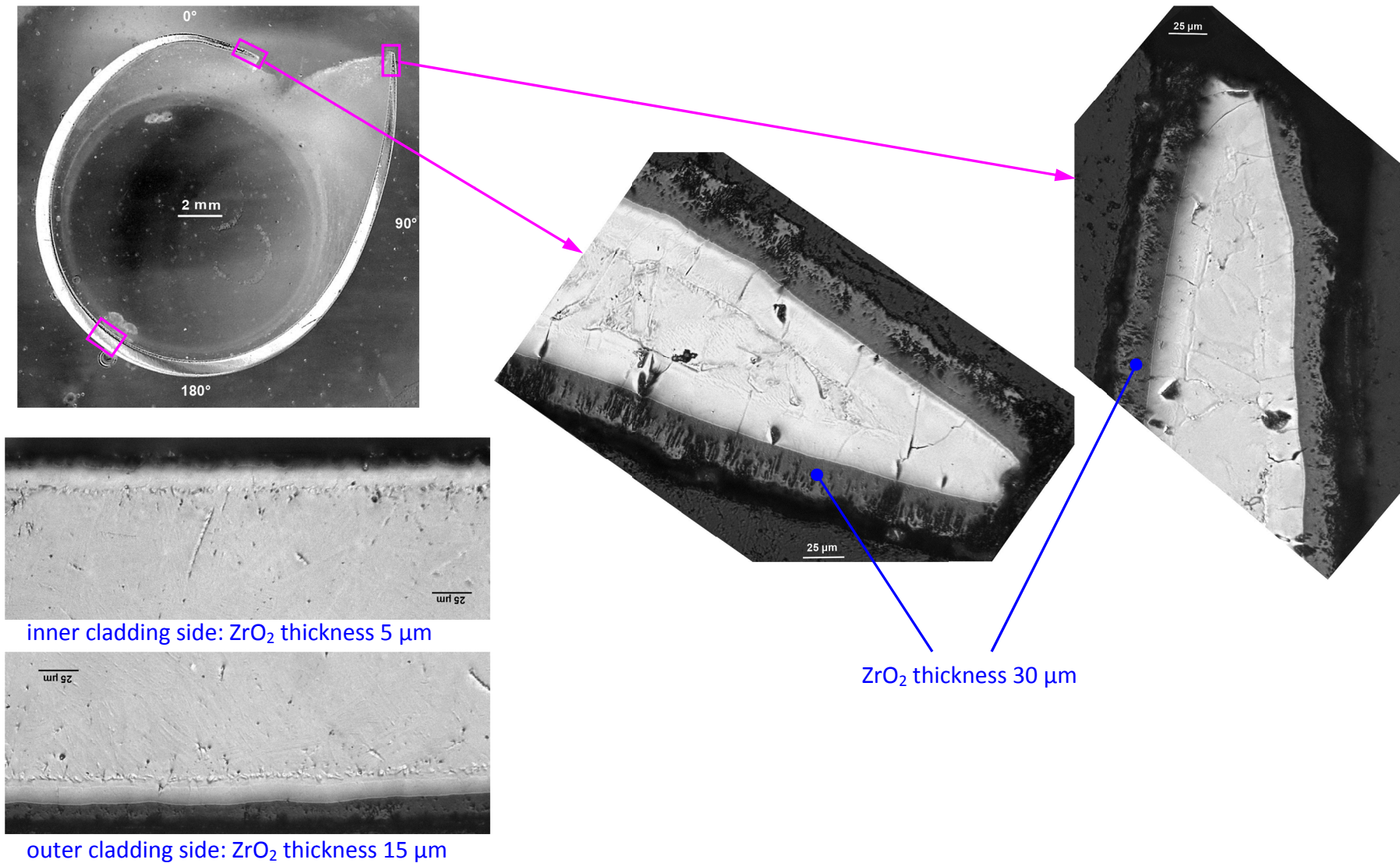


Fig. 92: QUENCH-L0; Top view of cross section of rod #8 at elevation 1004 mm. Very thin internal oxide layer at inner surface oppositely to burst opening.

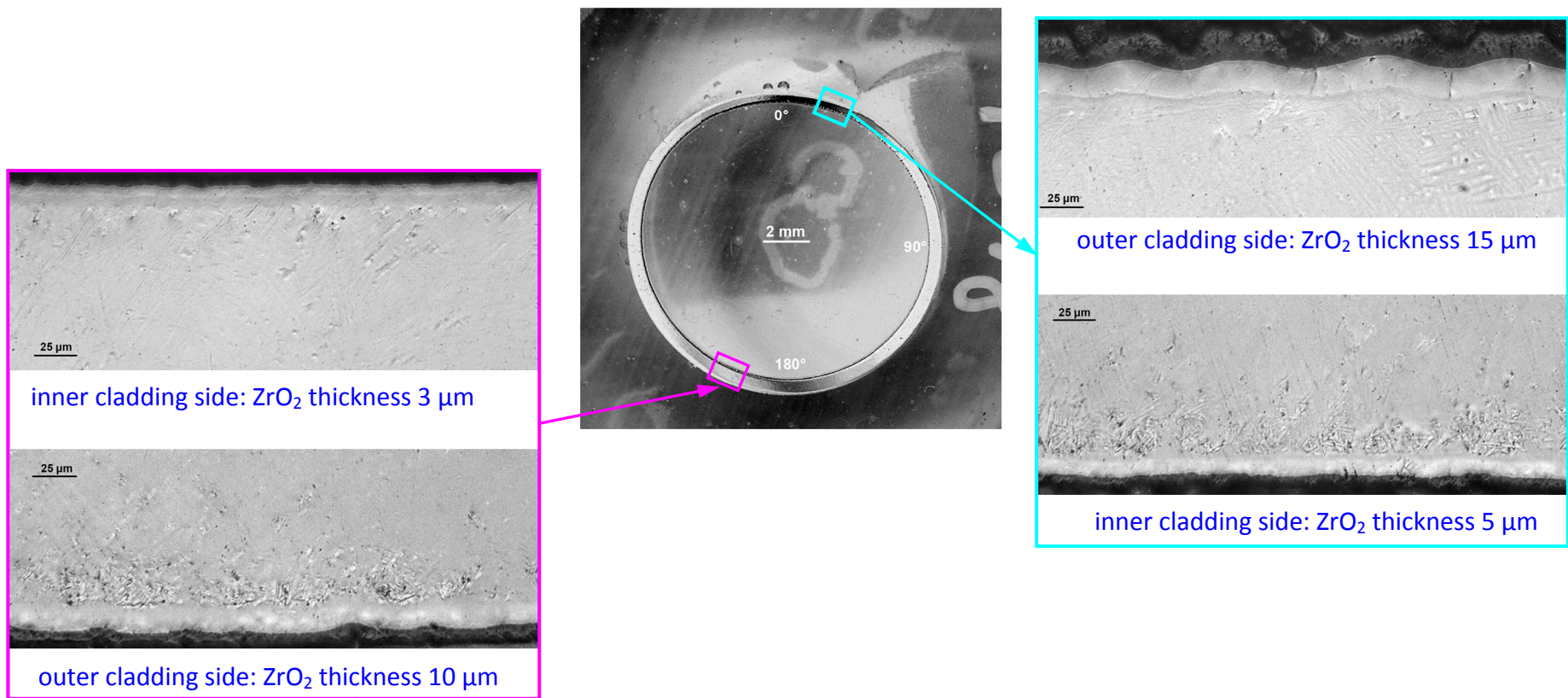
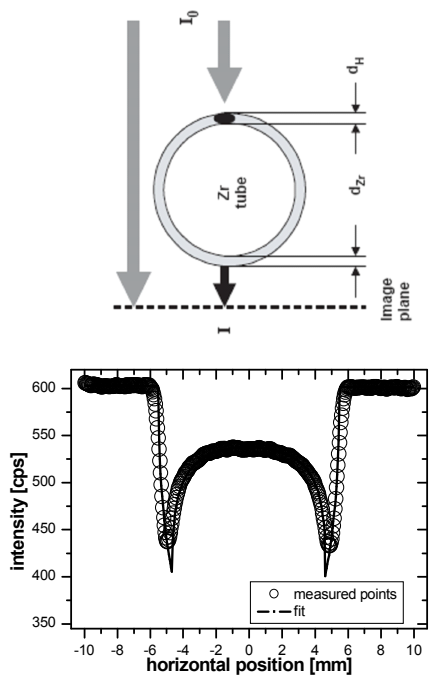


Fig. 93: QUENCH-L0; Top view of cross section of rod #8 at elevation 1018 mm. Very thin internal oxide layer at inner cladding surface.





Neutron transmission:

$$T(x, y) = \frac{I(x, y) - I_B(x, y)}{I_0(x, y) - I_B(x, y)}$$

Total macroscopic neutron cross section:

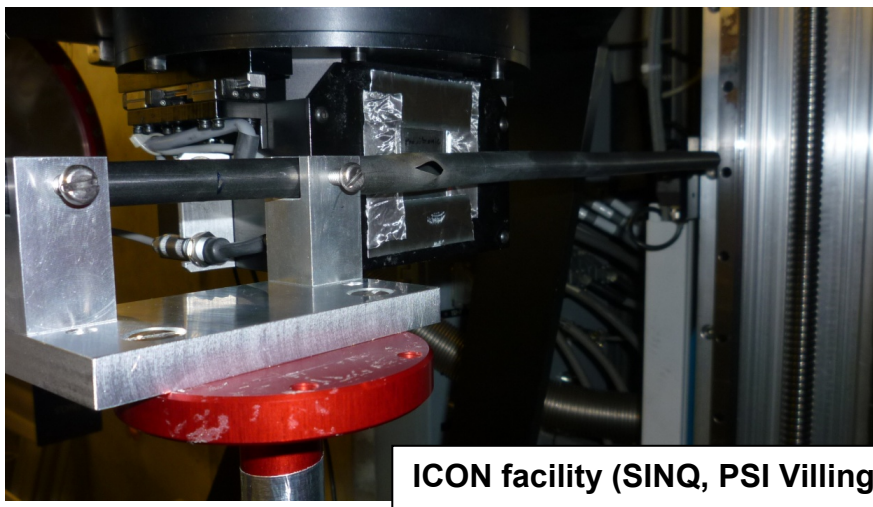
$$\Sigma_{total}(x, y) = \frac{-\ln(T(x, y))}{s(x, y)}$$

$$\Sigma_{total}(x, y) = \sum_i \sigma_i \cdot N_i =$$

$$\underbrace{N_{Zry}(x, y)}_{\Sigma_{sample \text{ as received}}} \sigma_{Zry} + N_O(x, y) \sigma_O + N_H(x, y) \sigma_H$$

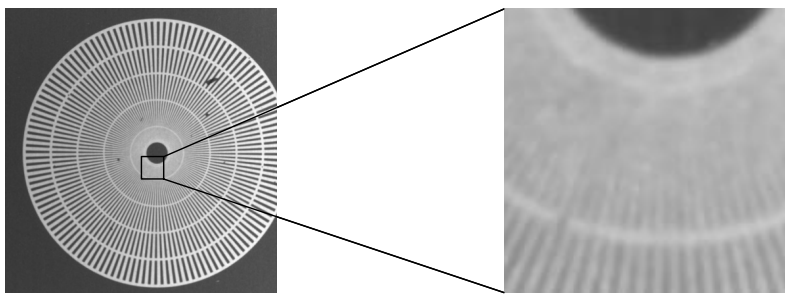
N : Number of density of the isotope  
 $\sigma$  : Microscopic neutron cross section

Fig. 94: QUENCH-L0; Neutron radiography method.



**ICON facility (SINQ, PSI Villingen, CH)**

13–16.08.2010 (radiography); 09–17.09.2010 (tomography)



Illumination time per image:  
 300 s (radiography) ;  
 625 x 90 s (tomography)

Spatial resolution: ~ 23  $\mu$ m

Fig. 95: QUENCH-L0; ICON facility for neutron radiography.

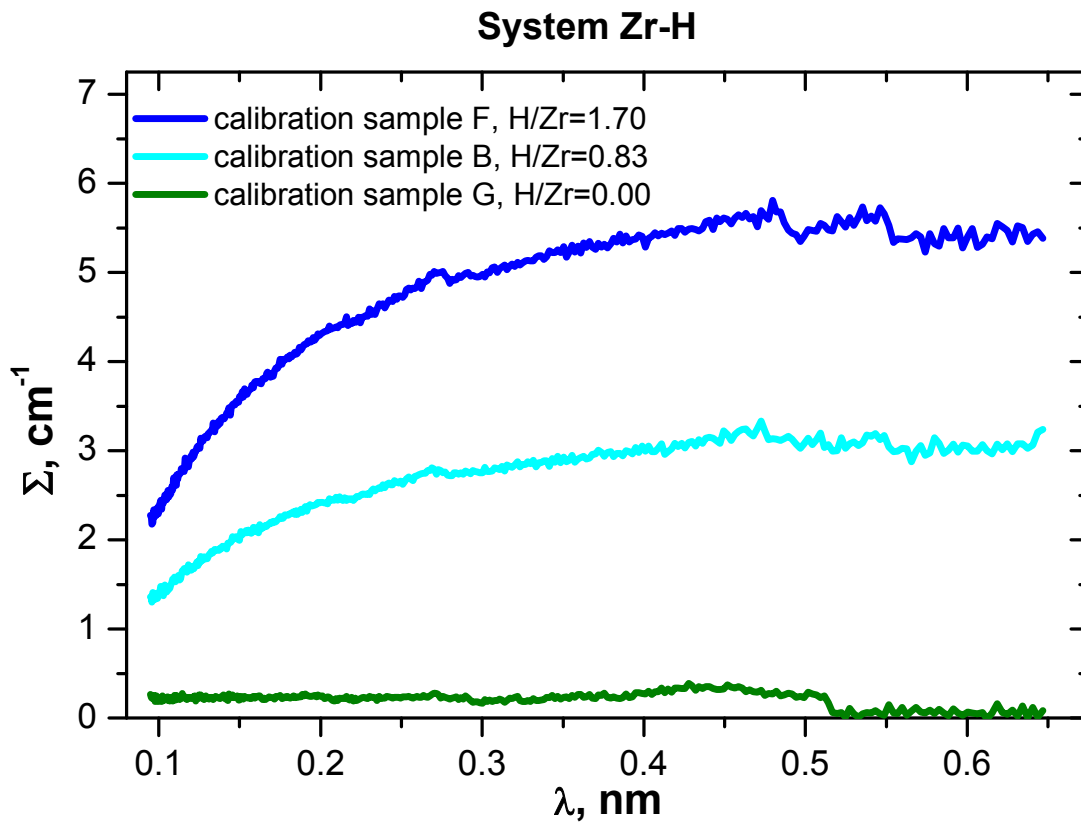


Fig. 96: QUENCH-L0; Neutron radiography, calibration specimens.

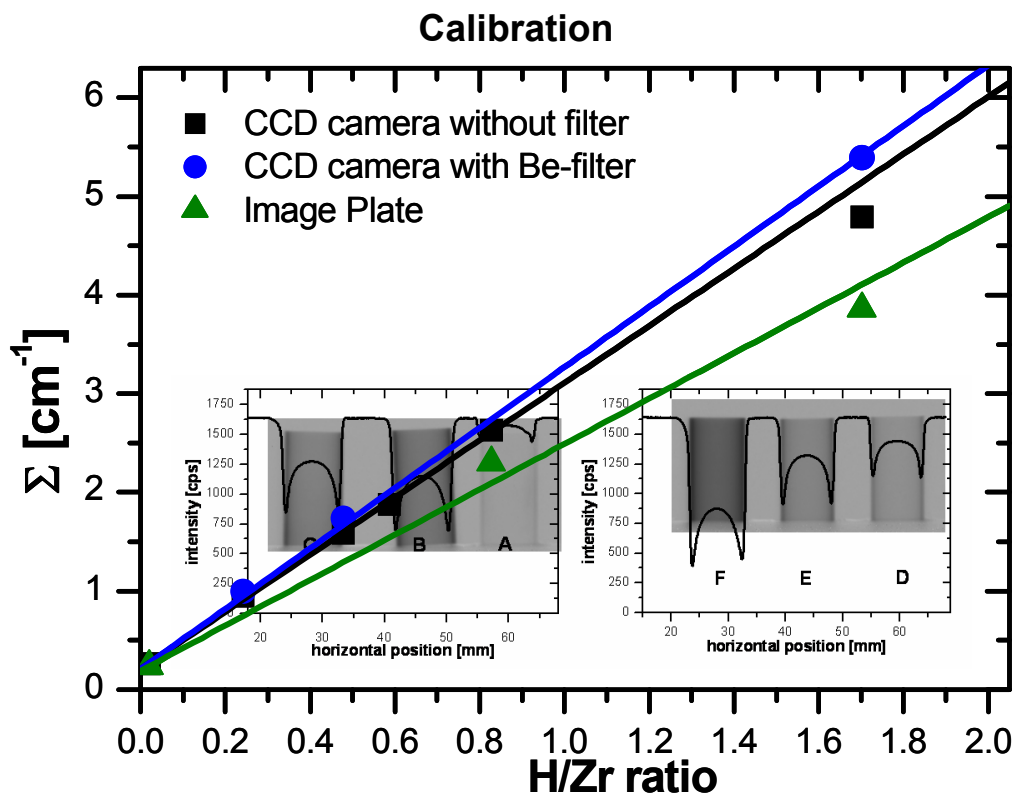
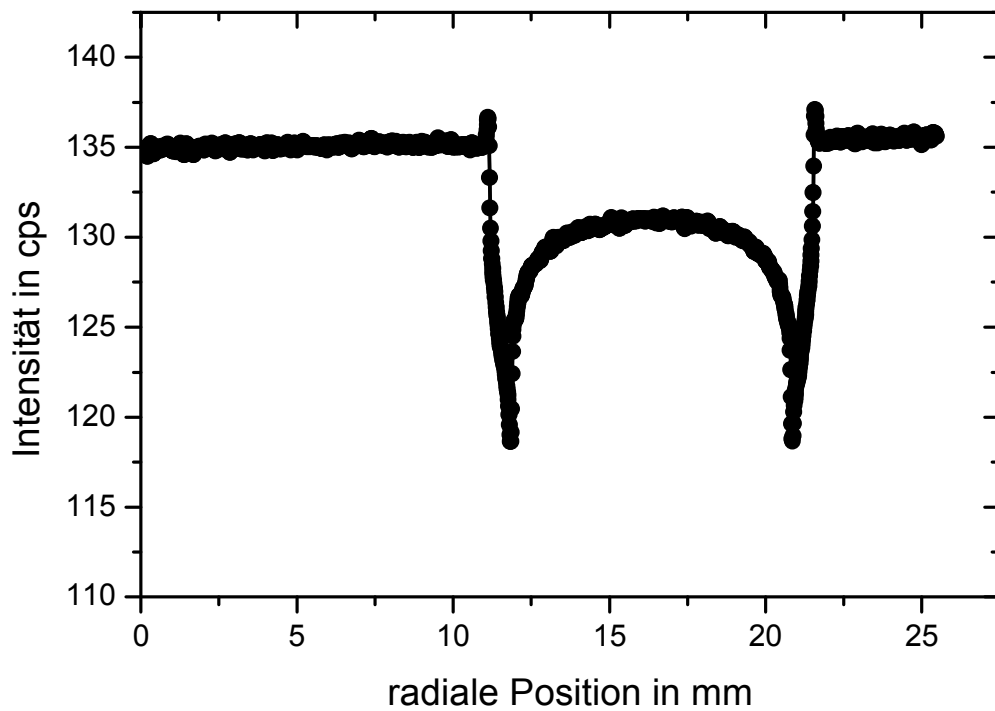
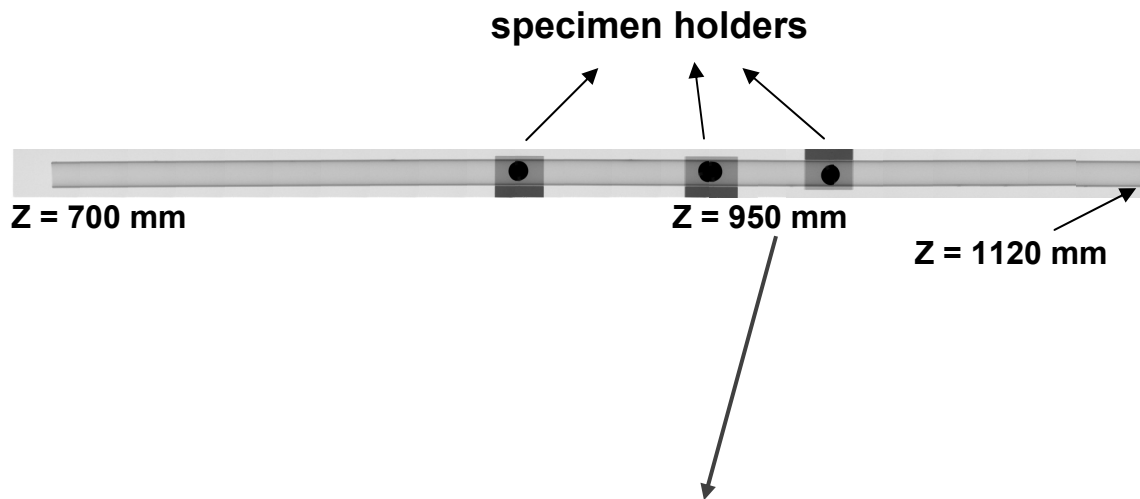


Fig. 97: QUENCH-L0; Neutron radiography, calibration procedure.



Total neutron cross section  $\Sigma = 0.215 \text{ cm}^{-1}$   
 is measured in the range for not oxidized Zry-4  
 (  $\Sigma = 0.197 \dots 0.216$  ).

Fig. 98: QUENCH-L0; Radiography, rod #15 ( $p_i = 3 \text{ bar}$ ).

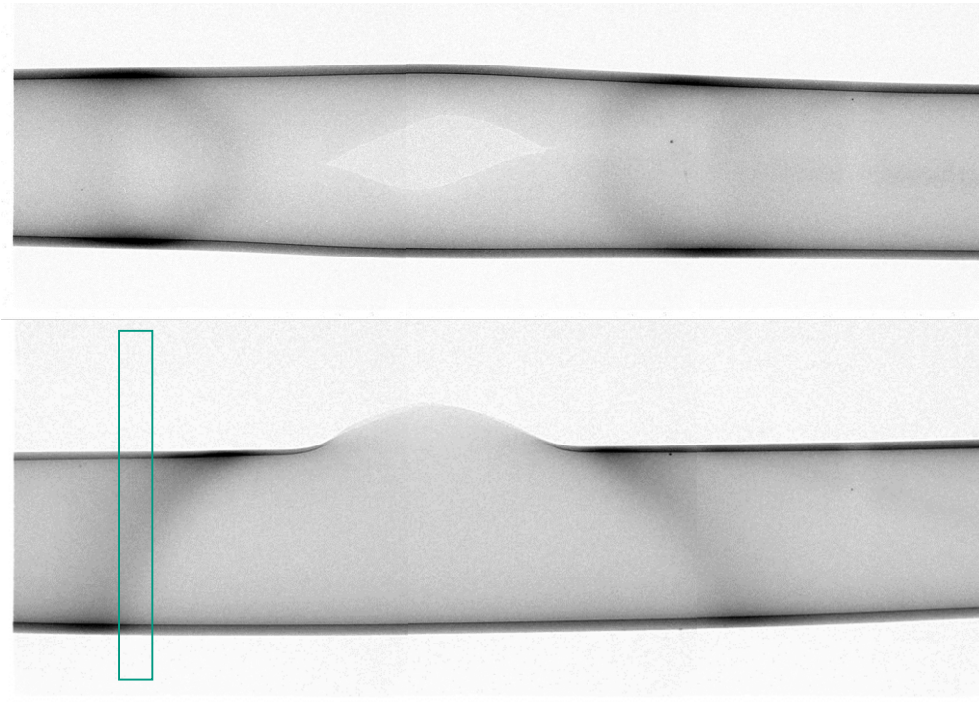


Fig. 99: QUENCH-L0; Radiography, rod #3 (initial pressure  $p_i = 55$  bar, time between burst and quench  $\Delta t_q = 104$  s).

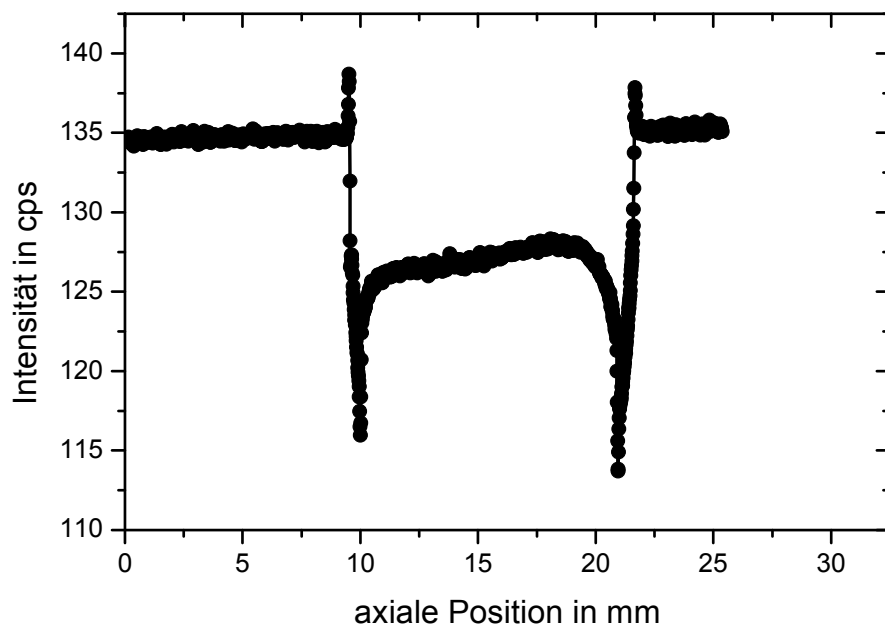


Fig. 100: QUENCH-L0; Neutron radiography for rod #3: intensity distribution.

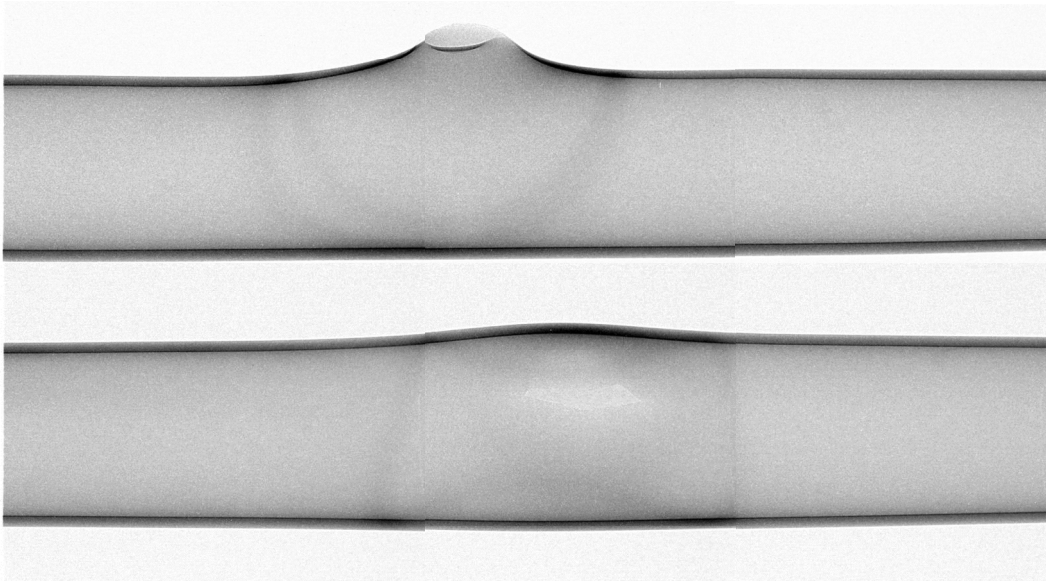


Fig. 101: QUENCH-L0; Radiography, rod #6 (initial pressure  $p_i = 35$  bar, time between burst and quench  $\Delta t_q = 93$  s).

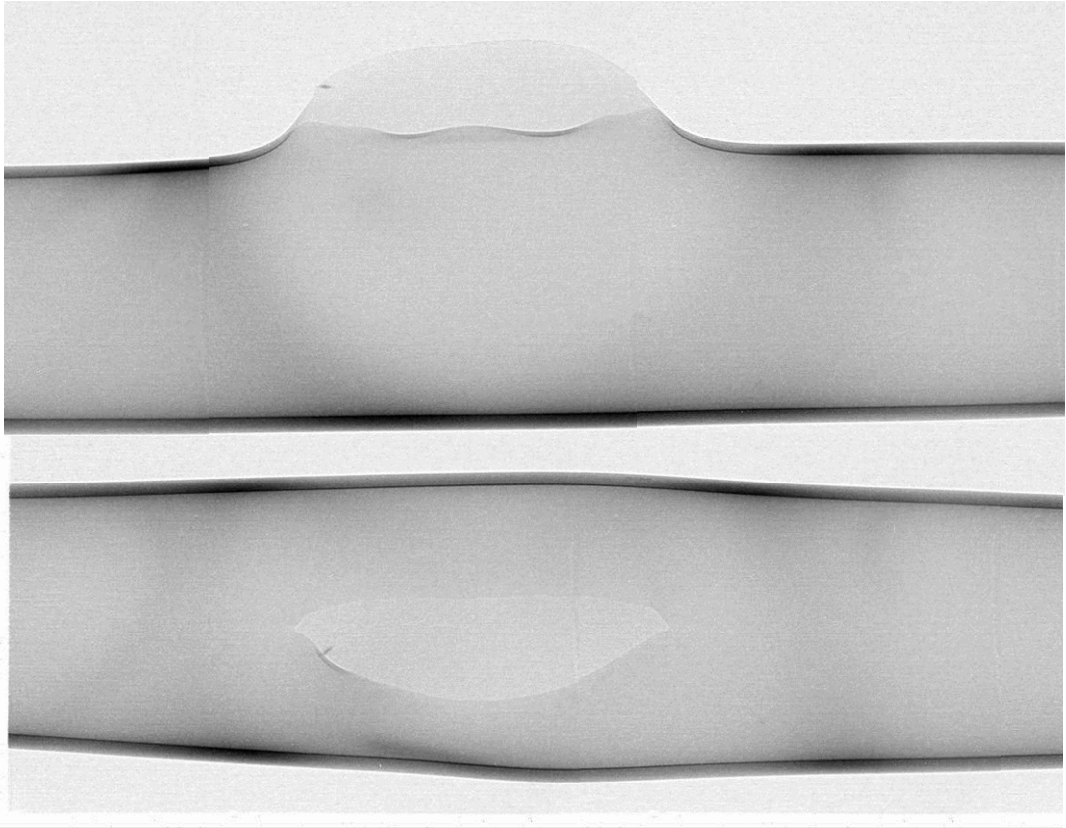


Fig. 102: QUENCH-L0; Radiography, rod #8 (initial pressure  $p_i = 50$  bar, time between burst and quench  $\Delta t_q = 101$  s).

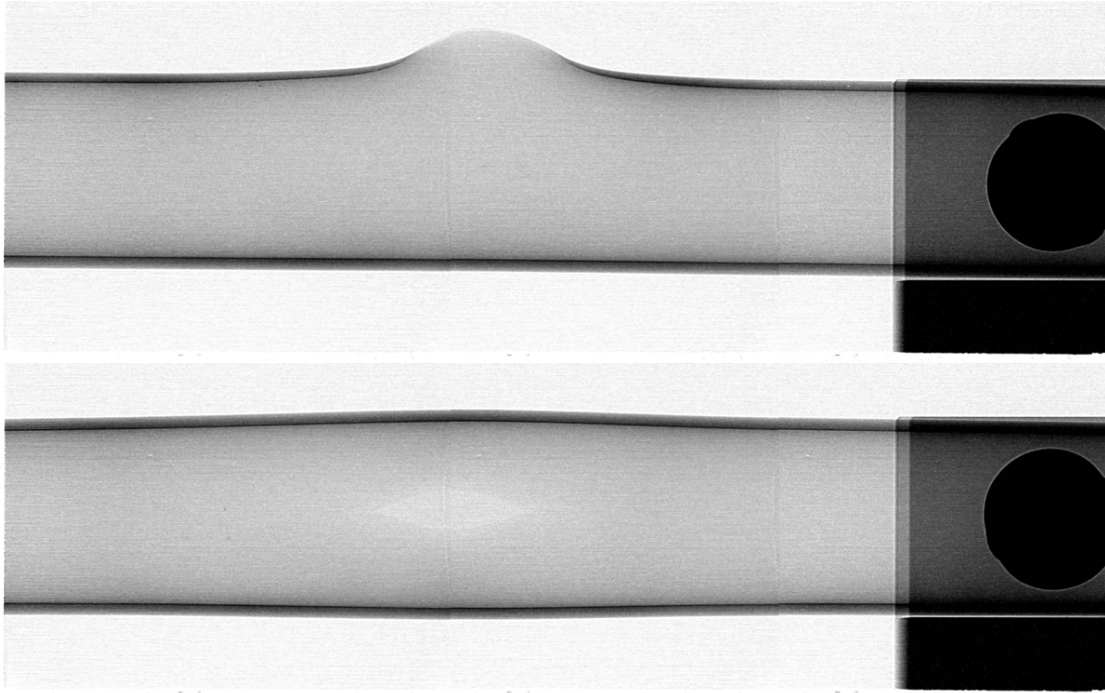


Fig. 103: QUENCH-L0; Radiography, rod #10 (initial pressure  $p_i = 50$  bar, time between burst and quench  $\Delta t_q = 49$  s).

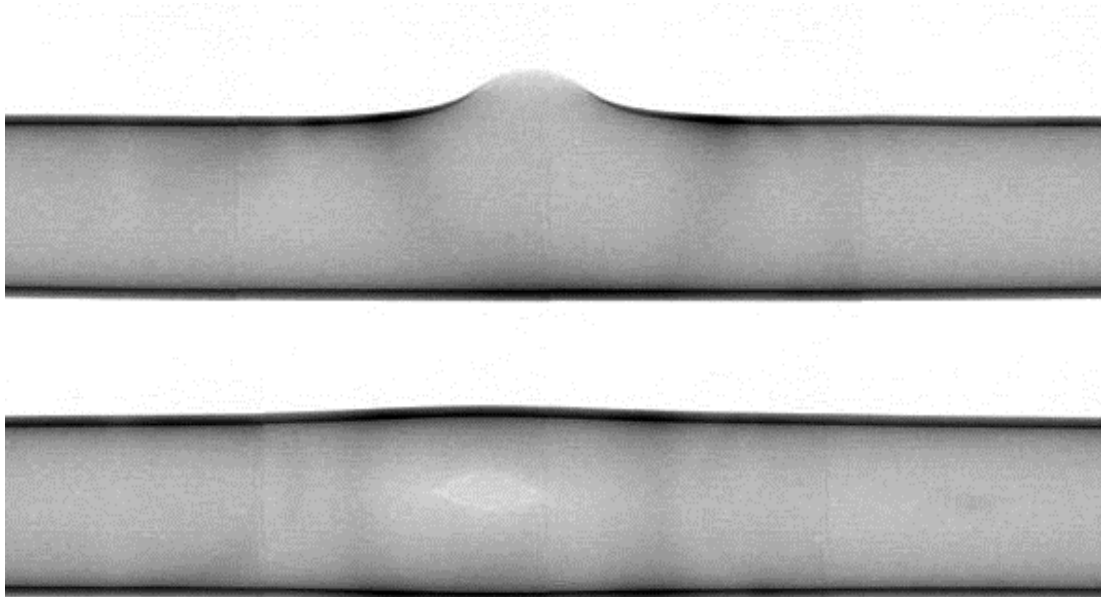
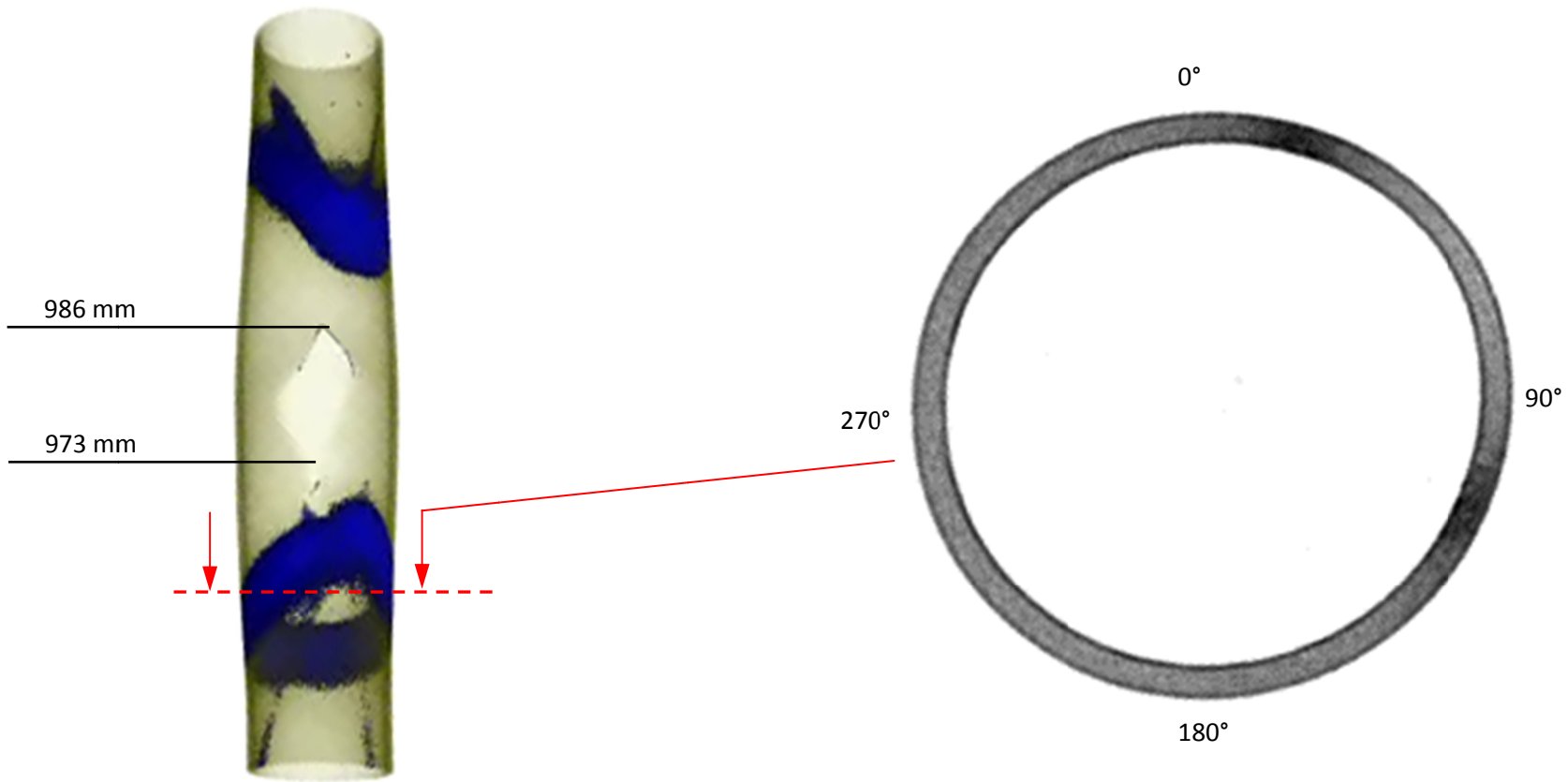


Fig. 104: QUENCH-L0; Radiography, rod #17 (initial pressure  $p_i = 40$  bar, time between burst and quench  $\Delta t_q = 71$  s).

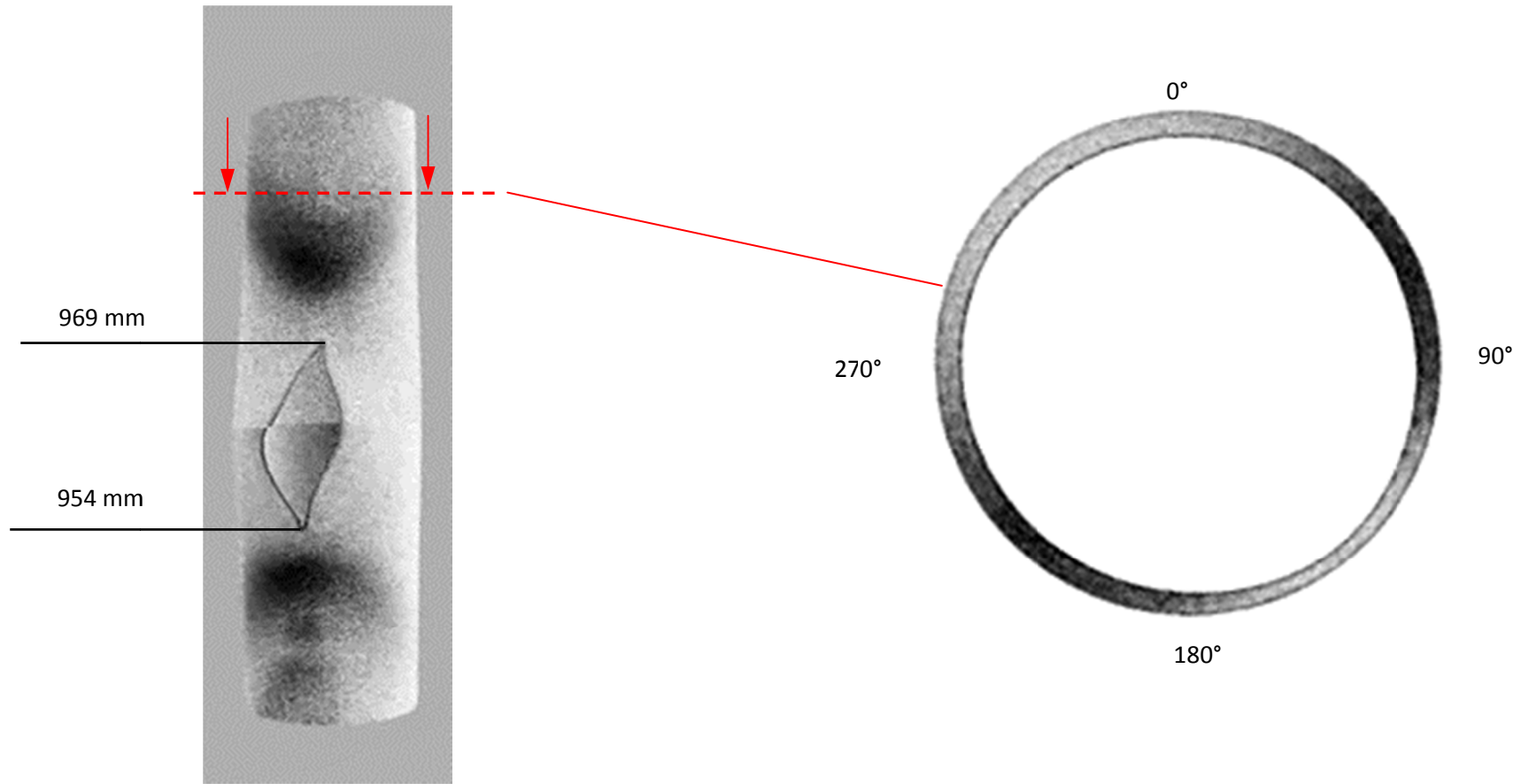


Cladding part with hydrogen bands (blue). Hydrogen concentration in bands about 2560 wppm.

Cross section of tomography image at 960 mm: black segments evidence high hydrogen concentration

Fig. 105: QUENCH-L0; Neutron tomography of rod #1.



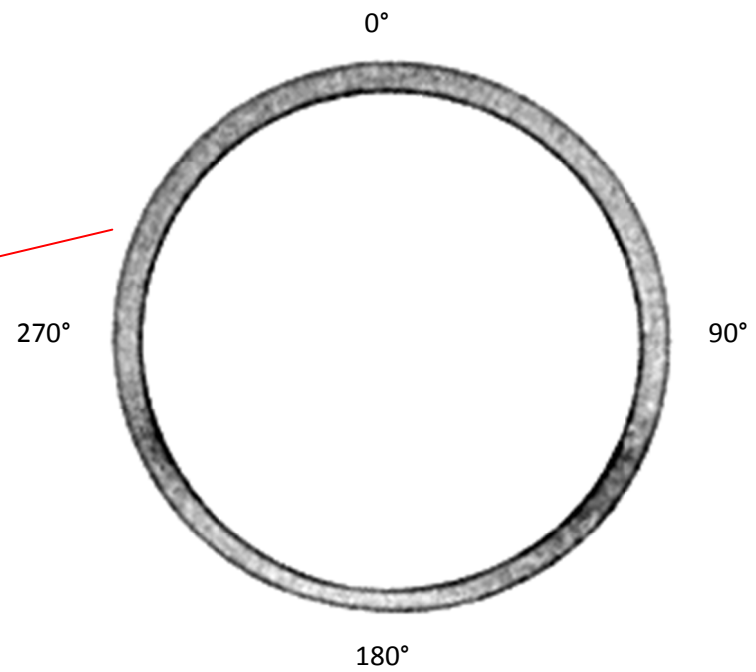
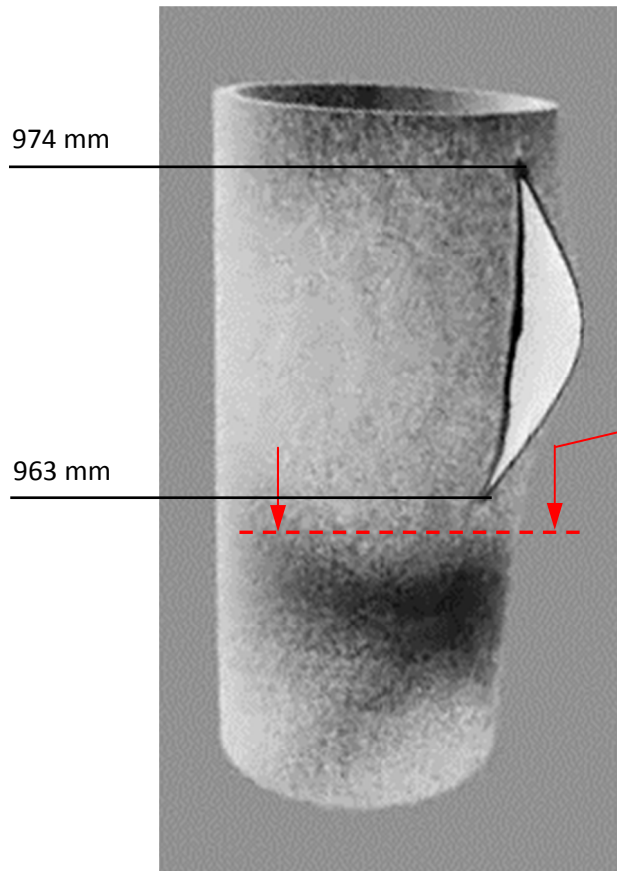


Cladding part with hydrogen bands (black). Hydrogen concentration in bands about 2140 wppm.

Cross section of tomography image at 980 mm: black segments evidence high hydrogen concentration

Fig. 106: QUENCH-L0; Neutron tomography of rod #3.





Cladding part with hydrogen bands (black). Hydrogen concentration in bands about 1060 wppm.

Cross section of tomography image at 960 mm: black segments evidence high hydrogen concentration

Fig. 107: QUENCH-L0; Neutron tomography of rod #5.

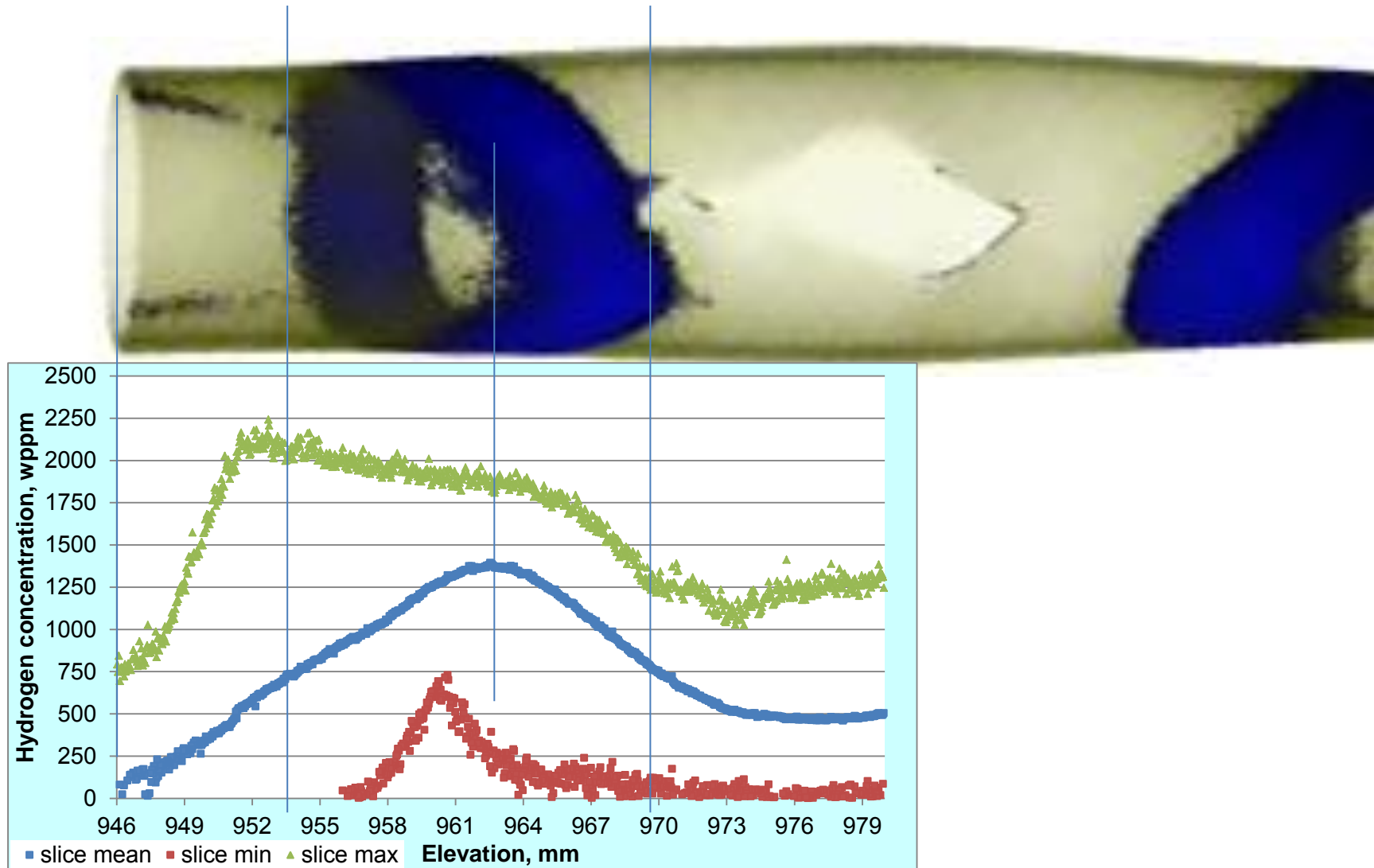


Fig. 108: QUENCH-L0; correspondence between reconstruction of tomography image and plots of mean, minimal, and maximal (for each axial slice of cladding) values of hydrogen concentrations in rod #1.

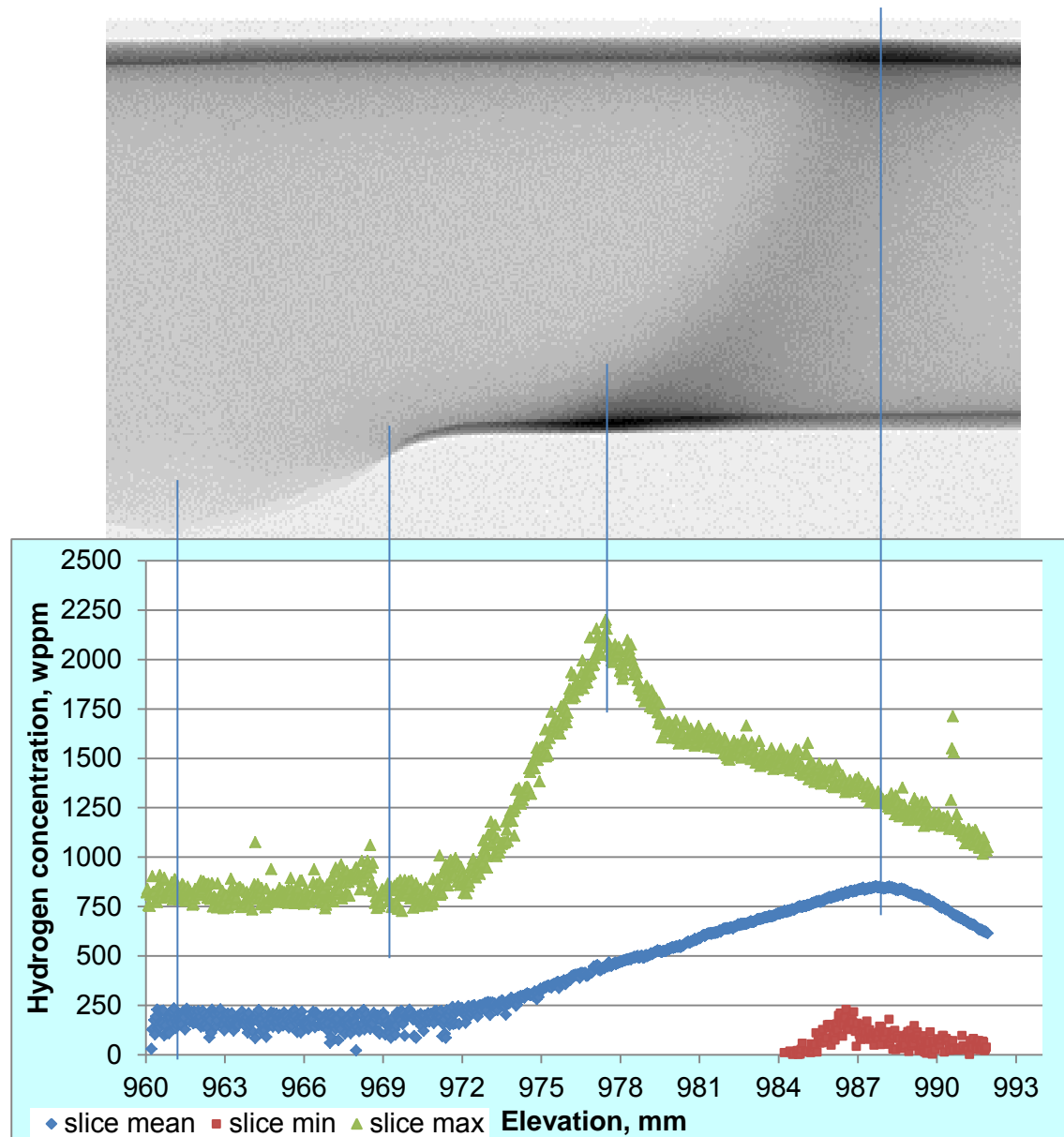


Fig. 109: QUENCH-L0; correspondence between radiography image and plots of mean, minimal, and maximal values of hydrogen concentrations in rod #3.

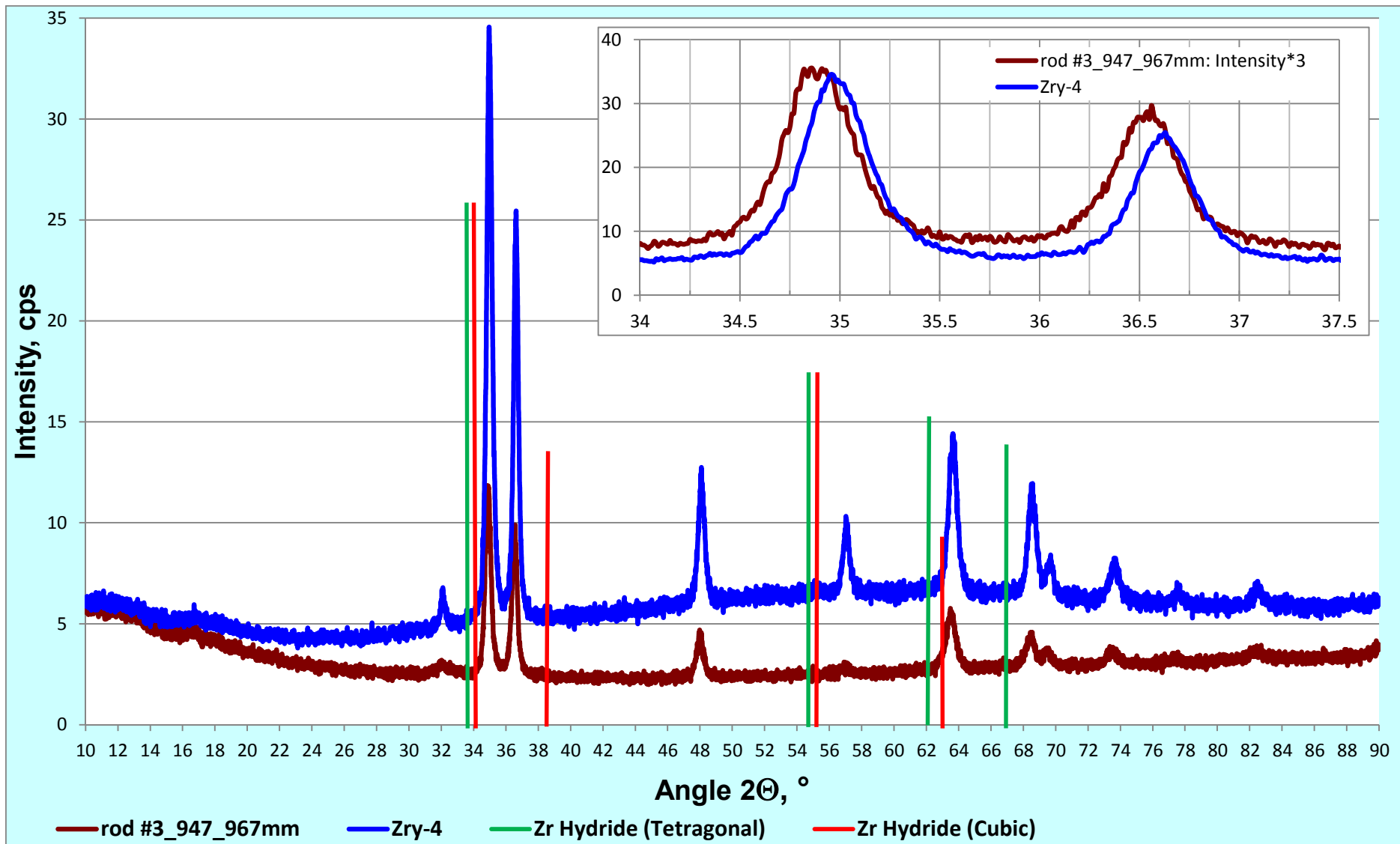


Fig. 110: QUENCH-L0; Results of X-ray diffractometry for the rod #3 at the hydrogen band.

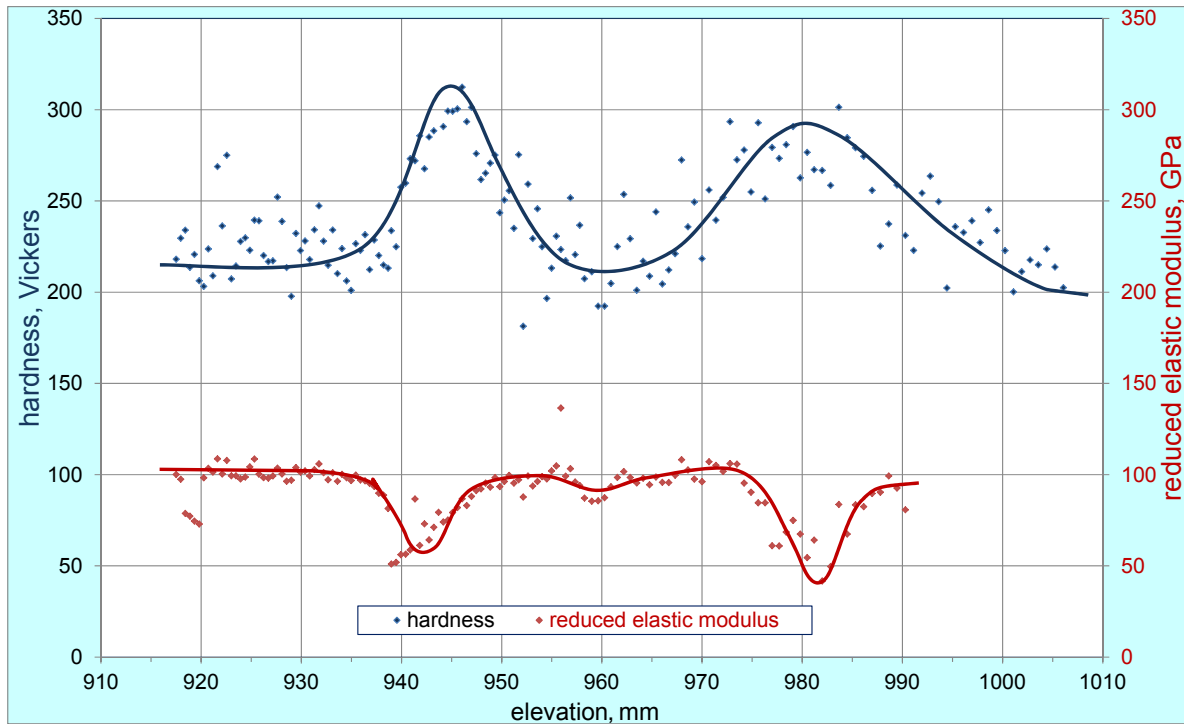


Fig. 111: QUENCH-L0; Microhardness and reduced elastic modulus of rod #3 at 225°.

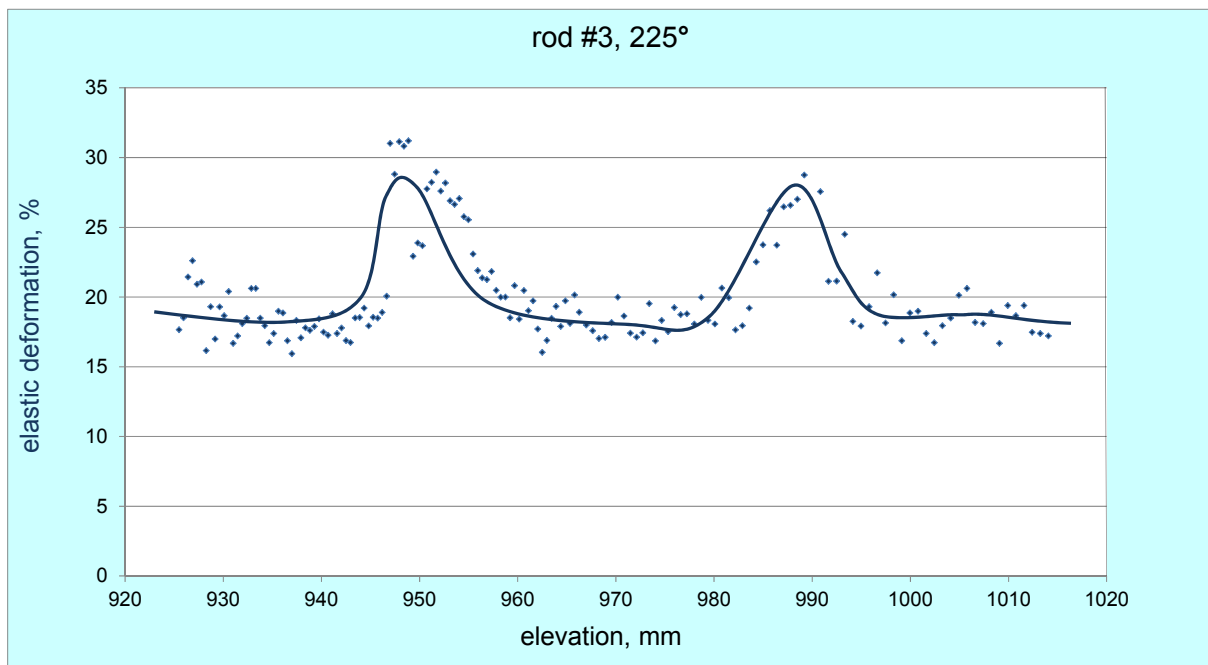


Fig. 112: QUENCH-L0; Elastic deformation obtained during microhardness testing. Rod #3 at 225°.

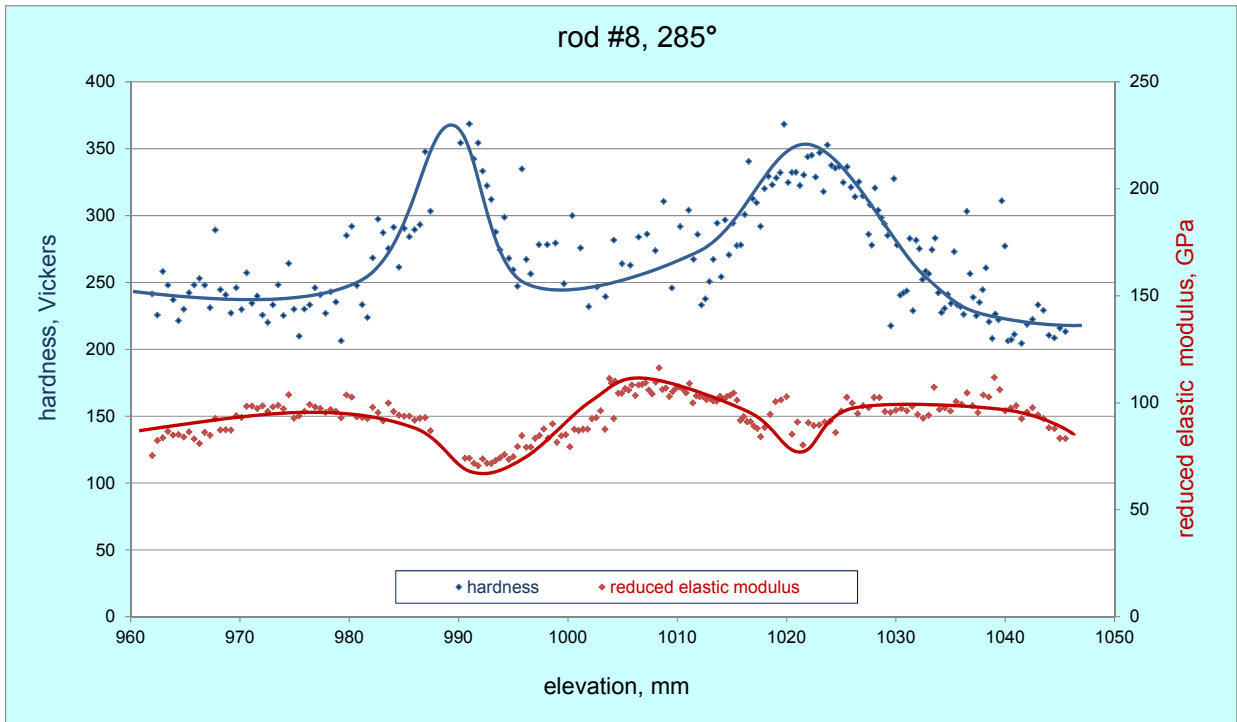


Fig. 113: QUENCH-L0; Microhardness and reduced elastic modulus of rod #8 at 285°.

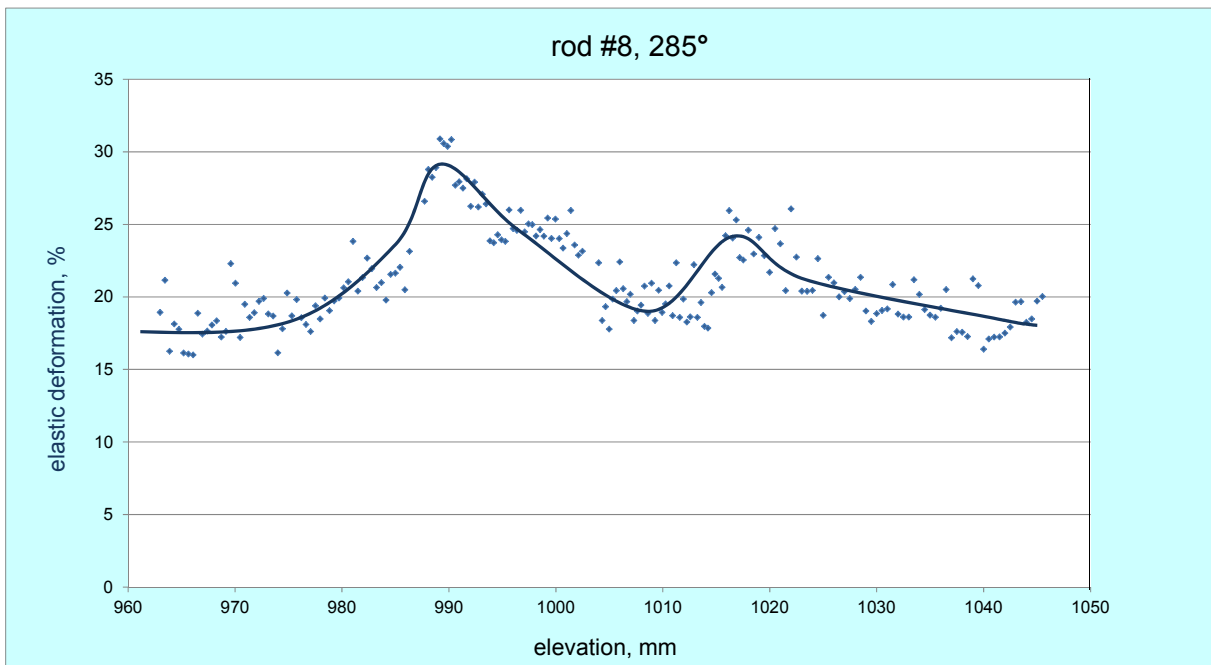


Fig. 114: QUENCH-L0; Elastic deformation obtained during microhardness testing. Rod #8 at 285°.

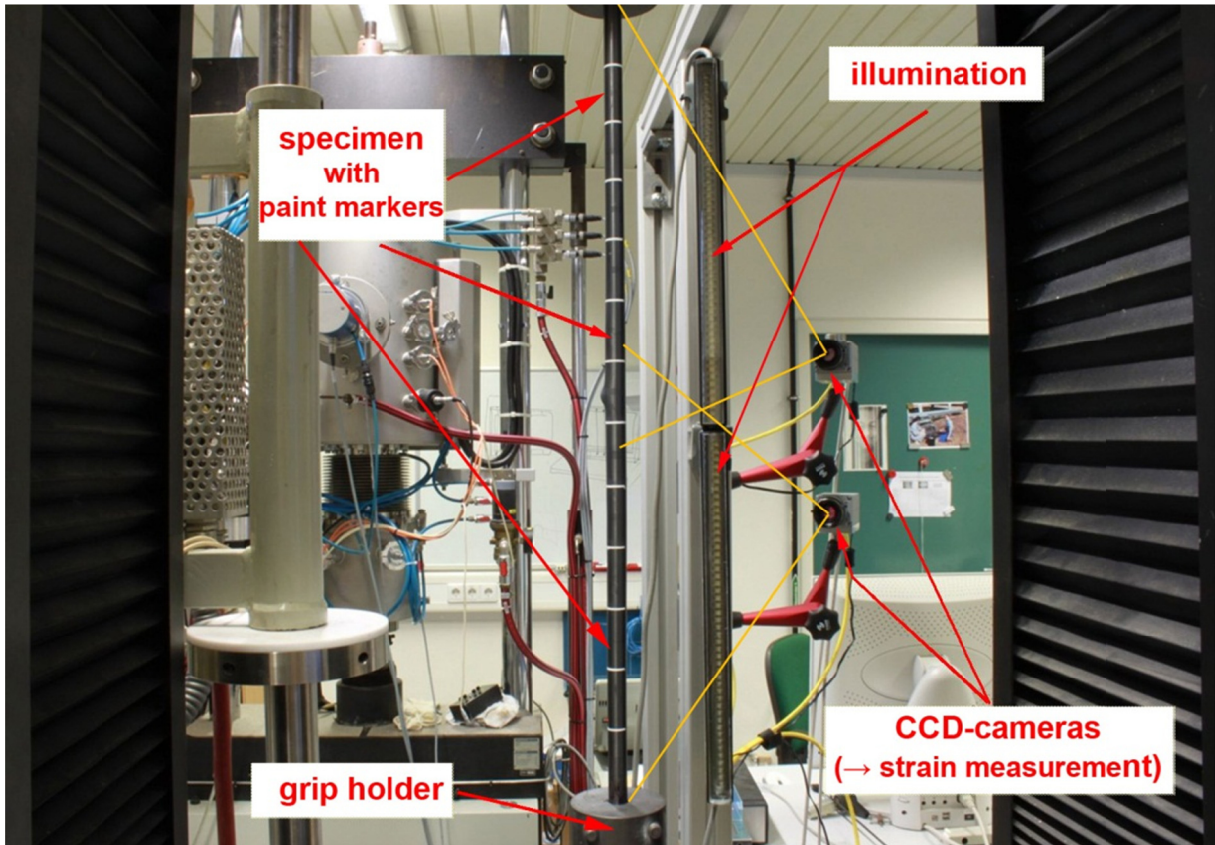


Fig. 115: QUENCH-L0; Testing facility for tensile tests.



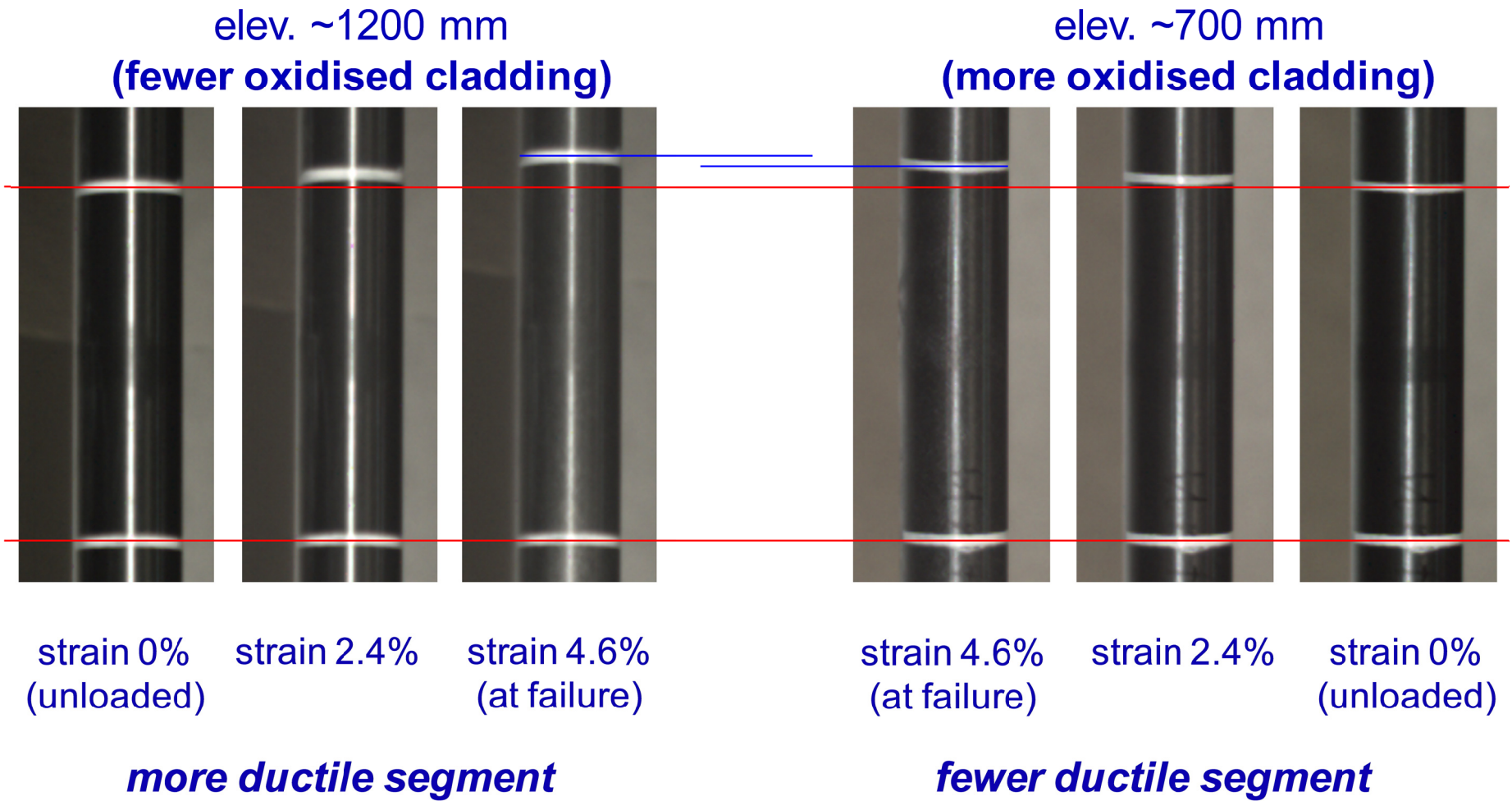
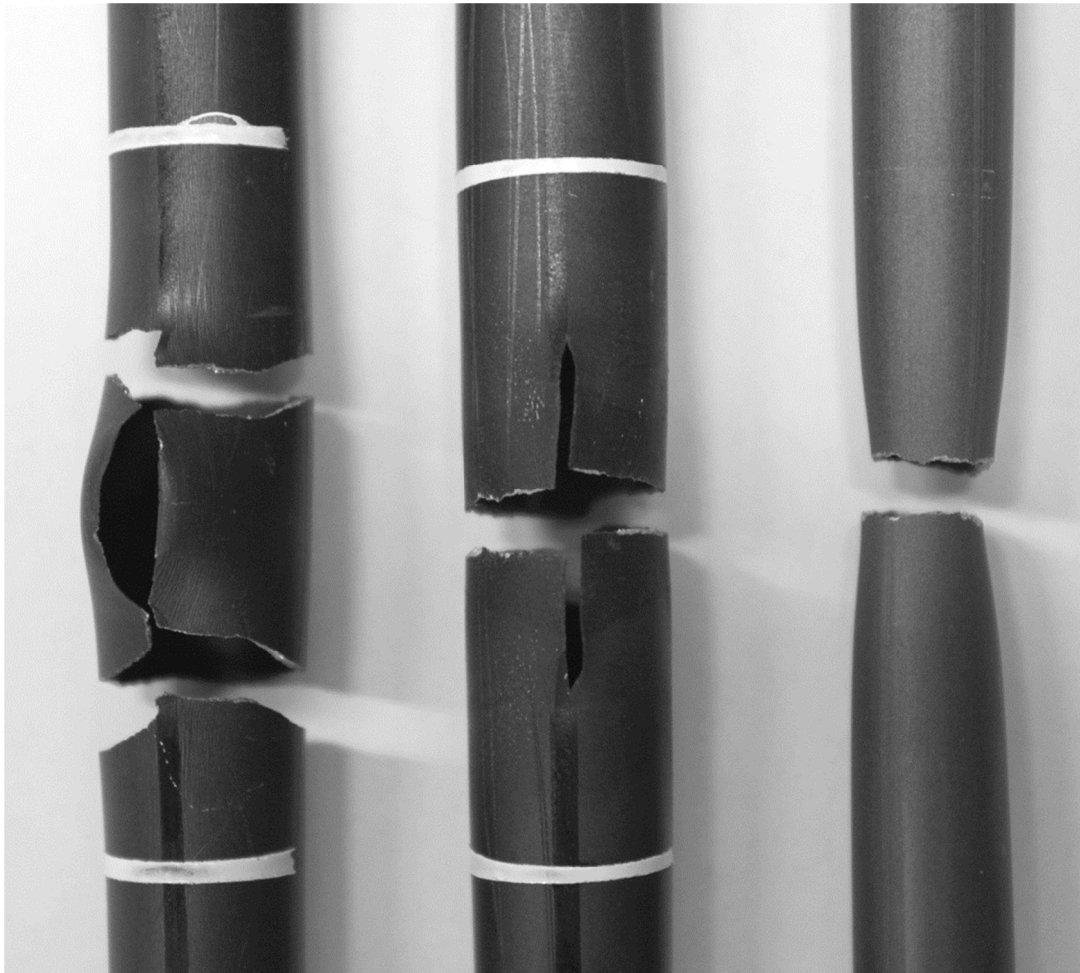


Fig. 116: QUENCH-L0; Tensile test at rod #17: dependence of tube segment ductility from oxidation degree.



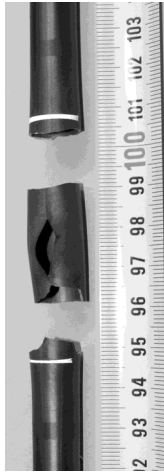


Two ruptures near to burst opening due to hydrogen embrittlement.

Rupture across the burst opening middle due to stress concentration.

Rupture near end plugs after plastic deformation.

Fig. 117: QUENCH-L0; Three types of cladding failure during tensile tests.



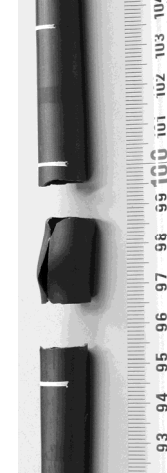
rod #1: 2 ruptures along hydrogenated bands



rod #2: 2 ruptures along hydrogenated bands

-

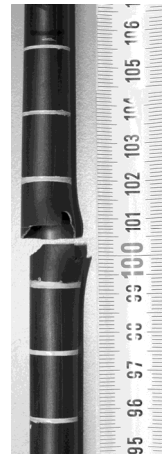
rod #3



rod #4: 2 ruptures along hydrogenated bands



rod #5: rupture and crack at upper hydrogenated band



rod #6: : rupture at burst middle



rod #7: middle cross crack and rupture at low hydrogenated band



rod #9: rupture at upper rod holder

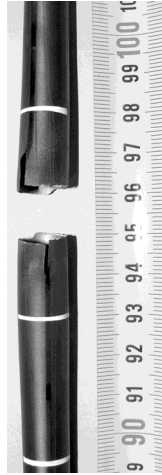
Fig. 118: QUENCH-L0; Rupture positions of rods of inner group after tensile tests; ruler position adjusted to burst middle.



rod #10: rupture at low sample holder



rod #11: rupture at upper sample holder



rod #12: rupture at burst middle



rod #13: rupture at burst middle



rod #14: rupture at burst middle

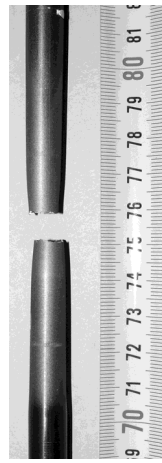
rod #15



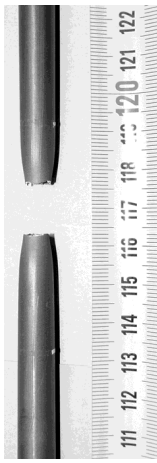
rod #16: rupture at upper sample holder



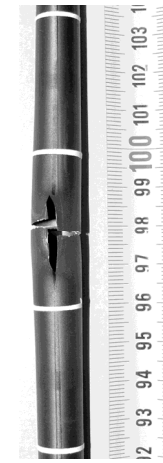
rod #17: rupture at stuck pellet



rod #18: rupture at low sample holder



rod #19: rupture at upper sample holder



rod #20: rupture at burst middle



rod #21: rupture at burst middle

Fig. 119: QUENCH-L0; Rupture positions of rods of outer group after tensile tests; ruler position adjusted to burst middle.

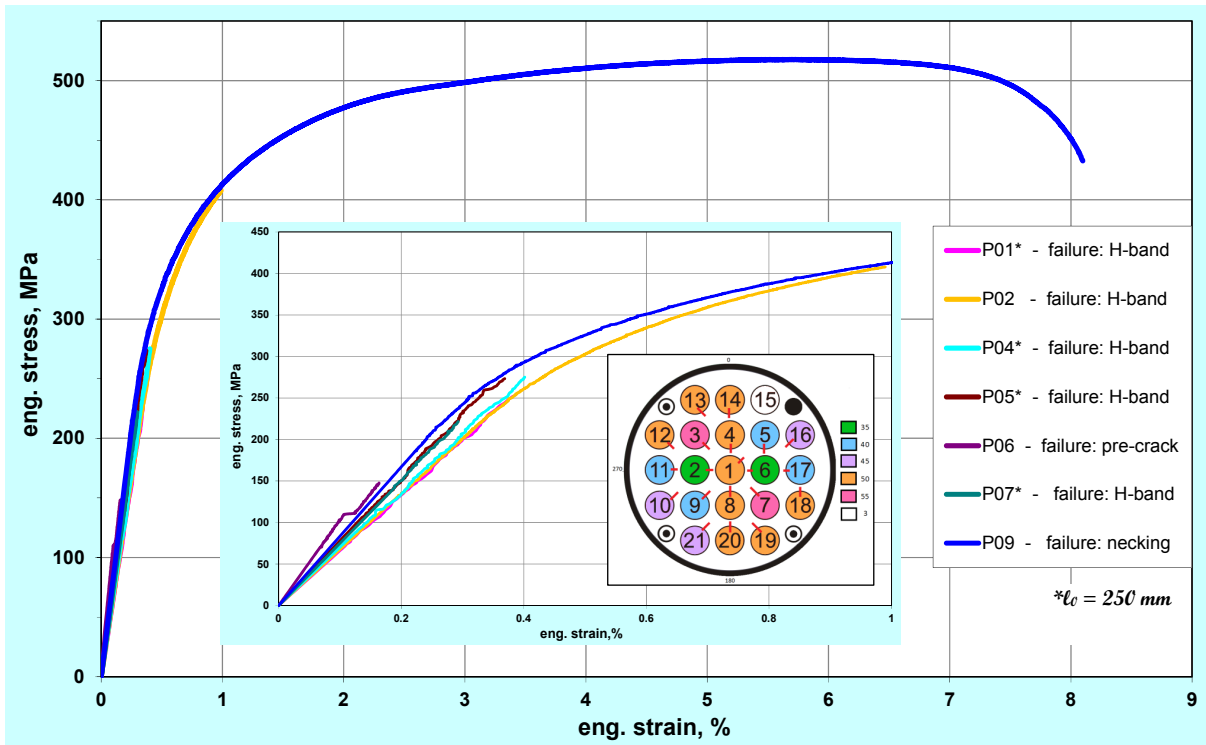


Fig. 120: QUENCH-L0; Results of the tensile tests: claddings from the inner group of the bundle.

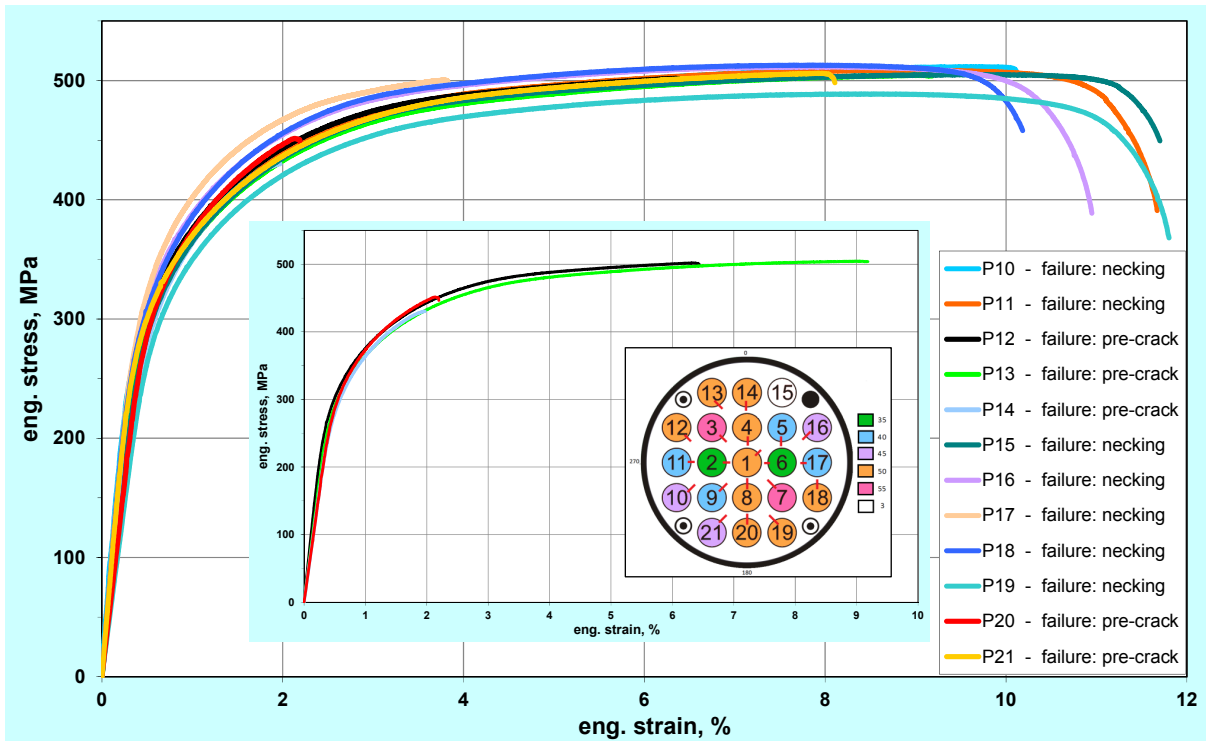


Fig. 121: QUENCH-L0; Results of the tensile tests: claddings from the outer group of the bundle.

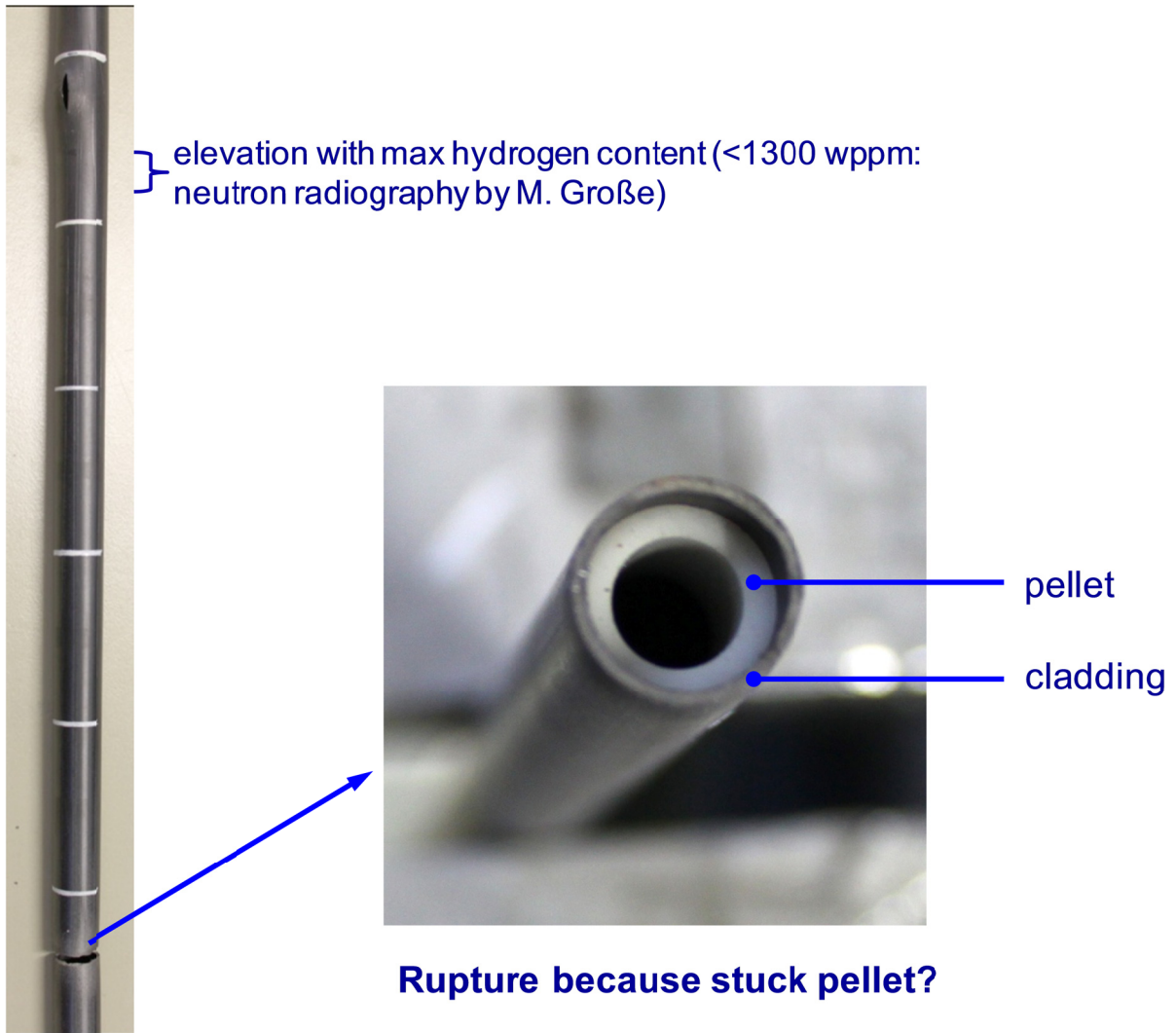


Fig. 122: QUENCH-L0; Rupture position outside ballooning rod #17 (40 bar).

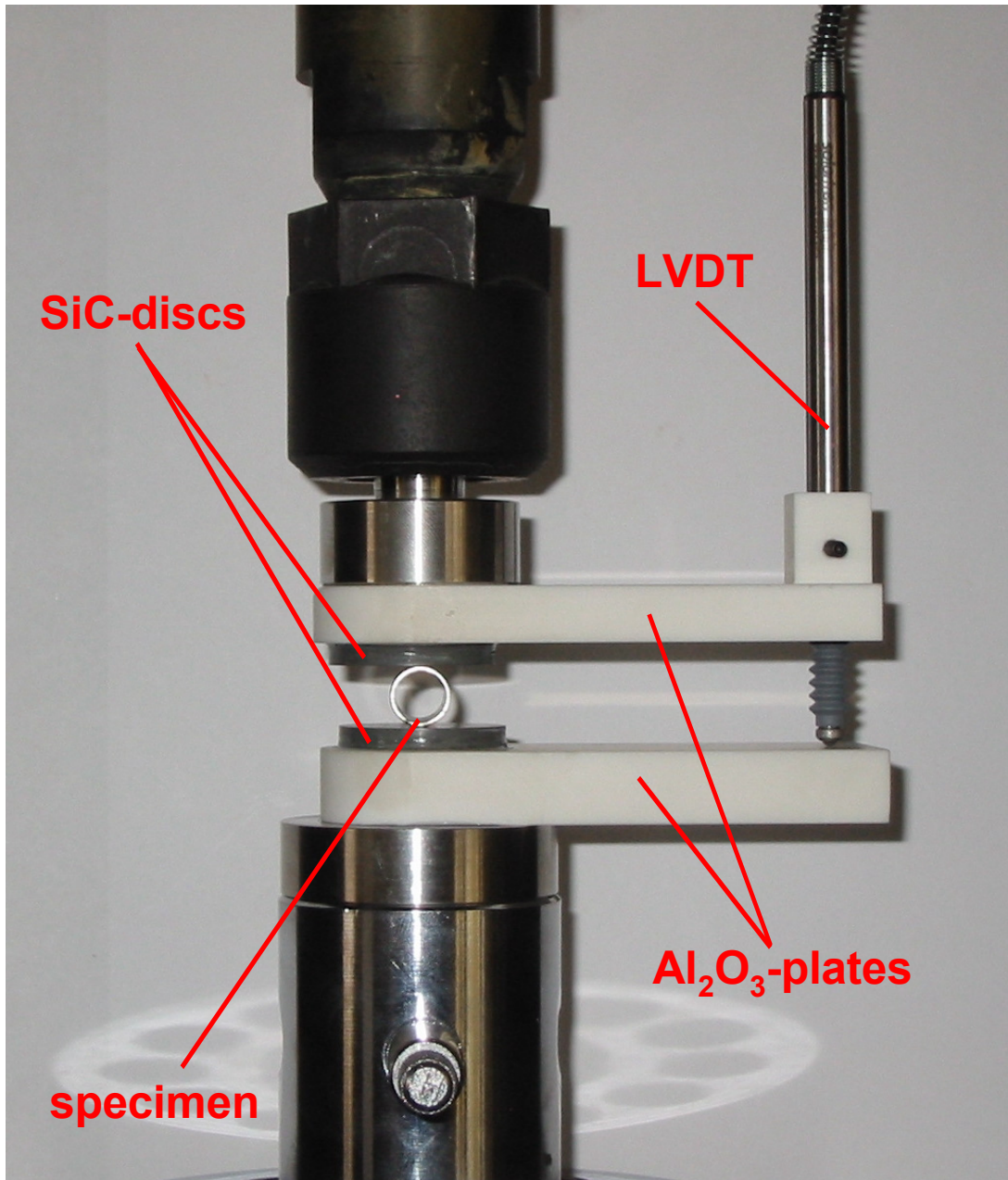
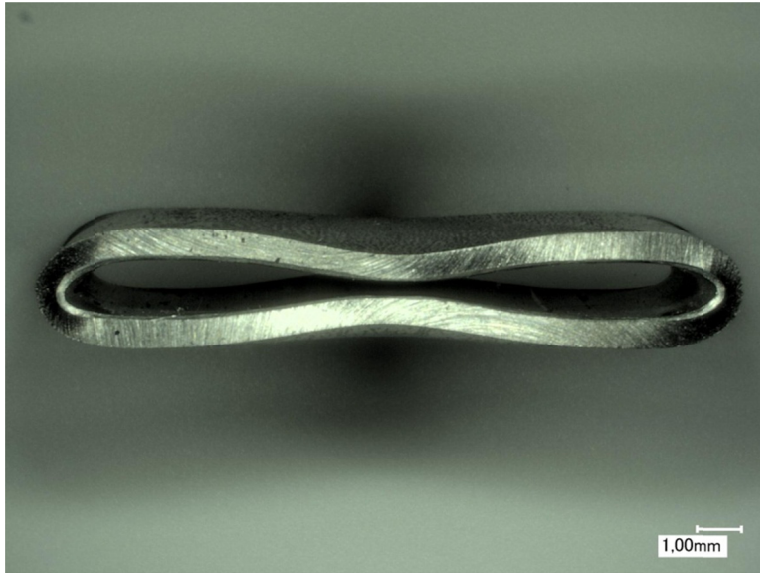
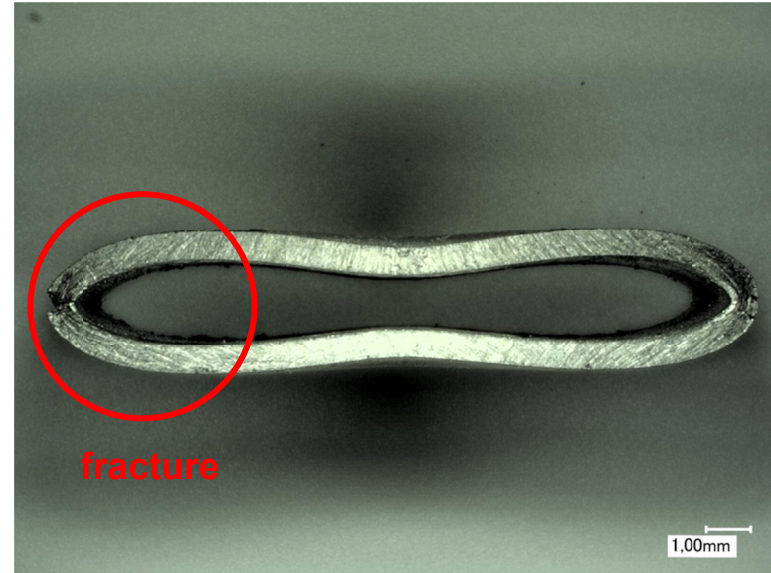


Fig. 123: QUENCH-L0; Test setup machine for the ring compression tests.





failure caused by plastic instability



failure caused by fracture

Fig. 124: QUENCH-L0; General failure behaviour of the rings.

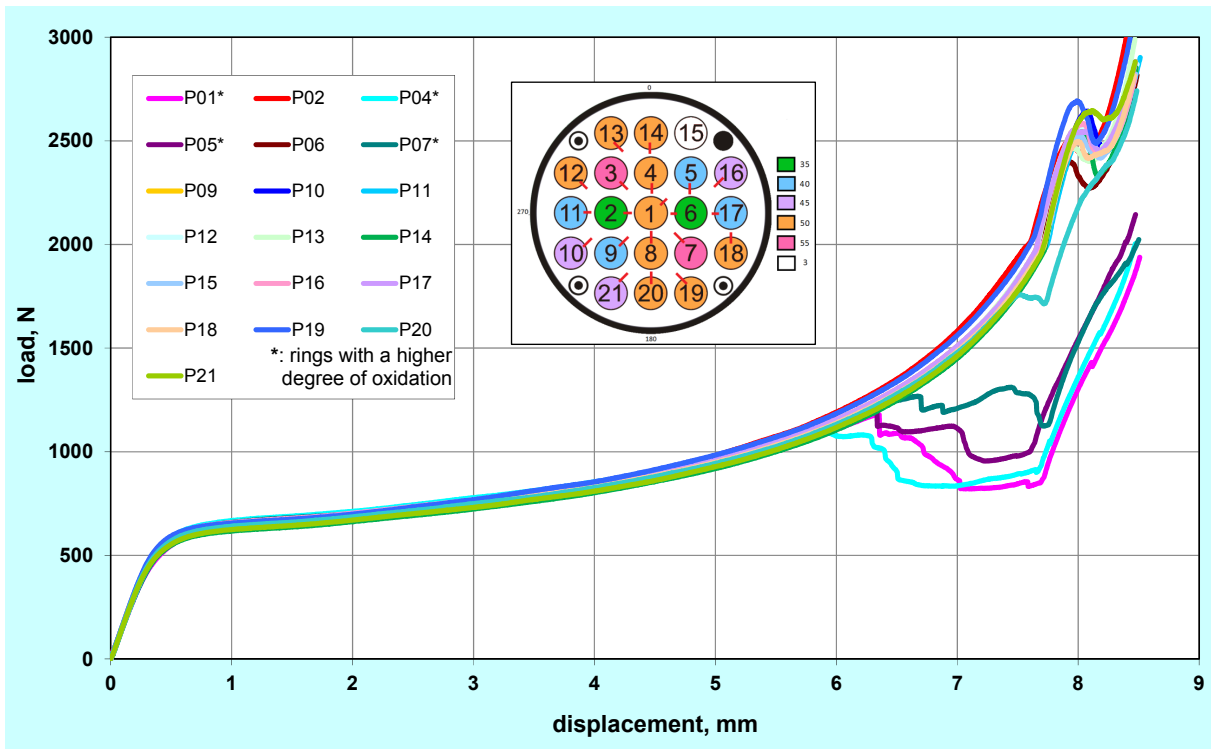


Fig. 125: QUENCH-L0; Results of the ring compression tests: rings of the upper part of the claddings.

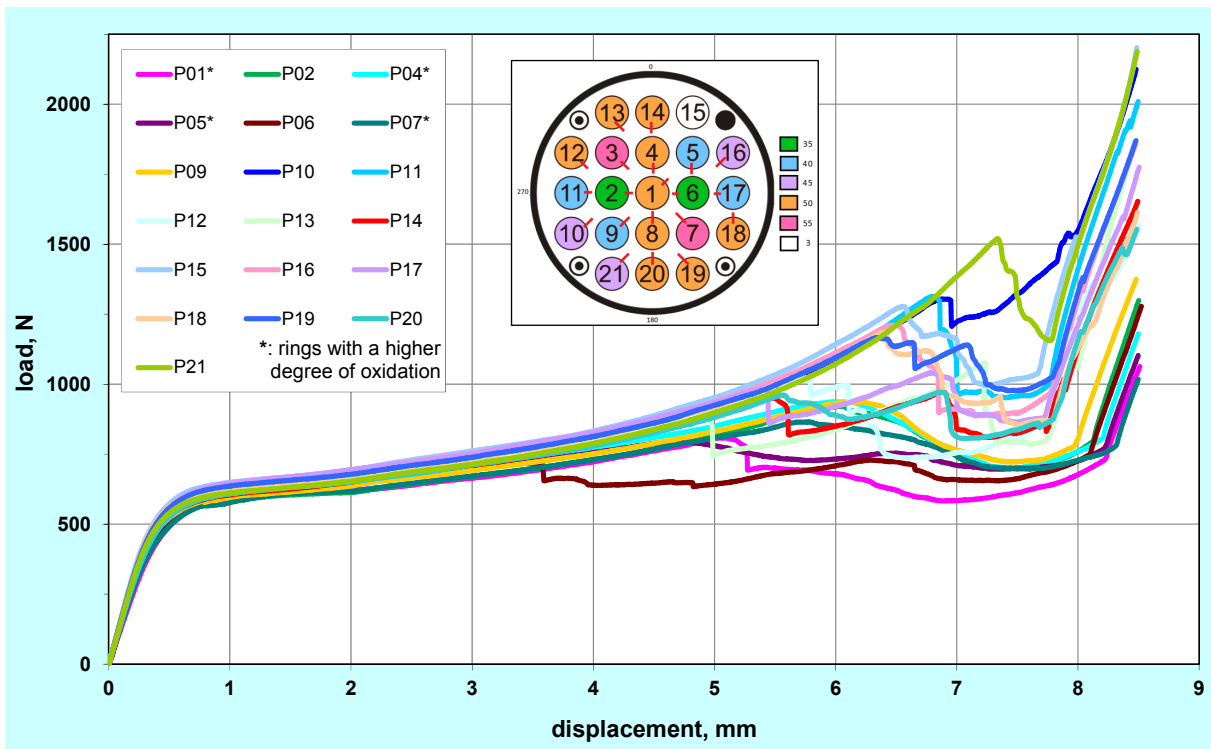



Fig. 126: QUENCH-L0; Results of the ring compression tests: rings of the lower part of the claddings.





The QUENCH-LOCA project on out-of-pile bundle tests under conditions of a loss-of-coolant reactor accident is integral part of the Nuclear Safety Program at the Karlsruhe Institute for Technology. The overall objective of this bundle test series is the investigation of ballooning, burst and secondary hydrogen uptake of the fuel cladding tubes under representative design basis accident conditions.

The project was started in 2010 with the QUENCH-L0 scoping test used 21 heated rods with as-received Zircaloy-4 claddings. The total length of each fuel rod simulator, electrically heated by central tungsten heater, is 2.5 m. Each rod was separately pressurized with krypton with initial pressures of 35, 40, 45, 50, and 55 bar. The duration of transient from 520 to 1070°C was 185 s. The decreased yield strength and increased ductility of the heated cladding resulted in a progressive ballooning and consequent burst of all of the pressurized rods. The first burst occurred on 110 s after transient initiation. All pressurized rods failed within the next 60 s. The experiment was terminated by rapid cooling to 130°C. Post-test investigations showed strain values between 20 and 35% at hottest cladding positions with oxidation degree corresponding to 2% ECR. Maximal blockage of cooling channel is 21%. Neutron radiography of cladding tubes from the inner rod simulator group revealed so called secondary hydrogenation with hydrogen concentration up to 2560 wppm in cladding regions near to burst positions. The formation of hydrogen containing bands with increased microhardness and a width of about 10 mm was observed at the boundary of the cladding inner oxidized area. The tensile tests with these claddings showed that the specimens fail mainly within the region of the hydrogen affected zones.